DISS. ETH NO. 23827

PHYSICAL PROCESSES IN PULSED LASER DEPOSITION

A thesis submitted to attain the degree of

DOCTOR OF SCIENCES of ETH ZURICH

(Dr. sc. ETH Zurich)

presented by

ALEJANDRO OJEDA GONZÁLEZ-POSADA

MSc. Eng., Oxford Brookes, United Kingdom

born on *24.08.1981*

citizen of Spain

accepted on the recommendation of

Prof. Dr. A. Wokaun, examiner
Prof. Dr. T. Lippert, co-examiner
Prof. Dr. D. Günther, co-examiner

2016

"It took them only an instant to cut off that head, and a hundred years may not produce another like it"

J. L. Lagrange after A. Lavoisier,

on the fragility of Science

Preface

Acknowledgements

Index

List of abbreviations

Index	Description
AES	Auger electron spectroscopy
AF	Anti-ferromagnetic
AOTF	Acousto-optic tunable filter
CAD	Computer aided design
CAF	Canted anti-ferromagnetic
CO	Charge ordered
EDX	Energy-dispersive X-ray spectroscopy
ERDA	Elastic recoil detection analysis
FI	Ferromagnetic insulator
FM	Ferromagnetic
FWHM	Full width at half maximum
ICCD	Intensified charge coupled device
MFP	Mean free path
MS	Mass spectrometer
PIXE	Particle-induced X-ray emission
PLD	Pulsed laser deposition
PSI	Paul Scherrer Institut
QCM	Quartz crystal microbalance
RBS	Rutherford backscattering spectrometry
RHEED	Reflection high-energy electron diffraction
SDD	Silicon drift detector
SEM	Scanning electron microscope
SIMS	Secondary ion mass spectrometry
ToF	Time of flight
UHV	Ultra high vacuum
XPS	X-ray photoelectron spectroscopy

XRF	X-ray fluorescence
YAG	Yttrium aluminium garnet
YSZ	Yttria stabilized zirconia

Abstract

The apparent ease to prepare thin films with a complex composition and for a wide range of materials is one of the reasons for the widespread use of pulsed laser deposition (PLD). However, this congruent transfer using PLD does not always take place. The influence, in terms of film thickness and composition, of fundamental process parameters of pulsed laser deposition is explored in detail. Initially RBS measurements of films deposited at different angles of $BaTiO_3$, $CaTiO_3$, $La_{0.4}Ca_{0.6}MnO_3$, $EuAlO_3$, and $LiMn_2O_4$ were performed to study the influence of the background gas pressure when depositing multi-elemental oxide materials. With increasing gas pressure the typical forward directed deposition of PLD changes to a constant thickness at all angular locations. A linear relationship was found between target mass-ratios and compositional deviations. This can lead to compositional deviations of up to 70% for large mass-ratios in certain pressure regimes.

This effect is investigated further for the thesis' model system $La_{0.4}Ca_{0.6}MnO_3$ by time and space resolved imaging in vacuum, $1x10^{-2}$mbar and $1x10^{-1}$mbar O_2 and Ar. The ablation in vacuum shows dissimilar arrival times for the different neutral species and a backscattering of the impinging species from the substrate. At $1x10^{-2}$mbar, a specie-dependent plume splitting appears and preferential scattering of the lighter elements is detected generating a cation off-stoichiometry along the plume axis. In addition at $1x10^{-1}$mbar the plume expansion in this relatively high pressure traps a portion of the background gas against the substrate holder, thereby creating a transient high local pressure with remarkable effects once the plume reaches the substrate. In an O_2 background it creates a long-lived volume of excited species (mostly LaO I), while in Ar a rebound wave is seen which travels backwards and recoats/contaminates the target with a different composition than the original target (background gas dependant). This has important effects on film composition and is in agreement with the RBS film measurements. It may provide a new path for an increase in oxygen content in thin films by careful engineering of an appropriate substrate holder for utilizing the volume of excited metal oxygen species. The same effects are also detected in Ag ablation and are probably valid for most target materials. There is a clear influence of substrate heating on the plasma expansion due to the background gas density gradients, reducing the stopping power of the background gas and already detectable 2 cm away from the substrate. Both rebound and excitation effects are reduced in intensity due to the substrate heating.

Complimentary angle-resolved mass spectrometry (MS) measurements are performed for $La_{0.4}Ca_{0.6}MnO_3$ and $CaTiO_3$ in vacuum, O_2 and Ar environments. The results in terms of ionic counts are qualitatively in good agreement with film thickness measurements. They confirm the preferential formation of metal oxygen species with higher dissociation energies than O_2. The efficiency for O_2 background dissociation seems linked to the kinetic energies of the participating elements. It was found that the kinetic energy dependence is strongly correlated

with the mass of the participating elements: Higher masses yielding higher kinetic energies and, thus, a higher O_2 dissociation.

Additionally, the effect of laser spot geometry is analysed by angle-resolved film RBS measurements for vacuum, $1x10^{-2}$mbar and $1x10^{-1}$mbar Ar and by MS measurements for vacuum. The results show the prevalence of the flip-over effect for all pressures except for the highest, i.e. $1x10^{-1}$mbar, where the film thickness is constant for all angles due to the rebound effect. The composition profiles show noticeable compositional variations of up to 30% with respect to the target material depending on the background gas pressure, the angular location, and the laser spot dimensions. The MS measurements show the variation of the angular kinetic energy profiles which is in agreement with the broadening of the plume when less species are travelling together (i.e.: for the smaller laser spot).

Finally the effect of laser fluence and background pressure on plasma plume shape is assessed by imaging. It shows that fluence and pressure are directly linked to achieve a similar plume shape. Higher fluences yield higher ablation rates and higher kinetic energies and can match higher pressure regimes to achieve similar plume forms. The shape of the plume is found to be a strong identifier of the deposition regime and depends on the stopping power (scattering cross section and mass) and pressure of the background gas with O_2 requiring higher pressure than Ar to achieve similar effects. Fluences close to the ablation threshold show unstable preferential ablation and should be avoided.

In summary, in PLD congruent transfer is not always the case, compositional changes with respect to the target show dependencies on (in order of influence): target material, deposition pressure, fluence, target-to-substrate distance and angular location (substrate size).

Zusammenfassung

Die scheinbare Leichtigkeit verschiedenste Materialien mit einer komplexen Zusammensetzung als dünne Schichten darzustellen, ist einer der Gründe für die große Verbreitung und Nutzung der gepulsten Laserablation (PLD). Der damit implizierte kongruente Transfer der Materialzusammensetzung ist allerdings nicht notwendigerweise gegeben. Um dieses besser zu verstehen, wird in dieser Arbeit der Einfluss fundamentaler Prozessparameter der gepulsten Laserablation auf Schichtdicke und deren Zusammensetzung im Detail untersucht. Zunächst wird die Druckabhängigkeit der Filmzusammensetzung von $BaTiO_3$, $CaTiO_3$, $La_{0.4}Ca_{0.6}MnO_3$, $EuAlO_3$, und $LiMn_2O_4$, abgeschieden unter verschiedenen Depositionswinkeln, mittels Rutherford Backscattering (RBS) bestimmt. Mit steigendem Gasdruck geht dabei die typisch vorwärts gerichtete Deposition in eine isotrope über mit einer konstanten Schichtdicke für alle Depositionswinkel. Dabei wurde ein linearer Zusammenhang zwischen den Target Massenverhältnissen und der Filmzusammensetzung gefunden, die für bestimmte Druckbereiche bis zu 70% betragen kann.

Dieser Effekt wurde genauer mittels räumlich und zeitaufgelösten Abbildungen am Modellsystem $La_{0.4}Ca_{0.6}MnO_3$ für verschiedene Druckbereiche (Vakuum, $1x10^{-2}$mbar, $1x10^{-1}$mbar in O_2 und Ar) untersucht. Ablation in Vakuum zeigt unterschiedliche Ankunftszeiten für verschiedene neutrale Plasmaspezis und ein Zurückstreuen von aufprallenden Spezies von der Substratoberfläche. Bei einem Druck von $1x10^{-2}$mbar tritt eine speziesabhängige Aufspaltung der Plasmaplume auf. Darüber hinaus wird ein bevorzugtes Streuen der leichteren Elemente beobachtet welches eine abweichende Kationenzusammensetzung entlang der Plume-Achse zur Folge hat. Die Plumeausbreitung in dem relativ hohen Druckbereich von $1x10^{-1}$mbar drückt das Hintergrundsgas gegen den Substrathalter und erzeugt dabei kurzfristig lokal einen höheren Druck. Als Folge dessen werden in einem O_2 Hintergrund in einem definierten Volumen angeregte Spezies erzeugt (überwiegend LaO I) und in Ar ist eine zurückgestreute Welle zu beobachten die das Target mit einer Zusammensetzung beschichtet die deutlich verschieden zu der Targetzusammensetzung ist. Diese Beobachtungen haben wichtige Auswirkungen. Zum einen auf die Gesamtfilmzusammensetzung die in Übereinstimmung mit RBS Messungen ist. Darüber hinaus könnte man einen geeigneten Substrathalter konstruieren, der das komprimierte Sauerstoffvolumen und die darin erzeugten Metall-Sauerstoffspezies zur Erhöhung des Sauerstoffgehaltes in den Oxiden nutzt. Diese beschriebenen Effekte lassen sich auch für eine Ag-Ablation nachweisen, und sie sind vermutlich für andere zu ablatierende Materialien gültig. Es gibt auch einen klaren Einfluss der Substraterhitzung auf die Plasmaexpansion. Dabei bildet sich ein Druckgradient oberhalb der erhitzten Oberfläche aus, der das Stoßverhalten des Hintergrundsgases deutlich ändert. Der Effekt ist bereits 2cm oberhalb der erhitzten Oberfläche zu beobachten mit der Folge einer reduzierten Rückstoßwelle und einer Verringerung der Intensität der angeregten Spezies.

Komplementäre, winkelaufgelöste massenspektroskopische (MS) Messungen wurden für $La_{0.4}Ca_{0.6}MnO_3$ und $CaTiO_3$ in Vakuum, O_2 und Ar durchgeführt. Die Ergebnisse sind in guter qualitativer Übereinstimmung mit den Filmdickenmessungen. Sie bestätigen auch die bevorzugte Bildung von Metall-Sauerstoff Spezies mit einer Dissoziationsenergy größer als die von O_2. Die Effizienz der Dissoziation in O_2 scheint verknüpft zu sein mit der kinetischen Energie der beteiligten Elemente. Eine höhere Masse korreliert mit einer höheren kinetischen Energie und damit einer höheren O_2 Dissoziation.

Die Auswirkungen der Laserspotgeometrie wurden mittels winkelaufgelöster RBS Messungen in Vakuum, $1x10^{-2}$ mbar und $1x10^{-1}$ mbar Ar untersucht sowie mit MS Messungen in Vakuum. Die Ergebnisse zeigen die Auswirkungen des flip-over Effektes für alle Drücke, außer für den $1x10^{-1}$ mbar Bereich. Hier ist die Filmdicke konstant für alle Depositionswinkel aufgrund des Rückstoßeffektes. Die Filmzusammensetzungen zeigen deutliche Abweichungen von bis zu 30% bezüglich der Targetzusammensetzung, Hintergrundsgasdruck, Winkel, und Laserspotgröße. Die MS Messungen zeigen darüber hinaus die Variation der kinetischen Energie als Funktion des Winkels in Übereinstimmung mit der Verbreiterung der Plume wenn sich weniger Spezies in der Plasmawolke zusammen bewegen in Analogie zur Ablation mit einem kleineren Laserspot.

Zum Schluss wurde der Effekt der Laser Fluence und des Hintergrundsdruckes auf die räumliche Ausprägung der Plasmawolke mittels räumlich und zeitaufgelöster Abbildung untersucht. Es konnte gezeigt werden, dass Fluence und Druck direkt mit der Form der Plume korrelieren. Höhere Fluencen ergeben höhere Ablationsraten und höhere kinetische Energien. Die korrespondierenden Formen der Plasmawolken entsprechen dann Formen wie man sie mit einem höheren Druck erhalten würde. Die Form der Plasmawolke ist ein starker Indikator für das Depositionsregime und abhängig von dem Streuquerschnitt (Masse) und des Druckes des Hintergrundgases. Für O_2 benötigt man einen höheren Depositionsdruck als für Ar um einen vergleichbaren Effekt auf die Form der Plasmawolke zu erzielen. Fluenzen an der Schwelle zur Ablation zeigen eine instabile, präferentielle Ablation und sollten vermieden werden.

Zusammenfassend kann man sagen, dass ein kongruenter Transfer für PLD nicht die Regel ist und Änderungen in der Zusammensetzung des Filmes im Vergleich zum Target signifikante Abhängigkeiten zeigen. Die wichtigsten Abhängigkeiten sind Targetmateria bzw. Targetzusammensetzung, Abscheidungsdruck, Fluence, Target-Substrate Distanz, und Winkel bzw. Substratgröße.

1 Pulsed Laser Deposition: Is congruent transfer possible?

The process of pulsed laser deposition (PLD), a pulse of photons exits the laser, travelling through a path guided by mirrors until they are focused by an optical lens into a vacuum chamber. Inside, in a low pressure environment, they hit the ablation target, transferring the energy to the material through the electrons of the target atoms up to a depth of tenths of nanometres. Free and bound electrons are excited. Some bound electrons are immediately freed (non-thermal), others receive high energy levels. The excited electrons start to transfer their energy to the lattice (electron-phonon coupling) in the order of ps initiating a thermal process. While the ns pulse continues to arrive a plasma is generated just above the target from the combination of non-thermal (electronic) and thermal (evaporation) ejection mechanisms, which continues to absorb the pulsed photons that have not yet ceased to arrive. Then the plume expands adiabatically at velocities of ~100'000 km/h and the species travel the 40 mm distance to the substrate in a matter of μs. Some might encounter background gas species and interact chemically or elastically, others might not (depending on the pressure). Upon arrival to the substrate its high temperature completes the process by allowing the mobility of atoms to form the desired lattice structure. This process is repeated over and over again, resulting in a process named pulsed laser deposition (PLD). An extremely versatile technique for the deposition of complex materials which appears simple at first, but hides a fascinating complexity.

It is indeed the preferred choice when growing functional films of multi-element oxides and has been a fundamental contributor to material science developments since 1987 in a wide range of fields, from superconductivity, to electrocatalysis or electrochemistry [1-3]. It provides a great versatility and gained its status after discovering its capability to transfer the composition of complex target materials to thin films [3].

In most of those cases the film composition is often critical to achieve the desired properties. The importance of a composition control is illustrated in the composition diagram of this thesis'

model system (Fig.1.1), $La_xCa_{1-x}MnO_3$ (0≤x≤1) [4], in which small variations in the La/Ca ratio can significantly change its physical properties, e.g. electrical conductivity, charge ordering or the magnetic ground state.
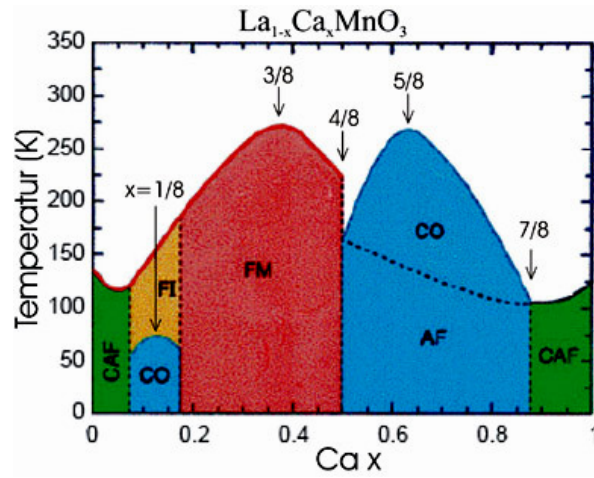
Fig.1.1. Properties of $La_{1-x}Ca_xMnO_3$ films vs. "Ca concentration" showing how the ability to control the composition of the deposited films can steer the film to desired properties (from [4]). Properties shown: ferromagnetic (FM), anti-ferromagnetic (AF), canted anti-ferromagnetic (CAF), and charge ordering (CO), and ordering as a ferromagnetic insulator (FI).

Although it is commonly assumed that in PLD a congruent composition transfer from target to film takes place, this is not necessarily the case. Often it is difficult to find suitable process parameters or users resort to over-stoichiometric targets to achieve the desired film compositions [5]. The causes for such compositional deviations are a multitude of processes that are reviewed in [2, 6, 7] and references therein. They can be classified into three main areas which are also the core of this thesis: target-laser, plume, and substrate effects.

Some of them have been previously investigated by former group members. For example, Stela Canulescu investigated the compositional deviations by species resolved plume imaging and emission spectroscopy of $LiMn_2O_4$ as well as the influence of fluence and target to substrate distance on the deposition of $La_{0.6}Ca_{0.4}MnO_3$. Matthias Bator used optical emission spectroscopy, plasma imaging and plasma MS to correlate the plasma species composition to the multiferroic properties of the deposited *RE*MnO$_3$ films. Martin Esposito did MS measurements of the plasma plume of $La_{0.4}Ca_{0.6}MnO_3$ discovering that the plasma with the highest amount of metal oxygen species and negative ions often brought the highest crystalline quality. In addition, Jikun Chen performed MS analysis using ^{18}O labelling of the target to trace the origin of the plasma oxygen which was found to originate mostly from the background gas except for the vacuum depositions. In general, the findings have been valuable and strengthened the motivation to analyse the source of the compositional deviations in the three areas mentioned before.

1.1 Target-laser ablation effects

When ablating the target with laser fluences slightly above the ablation threshold the film composition may deviate considerably, either towards stoichiometric values (e.g.: $LiCoO_2$ [8] or $SrTiO_3$ [9]) or not, as in the case of $BaTiO_3$ [10], where stoichiometric films are mostly obtained at fluences much higher than the threshold fluences.

The ablation effects are also strongly dependant on the precise target material. Thermal segregation due to thermal processes (ns pulses) will vary considerably depending on the material i.e. metal alloys or oxides, with metal alloys being more prone to such segregation. The choice of a ps/fs pulse instead might avoid these heat transfer effects and be more efficient (plasma shielding is avoided), but results in high numbers of undesired nano-particles instead in addition to the created plasma species [8].

The wavelength of the laser also affects the ablation process strongly. In general, the shorter the wavelength the larger the ablation rate [9] as they offer higher photon energies that may allow bond breaking of the atomic lattice and ionization, causing atom and ion ejection without heating effects [10]. Furthermore UV irradiation reduces the amounts of nano particles in contrast to longer wavelengths which yield higher densities and size of particulates [2]. This may contribute to stronger compositional deviations in a film [11] . Interestingly, the wavelength affects the size and frequency of the periodic structures appearing on its surface [12]. The wavelength not only affects the absorption by the target material but also the absorption by the laser generated plasma plume with, interestingly, higher absorption at longer wavelengths [13]. Typically, the useful range for ablation lies between 200-400 nm and most depositions are performed with either excimer (157,193, 222, 248, 308 or 351 nm) or Nd^{3+}: YAG lasers (355 or 266 nm) [2].

Furthermore the choice of the laser spot geometry impinging on the target is not trivial and has a strong influence on the angular profiles of film thickness and composition [2, 8, 14-20]. One of the most fascinating effects of spot choice is the so-called flip-over effect: where the use of a non-circular laser spot changes the plasma plume expansion dynamics strongly.

Of course, the conditions of the target itself in terms of morphology (polished or already ablated, with periodic structures like cones, ripples…), density or composition (i.e.: preferential segregation) also play an important role in the deposition. For example in [21] it is shown that for $La_{0.64}Ca_{0.35}Co_{0.95}O_{2.95}$ and certain process parameters, after 1.5 million pulses the target surface composition changes to $La_{0.72}Ca_{0.28}Co_{0.99}O_{2.7}$, although the original target composition can be recovered by mechanical polishing. However, plasma plume effects and species interactions with the background gas are usually the origin of major compositional changes.

1.2   Plume effects

Concerning the plume effects, there have been numerous publications investigating its fundamentals [22-26]. For instance, the use of a background gas, either inert or reactive [2, 3, 7, 27, 28], has important effects on the final film composition as well as on its thickness [6, 29, 30]. In [29] it is shown that for $BiFeO_3$ the Bi/Fe ratio decreases with oxygen pressure during the deposition, which negatively affects the pursued ferroelectric properties of the films. For $LiCoO_2$, Ohnishi *et al.* [31] show that in relatively high oxygen background pressures, where the mean free path (MFP) becomes shorter than the target-to-substrate distance, Li may be preferentially scattered leading to Li deficient films. This is also shown by Dumont *et al.* when producing $LiMn_2O_4$ electrodes by PLD [32] where high background gas pressures have a strong influence on the Li content of the film and the electrochemical activity. Furthermore, Canulescu *et al.* [23] report such an effect experimentally by using time resolved plume imaging to analyse the expansion of the plasma formed by the ablation of $LiMn_2O_4$ for different oxygen background pressures. This leads to the conclusion that the ablation of materials containing a combination of light and heavy elements are prone to be deficient with respect to the light element in as-grown films for certain pressure regimes (preferential scattering). Sambri *et al.* [24] reach the same conclusion with a similar imaging approach for $LaGaO_3$, finding a cation off-stoichiometry at the forefront of the plume. Progress on its modelling has also been achieved by Packwood *et al.* [25] who used experimental data from [33] and developed an analytical model of a collision-induced plume expansion that matches the film Li deficiencies with increased oxygen pressure. Nonetheless, no systematic analysis for additional cation mass ratios has been reported.

1.3   Substrate effects

Alternatively, during film growth it might happen that sticking coefficients of the various elements may differ as they are a function of atomic masses, kinetic energies, incidence angles, and surface energies. This could be a source for compositional deviations. Nevertheless, measurements for different single element depositions have shown that sticking coefficients can be close to unity [34, 35]. A more often described compositional issue during PLD growth of films is preferential sputtering of the growing film by arriving species [6, 34], which is a function of mass, incidence angles, and kinetic energies of the arriving atoms. This has been identified as a source of compositional deviations due to preferential sputtering [33]. For example, for energies above 50eV (easily achieved for fluences of e.g. 2 J/cm^2) the sputtering yield increases considerably with energy and differs for different elements. This has been shown experimentally for many materials (i.e.: Cu, Ni, V, C…) using various ions (i.e.: He$^+$, Ne$^+$, Hg$^+$…) [36] and also by calculations [37]. Furthermore, for heated substrates a "re-vaporization" of certain film components of the deposited material can also take place, for example Li [38, 39].

Apart from the aforementioned effects, the influence of the substrate on film composition is very strong and surprisingly indirect. The exact location of the substrate in terms of distance and misalignment to the plume is critical giving rise to changes of film composition and thickness. There is also the influence of substrate heating on the plasma plume expansion. This is a parameter which is considered to have a strong influence on film growth once the species arrive at the substrate, but does not seem to have a direct influence on the plume expansion. However, several studies show that it does have an influence [40, 49, 50], as the heat transfer from the substrate to the background gas creates a density gradient that affects the expansion dynamics of the plasma plume. This influence of substrate temperature on the background gas density and deposition rates has even been modelled mathematically in [49, 50] using a simplified model of plume front propagation which resolves the equation of motion between the traveling mass of the plume in addition to the swept gas and the external pressure force.

The most surprising and scarcely reported substrate effect, however, is the physical effect that the geometry of the substrate and its holder have on the deposition process. For example Geohegan *et al.* [40] showed that the interactions of incoming and substrate reflected fluxes from pyrolytic carbon ablation in vacuum caused an emission in the near substrate region lasting a few µs. Voevodin et *al.* [41] showed a similar excitation for Zr I in Ar from yttria stabilized zirconia ablation. It seems that the presence of the substrate and its holder change the plasma plume expansion dynamics but very few literature reports on such effect in detail.

1.4   Scope of this work

In summary, it is rather a combination of many interdependent depositing parameters (e.g.: target composition, fluence, background pressure, background gas element, target-to-substrate distance, spot size, or substrate temperature) that may enable the PLD user to deposit a film with the desired composition. Although very often and for practical reasons one must fix some of those process parameters (i.e.: for geometrical reasons) and vary the remaining ones. Even today data from students from the group raises questions on the performance of the films with a strong link to compositional deviations. For instance, Kenta Shimamoto recently discovered that the ferroelectric order of the $TbMnO_3$ films he deposited was severely disturbed due to a Tb enrichment originating from the background gas pressure [42].

It would be therefore very valuable to understand the PLD process better, to have guidelines on how much a film composition can deviate, if it is more pronounced or not in certain material combinations and which process parameters to vary to adjust the composition. This would not only raise awareness among PLD users that a congruent transfer is not guaranteed, but also open the door to on-demand composition variations.

The work presented in this thesis takes this aim and uses a variety of diagnostic techniques to accomplish it (i.e.: plasma imaging, ion beam analysis, mass spectrometry, profilometry…) as

very often each of them only allows a limited view of the whole components involved in the PLD deposition (i.e.: neutrals, ions, excited species…). Therefore only through the overlap of different techniques and a good understanding of their capabilities and limitations can a comprehensive overview of the PLD process be attained.

The thesis is structured in 7 chapters. Chapter 2 will briefly introduce the instrumental arrangements used (RBS, ICCD, SEM…), chapter 3 will focus on the effect of the background gas pressure by analysing deposited films angle-resolved for $La_{0.4}Ca_{0.6}MnO_3$ and then extend the findings to 4 additional materials, while chapter 4 will look at the cause of the detected compositional changes by plasma plume imaging, add substrate heating, and encounter surprising rebound effects. Chapter 5 will analyse the effects of the laser spot geometry (flip-over effect) by film and probe based methods, chapter 6 will complete the overview between plasma imaging (chapter 4) and angle-resolved film measurements (chapter 3) by angle-resolved MS measurements to provide an insight into the plasma chemistry. Finally Chapter 7 will combine plasma imaging and MS measurements to understand the effects and interrelation between laser fluence and background gas on the PLD process. More specific remarks, relevant literature, and motivation are given at the beginning of each chapter.

2 Experimental apparatus

The following chapter provides specific and concise descriptions of the equipment used for the experiments performed in this thesis. The working principles of the devices are briefly outlined with the focus on the practical performance and limitations of the equipment. Those experimental setups custom built for these investigations, are described in more detail.

2.1   The PLD setup

2.1.1   Excimer Laser

All experiments presented were performed with the most commonly used laser in PLD, a KrF excimer laser (Lambda Physik LPX 300, 20 ns pulses, λ = 248 nm with a photon energy of ~5eV). In its current state the laser has a maximum pulse energy of 800 mJ at the laser window exit and due to the use of a mask to shape the ablation spot and 3 guiding mirrors, the energy at the chamber entrance is ~100 mJ/pulse. Inside the chamber the energy is further reduced by 10-20% depending on the coating accumulation of the entrance window. For this reason, the energy of the laser spot is constantly monitored to maintain a high degree of reproducibility. The maximum laser fluence attained for a spot size of 1x1.4mm on the ablation target was ~5 J/cm^2. A sketch of the optical setup is shown in Fig.2.1.
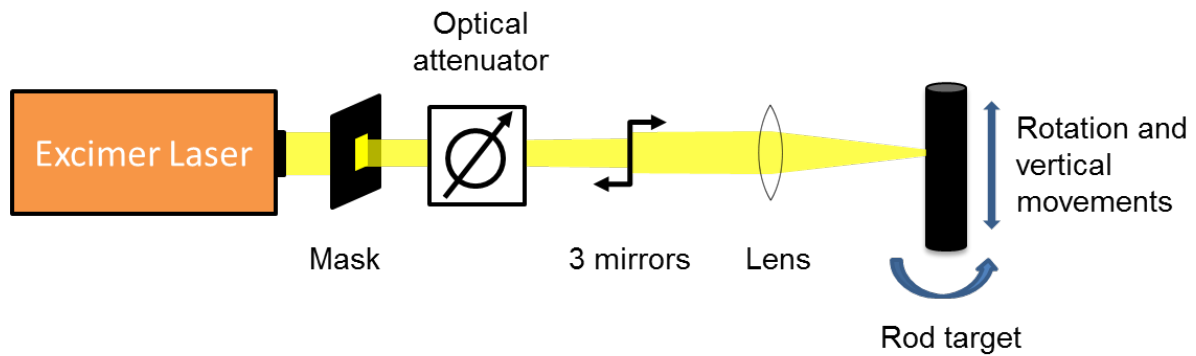
Fig.2.1. Sketch of optical beam path from the excimer laser (left) up to the ablation on the target (right). The devices and distances are not to scale.

2.1.2   Optical attenuator

To finely adjust the laser power arriving at the target an optical attenuator with double dielectric plates was used. It allows adjusting the ablation energy without displacing the beam position as the opposite dielectric plate tilts and cancels the induced beam displacement caused by the tilting of the first dielectric plate.

2.1.3   Laser power meter and fluence calculations

For all fluence selections the laser energy was measured using a Gentec SOLO PE power meter equipped with a power sensor head QE50-SP-H-MB-D0. The spot dimensions were measured by ablating thermal paper and measuring the spot dimensions using an optical microscope.

2.1.4   UHV Chamber

All the experiments were performed in the same PLD chamber. An instrumented UHV chamber (base pressure of 1x10^{-9}mbar and equipped with i.e.: Langmuir probe, mass spectrometer…)

with a 350 mm quartz window to allow plasma plume imaging and optical emission spectroscopy. It is equipped with a target holder capable of storing 5 different rod targets and can also use disk targets with an alternative holder. O_2, Ar or N_2O can be used as background gases.

The laser pulses arrived at the target inside the chamber 45° with respect to the target-to-substrate axis and in the same horizontal plane. A mask was used to obtain a rectangular laser spot, usually with dimensions of 1mm x 1.4mm, which was imaged on the target.
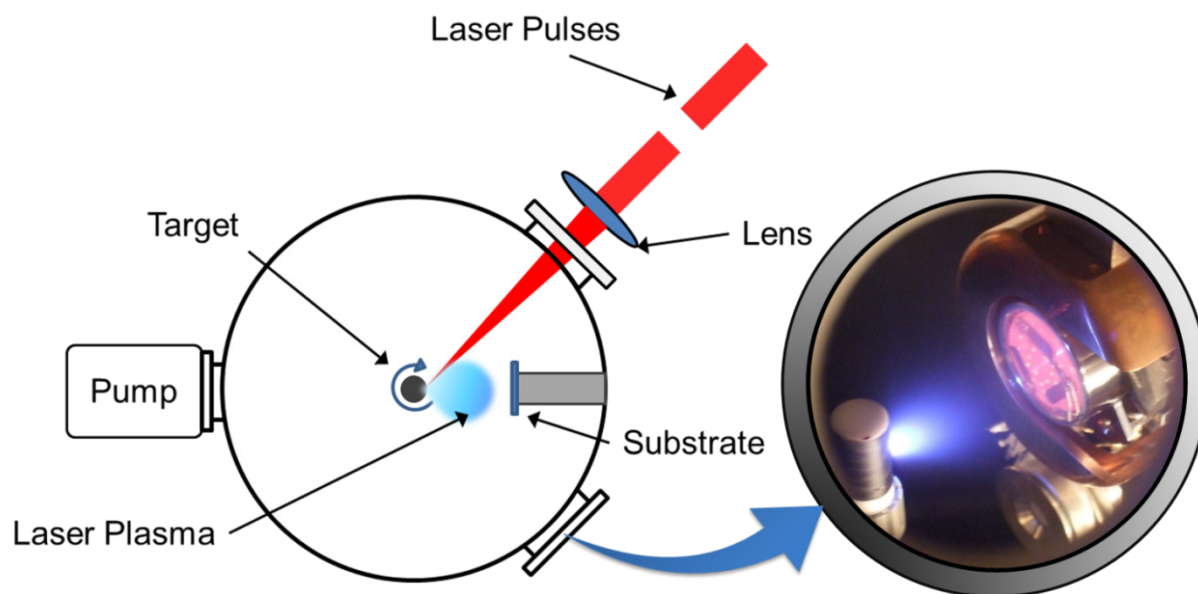
Fig.2.2. Top view sketch of the used UHV chamber with the laser pulse interacting with a rod target. An image from a side window is also shown with the target on the left, the substrate on the right, and the plasma plume in the middle. The devices and distances are not to scale.

2.1.5 Targets

Five cylindrical ceramic targets of $La_{0.4}Ca_{0.6}MnO_3$, $BaTiO_3$, $CaTiO_3$, $EuAlO_3$, and $LiMn_2O_4$ were used for the depositions with a diameter of 10-12mm, a length of 10-40mm and their compositions were verified by RBS or ERDA (for $LiMn_2O_4$). $BaTiO_3$ and $La_{0.4}Ca_{0.6}MnO_3$ had the expected composition, while $CaTiO_3$ and $LiMn_2O_4$ had compositions of $Ca_{1.1}Ti_{0.9}O_{2.9}$ and $Li_{0.7}Mn_2O_{3.8}$ respectively. $EuAlO_3$, due to the much higher scattering cross-section of Eu vs. Al, had an uncertainty of ~7%. With the purpose of avoiding cratering, the targets were continuously rotated and displaced along their main axes.

Additionally two disk targets of $La_{0.33}Ca_{0.66}MnO_3$ and of $CaTiO_3$ were used for the angular MS measurements as the cylindrical shape of the rod targets was not suitable for these experiments.

2.1.6 Special substrate holders

Apart from the traditional frontal substrate holder, two particular holders were designed and manufactured to enable capturing the angular distribution of species:

1. A semi-sphere like substrate holder named the "semi-sphere" holder (Fig.2.3a), in which the target to substrate distance is kept constant at 40mm due to its intrinsic spherical geometry and which has an angular range of ±82°. It can carry up to 20 substrates and has easy optical access for other potential plasma plume measurements.

2. Secondly, a flat substrate holder named the "planar" holder (Fig.2.3b), on which a long substrate can be positioned and which consists of a simple planar surface perpendicular to the plasma plume axis. The angular range covered when positioned at 40mm with respect to the target is +60°. The larger the angular location the longer the travelled path by the arriving species.

Both substrate holders have a central hole. It is used to centre the plasma plume with respect to the holders as it allows the ejected species to travel into the mass spectrometer entrance and find the exact position with the maximum counts at high energies. The manufacturing of the "planar" holder was straightforward, however, due to its complexity, the "semi-sphere" holder was produced by 3D printing using a selective laser melting process (additive manufacturing).
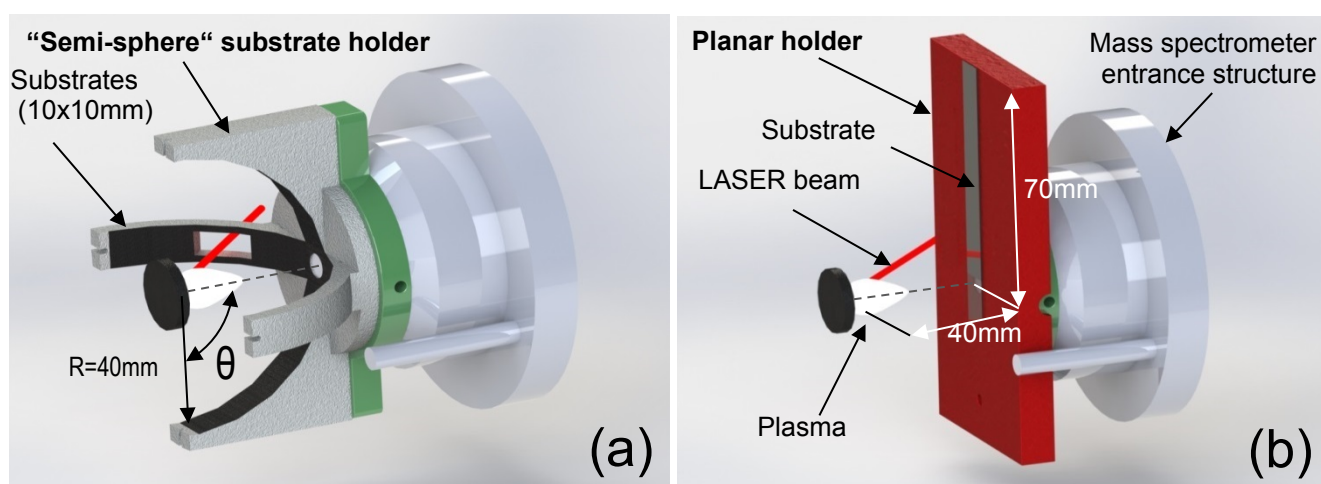
Fig.2.3. 3D representation of (a) "Semi-sphere" holder with multiple substrates (10x10mm) and (b) "Planar" holder with three long substrates (10x70mm), both mounted on structure from UHV chamber.

2.1.1 Quartz crystal microbalance (QCM)

The chamber is equipped with a quartz crystal microbalance which measures very small mass variation by analysing frequency changes on a quartz crystal resonator. The crystal's resonance is changed by the deposition of material on its surface allowing the estimation of the deposition rate per pulse. It can be positioned at the same distance as the substrate to target distance (i.e.: 40mm). It consists of a 14 mm Ø flat crystal with a 6 MHz resonance frequency which is reduced with increased mass. This reduction is proportional to the deposited mass according to the Sauerbrey equation [43]:

$$\Delta f = -\frac{2f_0^2}{A\sqrt{\rho_q\mu_q}} = -K.\Delta m \qquad (2.1)$$

where f_0 is the resonant frequency (Hz), Δf the frequency change (Hz), Δm the mass change (g), A the piezo-electrically active crystal area between the electrodes (cm^2), ρ_q the density of the quartz (2.648 g/cm^3), and μ_q the shear modulus of quartz for AT-cut crystal (2.947x10^{11} g/cm.s^2). As the film is treated as an extension of thickness, the equation only applies to systems in which the deposited mass is rigid, evenly distributed and the frequency change <0.02 [44]. The crystal's frequency is monitored by a frequency analyser Pendulum CNT-90 which is controlled and read out using a LabVIEW^{TM} program.

2.2   Plasma plume characterization techniques

2.2.1   Monochromator

Emitting species in the plasma plume and products of collisions/reactions were investigated by spectroscopic analyses using a monochromator Acton research Spectra Pro 500. The light emitted by the plasma plume between the target and the substrate was captured using an achromatic lens (200-2000 nm, f = 500 mm and 50 mm diameter) directly in front of the window and the beam was then directed to the monochromator using a set of mirrors. These measurements were externally triggered by a photodiode activated by stray light from the laser pulse and gated using a Princeton Instruments pulse generator (PG-200) with a 200 ns delay and a gate-width of 10 µs. An accumulation of 20 measurements per image was used to improve the signal to noise ratio. To improve the wavelength resolution the measured wavelength range (i.e.: 500-825 nm) was divided into smaller range measurements (~15nm, using a high resolution grating) which were then subsequently assembled. An example for Ag ablation in different background gases is shown in Fig.2.4a and for La$_{0.4}$Ca$_{0.6}$MnO$_3$ in vacuum in Fig.2.4b.
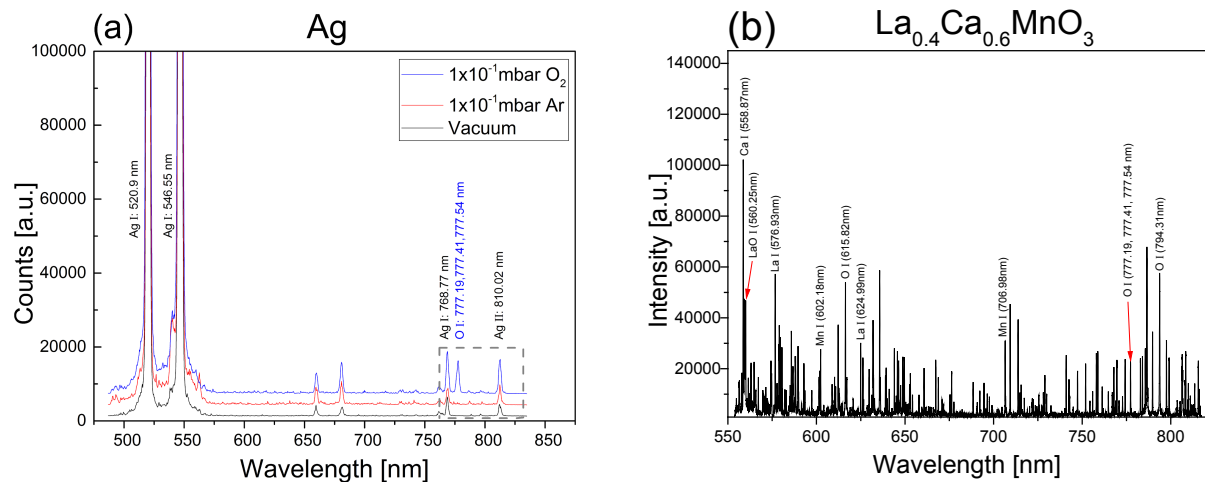
Fig.2.4. Examples of emission spectra for the ablation of Ag in vacuum, Ar and O_2 background (a) and for $La_{0.4}Ca_{0.6}MnO_3$ in vacuum (b).

2.2.2 Intensified charge-coupled device

An intensified charge-coupled device (ICCD) "Andor New i-star" DH334T-18F-03 was used to record the time evolution of the highly emitting plasma plume formed by laser ablation. It allows short gating (up to 2 ns) and uses a gated image intensifier to artificially increase the intensity of the signals. The sensor has a 1024 x 1024 pixels size and the pixel to distance ratio was calculated using the reference distance of 40 mm (from target to substrate as seen in Fig.2.5). The images were recorded for either all light passing through the quartz window (200 nm-1000 nm) or for selected wavelengths using the Acousto-optic tuneable filters (AOTF, 400-1000 nm) described later.

The camera was triggered externally by the laser pulse using the same photo-diode mentioned before. The ICCD on-board digital delay generator was used for gating the image intensifier and increasing time-delays were used to capture its time evolution. Typically, a gate width of 5 ns for the plume expansion below 2.5 µs and 50 ns above was used while for the AOTF measurements a gate width of 100 ns below 2.5 µs and 1000 ns for longer time scales. A gain value of 3500 was used for all non-AOTF and 4095 for all AOTF measurements. For each time-frame an accumulation of 40 images was used to improve the signal to noise ratio.
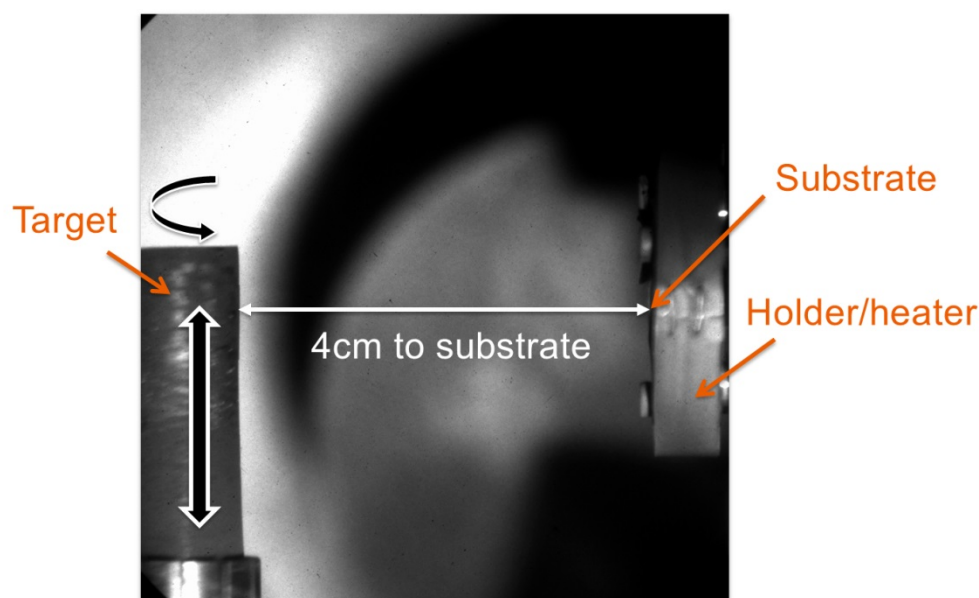
Fig.2.5. Image of the experimental setup with the $La_{0.4}Ca_{0.6}MnO_3$ target on the left and a substrate 40 mm away on the right hand side. The substrate is mounted on an un-heated substrate-holder. The image was captured using the same ICCD at the same position as for the experiments.

2.2.3 Acousto-optic tunable filter (AOTF)

Two AOTFs from Brimrose models VA210-0.55-1.0-H and VA210-0.40-0.65-H were used. They allow user defined selective imaging of specific wavelengths with a high resolution (i.e.: 1.3 nm at 633 nm). They filter light wavelengths by vibrating a TeO_2 crystal through which the light passes (Fig.2.6). The vibration is generated by radio frequencies (sinusoid) coming from a piezoelectric transducer and causes the TeO_2 crystal to change the index of diffraction. The piezo electric transducer is driven by an external high-frequency source, the SPS/SPF devices from Brimrose. The piezo induces a soundwave inside the TeO_2 crystal. The minima and maxima of the wave form a regular arrangement of regions with smaller and larger optical densities, effectively acting as a diffraction grid.
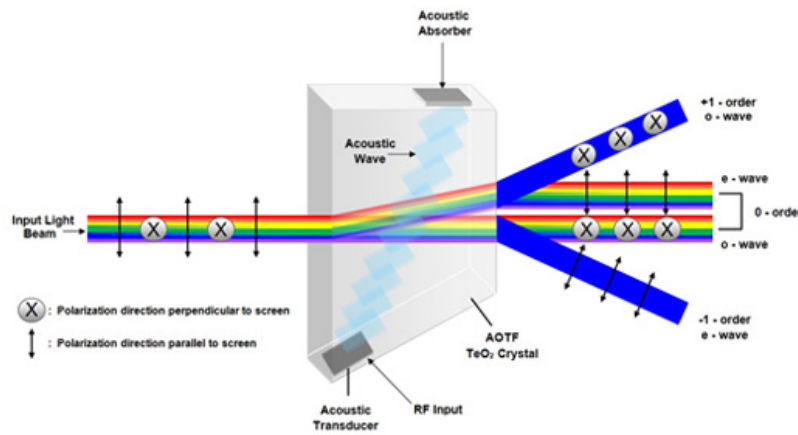
Fig.2.6. Sketch with operating principle of an AOTF selecting blue light. A piezo-electric transducer is used to induce a travelling or standing wave in a TeO_2 crystal. The resulting minima and maxima act as a optical diffraction grid for transmitted light [source: Brimrose]

Different to a normal grating, this one is defined by the sound wavelength traveling in the crystal. Therefore, a diffracted beam is observed at an angle θ that depends on the wavelength of the light λ and of the sound wave Λ. When the incoming light is normal to the soundwave, the angle is described by:

$$sin\theta = \frac{mn\lambda}{\Lambda} \qquad 2.2$$

where m = ..., −2, −1, 0, +1, +2, ... is the order of diffraction with the first order beam having the highest efficiency, and n = 2, if the Bragg condition is fulfilled. In the case where only one piezo-electric transducer is used, the resulting wave is traveling in the crystal with the respective speed of sound. This leads to additional changes in the measurements such as a Doppler shift of the light. However the Brimrose AOTFs have two transducers leading to a standing wave in the crystal and therefore no shifts of the transmitted light. A more detailed description of this specific equipment can be found in [45].

The AOTF is mounted between a 28-300 mm f/3.5-6.3 macro lens and the ICCD camera mentioned before. The setup allows time-resolved imaging of selected species from the plasma plume (specific wavelength). It does, however, cause a reduction of the signal to noise ratio which worsens the overall resolution of images (diffraction efficiency ~70-90 %), forcing the need for longer gating times and higher gains on the intensifier to achieve similar light intensities. In addition the reduction of light intensity is not constant with frequency and prohibits a direct comparison of intensities between different selected wavelengths.

AOTF model	Frequency range	Resolution
VA210-0.40-0.65-H	400-650 nm	1.1-2.1 nm
VA210-0.55-1.0-H	550-1000 nm	0.6-3 nm

Table 2.1 Specifications of the Brimrose AOTFs used in the experiments.

2.2.4 Mass spectrometer

To characterize the laser generated plasma plume an ion energy analyser and quadrupole mass spectrometer from Hiden Analytical Ltd. was used (HAL EQP). It is installed in the UHV chamber and can measure positive and negative ions up to energies of 1'000 eV (using a 45° sector field). Neutrals cannot be measured directly. To measure them, they require an electron impact ionization at the entrance of the MS. The maximum attainable mass-to-charge ratio by the quadrupole mass filter is 510.

An MS entry orifice of 30 µm was used following the recommendations from Hiden Analytical due to the very high intensity counts from the gated measurements of the plasma plume. In addition such small orifice dimension allowed MS measurements at relatively high pressures without compromising the equipment.

The gating of the MS was achieved by using an adjustable Stanford Delay Generator DG535 triggered by a photodiode activated by the laser beam. It allowed adjusting the gate delay (A) and width (B). Typically for MS measurements a delay of $A = 100$ ns and a gate width $B = 500$ µs were used (plasma expansion lasts ~5-150 µs at a distance of 40 mm).

The MS was specifically tuned by the PhD student *Xiang Yao* following the guidance from Hiden Analytical Ltd. UK and in-house software simulations using Simion®. Once the measurements were in agreement with Langmuir probe measurements the tuning parameters were fixed. They were the same for all elements and for all pressures as Hiden Analytical experts had recommended.

2.2.4.1 Angle resolved setup

With the aim of performing angular resolved MS measurements of the plasma plume an angular target holder was designed in close collaboration with the PSI engineering group and

built at PSI workshop. It enabled the rotation of a disk target around the fixed MS as the plasma plume will inherently expand along the target's surface normal [2]. For proper plasma probing it was necessary that the centre of rotation should always be positioned at the target surface as shown in Fig.2.7a. This was attained by having a target mounting close to the rotational axis and several adjusting screws for the fine tuning when using targets with different thicknesses. A draft of the conceptual design is shown in Fig.2.7a, the CAD model in Fig.2.7b, and the final device in Fig.2.7c.
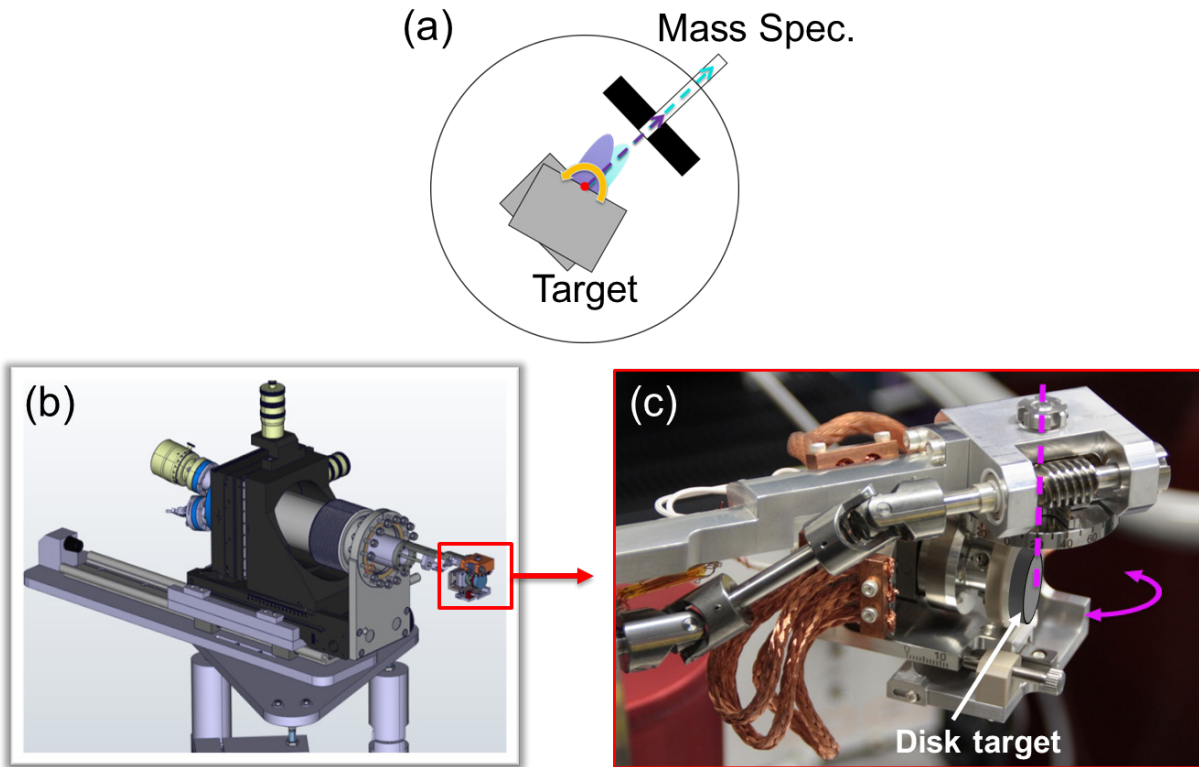
Fig.2.7. Sketch with the working principle of the target rotator (a), CAD view of the design (b) and image of the installed system with the target and its axis of rotation highlighted (c).

Two Attocube piezo motors enabled the rotation and linear displacement of the disk targets during operation to avoid cratering. They were controlled using a LabVIEW^{TM} program in combination with an Attocube controller (ANC 300). The choice of piezo motors was due to the space limitations given by the required angular rotations. Stepper motors are intrinsically much larger.

An additional challenge to the angular probing was the fixed position of the laser beam. As angular rotations of the target cause a change in the laser spot dimensions whenever the angular location is varied thereby changing the laser fluence and hence ablation rates. This is graphically explained in Fig.2.8 where it can be seen that angular variations will produce changes in the laser spot dimension normal to the rotation axis.
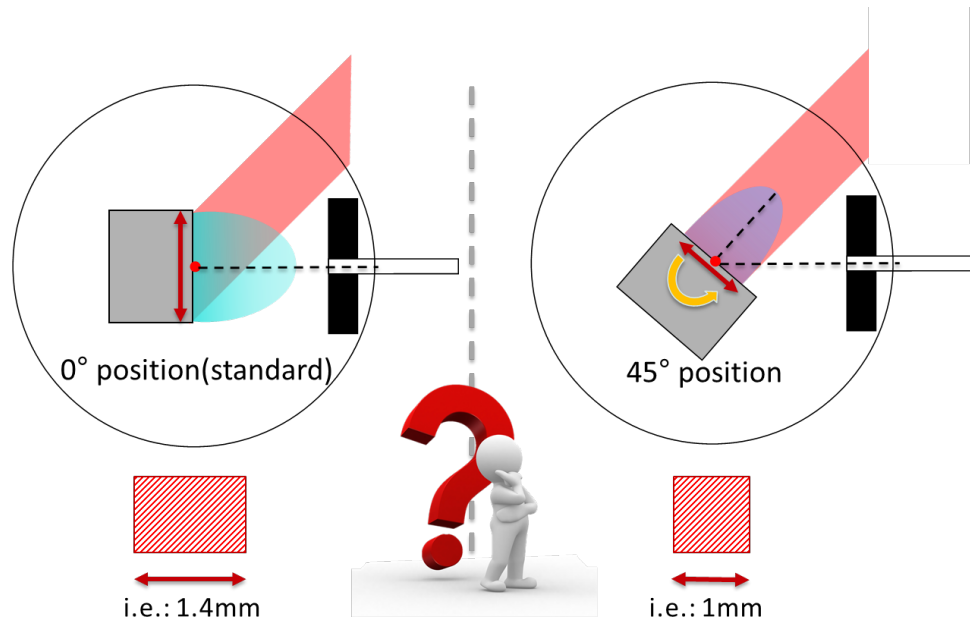
Fig.2.8. Sketch explaining the changes in laser spot width due to angular rotations of the target while the laser beam and MS are at fixed positions.

To solve this issue a limited set of laser beam masks (5 in total) was used to "compensate" for the deformation of the laser plume with angular variations. All masks had the same vertical dimension and varied in horizontal dimension. Several rounds of ablation experiments on polyimide at an angular range from 0-90° with different mask combinations were performed to make the final selection. The ablated spots on polyimide for the different angular locations were measured by optical imaging and compared to the original 1x1 mm spot. The final choice of masks achieved a deviation <0.028mm and some of them are presented in Fig.2.9 together with the theoretical curve of spot widening for a laser spot of 1x1mm (with the target facing the laser beam and at 45° with respect to the MS). Each mask switch would keep similar spot dimensions at their corresponding angular locations, however, the arriving energy would change. To keep the fluence constant the optical attenuator described earlier was adjusted after each mask switch.
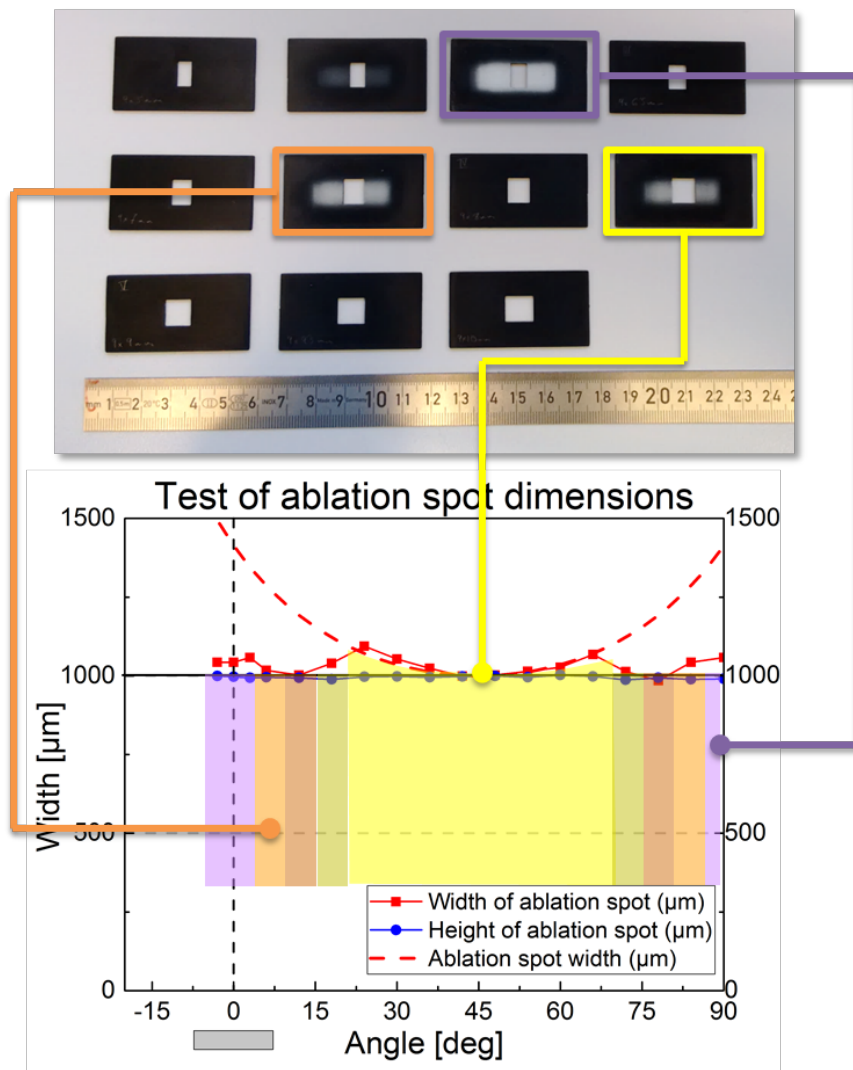
Fig.2.9. Ablation spot width variation with target angle. Mathematical calculation (dashed line) and experimental measurements of ablated spots on polyimide. Angle defined masks were used to compensate for the width variations and some of them are highlighted in the figure.

2.3 Film Characterization Techniques

When measuring small compositional deviations the method of choice for determining the composition of the thin films becomes fundamental. A list with the most commonly used methods for thin films measurements and their characteristics is shown in table 2.1. It is important to remark that the accuracy of most methods may vary strongly with the skills of the equipment operator. For this reason an accuracy range has been added. From the given specifications and availability, the selection of RBS/ERDA as the method of choice was clear. Both show the highest accuracies while not requiring any standard (lateral resolution was not critical in this study).
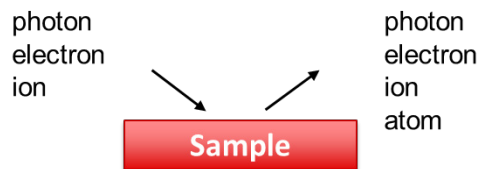
Method	RBS	ERDA	XRF	SEM-EDX	AES	XPS	SIMS
Elements accessible	Be-U	H-U	Be-U	B-U	Li-U	Li-U	H-U
Destructive	No	No	No	No	No	No	Yes
- Lateral resolution	1mm	20'000 nm	0.1mm	300nm	7nm	10'000nm	10'000 nm
- Depth resolution	5nm	5nm	5nm	500nm	2nm	2nm	0.5nm
Accuracy	0.5% (rel.)	3% (rel.)	2-10%	1-20%	4-30%	4-30%	4-30%
Standards req.?	No	No	Yes	Y/N	Yes	No	Yes

Table 2.1. Common approaches to thin film composition measurements and their characteristics. Where: RBS (Rutherford backscattering spectrometry), ERDA (Elastic recoil detection analysis), XRF (X-ray fluorescence), SEM-EDX (SEM Energy-dispersive X-ray spectroscopy), AES (Auger electron spectroscopy), XPS (X-ray photoelectron Spectroscopy) and SIMS (Secondary ion mass spectrometry)

2.3.1 Material analysis by nuclear techniques

2.3.1.1 Rutherford backscattering spectrometry (RBS)

Rutherford backscattering spectrometry has been the backbone of this work providing highly accurate compositional and thickness measurements. These measurements have been conducted at the Ion beam physics group (ETH Zürich) and their measuring facilities.
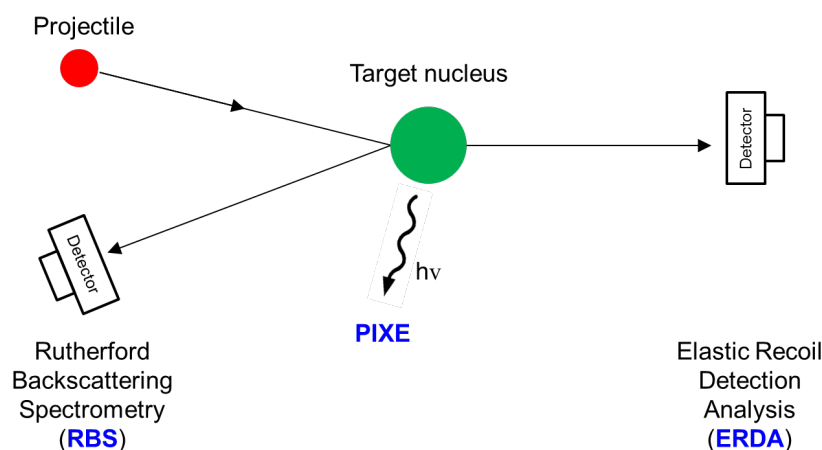
Fig.2.10. Sketch depicting the elastic scattering of MeV Ions in vacuum for RBS and ERDA measurements as well

as PIXE.

RBS is a non-destructive compositional analysis technique with depth profiling capabilities in the same measurement. It is based on the measurement of the energy of the backscattered ions after impinging on a sample with a fixed energy (Fig.2.10, usually a 2 MeV [4]He beam is used for the measurements in this thesis). The relationship between the energy of backscattered ions and the incident beam energy can be calculated by conservation of momentum and energy giving the following formula:

$$\frac{E_{Backscattered}}{E_{Projectile}} = \left[\frac{\sqrt{(1-(\frac{M_1}{M_2})^2\sin^2\theta)}+(\frac{M_1}{M_2})cos\theta}{1+\frac{M_1}{M_2}}\right]^2 \tag{2.2}$$

where θ is the scattering angle (defined by the angle between the detector and the ion beam), M_1 the mass of the projectile and M_2 the mass of the target atom to be determined. Additionally the deeper inside the film the target atom is, the lower the measured energy due to energy losses of "viscous friction" in the electron gas and small angle scattering with atomic nuclei [46]. The elastic backscattering is only a tiny side-effect during the passage of an MeV particle beam through matter. In summary, this allows determining not only the mass of the atom but also its depth location. The energy measurements are thus mass and depth scaled and can provide quantitative depth profiles of the sample composition under well chosen conditions.

Furthermore, no standards are necessary. Elements ranging from Be-U can be measured with a depth resolution from 1 to 10 nm [47, 48]. For thin film samples where signals from different elements can be completely separated the systematic accuracy of the RBS composition measurements are expected to be better than 0.5% [49] as for elemental ratios the main uncertainty contribution comes from the systematic error of the scattering cross-sections. The precision of the experimental data is mainly determined by counting statistics. The thickness is obtained as an areal density usually given in units of 1×10^{15} at/cm^2 with an accuracy of <5% which is mainly determined by the uncertainty of the energy loss of He ions in the material. The natural thickness unit for RBS is at/cm^2 and distance units such as nm require a conversion of the areal density via an estimated atomic density, which may vary as a function of thickness and increase the uncertainty. Surface sensitivity is 1 to 10^{-4} monolayers. The data analysis was performed using RUMP software and software developed at the Ion beam physics group for large batch calculations (i.e.: substrate signal and noise removal, integration of areas, etc.).

The main disadvantages of RBS being the limited accessible depth of ~1 µm, that light elements are not detectable on heavy substrates (substrate choice is critical), heavy elements are not distinguishable and no chemical information is obtained.

The collection for each RBS data point takes 3 - 10 min to guarantee the same counting statistics for all film thicknesses measured depending on the substrate's deposition angle and deposition pressure. The technique yields ratios between elements in the material and for each target material the corresponding elemental ratios were obtained (e.g.: Mn/La and Ca/La or Ti/Ba). In general, the elemental ratios were fixed to the heaviest of the target elements as it is expected to undergo fewer variations for the final composition within the different pressure regimes [50, 51].

2.3.1.2 Elastic recoil detection analysis (ERDA)

Similar to RBS, ERDA is based on elastic scattering but using a primary heavy ion beam (iodine or gold) at higher energies (10-100 MeV) to displace the substrate atoms and measure their mass and energy at a detector positioned in forward direction (Fig.2.10). In this case the measured energy and its relationship to the sample mass is given by:

$$\frac{E_{Recoil}}{E_{Projectile}} = \frac{4M_1 M_2}{(M_1 + M_2)^2} cos^2\theta \qquad (2.3)$$

where θ is the scattering angle (defined by the angle between the detector and the ion beam), M_1 the mass of the projectile and M_2 the mass of the recoiled atom to be determined. It is complimentary to RBS because it can measure light and heavy elements ranging from H to U. Light elements are detectable on heavy substrates making it an ideal tool to measure e.g. O and N concentrations in thin films unless the substrate also contains those elements which then reduces the accuracy of the estimations. It provides an accuracy of 3-4% in terms of composition and <5% in terms of thickness. The accessible depth range is limited to 1 µm and the depth resolution is 1-10 nm [52]. Simultaneous profiles of all elements are possible thanks to the combination of a ToF (time of flight) spectrometer with a detector for the total energy of the recoiling ions.

2.3.1.3 In air micro-Proton Induced X-ray emission (µPIXE)

The in-air capillary microprobe is a fast and simple tool to map elemental concentrations on objects that are difficult to be managed in a vacuum chamber (i.e.: rod targets). It is a non-destructive technique based on the analysis of the intensities of X-ray emissions from the sample atoms after in-air proton bombardment (2 MeV in this case). The specific setup used is described in more detail in [53] and a brief explanation is provided hereafter. It uses a glass capillary with an outlet diameter of about 15 µm having a wall thickness large enough to absorb the X-rays produced on the inner surface of the capillary. This rules out the need for extra shielding towards the silicon drift detector (SDD). The setup is shown in Fig.2.11 where the capillary can be seen on the left, a measured $CaTiO_3$ target in the middle (with a particular

surface pattern caused by repeated ablation) and the SDD detector just next to it (top left corner).
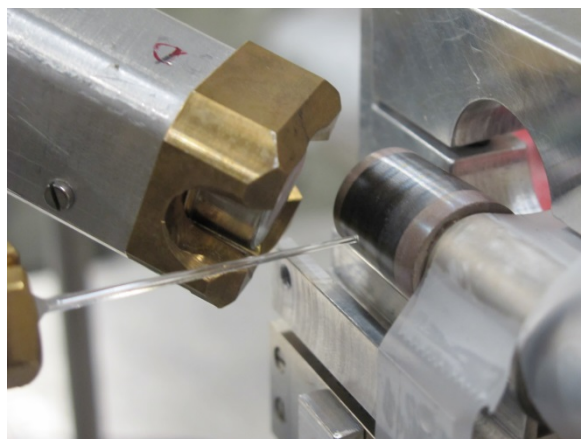
Fig.2.11. Image of in air µ-PIXE surface mapping of an ablated $CaTiO_3$ rod target. The beam collimating glass capillary enters from the left, the SDD X-ray detector is at the top left corner.

An example of a µPIXE experiment is shown hereafter. The surface of a PLD target was linearly mapped to verify its composition change during the ablation process. Several line scans were carried out along the cylinder axis of a $CaTiO_3$ target and one example is shown in Fig.2.12. It shows the Ca/Ti elemental ratio from the K_α X-ray line intensities measured on the surface along a straight line perpendicular to the well visible "zebra" pattern from the target seen on Fig.2.11. This pattern is produced by the periodic linear and rotational movement of the target during laser ablation to avoid cratering. The measurements show that the dark colour change on the surface is probably due to a preferential loss of Ti in the strongly ablated areas.
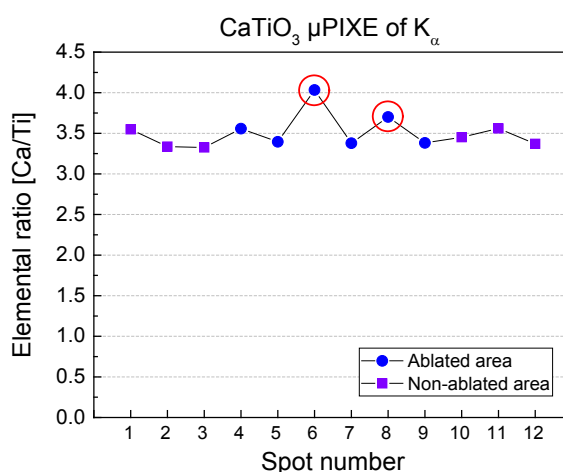
Fig.2.12. Elemental ratio of Ca/Ti K_α X-ray intensities along a linear surface scan. Red circles mark positions of dark areas in the "zebra" pattern.

2.3.2 X-ray diffraction

X-ray diffraction was used to investigate the crystalline structure of the films. It is based on the diffraction of the incoming X-rays by the atoms forming the crystals (through their electrons). The diffraction pattern follows Bragg's law:

$$2d\ sin\theta = n\lambda \tag{2.4}$$

Where d is the spacing between diffracting planes, θ is half of the scattering angle, n is any integer, and λ is the wavelength of the beam. The diffraction patterns were acquired with a Siemens D500 in Bragg-Brentano geometry using Cu Kα radiation (λ =1.5418 Å). The patterns were detected in symmetric scan mode in a suitable θ-2θ range. The identification of Bragg peaks was done using powder references from literature.

2.3.3 Profilometer

The film thicknesses were also measured mechanically using a Veeco Dektak 8 stylus profilometer. It takes measurements electromechanically by moving a diamond-tipped stylus over the sample. The measurements are performed at the border between a coated and an uncoated area, obtaining the film thickness by measuring the step. The accuracy of the profilometer is in the ~5nm region limiting its use for films with a thickness larger than 40 nm.

2.3.4 SEM / EDX

A scanning electron microscope SEM Zeiss ULTRA^{TM} 55 was used for imaging the film surface morphology. It is also equipped with an Energy-dispersive X-ray sensor (EDX) for compositional measurements. In the SEM a focused beam of energetic electrons is scanned across the specimen in a raster mode. The interaction of the electron beam with the sample is complex and provides a variety of physical signals that may contain information about the local sample topography, chemical composition and structure, and may be analysed using specialized detectors (i.e.: EDX). In scanning electron microscopy the secondary (SE) and backscattered electrons (BE) produced by inelastic and elastic scattering at a bulk sample's surface respectively are most commonly detected to provide a topographical image with a maximum achievable resolution of ~1 nm. A more detailed description of this specific equipment can be found in [54].

3 The influence of background gas pressure and angular location on film thickness and composition

The apparent ease to prepare thin films with a complex composition and for a wide range of materials is one of the reasons for the widespread use of pulsed laser deposition (PLD) [3]. However, the congruent transfer using PLD does not always take place and depends on many process parameters [6, 55-58].

This chapter investigates such deviations by analysing the composition of the films using RBS to measure the effect of background pressure, substrate angular location, and target-to-substrate distance on film thickness and composition. It starts with $La_{0.4}Ca_{0.6}MnO_3$ and then expands to other relevant perovskite materials based on their elemental mass ratios.

3.1   Introduction

In PLD one of the main causes for compositional deviations is the misalignment between the plasma plume expansion axis and the substrate, as in PLD there is often a strong non-uniformity in the angular profiles of thickness and also composition [55, 59]. Although these variations might not be critical for many applications, in other cases even small variations of the film composition can have a strong impact on the physical properties of the deposited films. In the case of oxide thin films, outstanding physical properties such as superconductivity, colossal magneto resistance or enhanced catalytic activity are reported [60-62], and it is in their precise composition where such electronic properties originate.

In general, there are two different approaches to measure the angular distribution of species in the laser generated plasma plume:

- Plume-based methods [2]: a probe is positioned at different angular locations of the plasma plume and the source-angular distribution is measured directly (i.e.: with a Langmuir probe, a quartz crystal microbalance or a mass spectrometer [63-66]). This will be explored in chapter 6.

- Indirectly, by film-based methods [2]: in this case the angle-resolved composition of species is calculated indirectly by analysing the final film composition after the deposition on substrates located at various angular locations.

This chapter focuses on the latter (film composition and thickness on substrates) due to the simplicity and accuracy and will serve as complimentary results to those presented in chapter 6. Nevertheless, it is important to understand that these measurements rely on the assumptions that particle-sticking coefficients are unity (or equivalent for all species) and that there is no re-sputtering or preferential re-sputtering of the species forming the film by the arriving species. Still, it is the final film composition what is of relevance to the user.

3.2   Investigation for $La_{0.4}Ca_{0.6}MnO_3$

3.2.1   Specific experimental details

In order to capture the angular distribution of species, the two different substrate holders described in chapter 2 were used: the "semi-sphere" holder (Fig.2.3a) and the "planar" holder (Fig.2.3b). The former keeps the target to substrate distance constant at 40 mm due to its intrinsic spherical geometry and has an angular range of ±82°, while the latter consists of a simple planar surface perpendicular to the plasma plume axis and has a +60° angular range with an increasing target to substrate distance as the angle is increased. Silicon substrates (10x10mm) were used on the "semi-sphere" holder, while on the "planar" holder a 20 µm thick aluminium foil with 99.999% purity was used to avoid substrate channelling effects during the RBS measurements. Such effects were encountered on the silicon substrates (used on the

"semi-sphere" holder), which increased the RBS measurement time and complexity of the data analysis on the thinnest films. To simplify procedures an aluminium foil was used for the "planar" holder. In addition, its continuous geometry simplified the measuring process itself.

The target was ablated using the 248nm KrF excimer laser with a constant fluence of 2 J/cm^2 at 3 Hz and a rectangular spot size of 1x1.4 mm^2. All the depositions lasted 40 min, took place at room temperature, and at four different background-gas pressures: vacuum (1x10^{-6}mbar), 1x10^{-3}mbar, 1x10^{-2}mbar and 1x10^{-1}mbar. Ar was used as background-gas in order to avoid any possible chemical reactions that might mask the results and complicate their interpretation. Except vacuum, the other three pressures were chosen to capture the evolution from a free expansion of the plasma plume (1x10^{-3}mbar), with hardly any interactions with the background-gas, to a full interaction with background gas (1x10^{-1}mbar). The mean free paths (MFP) of the different relevant species for this chapter at such Ar pressures and at room temperature are shown in Table 3.1 and are given by the formula:

$$\lambda = \frac{k_B \cdot T}{\sqrt{2} \cdot P \cdot \pi \cdot d_m^2} \tag{3.1}$$

where T is the temperature of the gas, P the pressure and $d_m = (d_{Ar} + d_{species})/2$.

Element	Mass (amu)	Radius (pm)	MFP (mm) at different Ar pressures			
			1x10^{-6}mbar	1x10^{-3}mbar	1x10^{-2}mbar	1x10^{-1}mbar
Li	6.94	145	198478	198	20	2.0
O	16	60	539606	540	54	5.4
Al	27	125	241065	241	24.1	2.4
Ca	40	180	146985	147	15	1.5
Ti	47.9	140	207996	208	21	2.1
Mn	54.9	140	207996	208	21	2.1
Ba	137.3	215	113211	113	11	1.1
La	138.9	195	130875	131	13	1.3
Eu	152	185	141308	141	14.1	1.4

Table 3.1. Mean free path values for the different species in Ar gas calculated for the four pressures used in the depositions. The average target-to-substrate distance was 40mm, which means that the mean free path of the ablated species becomes shorter than the target-to-substrate distance at pressures above 1x10^{-3}mbar Ar (dashed line)

After the deposition, the composition and the thickness of the films were measured using RBS at the Ion Beam Physics group facilities from ETH Zürich. Additionally, the film thicknesses were measured also using a Veeco Dektak 8 stylus profilometer. Finally, the surface morphology was studied using a Scanning Electron Microscope (SEM) Zeiss ULTRA^{TM} 55.

3.2.2 Film thickness and composition results

3.2.2.1 Semi-sphere substrate holder

The RBS thicknesses are measured as atoms per unit area (1×10^{15} at/cm^2: the natural thickness unit for RBS) and are plotted as such to avoid the uncertainty of determining the density of the material which may vary as a function of thickness or deposition conditions.

These thickness measurements are presented in Fig.3.1. In all graphs the centre position of the plasma plume is marked with a dashed line at 0° while the typical deposition area for most PLD users (1 cm^2) is highlighted by a grey rectangle (±10° for a target to substrate distance of 40 mm). The results show a strongly forward oriented deposition at low pressures with a peak thickness four times the thickness at the 70-80° angular range. Still, a certain film thickness was achieved even at such steep angles. This would be consistent with the reported double deposition component of a forward peaked angular component superimposed on a background evaporated component, which varies more slowly over the angular range [55], however, angle-resolved MS measurements in chapter 6 prove that the kinetic energies are much higher than those expected from thermal evaporation (>100 eV vs. ~ 0.1 eV) denying such possibility. The most likely origin for the distribution of species in vacuum is rather the collisions of the plasma plume species between themselves.

With increasing pressure the transition from a freely expanding plasma plume to multiple scattering events with the background gas takes place. As a consequence a broadening of the angular distribution can usually be seen. At a pressure of 1×10^{-3}mbar the MFP is ~100mm, still larger than the target-substrate distance of 40mm. At such pressure collisions with the background gas should hardly take place and the measured thickness profile was very similar to the vacuum deposition. At 1×10^{-2}mbar the MFP is 10 mm, several times smaller than the target-substrate distance. A certain number of collisions are expected, but they did not seem sufficient to affect the deposition and only minor changes in the thickness profile could be noticed. At a pressure of 1×10^{-1}mbar a noticeable change in film deposition is observed. The MFP is <1mm and a uniformly deposited film thickness could be measured over the entire angular range. Furthermore, the thicknesses measured at 80-90° were larger than for depositions at lower pressures. Overall, the calculated thickness integrals show a loss in deposited material as the pressure is raised. The thickness values measured by profilometry showed a similar trend (Fig.3.2), but with a reduced number of measurement points because of the limited amount of uncoated areas.
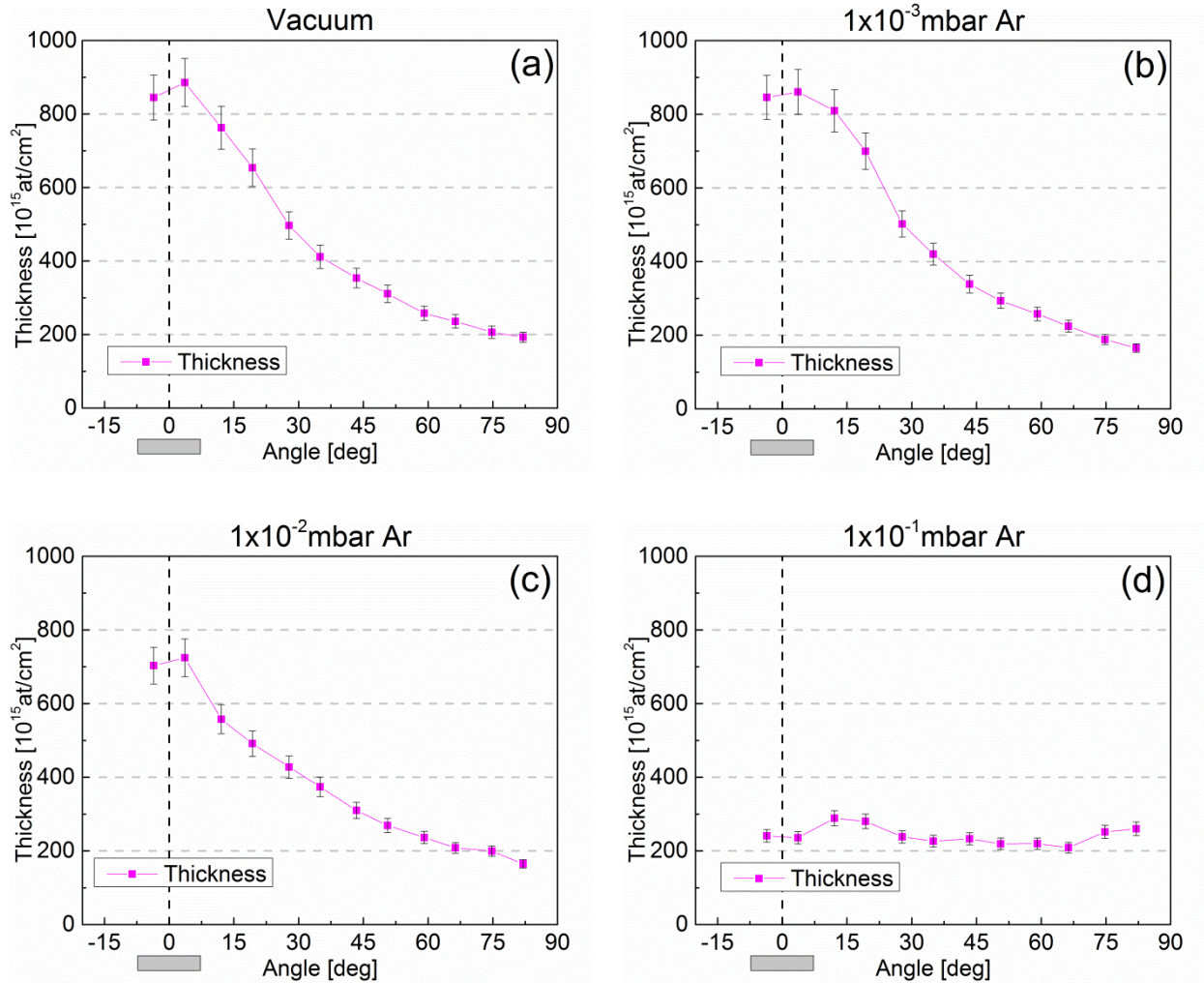
Fig.3.1. Angle-resolved film thickness profiles measured by RBS for four different argon background-gas pressures.
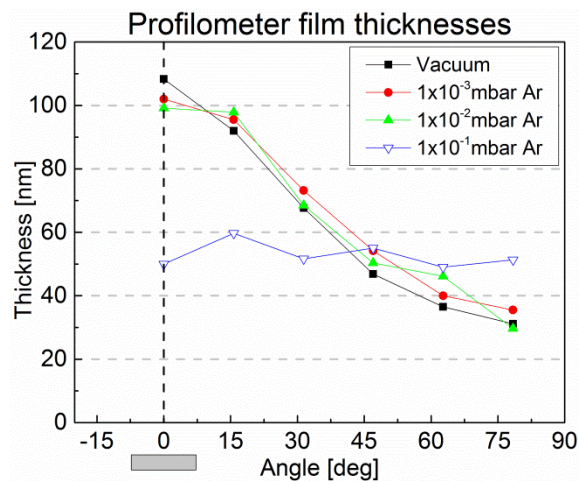
Fig.3.2. Angle-resolved film thickness profiles measured by stylus profilometry for four different argon background-gas pressures.

In addition to thickness information, the RBS measurements also provide accurate composition profiles. They are plotted in Fig.3.3 and reveal that for vacuum the film composition was not uniform over the angular range and different from the composition of the ablated target.

The Ca/La ratio presented small variations and the Mn/La varied above and below the target composition (Fig.3.3a, blue horizontal line). It peaked at a value of 2.75 in the 70-82° range (this particular deviation at high angles is discussed later in 3.3.4). This evidences a non-congruent transfer for such deposition conditions. Like with the thickness measurements, composition profiles at $1x10^{-3}$mbar show a similar profile like in vacuum for each particular elemental ratio. In contrast, at $1x10^{-2}$mbar, a pressure at which interactions with the background-gas are expected but hardly any thickness variation was detected, the strongest compositional deviations occur. Although the composition from 45-65° seems similar for the three lowest pressures, a strong reduction of the lighter elements was detected close to the plasma plume axis (0-35°): 13% for Mn/La and 16% for Ca/La. These were the locations where the measured film thickness was the highest. This reduction can be explained as a consequence of the scattering events of the elements with the Ar background gas. As the pressure rises, the probability of collisions with the background gas increases and, considering the energies of the elements in the expanding plasma plume (many of them above 200eV as will be shown in the following chapters), a certain number of collisions are required in order to scatter those elements. However, due to their differences in mass, some elements are more easily scattered than others. Thus, a possible explanation for the compositional variation and reduction of the lighter elements is the fact that elements such as Ca (A=40) and Mn (A=55) are preferentially scattered in comparison to La (A=139), which has a mass 2.5-3.5 times higher. Additionally, at the highest deposition pressure of $1x10^{-1}$mbar (Fig.3.3d) even the heaviest element La is scattered. For these conditions, the measured composition profile shows a homogeneous film composition over the entire angular range similar to what was found in the thickness profile. Furthermore, the composition was not the same as the composition of the ablated target material, with the Mn/La ratio above the target value and the Ca/La below. Overall, the results show that for the given deposition conditions and using the "semi-sphere" holder, changes in film composition can reach deviations of up to 16% with respect to the target composition.
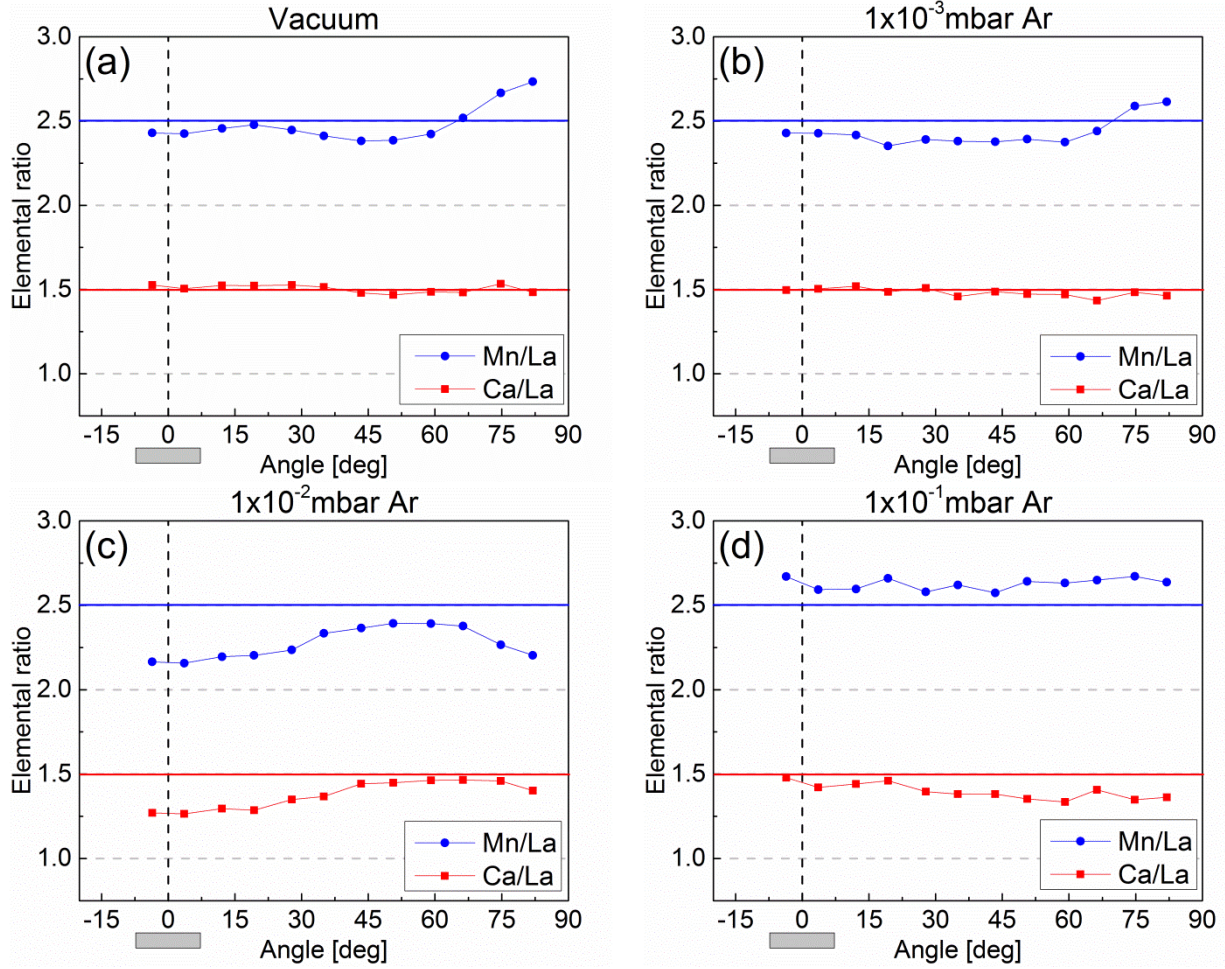
Fig.3.3. Angle-resolved film composition for four different argon background-gas pressures. The films were deposited using the "semi-sphere" substrate holder, which kept the distance of target to substrate constant and at 40mm. The compositions were obtained by RBS. The horizontal lines represent the target composition. Note: error bars are smaller than the symbols.

Concerning the surface morphology of the deposited films, SEM micrographs (Fig.3.4) show a homogenous coating for the entire angular range for vacuum and $1x10^{-3}$ mbar. In the case of $1x10^{-2}$ mbar, a homogeneous coating was also observed for angles below 60°. However, for angles above 60°, a non-homogenous coating was found. This non-homogeneity becomes evident for higher pressures and at $1x10^{-1}$ mbar it covers the entire angular range of films. Given the fact that all the depositions took place at room temperature and that these particular ones were at higher pressures, it is expected that the kinetic energy of the arriving species will be much lower than at the other pressures and therefore their mobility greatly reduced. Nevertheless, the main reason for the transition to such surface morphologies is not yet clear.
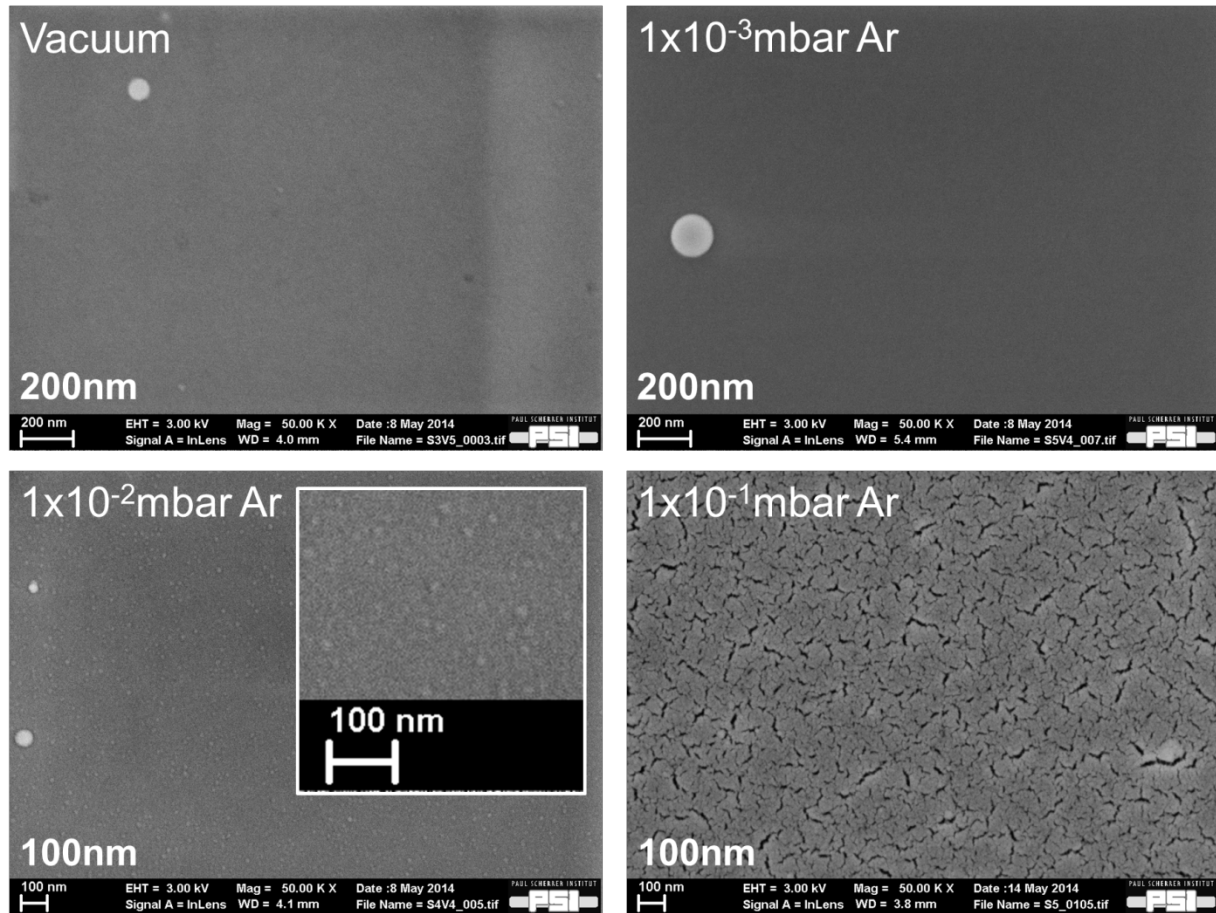
Fig.3.4. Scanning electron micrographs of several of the films deposited at four different pressures (note that the scales are different). The transition from a non-homogenous coating at 1×10^{-1} mbar (for all angles) to a homogenous one at lower pressures, is visible at those films deposited at 1×10^{-2} mbar and at angular locations above 65° (enlarged picture)

3.2.2.2   Planar substrate holder

For the particular case of the "planar" substrate holder due to its flat geometry, the variation of the angular location entails a variation of substrate to target distances (as can be seen in Fig.3.5) and which can be calculated by simple trigonometry. This translates into a distance from target to substrate of 40 mm at 0° angular location, while at 60° angular position it goes up to 81 mm. As a consequence for a given MFP, an increase in angular location implies a significant increase in the number of scattering events.

The film depositions were carried out for two pressures: 1×10^{-3} and 1×10^{-2} mbar Ar. The film thickness profiles were measured by RBS only (Fig.3.6a) and show similar profiles as for the "semi-sphere" holder. The maximum film thickness could be found at an angle of 0° for both pressures and had a similar value as with the previous "semi-sphere" substrate holder. Nonetheless, the change in film thickness as the angular location is increased is much more dramatic with a film thickness 30 times thinner at a 60° angle for the films deposited at 1×10^{-3} mbar. This is in strong contrast with the "semi-sphere" substrate holder in which the film

thickness was 4 times thinner for the same depositing conditions and angle. In the case of the deposition at 1×10^{-2}mbar on the "planar" holder, the measurements show a slight reduction in film thickness which is mostly detected around the 0° angular location. In general, the thickness profiles of both deposition pressures on the "planar" holder provide a consistent picture. They both show that the probability of interactions with the background gas, either because of target to substrate distance or of the deposition pressure (MFP), plays a major role in defining the film thickness angular distribution.
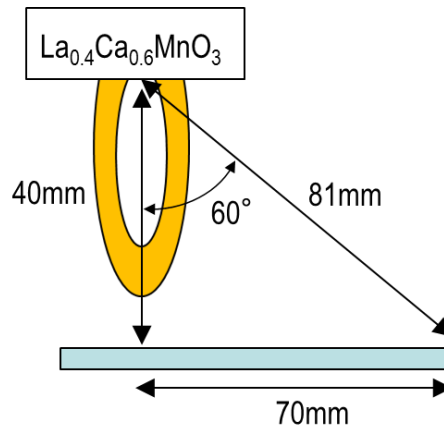
Fig.3.5. Schematic drawing of the effect in target to substrate distance as angular location is increased for the "planar" substrate holder.
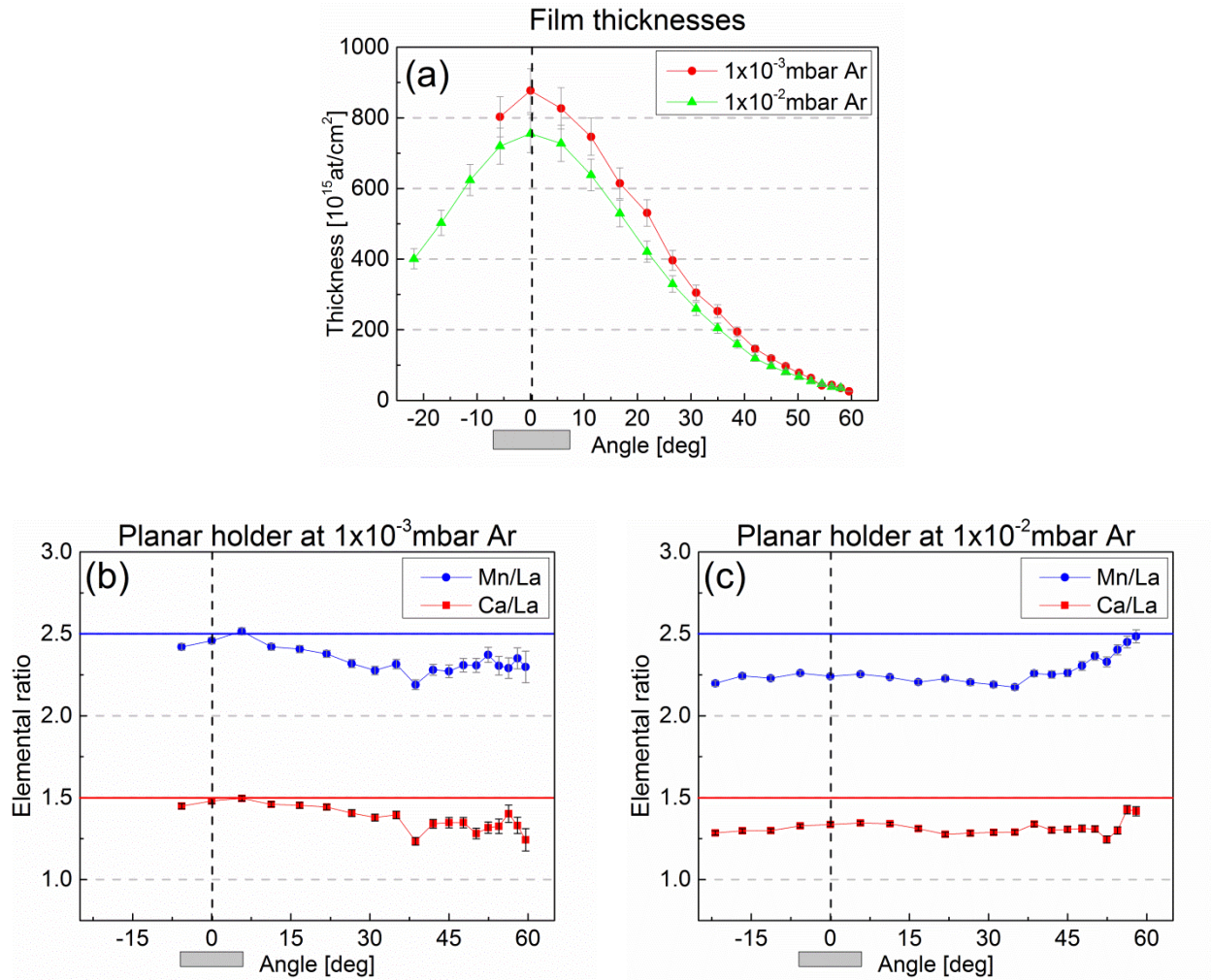
Fig.3.6. Angle-resolved film thicknesses (a) and composition (b and c) for argon background-gas pressures of 1×10^{-3}mbar and 1×10^{-2}mbar. The films were deposited using the "planar" substrate holder.

With respect to the angle-resolved film composition (Fig.3.6bc), the results highlight the intrinsic differences between both holders. In the "semi-sphere" holder the MFP and possible collisions with Ar were the same for all angles and the results provide information about the angular distribution of elements related to the plasma plume expansion dynamics. In the "planar" holder, the composition profile of the deposited film is affected by the increase in path distance for higher angles (increased number of collisions). This is already noticeable at 1×10^{-3}mbar. With the "semi-sphere" holder the number of scattering events were limited (substrate-target distance of 40mm, MFP ~100mm), while with the "planar" holder as soon as the angle is increased a growing number of scattering events start affecting the composition profiles in comparison to the "semi-sphere" holder. At 0° the compositions are similar, but once the angle is increased the ratios of Mn/La and Ca/La decrease noticeably. This can be explained by the increase in collisions with the background gas which deters the lower mass elements from arriving at the substrate more than the heavier La. The content of Mn is reduced by ~10% with respect to the target composition while for Ca a reduction of ~17% is detected.

Such a reduction of the light elements is similar to those detected for the films deposited on the "semi-sphere" holder, although for a pressure of 1×10^{-2}mbar. Moreover, for the "planar" holder at a pressure of 1×10^{-2}mbar the strong deviation in composition was again found at 0° angular location. It is not until an angular location above 40° is reached, that the film composition begins to return to the target values as the heaviest element La is also being scattered.

3.2.3   Verification of compositional deviations using heated substrates

Until now all the results presented have been for RT depositions due to the impossibility to heat the custom made substrate holders up to the required temperatures (~780°C). This raises the question whether the findings can be extrapolated to depositions at elevated or even high temperatures

To verify this a limited number of films were deposited at 780°C on MgO substrates (ideal for RBS measurements and suitable for epitaxial film growth of $La_xCa_{1-x}MnO_3$). Two important issues need to be commented. First, as will be explored in chapter 4, substrate heating reduces the background gas density and thus its stopping power. To compensate for this the Ar background pressure is adjusted following the estimated decays in gas density (see chapter 4.1.3). This means that pressures of 4×10^{-2}mbar and 4×10^{-1}mbar will be used when heating the substrate to 780°C to be equivalent to 1×10^{-2}mbar and 1×10^{-1}mbar used at RT. Second, angular movements of the substrate heater are limited and only the rotation in the horizontal plane is achievable. The results presented in the previous sections were on vertical angular locations. For this reason the results from chapter 5 will be used as in that case both the vertical and the horizontal planes were used to capture the angular deposition.

Once deposited, the film crystallinity of the grown films was analysed by X-ray diffraction. The results for the 6 films produced at high temperature are shown in Fig.3.7. Unlike the RT films which showed an amorphous nature, the ones deposited at 780°C are crystalline and grow in an oriented manner (confirmed by rocking curve scans). The film deposited in vacuum shows the expected 00ℓ orientation [67]. Interestingly the films deposited at 80° with respect to the plasma plume centre are also crystalline. Due to the non-optimized deposition conditions and large lattice mismatch between the substrate and $La_{0.4}Ca_{0.6}MnO_3$, the film's crystallinity is poor as shown by the very large FWHM of the rocking curves (see table 3.2). In addition the compositional deviations will also contribute to the poor crystallinity (especially for the films grown at 1×10^{-2}mbar Ar).

Film	FWHM [deg]
0° angle, in vacuum	1.363
0° angle, at 1×10^{-2}mbar Ar	2.841
0° angle, at 1×10^{-1}mbar Ar	1.154
80° angle, in vacuum	1.541
80° angle, at 1×10^{-2}mbar Ar	1.536
80° angle, at 1×10^{-1}mbar Ar	1.257

Table 3.2. FWHM of the XRD rocking curves of films produced at 0° and 80° angular position with substrate heating and at different pressures.

Due to the expected different thicknesses and compositions a comparison between diffraction patterns is difficult. In any case, it is expected that the film compositional deviations will affect the lattice parameters. The film strain is also likely to be affected by the compositional deviations but is not discussed here.
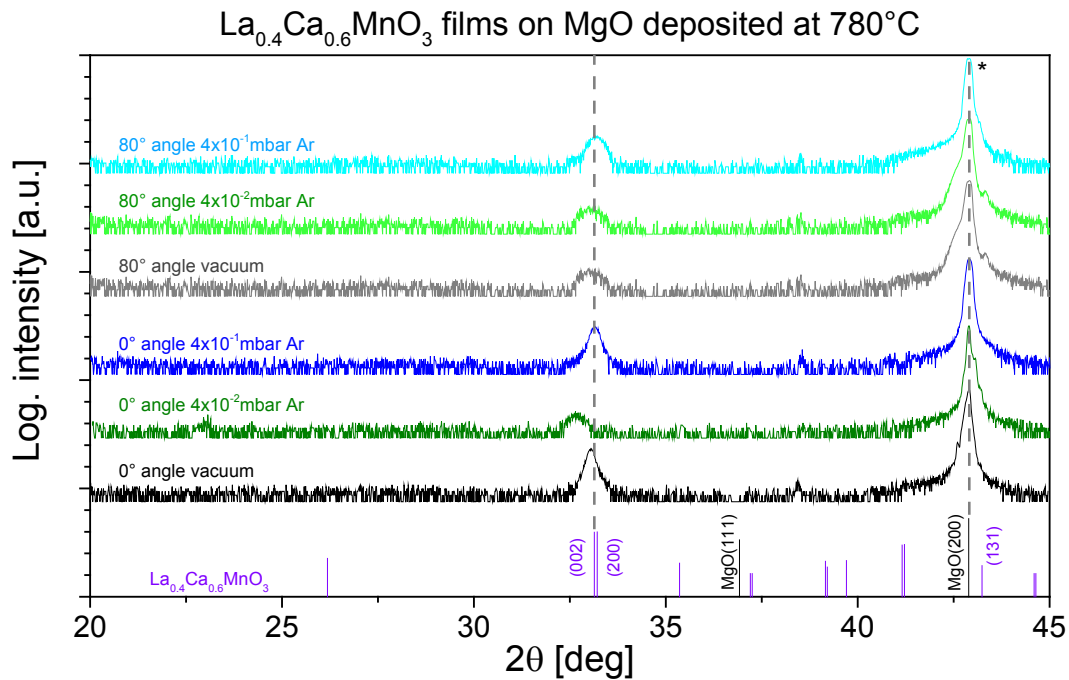
Fig.3.7. X-ray diffraction patterns of $La_{0.4}Ca_{0.6}MnO_3$ films deposited on MgO substrates (100) at 780°C in vacuum, 4×10^{-2}mbar and 4×10^{-1}mbar Ar (to compensate for the reduction in background gas density due to heating). Three films were positioned at the centre of the plasma plume (0° angular location) and other three at ~80°. The (200) reflection of the MgO substrate is marked with an asterisk. The diffraction pattern of $La_{0.4}Ca_{0.6}MnO_3$ powders from [68] is included as reference.

In terms of thickness the films show similar trends like the RT depositions (Fig.3.8). The films deposited in vacuum are the thickest at 0° and the thinnest at 80°, while for higher pressures the films at 0° decrease in thickness and slightly increase at 80° (due to scattering). The thickness numbers at 0° are not matching exactly to the RT results but show similar trends. The most noticeable difference, however, is the film prepared at 4×10^{-1}mbar Ar with the plume expansion normal to the substrate. RT films showed a regular thickness throughout the entire

angular range for this pressure (1×10^{-1}mbar at RT). This is not the case at 780°C and will be explored by plume imaging in 4.1.3.
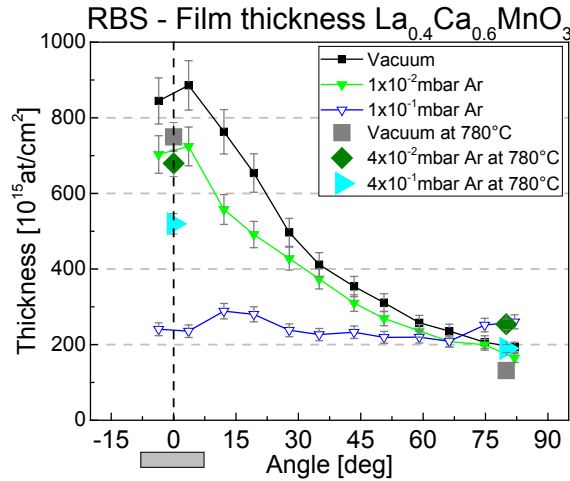
Fig.3.8. Comparison of angle-resolved $La_{0.4}Ca_{0.6}MnO_3$ film thicknesses at room temperature vs. films deposited at ~780°C on MgO substrates (at 0° and 80° angular location) for vacuum, 1×10^{-2}mbar Ar/4×10^{-2}mbar Ar for 780°C films, and 1×10^{-1}mbar Ar/4×10^{-1}mbar Ar for 780°C films.

With respect to film composition the results are shown in Fig.3.9 superimposed to the angle resolved composition results from chapter 5 (horizontal angular range). They show very similar values for 1×10^{-2}mbar Ar (Fig.3.9b) and 1×10^{-1}mbar (Fig.3.9c) but not for vacuum (the latter is not yet understood). The trends for 1×10^{-2}mbar and 1×10^{-1}mbar are matching nicely. Most importantly, the location and pressure at which the strongest compositional changes were detected at RT are reproduced for 780°C: the centre of the plume at 1×10^{-2}mbar Ar (Fig.3.9b). In that case the reduction of the lighter elements Ca and Mn in comparison to La is detected. Furthermore, the La enrichment seems to negatively affect the crystalline quality as seen in Fig.3.7.

Overall, despite the discrepancy in vacuum, the high temperature depositions show that the core findings at RT can be extrapolated to a higher temperature deposition as long as the changes in background gas density are taken into account when estimating the pressure ranges. This is also the case when changing the laser fluence as will be explored in chapter 7 by plasma plume imaging.
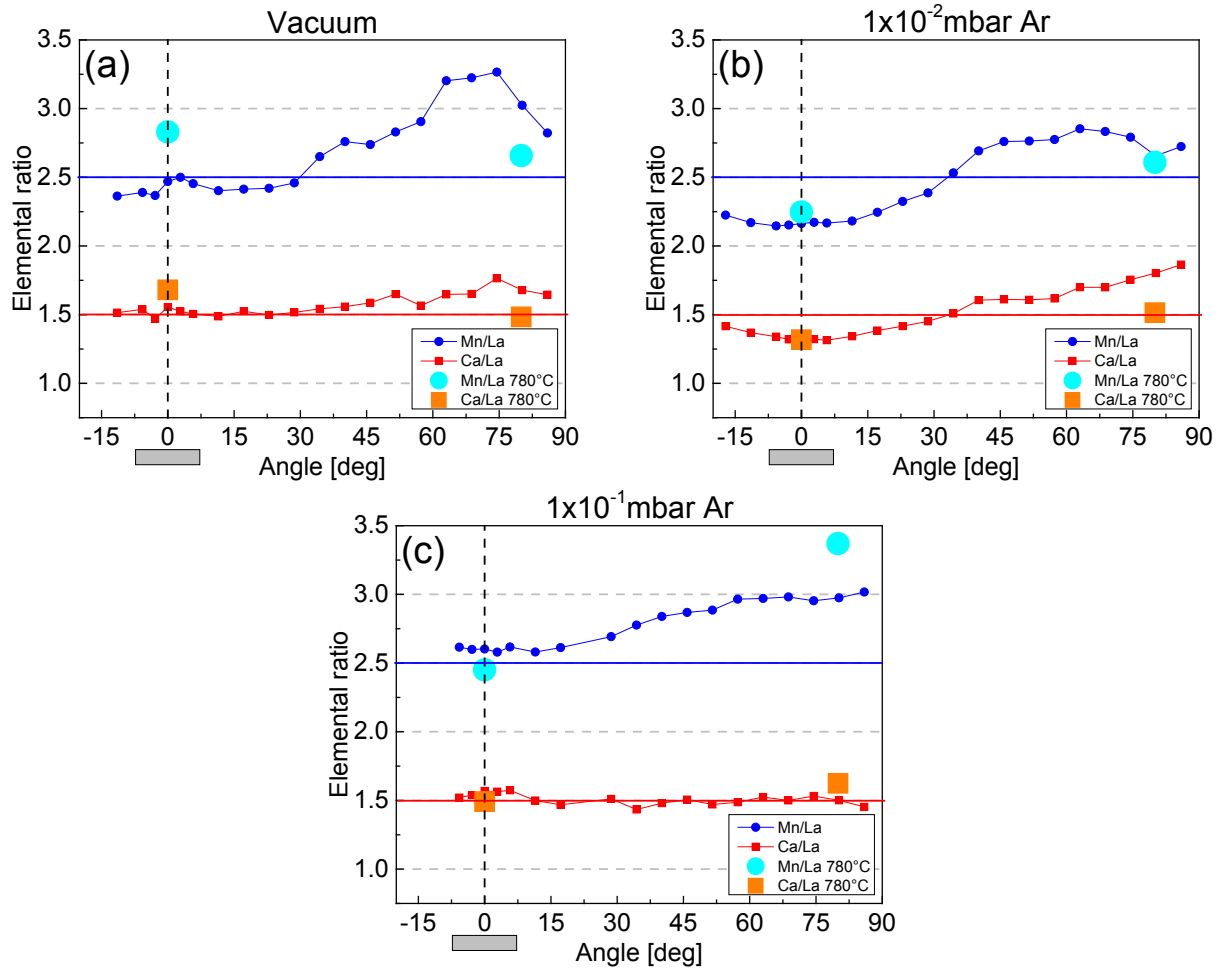
Fig.3.9. Comparison of the angle-resolved $La_{0.4}Ca_{0.6}MnO_3$ film composition at room temperature vs. films deposited at ~780°C on MgO substrates (at 0° and 80° angular location). For vacuum (a), $1x10^{-2}$mbar Ar/$4x10^{-2}$mbar Ar for 780°C films (b), and $1x10^{-1}$mbar Ar/$4x10^{-1}$mbar Ar for 780°C films (c). The compositions were obtained by RBS. The horizontal lines represent the target composition. Note: error bars are smaller than the symbols.

3.2.4 Conclusions for $La_{0.4}Ca_{0.6}MnO_3$

The angular distribution of species in the plasma plume of $La_{0.4}Ca_{0.6}MnO_3$ has been investigated using RBS. The films have been deposited at different background-gas pressures and with two different substrate holders. One of them kept the distance from target to substrate constant as the angular positions were increased, while with the second the distance was continuously increased. In terms of film thickness, the results show the expected strongly forward oriented deposition in which most of the deposited material is contained in a ±30° angular range. This strong variation of thickness with angle was detected for vacuum and most of the low Ar pressures. Once the interaction with the background-gas is sufficient, the deposition is no longer strongly forward oriented and a uniform film thickness was found over the entire angular range.

Regarding film composition, the measurements revealed that the film composition varies with angular location as well as other process parameters (i.e.: pressure or target to substrate distance). It was found that for this particular material, the masses of the participating elements

play a major role in film compositional deviations because of the preferential scattering of the ejected elements with the background gas. Furthermore, these findings at RT can be extrapolated to a higher temperature deposition as long as the changes in background gas density are taken into account when estimating the pressure ranges. Overall, it has been confirmed that assuming a congruent transfer of species for all points or for all depositing conditions can lead to erroneous conclusions.

This raises the question whether such findings can be extrapolated to other relevant PLD materials and if larger mass ratios of the participating elements will lead to even larger compositional variations. With this aim, the remaining part of the chapter investigates this assumption further by selecting four additional target materials based on their elemental mass ratios: $BaTiO_3$, $CaTiO_3$, $EuAlO_3$ and $LiMn_2O_4$.

3.3 Expansion to additional multi-element oxide materials: $BaTiO_3$, $CaTiO_3$, $EuAlO_3$ and $LiMn_2O_4$

3.3.1 Specific experimental details

Taking $La_{0.4}Ca_{0.6}MnO_3$ as starting point, four additional target materials were chosen based on their elemental mass ratios: $BaTiO_3$, $CaTiO_3$, $EuAlO_3$, and $LiMn_2O_4$. These targets range from having very similar cation masses (ratio of 1:1.17 for Ca:Ti) to very dissimilar (ratio of 1:5.6 for Al:Eu and 1:8 for Li:Mn) and a mass ratio similar to $La_{0.4}Ca_{0.6}MnO_3$ (1:2.9 for Ti/Ba vs. 1:2.5 for Mn/La).

The same deposition parameters like for $La_{0.4}Ca_{0.6}MnO_3$ were used. The composition of the four cylindrical ceramic targets of $BaTiO_3$, $CaTiO_3$, $EuAlO_3$, and $LiMn_2O_4$ was verified by RBS or ERDA (used for $LiMn_2O_4$). $BaTiO_3$ had the expected composition, while $CaTiO_3$ and $LiMn_2O_4$ had compositions of $Ca_{1.1}Ti_{0.9}O_{2.9}$ and $Li_{0.7}Mn_2O_{3.8}$ respectively and are presented as such hereafter. $EuAlO_3$, due to the much higher scattering cross-section of Eu vs. Al had an uncertainty of ~7%.

All films, except for $EuAlO_3$, were deposited onto 20 µm thick aluminium foils (99.999% purity), which allowed a straightforward RBS/ERDA measurement and avoided channelling effects that would affect the accuracy of the measurements. In the case of $EuAlO_3$, a conductive carbon tape was used to avoid the overlapping of both Al signals on the RBS spectra (thin film and substrate). All foils/tapes were placed on the "semi-sphere" holder in its vertical arm.

3.3.2 Film thickness variation with background gas pressure

The angular thickness profiles obtained by RBS/ERDA measurements are shown in Fig.3.10. The film thickness profiles of all five target materials show a consistent picture on the effect of pressure on the deposition with the characteristic strong forward directed deposition of PLD ($La_{0.4}Ca_{0.6}MnO_3$ has been added as reference). Such a thickness profile is maintained for most deposition pressures (vacuum, $1x10^{-3}$mbar and $1x10^{-2}$mbar) and only changes at the relative high pressure of $1x10^{-1}$mbar to a quasi-constant thickness for the entire angular range. Vacuum and $1x10^{-3}$mbar show very similar profiles consistent with a MFP larger than the target-to-substrate distance, while at $1x10^{-2}$mbar there is a slight reduction in thickness at the peak location (0°). The exception is $Li_{0.7}Mn_2O_{3.8}$ where such a reduction is larger, since the MFP (Table 3.1) is already shorter than the target-to-substrate distance and one scattering event with the Ar gas will scatter the Mn species and the much lighter Li (Fig.3.10d). The mentioned behaviour for the four pressures is observed for all deposited materials, although with noticeable differences in the amount of deposited material due to differences in ablation rates, as described in table 6.6.
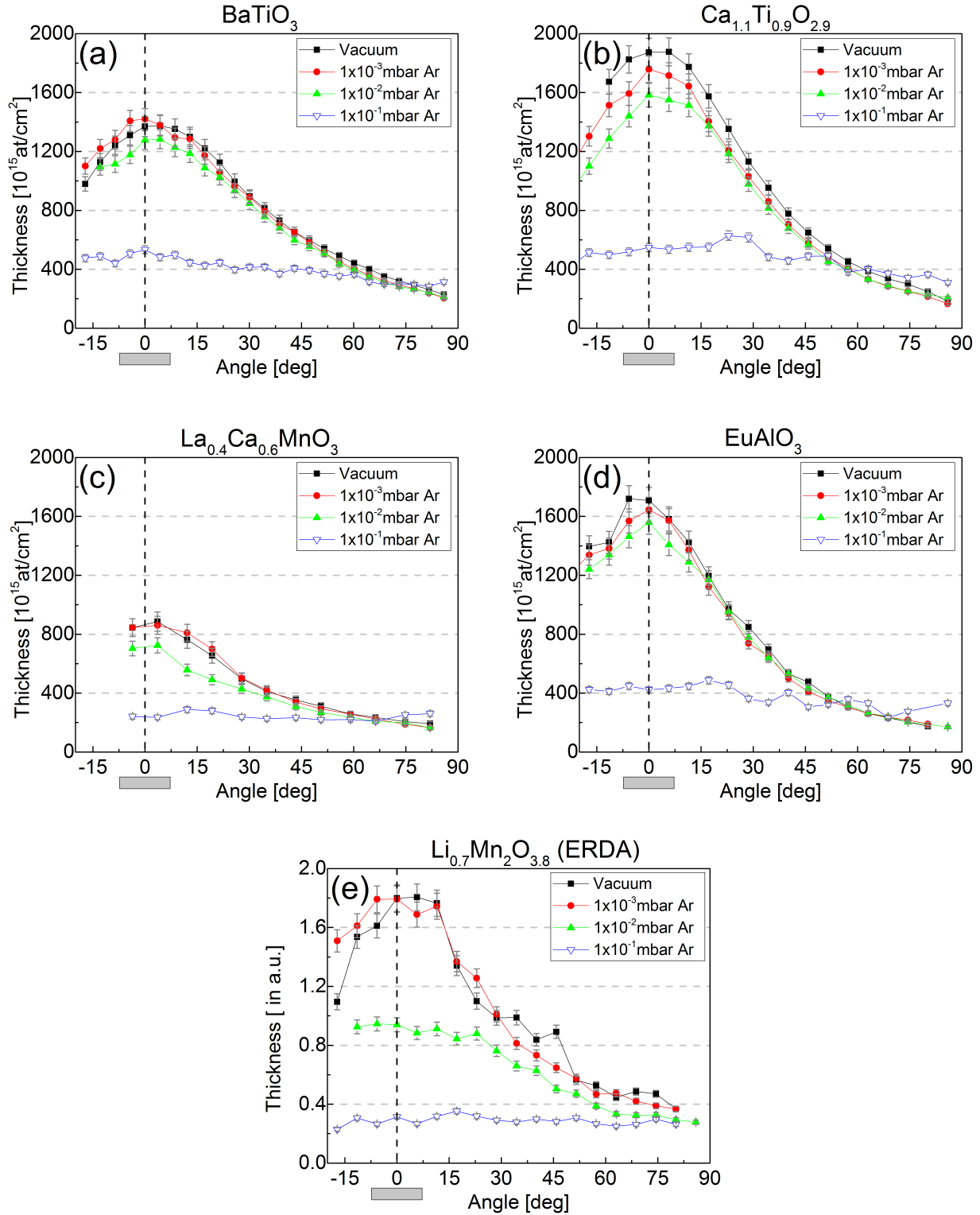
Fig.3.10. Angle resolved film thickness profiles of BaTiO$_3$ (a), Ca$_{1.1}$Ti$_{0.9}$O$_{2.9}$ (b), La$_{0.4}$Ca$_{0.6}$MnO$_3$ (c), EuAlO$_3$ (d) and Li$_{0.7}$Mn$_2$O$_{3.8}$ (e) for four different Ar background gas pressures. Note: ERDA results are presented in normalized units instead of at/cm^2 as the RBS results.

A comparison of the deposited material (as percentage of maximum for each material) is shown on Fig.3.11 to highlight the considerable material loss when depositing at 1x10^{-1}mbar. The deposited amount is reduced by ~50% compared to the vacuum deposition for most target materials (Fig.3.11a). This represents a remarkable loss of deposition efficiency. Besides, the

typical angular range covered in a PLD deposition for a substrate of 1cm² at a distance of 40mm is ±10°. In this case, the loss of material is significant ~70% (Fig.3.11b). The reason is that at this pressure the deposition is no longer forward peaked but spherical (redistribution of material due to strong scattering and other effects that are reported later in chapter 4), and due to geometrical limitations the substrate holder fails to capture it (Fig.3.12). The aluminium/carbon substrate has a finite area that covers most of the central part of the plume, but only a reduced portion at high angles (red areas in Fig.3.12b).
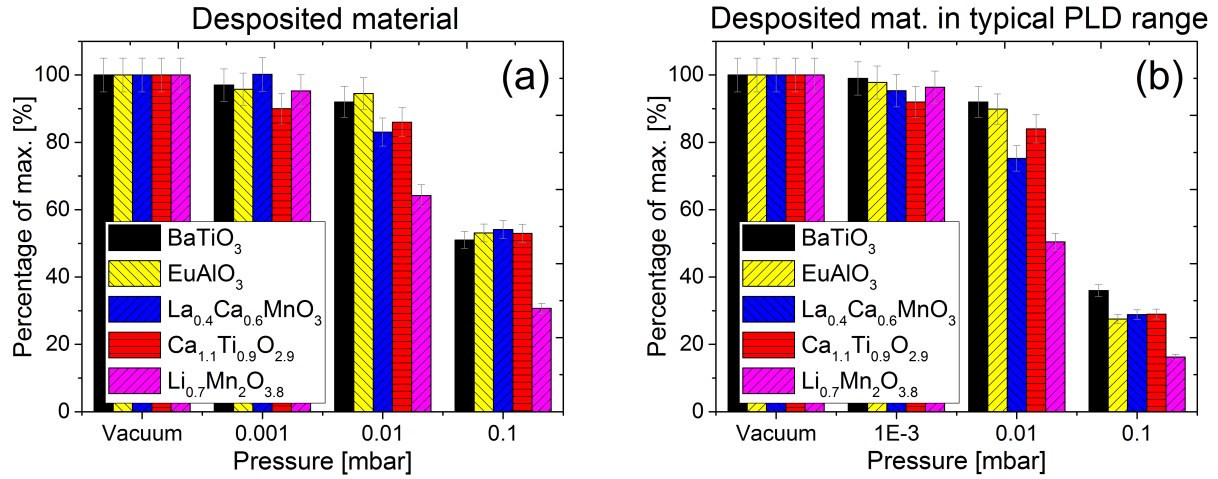
Fig.3.11. Percentage bar charts of deposited material for the different materials and deposition pressures. The percentages were calculated with respect to the maximum amount (vacuum) either for (a) the entire angular range or (b) for ±10°.
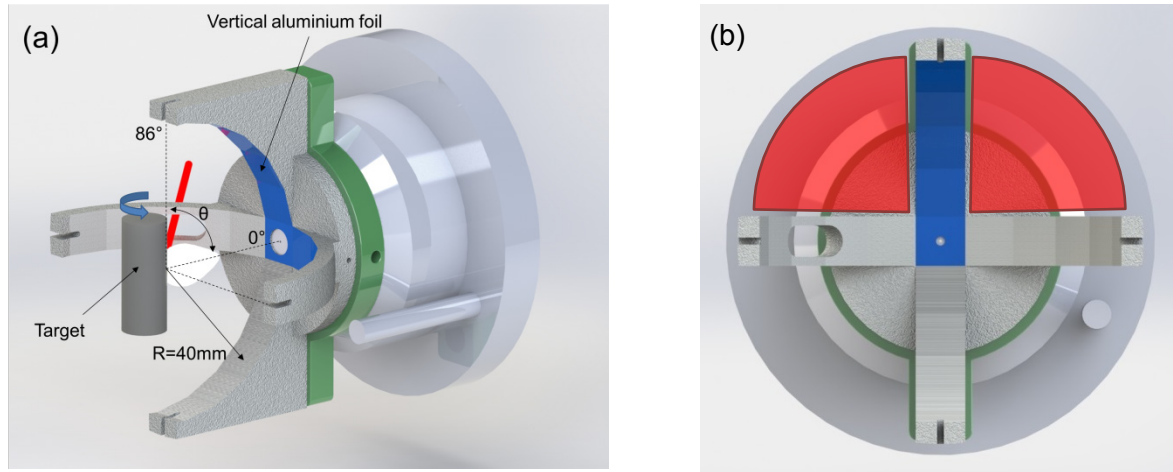
Fig.3.12. Schematic view of the substrate holder with the rod target (a) and frontal view explaining the limitations of the holder when having a fully scattered plume (b) red 3D areas are not captured

3.3.2.1 Estimation of the average scattering angle from the thickness data

From the thickness data it is possible to obtain an estimate of the average scattering angle of the species with the background gas. The convolution of the vacuum profile with a Gaussian distribution gives the non-vacuum profile in which the width of the best fitting Gaussian

corresponds to the average scattering angle. An example for $BaTiO_3$ is shown in Fig.3.13, in which an average scattering angle of 13.5° (σ) is estimated at $1x10^{-2}$mbar Ar.
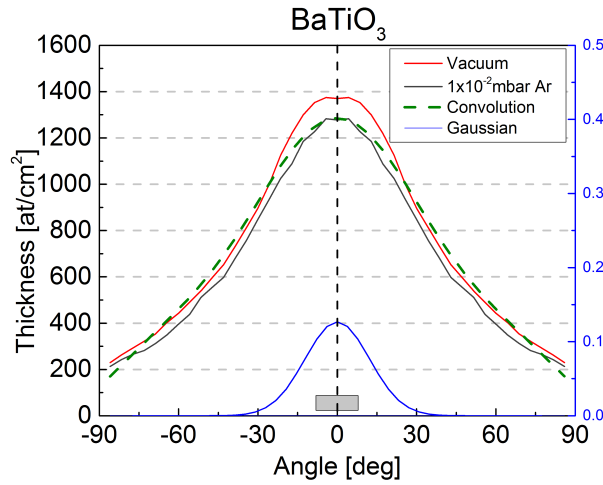
Fig.3.13. Example for $BaTiO_3$ in which the original vacuum signal and a Gaussian signal are convoluted to fit the measured film thickness at $1x10^{-2}$mbar Ar and estimate the average scattering angle (in this case 13.5°).

The results for the different target materials at a pressure of $1x10^{-2}$mbar are shown in table 3.3. They show an inverse relationship between the average scattering angle and the average mass of the species involved. This is expected from simple scattering laws since the heavier particles undergo a smaller momentum change [2]. The use of such average atomic mass units of the unit cell is not ideal, but provides a rough estimate. The calculations were only performed for this pressure as in vacuum and $1x10^{-3}$mbar no scattering with the background gas is expected and at $1x10^{-1}$mbar the plume seems fully scattered. Nonetheless, it would be interesting to explore the trend of the average scattering angle between $1x10^{-3}$mbar and $1x10^{-1}$mbar with further experiments.

Material	Average mass [amu]	Average scattering angle at $1x10^{-2}$mbar Ar
$BaTiO_3$	46.6	13.5°
$EuAlO_3$	45.4	14.5°
$La_{0.4}Ca_{0.6}MnO_3$	36.5	16.2°
$Ca_{1.1}Ti_{0.9}O_{2.9}$	27.3	19.0°
$Li_{0.7}Mn_2O_{3.8}$	25.8	55.5°

Table 3.3. Average scattering angle values for the different target materials at an Ar background gas pressure of $1x10^{-2}$mbar. Ordered in decreasing average amu of unit cell and obtained by convoluting the thickness data

3.3.3   Film cation composition variation with background gas pressure

The results of the RBS analyses are plotted in Fig.3.14 for $BaTiO_3$, $Ca_{1.1}Ti_{0.9}O_{2.9}$, $La_{0.4}Ca_{0.6}MnO_3$ and $EuAlO_3$. In Fig.3.15 the ERDA composition results for $Li_{0.7}Mn_2O_{3.8}$ are presented (as RBS is limited in accuracy when measuring light elements such as Li or O). In all graphs, the horizontal black lines represent the composition of the target material. An initial

overview of all target materials is provided hereafter while the material specific analyses are given in separate sections.

Overall, the compositional profiles exhibit noticeable variations showing that consistent congruent transfer by PLD is not necessarily the case. The variations are dependent on target material, pressure, and angular location. In terms of pressure, vacuum and $1x10^{-3}$mbar show very similar profiles for most materials, comparable to what was seen in the thickness profiles (Fig.3.10). While at $1x10^{-2}$ mbar the highest compositional changes take place (green markers and line in Fig.3.14 and Fig.3.15). This is very relevant as the biggest compositional changes at this pressure are often seen at the typical PLD angular range of ±10°. Finally, at $1x10^{-1}$mbar the film composition becomes uniform throughout the angular range in a similar way as with the thickness profiles (Fig.3.10). Although not necessarily with the same composition as the target material.
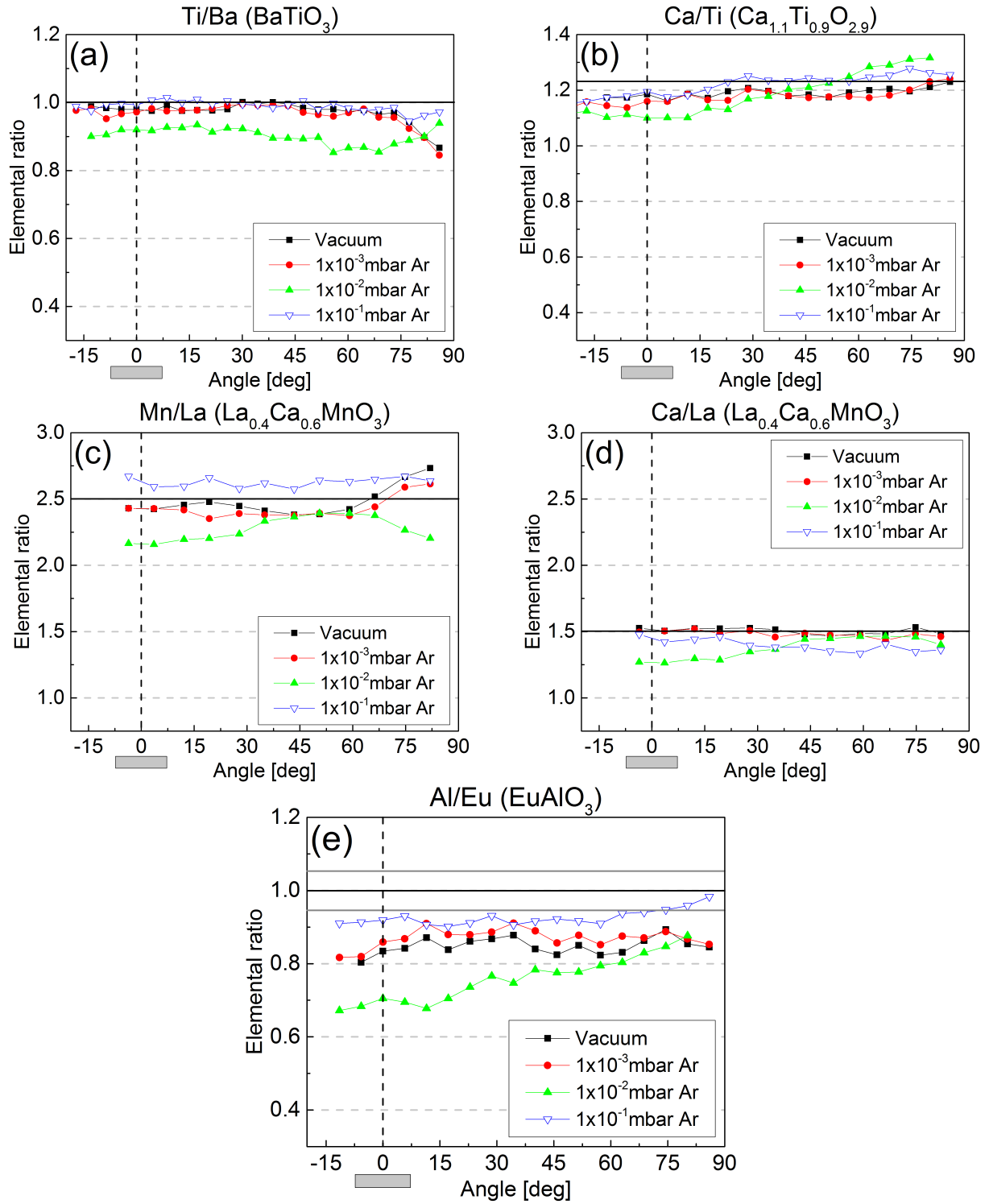
Fig.3.14. Angle-resolved film composition for $Ca_{1.1}Ti_{0.9}O_{2.9}$ (a), $BaTiO_3$(b), $La_{0.4}Ca_{0.6}MnO_3$ (c and d) and $EuAlO_3$ (e) at four different Ar background-gas pressures. Composition was obtained by RBS. The horizontal black lines represent the target composition (verified by RBS). The composition of $EuAlO_3$ had an uncertainty of 7% and is represented by the additional grey lines. The grey box represents the typical PLD deposition range. Note: error bars are smaller than the symbols.

3.3.3.1 Material BaTiO$_3$ (mass ratio of 1:2.9)

In the particular case of BaTiO$_3$ (mass ratio of 1:2.9), the film elemental ratio is close to the target composition for most pressures and angles except for 1×10^{-2}mbar (see Fig.3.14a). The composition profiles for vacuum and 1×10^{-3}mbar are nearly identical with a deviation at angles above 65° which highlight either an increase in Ba or a decrease of Ti. At 1×10^{-2}mbar and in contrast with the thickness profiles, a marked deviation takes place with a decrease in Ti/Ba of ~15% (~10% in ±10° region). This will be discussed later in the chapter. The film composition returns to the original target values at 1×10^{-1}mbar and is uniform throughout the angular range.

3.3.3.2 Material Ca$_{1.1}$Ti$_{0.9}$O$_{2.9}$ (mass ratio of 1:1.2)

As for Ca$_{1.1}$Ti$_{0.9}$O$_{2.9}$ (mass-ratio of 1:1.2 Ca:Ti) the behaviour with pressure is analogous (Fig.3.14b). Vacuum and 1×10^{-3}mbar have similar profiles, and 1×10^{-2}mbar shows the strongest deviation with pressure, although in this case it is mostly at 0° (~10%).

3.3.3.3 Material EuAlO$_3$ (mass ratio of 1:5.6)

The particular case of EuAlO$_3$ (Fig.3.14e) is very relevant as it possesses a high mass-ratio and participating cations which are still measurable by RBS (1:5.6 for Al/Eu). The composition profiles for vacuum and 1×10^{-3}mbar follow surprisingly matching patterns. Again, it is at 1×10^{-2}mbar were the strongest change in the composition can be seen with a deviation of ~33% and mainly in the central location where thin films by PLD are typically produced (±20° region). At 1×10^{-1}mbar the composition becomes uniform throughout the entire angular range, as with the other materials, but it is below the target composition.

3.3.3.4 Material Li$_{0.7}$Mn$_2$O$_{3.8}$ (mass ratio of 1:8)

There is a strong general loss of Li at all pressures and a strong angular variability. Vacuum and 1×10^{-3}mbar do not share similar angular profiles. The pressure that yields the strongest changes in composition (~70%) is in fact 1×10^{-3}mbar and not 1×10^{-2}mbar. The reasoning is that Li has a much smaller mass than the background gas Ar (Li $\approx$ 7 vs. Ar $\approx$ 40), meaning that solely one collisional interaction event with Ar is sufficient to scatter these light elements. Even at 1×10^{-3}mbar, where the MFP has a similar order of magnitude as the target-to-substrate distance, the light elements might already be stopped with one scattering event.

At 1×10^{-2}mbar the compositional deviations are reduced, possibly due to the stopping of the Mn by the background gas (inferred from La$_{0.4}$Ca$_{0.6}$MnO$_3$ composition profiles in Fig.3.14c). At 1×10^{-1}mbar the deviations increase again getting close to values seen at 1×10^{-3}mbar. This change in composition is not yet understood.
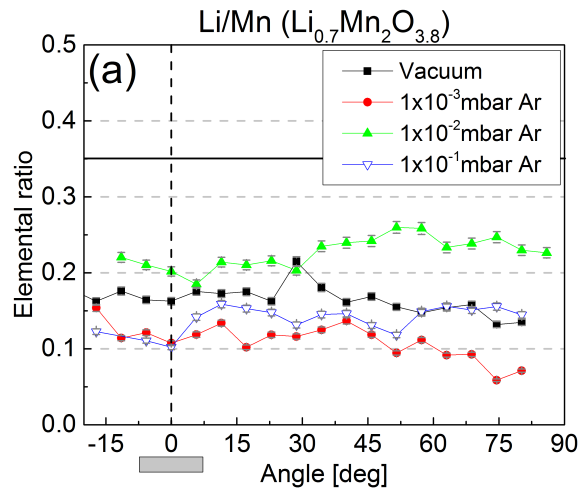
Fig.3.15. Angle-resolved film composition for $Li_{0.7}Mn_2O_{3.8}$ at four different Ar background-gas pressures. Composition was obtained by ERDA. The horizontal black line represents the target composition (verified by ERDA). The grey box represents the typical PLD deposition range.

3.3.4 General discussion

The general observation from all results is that when depositing multi-element oxide films by PLD it is very likely to have a different composition compared to the original target material (cation wise). Such variations can be strong and seem dependent on (in order of influence): target composition, pressure, target-to-substrate distance and angular location of the substrate.

With respect to the influence of pressure, the results show that the composition profiles for vacuum and $1x10^{-3}$mbar are very similar for most materials with the exception of $Li_{0.7}Mn_2O_{3.8}$. Furthermore, at such pressures two mass ratios exhibit an interesting variation at high angles. In vacuum and $1x10^{-3}$mbar, Ti/Ba (Fig.3.14 a) and Mn/La (Fig.3.14 c) both show deviations at angles above 65° towards the element with the lower sublimation energy. This is, an increase of the Ba and Mn content vs. Ti and La, respectively. This has been suggested in [69, 70], where a linear relationship was found between sublimation energies (vapour pressure) and broadness of the angular distributions for metals. However, for the case of oxides the explanation is not yet clear. The sublimation energy values are tabulated in table 3.4, and for Mn and Ba the behaviour seems independent of mass. This dependence on the sublimation energy was not noted in the case of Ca/Ti (Fig.3.14 b) and Ca/La (Fig.3.14 d) and alternatively, at $1x10^{-2}$mbar the enrichment behaviour is reversed at high angles suggesting that preferential sublimation is too simple as an approach to explain this behaviour.

Element	Mass (amu)	Sublimation energy at 25°C (KJ/mol)
Li	7	161
Ca	40	176
Eu	152	177.8
Ba	137.3	192
Mn	54.9	291
Al	27	321.9
La	138.9	430
Ti	47.9	470

Table 3.4. Mass and sublimation energies of elements in ascending order of sublimation energy (from Ref.[71, 72])

Nevertheless, the main compositional deviations appear at a pressure of 1×10^{-2}mbar for $BaTiO_3$, $Ca_{1.1}Ti_{0.9}O_{2.9}$, $La_{0.4}Ca_{0.6}MnO_3$ and $EuAlO_3$. With variations of (ordered with increasing mass-ratios): ~10% for Ca/Ti, ~13% for Mn/La, ~15% for Ti/Ba, ~16% for Ca/La and ~33% for Al/Eu. At this pressure the MFP is ~25-50% of the target-to-substrate distance (Table 3.1) and some collisions are expected. These interactions with the background gas have stronger effects on the lighter elements and are sufficient to stop or scatter them while heavier species continue to arrive (preferential scattering). In the particular case of $Li_{0.7}Mn_2O_{3.8}$ the loss of Li is seen at an even lower Ar pressure of 1×10^{-3}mbar, but this is caused by a different process. The pressure dependence of Li is difficult to assess due to its light nature and volatility: at very low pressures Li has a tendency of being re-sputtered or bounces off a surface as a consequence of the high arrival energies [33, 73], while at elevated pressures it is very easily scattered towards high angles.

Based on the presented data, we conclude that there is a strong enhancement of the compositional deviations with increasing mass-ratios. This is presented in Fig.3.16 where the compositional deviations are plotted vs. the mass-ratios. As an anchor point, Y/Zr≈1.025 is used from [54]. There is an almost linear dependence between the compositional deviations and the mass ratios, which implies that a congruent transfer from a multi-element target with high mass ratios is difficult and probably requires additional strategies to achieve it.
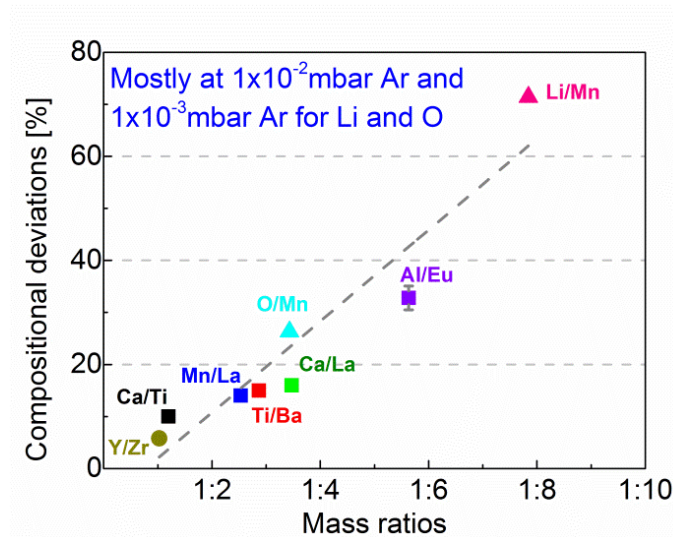
Fig.3.16. Maximum compositional deviations mostly at PLD relevant angular areas (±10°) vs. mass-ratios, mostly for $1x10^{-2}$mbar Ar. Except for O/Mn and Li/Mn in which the maximum deviations already appear at $1x10^{-3}$mbar Ar. Symbols ■ are for RBS measurements, ▲ for ERDA measurements and ● for data from [54]. Note: O/Mn deviation has a high uncertainty due to the suspicion of ambient water trapping by the amorphous film as described in the "anion composition" section. Error bars are smaller than the symbols except for EuAlO$_3$

3.3.5   Film anion composition variation with pressure

Both, RBS and ERDA measurements also provide the oxygen concentration of the films. ERDA measurements should provide a higher accuracy than RBS, as for RBS due to background and detection efficiency issues these values have an uncertainty of around 5 to 7 percent. Though, the main concern is not the accuracy of the measurements, but the source of the apparent oxygen of the film.

The results for all measured target materials are plotted in Fig.3.17 with the exception of EuAlO$_3$ in which due to the use of the carbon tape as substrate, the oxygen content could not be obtained properly. The oxygen concentration appears mostly above the oxygen concentration of the target material. There is a clear dependency of the oxygen concentration with film thickness. The thinner the film, the higher the apparent oxygen concentration as can be seen at high angular locations (>30°) as well as the films deposited at $1x10^{-1}$mbar. This is unexpected, as normally films deposited a low pressures are oxygen deficient. One explanation could be that the amorphous nature of the films (deposited at room temperature) makes them prone to capture ambient water.
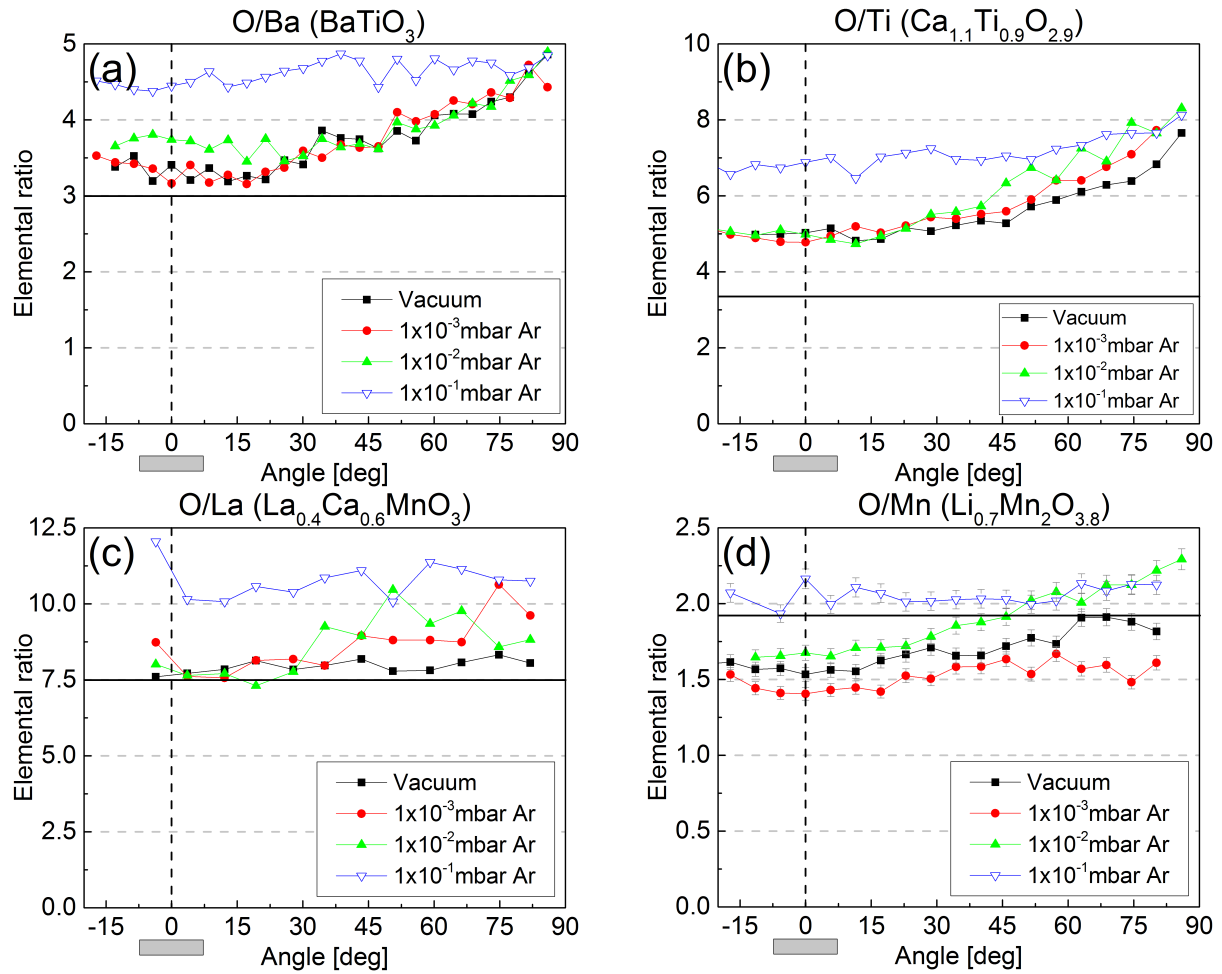
Fig.3.17. Angle-resolved oxygen concentration of films deposited at four different Ar background-gas pressures and using four different target materials: $BaTiO_3$ (a), $Ca_{1.1}Ti_{0.9}O_{2.9}$ (b), $La_{0.4}Ca_{0.6}MnO_3$ (c) and $Li_{0.7}Mn_2O_{3.8}$ (d) measured by RBS (a,b and c)/ERDA(d). The horizontal black line represents the target composition. The grey box represents the typical PLD deposition range.

In order to verify the potential trapping of ambient water, ERDA measurements with a 2 MeV He beam using the absorber foil technique to detect the hydrogen content were performed for all materials (except for $EuAlO_3$ on carbon tape). Only those films which had a strong oxygen enrichment and dissimilar angular profiles have been investigated in detail (vacuum and $1x10^{-1}$mbar Ar). The films were measured at three different locations (0°, ~45° and ~85°) using an ion beam of 4mm diameter at a glancing angle of 15° for the incidence beam and also for the detector.

The results are shown in table 3.5 and confirm that thinner films have a higher hydrogen concentration which in combination with the detected film oxygen excess suggest a common source of origin in the form of H_2O. With those located at high angles (85°) often having the highest concentrations compared to the central and intermediate locations (0° and 45°, respectively). In most cases, $1x10^{-1}$mbar films (thinnest films) have a higher hydrogen concentration than those deposited in vacuum. This does not have to be directly linked to the thickness itself, but thickness might be an indication of the mass transport mechanism [74, 75]

which could preferentially form porous films prone to ambient water trapping. This is the case for $La_{0.4}Ca_{0.6}MnO_3$ as reported in [76].

Moreover, the smallest ambient water/hydrogen concentration can be found in the $Li_{0.7}Mn_2O_{3.8}$, films, which were the only films that showed smaller oxygen concentrations than the target material Fig.3.17d. Alternatively, the $Ca_{1.1}Ti_{0.9}O_{2.9}$ films show the highest hydrogen concentrations in line with the oxygen results seen in Fig.3.17b.

ERDA measurements of film hydrogen content [at%]				
Material	Pressure	Angular location		
		0°	45°	85°
$BaTiO_3$	Vacuum	16	20.2	20.5
	$1x10^{-1}mbar$	12.6	15.2	16.7
$La_{0.4}Ca_{0.6}MnO_3$	Vacuum	8.7	12.3	12
	$1x10^{-1}mbar$	19.3	16.4	23.4
$Ca_{1.1}Ti_{0.9}O_{2.9}$	Vacuum	9	12.1	14.7
	$1x10^{-1}mbar$	22.3	19.9	20.9
$Li_{0.7}Mn_2O_{3.8}$	Vacuum	3.2	4.3	7.9
	$1x10^{-1}mbar$	11.6	11	11.6

Table 3.5. Hydrogen content of the different films in at%. They reflect the ambient water trapping by the amorphous films, with the thinner films often showing the highest concentrations (45° and 85° locations for those films deposited at $1x10^{-1}mbar$ Ar).

Is the ambient water being trapped at the surface or does it penetrate the entire film? The results, some of them plotted exemplarily in Fig.3.18 for $CaTiO_3$, show that the detected hydrogen was present through the entire films and not only at their surfaces. The thickness of the hydrogen profiles matches the thickness of the films (with vacuum at 0° being the thickest and 85° the thinnest).
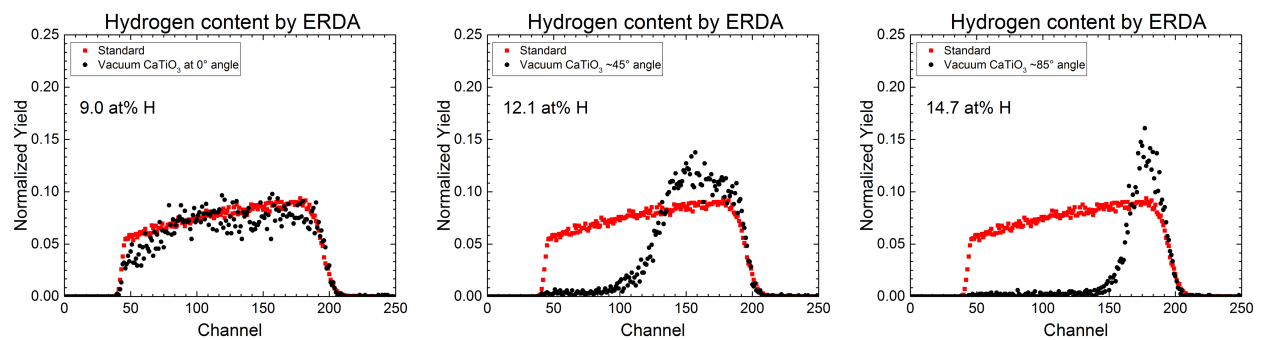
Fig.3.18. Depth profiles of H concentration vs. nm of $CaTiO_3$ films (black) with suspected trapping of ambient water. The plotted charts correspond to vacuum deposition conditions and at 0°,~45° and ~85° angular locations respectively. The red line represents the data from the standard used in the measurement.

With these data a rough estimate of the oxygen addition to the film from ambient water can be calculated. For instance, a 15% H content could mean a composition of $CaTiO_3+0.5H_2O$ making the oxygen content circa 3.5. This is a considerable oxygen enrichment which is even underestimated due to sample geometry and the measuring technique. The shadowing of the

signal by the wrinkles on the thin Al foil substrate combined with the glancing incidence angle might be causing an underestimation of the hydrogen content. The beam shape is an ellipse with axes of 1x4 mm. The ellipse was perpendicular to the foil, i.e. precision in "angular" position is 1 mm and the measurement averages over 4 mm of the foil along the same angle. The hydrogen signal was very sensitive to slight variations of the measured location.

In summary, it is not possible to assess the effect of pressure on oxygen concentration using the current depositing approach. Deposition of epitaxial films on suitable substrates and with heating is therefore needed.

3.4 General Conclusions

The deposition of five different multi-element oxides by PLD has shown the influence of background gas pressure on the angular distribution of film thickness and composition.

With respect to film thickness, the selected pressure might reduce or cancel the strong forward deposition character of PLD and bring in exchange a loss in material deposition efficiency of ~70%. Although a constant angular thickness distribution might still be interesting for industrial applications.

In terms of film composition, the conclusions are numerous. Overall, compositional deviations with respect to target composition are common. The reported results show the dependence on target composition, background pressure, target-to-substrate distance and angular location, as these were the parameters explored in these experiments.

The background gas can have a strong influence on the composition. An influence that increases with higher mass-ratios of the participating elements for a certain pressure regime. At $1x10^{-2}$mbar the deviations for Ca/Ti were ~10% while for Ca/La it was ~16% and for Al/Eu ~33%. Whilst for $1x10^{-3}$mbar, Li/Mn showed a deviation of ~70%. The assumption is that at this precise pressure window the number of scattering events with the background gas are sufficient to preferentially stop the light elements from reaching the substrate while the heavier species still arrive. As a consequence a compositional deviation is detected with larger deviations with increasing target-to-substrate distances, as evidenced by the results using the planar substrate holder. However, once the pressure is high enough to also affect the heavy elements, the compositional deviations are reduced, with the composition becoming uniform throughout the angular range but being not necessarily the same as the target. The anion compositional deviations could not be evaluated due to the detected large ambient water trapping by the amorphous films.

In addition, the results for the given pressures are for room temperatures conditions and it is therefore expected that the use of a higher deposition temperature will cause a shift of the regimes to higher pressure values [65]. This was validated for $La_{0.4}Ca_{0.6}MnO_3$ confirming that

the findings on film thickness and composition can be extrapolated to higher temperature depositions.

In summary, the main finding is that when depositing multi-element materials with high mass-ratios the selection of background gas pressure is critical (and probably the type of gas: mass, size…). This has been found by analysing the produced films as a result of the interaction with the background gas. The following chapter moves to the source of origin by using time resolved imaging to visualize these interactions between plasma plume species and background gas, enabling a better understanding of the dynamics that cause the reported changes in film thickness and composition.

4 Plasma plume dynamics: visualizing the effect of the background pressure and substrate heating

Continuing with the investigation from the previous chapter on the influence of the background gas during the PLD process, the study shifts to plasma plume imaging as a complimentary technique. By time and space resolved imaging the influence of different background gases, pressures, and substrate heating on the plasma plume expansion dynamics is visually presented. The ablation of silver is taken as model system, encountering excitation effects, rebounds and re-coating of the ablated target with a significant thickness. Something which directly affects film growth and composition. Additionally, the influence of substrate heating on the background gas is also analysed exploring its effects both experimentally and analytically. Furthermore, the research then moves to the thesis' material $La_{0.4}Ca_{0.6}MnO_3$, confirming the findings from Ag ablation and closes the loop with the film compositional deviations and thickness profiles reported in chapter 3.

4.1 Plasma plume of silver as model system

4.1.1 Specific experimental details and emission spectra

Using the KrF excimer laser (λ = 248nm) described in chapter 2, a mask was applied to image a rectangular cross section of the laser beam profile on a cylindrical silver target with dimensions of 1 mm x 1.4mm with the shortest dimension matching the vertical direction of the imaging device (as will be shown in chapter 5, the geometry of the beam profile is a fundamental factor to the angular distribution of species). The experiments were carried out with a fluence of 3 J/cm^2 at a repetition rate of 4Hz. Two different background gases were used: Ar and O_2. The experiments were performed in vacuum and at 1×10^{-2}mbar and 1×10^{-1}mbar. They were performed at room temperature, 600°C and in some cases at 800°C (O_2) to analyse the influence of the substrate heating on the plasma expansion dynamics.

The intensified charge-coupled device (ICCD) "Andor New i-star" described in chapter 2 was used to record the time evolution of the ablated material. The images were recorded for either all light passing through a quartz window (200 nm-1000 nm) or for selected wavelengths using an AOTF. An image of the experimental setup can be seen in Fig.4.1.
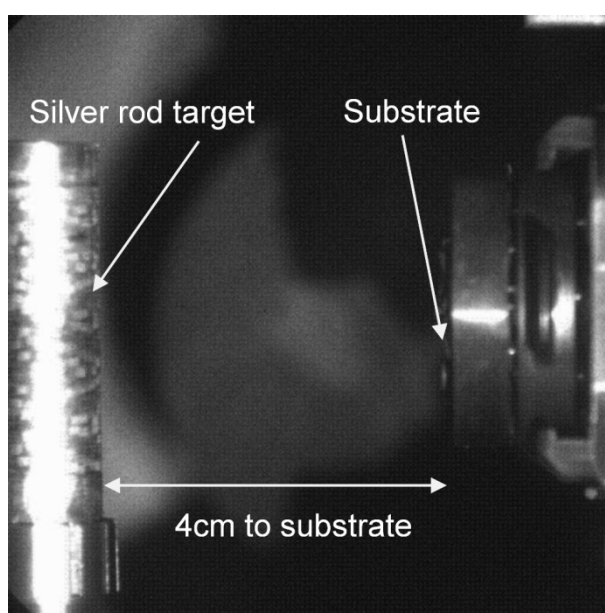
Fig.4.1. Image of the experimental setup with a silver rod target on the left and a substrate 4 cm away on the right hand side. The substrate is mounted on a heated substrate-holder. The image was taken using the same ICCD as for the experiments

Chemical reactions within the plasma plume and with the background gas were investigated by spectroscopic analyses using the monochromator described in detail in chapter 2 (Acton research Spectra Pro 500). The emission spectra were recorded for vacuum, Ar and O_2 background gases (both at 1×10^{-1}mbar). Initially a coarse grating was used to capture a broader spectrum from 500-830 nm (Fig.4.2a), while a higher resolution measurement was subsequently performed between 760-830 nm (Fig.4.2b). In this case the region of interest was

divided into smaller wavelength sections (~15nm, using a high resolution grating) which were subsequently stitched together.
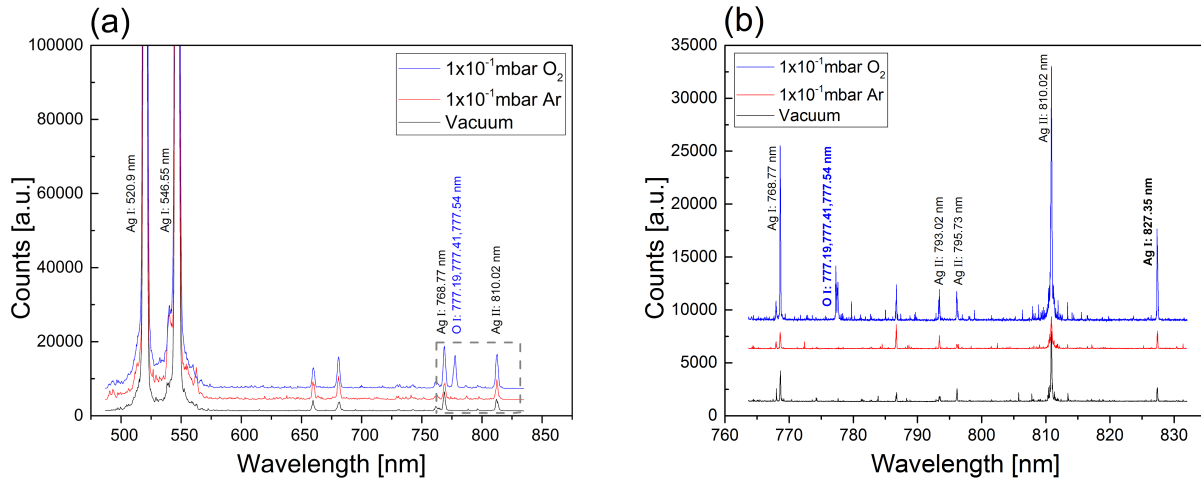
Fig.4.2. Emission spectra for silver ablation in vacuum, Ar and O_2 (both at 1×10^{-1} mbar) for wavelengths of 500-830 nm (a) and with a higher resolution for 765-830 nm (b)

The emission spectra from the silver ablation show a low number of emissions lines compared to other elements from the periodic table and is characteristically green to the human eye as the high intensity emission lines at 520.9 and 546.55 nm confirm (Fig.4.2a). There is a clear quenching of the emission intensity in Ar in the 765-830 nm range (Fig.4.2b), while in O_2 several overlapping high intensity peaks of O I arise (777.19, 777.41 and 777.54 m) and most emission intensities increase (suggesting that collisions with O_2 create more excited state species).

The emission lines were identified using references [77, 78] and the selected lines are listed in table 4.1. The selection was based on emission lines being among the strongest for the particular species, attainable by the range of the AOTF (550-1000 nm) and sufficiently separated to allow correct imaging. Although for Ar the selection was based on the recommended lines from [78]. The selected wavelength values were then used for the AOTF measurements to allow the time-resolved imaging of the different species. All the selected spectral lines except one were from neutral (I) rather than single ionized states (II).

Species	State	Emission wavelength [nm]	Intensity
O	I	777.19	870
O	I	777.41	810
O	I	777.54	750
Ag	II	810.025	810
Ar	I	811.531	35000
Ag	I	827.35	290

Table 4.1. Used emission wavelengths of Ag, O and Ar by either arc, spark or discharge excitation [77, 78]. The common nomenclature for emission spectroscopy is used with I = neutral state, II = single ionised and III = double ionised state. Remark: intensities are rough indicators as different observers use different scales and excitation sources.

4.1.2   Room temperature analyses

The measurements performed without substrate heating are shown in Fig.4.3 for the different pressure conditions and background gases. All images are taken with the same aperture and exposure times. The intensity scales are identical for all images to provide a clear understanding of the time evolution of emission intensities, even if this causes out-of-range values below 5 µs.

The plasma plume expansion in vacuum is the fastest to reach the substrate in less than 2 µs and shows a strong forward peaked shape (t = 1.75 µs). This is in accordance to the film thickness profiles seen in chapter 3. Interestingly after reaching the substrate there is a rebound of plasma species that modify the shape of the plasma front and push it towards the ablated target (visible at 5 µs and 7 µs images and marked with a dashed line). With an increase of pressure to 1×10^{-2} mbar the arrival is delayed for both background gases, O_2 and Ar ($t_{O2} \approx 2.75$ µs and $t_{Ar} \approx 3$ µs). At such a pressure the MFP becomes shorter than the target-to-substrate distance and collisions with the background gas are expected. There were indications in the thickness profiles (Fig.3.10) but it is now visually confirmed. The difference in expansion vs. vacuum is already visible at 1 µs with vacuum presenting a more elongated profile. The rebound effect is hardly visible. Comparing O_2 and Ar as background gases, the latter shows a later time of arrival due to its higher stopping power (already visible at 3 µs), a consequence of the different masses (A=32 vs. A=40) and also the van der Waals volume. The molecular volume of O_2 is 23.013 $Å^3$ (calculated using van der Waals radius of 1.52 Å and an interatomic distance of 1.2074 Å [77, 79]) while the atomic volume of Ar is 27.83 $Å^3$ (Van der Waals radius of 1.88 Å [77]).

At 1×10^{-1} mbar the arrival times for O_2 and Ar are $t_{O2} \approx 9.75$ µs and $t_{Ar} \approx 28$ µs, ~5-10 times longer than in vacuum. Apart from the arrival times, there are also changes in the plasma plume shape and light emission. In both cases the plasma plume quickly transforms from a forward peaked to a broadened spherical geometry (in the 2-5 µs range), which although 2D images on the expansion are reported, it is a 3D shape and resembles the expansion of an air bubble in water.
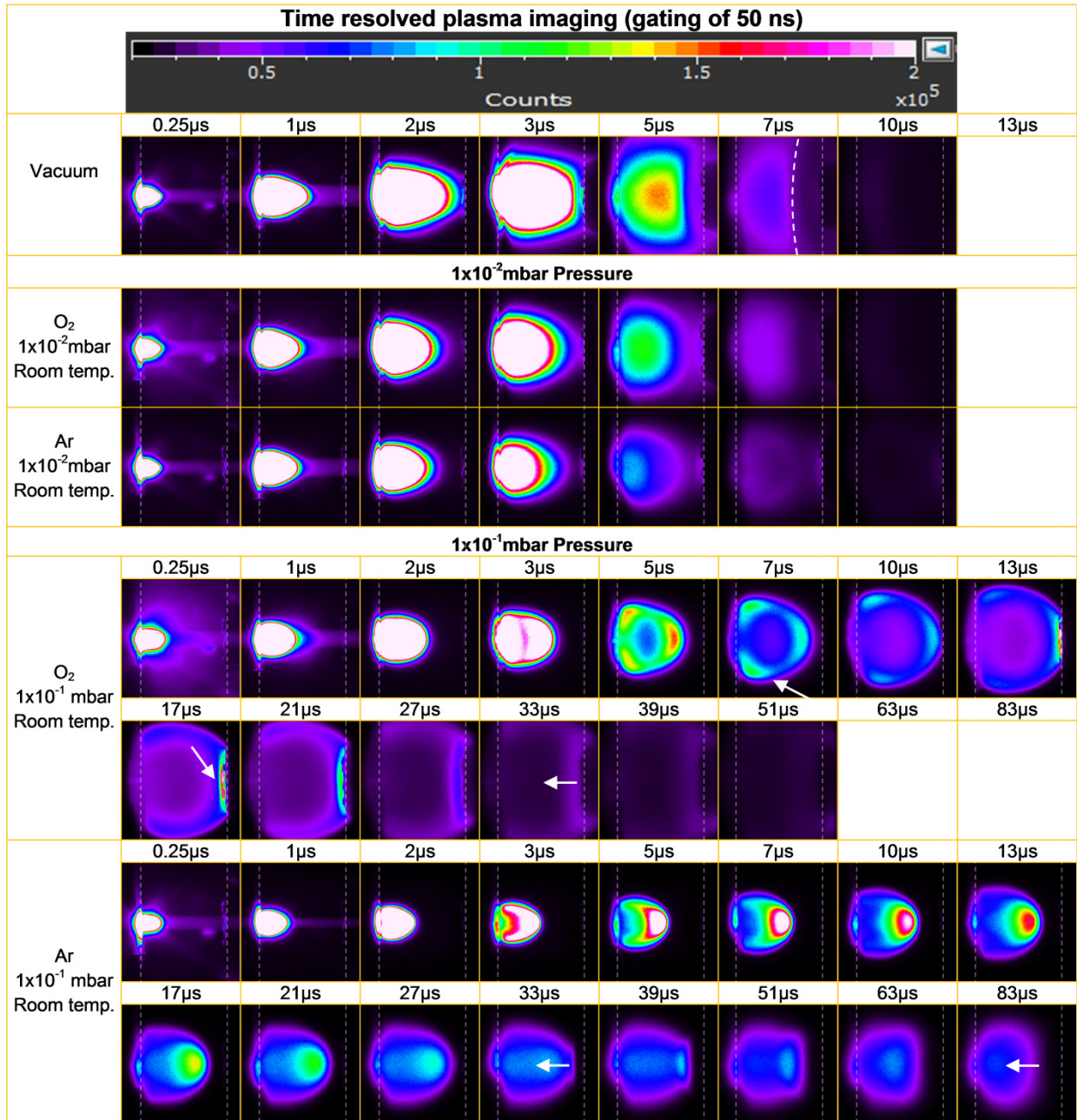
Fig.4.3. ICCD time resolved plasma imaging for vacuum, 1×10^{-2}mbar and 1×10^{-1}mbar for O_2 and Ar background gases without substrate heating. Images of visible light (200 nm-1000 nm) with no filter applied. The plume expands from the ablated target on the left to the substrate on the right (both marked with vertical dashed lines). Note: all images share the same intensity scale even if that means reaching saturation.

In terms of emission, there is a considerable amount of excitations evidenced by the longer emission times. This takes place mostly at the plasma plume front for Ar and around its entire perimeter for O_2 (a clear example can be seen in Fig.4.3 at t = 7 µs and marked with an inclined arrow). In the latter it includes chemical reactions between the plasma plume outer species and the O_2 background to form metal oxygen species and is further analysed in section 4.1.2.1. For Ar, it is mostly excitations due to collisional interactions taking place at the centre of the plasma front where the species travel with the highest kinetic energies.

On a larger time scale (>13 µs), O_2 shows an intense excitation of species just above the substrate (marked with an arrow on Fig.4.3 at t = 17 µs). It covers the substrate and its holder, resembling a boundary layer of 5 mm thickness and lasts for ~20 µs, twice the time it took the plasma to arrive at the substrate. A time resolved intensity profile is shown in Fig.4.5a to highlight the effect. It shows that once the plasma arrives at the substrate (~10 µs) there is a considerable increase in light emission, which is even higher than the intensities seen at 5 µs and lasts up to 27 µs before gradually disappearing (Fig.4.3 at 33-51µs).

It seems that this is a consequence of the trapping of the O_2 background gas against the frontal area of the holder as it is displaced by the rapid expansion of the plasma plume (the holder has a 2.5 cm diameter frontal area). Hence, an O_2 rich volume is squeezed just on top of the substrate/holder creating a transient high local O_2 pressure, leading to a very reactive environment (as sketched in Fig.4.4). This means that most of the deposited species will mainly react chemically with the O_2 gas in the last 5 mm of their path, instants before arriving at the substrate surface.
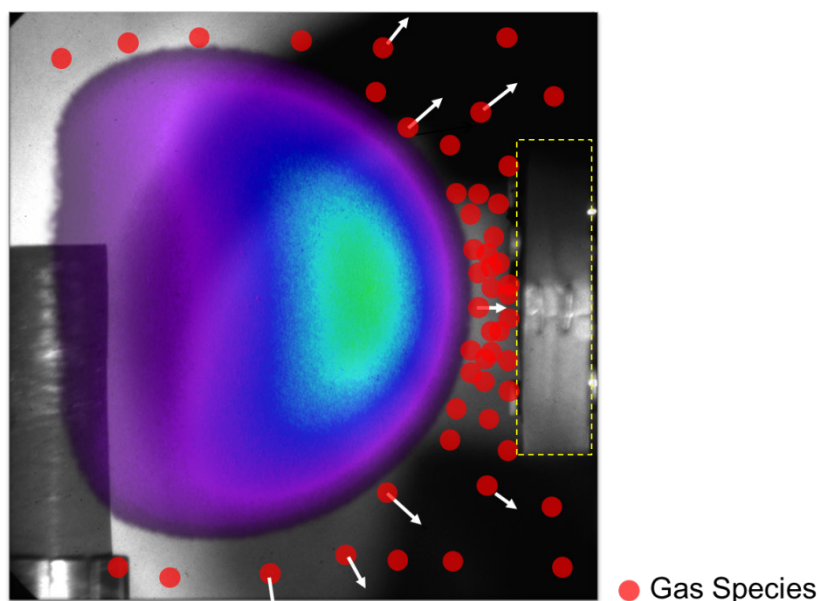
Fig.4.4. Explainer sketch of background gas trapping between expanding plume and substrate holder

An analogous emission in the near substrate region has been previously reported lasting a few µs. In vacuum it is formed by the interactions of incoming and reflected fluxes from pyrolytic carbon ablation [40] and for a Zr I excitation in Ar from yttria stabilized zirconia ablation [41]. Although for the latter the experimental pressure was too low to provide meaningful interactions with the expanding plume (at 1×10^{-3} mbar Ar the MFP is ~180 mm vs. the 60 mm target-to-substrate distance) and from the data it is not possible to judge if the emission intensity increased with respect to the previous time-frames.
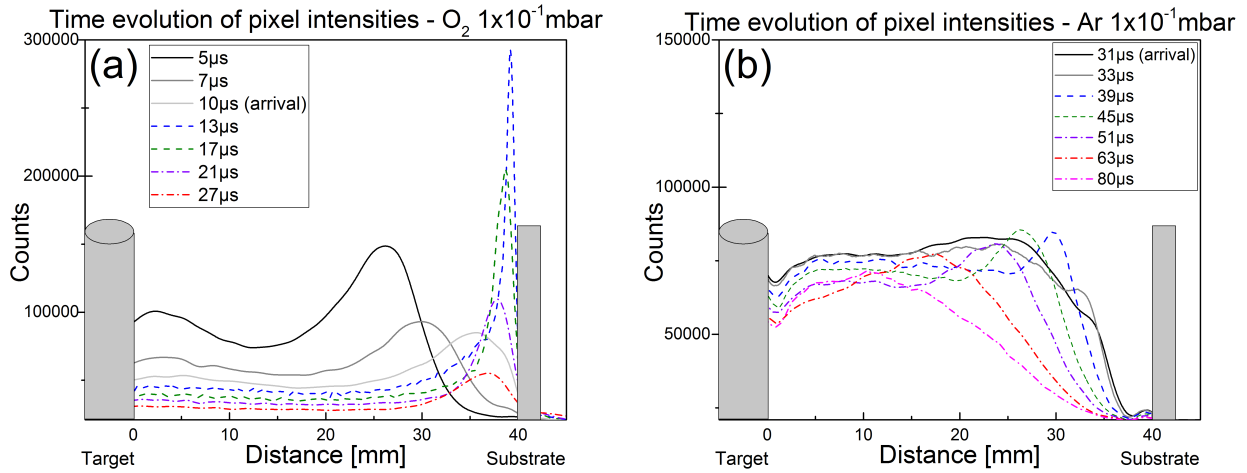
Fig.4.5. Time-resolved intensity profiles along the centre of the plasma plume from ablated target to substrate. For a background gas pressure of 1x10⁻¹mbar O_2 (a) and Ar (b). Both at room temperature.

This locally enhanced pressure has not been reported before nor implemented in any PLD mathematical model developed to date and which would have a critical role on deposition rates, chemistry and dynamics [80-82]. An approximation of the value of this transient pressure can be obtained by using Boyle's gas law (PV = constant). If it is assumed that the temperature and the amount of gas remains unchanged, a piston like compression of a cylindrical volume (Ø of the substrate holder) from a length of 30 mm to one of 3 mm is equivalent to a 10 fold rise in pressure. This would correspond to a local transient pressure of 1 mbar vs. the original 0.1 mbar of the background gas.

With respect to the Ar measurements at 1x10⁻¹mbar (Fig.4.5b and Fig.4.6b), there is no excitation/light emitting volume on top of the substrate holder. Just 5 mm before reaching the substrate, the light emitting plasma plume is stopped, no light is emitted from this region above the substrate (marked with an arrow in Fig.4.6b) and instants later a rebound wave can be seen traveling backwards (visible in the dashed intensity profiles in Fig.4.5b). This is also visible in Fig.4.3, starting at circa 31 μs and progressing up to 83 μs when some rebounded species arrive to the rod target. This rebound follows a different mechanism to those seen in vacuum and 1x10⁻²mbar, as it is not caused by the species reflected after hitting the substrate.

As with O_2, it seems that the rapid expansion of the plasma plume compresses a portion of Ar gas against the substrate holder. This compressed gas acts then as a spring once the plasma plume is stopped and forces it to rebound due to the remaining pressure gradient. Surprisingly this rebound travels at a higher velocity than the one of arrival to the substrate (~530 m/s ± 40 m/s vs. the arrival of ~280 m/s ± 47 m/s). A velocity which is nearly constant during the return to the target (measured from t = 35-57 μs) as it encounters no collisions with gas species to slow it down.
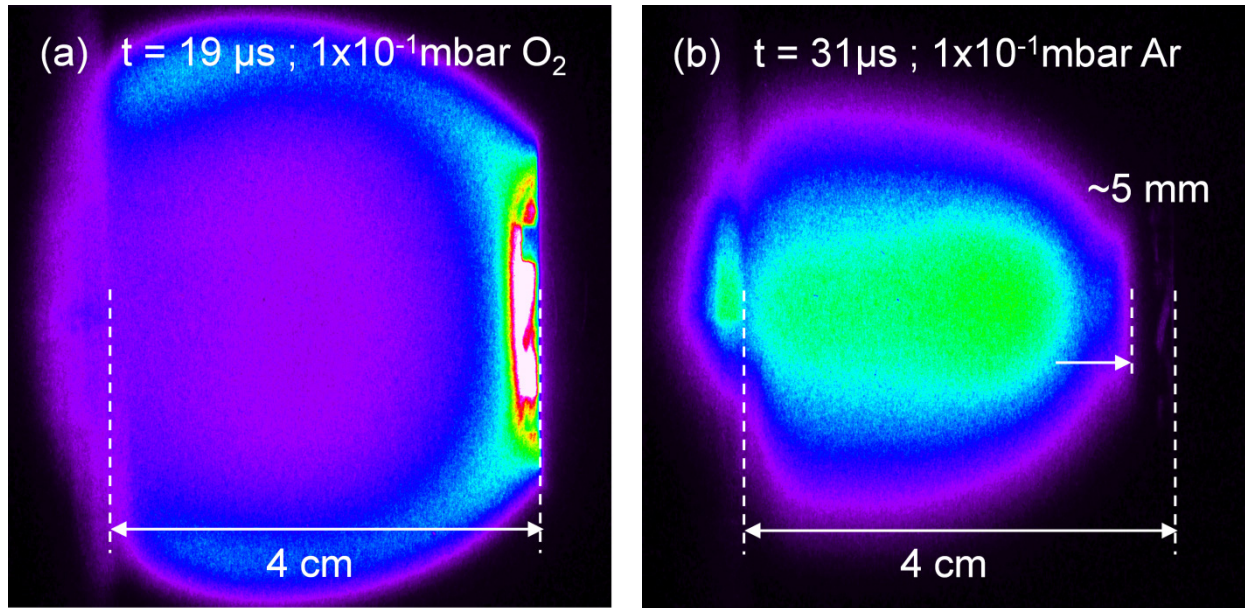
Fig.4.6. Plasma plume arrival behaviour for 1x10^{-1}mbar O$_2$ (a) (for *t*=19 µs) and Ar (b) (for *t*=31 µs), both at room temperature. The non-emitting area close to the substrate is highlighted in (b) as well as the positions of target and substrate. Both images share the same intensity scale.

The rebound arrives at the ablated target ~100 µs after the laser shot. Thus, redepositing material on its surface and very likely affecting its surface composition, if it would be a multi-element target. This possibility will be explored in detail in section 4.2.2.2 for La$_{0.4}$Ca$_{0.6}$MnO$_3$.

4.1.2.1   Time and space resolved study of selected species

The intense light emission close to the substrate surface observed in Fig.4.6b was subsequently analysed by recording the O I and Ag I emission wavelengths (Fig.4.7). No significant O I excitation was detected at that location, while Ag I showed a noticeable enhancement. Although it does not seem to be the sole contributor to it as the characteristic emission in the perimeter of the plume does not come from either Ag I or O I.

No AgO I emission lines could be found in the literature and no information concerning the temporal and spatial distributions of this species could be recorded. Due to this deficiency of our model system (Ag) it was decided to repeat the experiment with La$_{0.4}$Ca$_{0.6}$MnO$_3$, as for this particular material LaO I emission lines are well known [77]. The emission line at 560.25 nm was chosen and the results can be seen in Fig.4.33d together with those of other species.
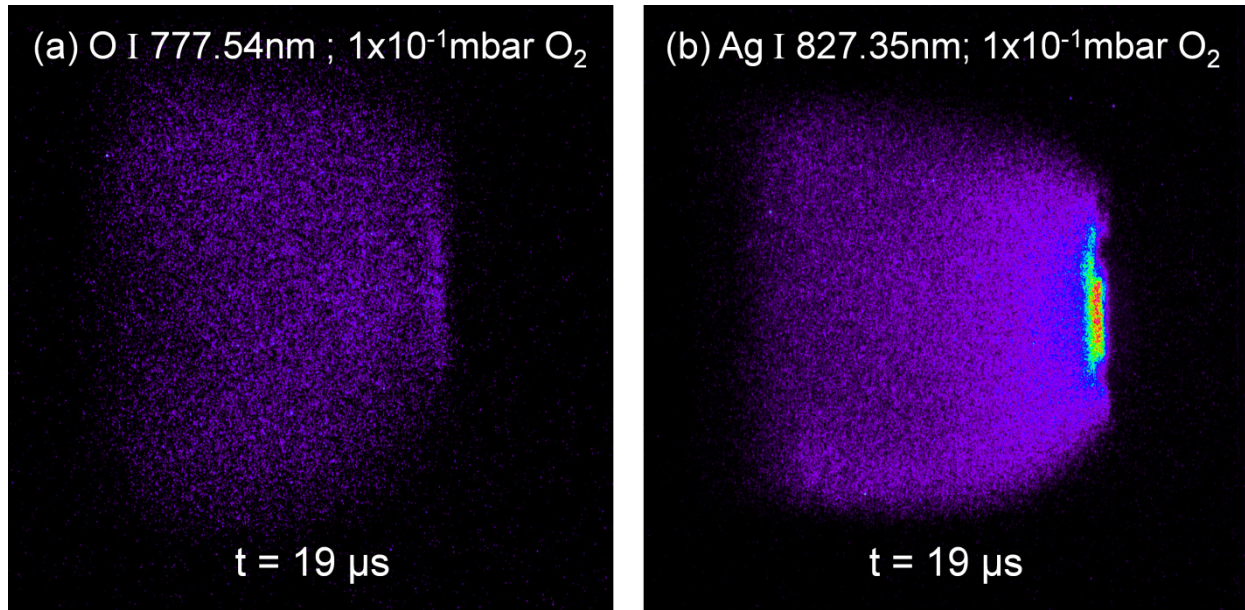
Fig.4.7. ICCD images showing the spatial distributions at *t*=19 μs of O I (a) and Ag I (b). An AOTF filter was used to capture the emission wave-lengths of 777.54 nm (for O I) and 827.35 nm for (Ag I). Due to the reduced light transmission when using the AOTF a gating time of 1μs and 100 accumulations were necessary to ensure visibility. The emission scales were selected to ensure maximum contrast

For $La_{0.4}Ca_{0.6}MnO_3$ the arrival time to the substrate is shorter than for Ag at the same O_2 gas pressures. This is likely caused by the higher ablation rates of $La_{0.4}Ca_{0.6}MnO_3$ vs. Ag (higher number of species and inertia of the expanding plume). This is seen for the general plasma emission image Fig.4.33b (shown later in 4.2.2.1), as well as for the different spatial distributions of species. With the spatial distribution of LaO I showing the high emissivity area close to the substrate Fig.4.33d, proving that this area with high oxygen concentration favours the generation of metal oxygen species. Moreover, at this specific time-frame of 16 μs, the late arrival of O I (the lightest participating element and easier to stop) is captured while it is still approaching the substrate Fig.4.33f.

In addition, the use of selective imaging allows to measure if neutral and ionic species have similar expansion dynamics. With this purpose a time resolved comparison between the distributions of ions and neutrals in vacuum is shown in Fig.4.8. The velocities and spatial distributions of neutrals (Ag I) and ions (Ag II) are slightly different up to 1 μs with the ions showing higher velocities and a slightly more elongated spatial distribution. After 1 μs the differences are weakened probably due to the shorter emission lifetime of Ag ions and/or their combination with electrons to form neutrals. This is in agreement with other reported results were ions have higher velocities than neutrals, for instance Zr and Zr^+ in the ablation of yttria stabilized zirconia using different background pressures (YSZ) [41] or Geohegan *et al.* in [83] where the ablation of $Y_1Ba_2Cu_3O_{7-x}$ in vacuum shows Ba ions having higher velocities than Ba neutrals.
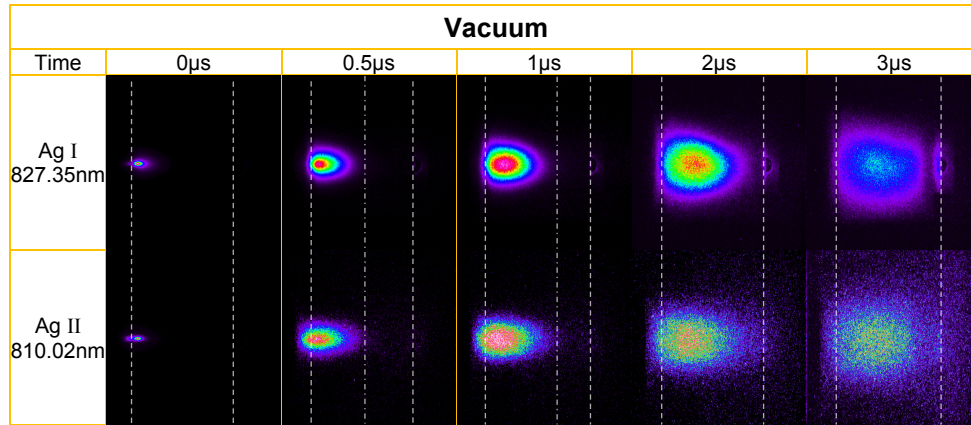
Fig.4.8. Spatial distributions in vacuum of Ag I (neutral) and Ag II (single ionized) without substrate heating. Note: the intensity scale of each single image has been adapted to maximize contrast as Ag II shows very low intensities with increasing time delays. The target and substrate positions have been marked using dashed lines as well as the Ag II plume front using a dash-dot line.

4.1.2.2   Analysis of position-resolved plasma velocities

To provide a better understanding of the expansion dynamics for the different pressures, a position-resolved velocity chart is presented in Fig.4.9. The chart shows the traveling velocities of the plasma front calculated by averaging the distances travelled with respect to time of 3 consecutive frames (250 ns delay between frames).

They reveal initial velocities of ~28'000 m/s which, for the case of vacuum, remain constant at ~20'000 m/s during the whole path to the substrate. In the case of $1x10^{-2}$mbar, there is no significant difference in velocities with respect to vacuum until a distance of 25 mm is covered, where both O_2 and Ar background gases begin reducing the velocity of the expanding plume. In these cases the plume lowers its velocity up to ~2'800 m/s moments before reaching the substrate, with Ar exerting a higher stopping power.

This difference is more pronounced at $1x10^{-1}$mbar. Ar is able to drop the initial velocity of 28'000 m/s down to ~2'800 m/s at a travelled distance of 15 mm, while in O_2 it still has ~4'200 m/s. From there onwards there is an exponential reduction of velocity with interesting periodic undulations (highlighted with a line in Fig.4.9a for O_2 $1x10^{-1}$mbar). It is suspected that they are caused by shockwaves generated by the background gas during the expansion. They are also detected in other directions in the same time frames (i.e. vertical expansion, parallel to the rod target). This is a phenomenon commonly detected by shadowgraphy methods when ablating at high background pressures [84]. Finally the arrival velocities to the substrate are ~280 m/s for Ar and ~1'400 m/s for O_2 as background gases, with a rebound then travelling backwards at a constant speed of ~530 m/s (Ar).
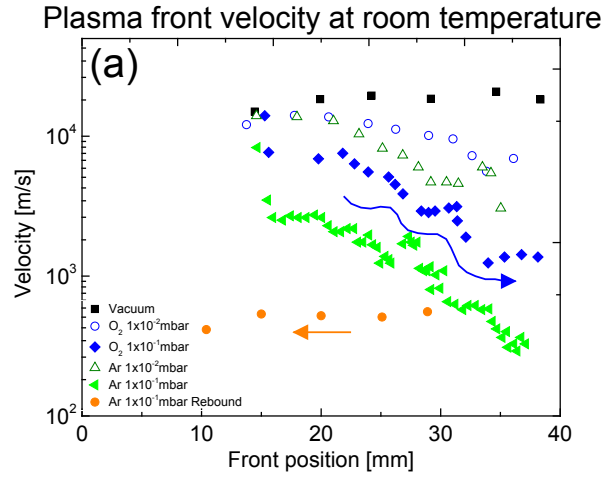
Fig.4.9. Position resolved plasma velocities of Ag ablation for different background gases and pressures at room temperature. The first 15 mm velocities could not be obtained due to sensor saturation (exposure gating was kept constant on purpose for all frames)

4.1.2.3   Resolving the initial stages of the plume expansion

Due to the saturation of the images during the initial stages (Fig.4.3 from t = 0-3 μs) the comparison between the different pressures and gases could not be performed. To capture the plasma expansion in these initial stages the measurements were repeated using shorter gate times (10 ns vs. 50 ns), which reduced the saturation of the sensor and allowed the visualization of the plume below the 3 μs time-frame. The results are plotted in Fig.4.10 confirming the dynamics observed when using O_2 or Ar.

The distribution of the plume species in vacuum is forward peaked with $1x10^{-2}$mbar already changings its shape into a spherical front. The interesting events take place at the highest pressure of $1x10^{-1}$mbar where the background gas strongly opposes the free expansion of the plasma plume. It divides the plume into two regions of light emission (plume splitting: a separation of the plasma plume into a fast component which undergoes none or very little collisions and a slow component which has been slowed down due to considerable scattering events [40]) and Ar turns it into an arrow shaped emission area (with higher intensity than O_2) as the plasma species breach the background gas. Above 3 μs the captured light was insufficient for imaging.
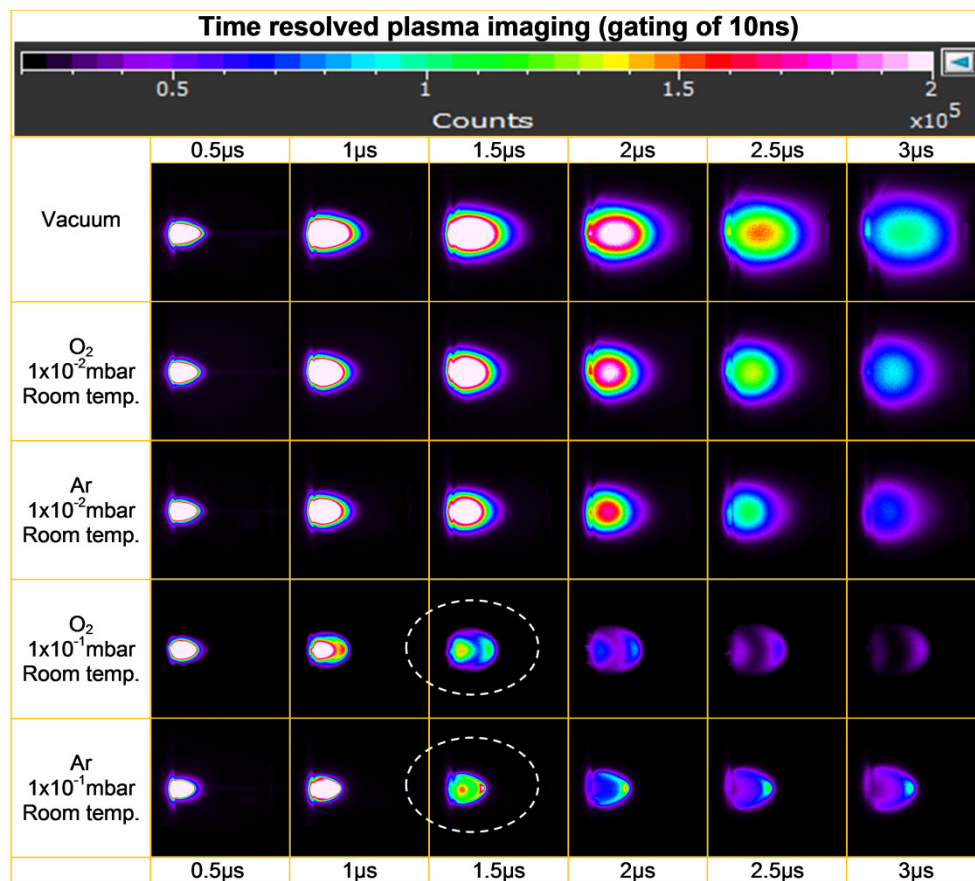
Fig.4.10. Time resolved plasma imaging of Ag ablation for vacuum, 1×10^{-2}mbar and 1×10^{-1}mbar for O_2 and Ar background gases without substrate heating. The plume splitting has been highlighted using dashed curves.

An analysis of the spatial distributions of species at 1×10^{-1}mbar using the AOTF setup is shown in Fig.4.11. The Ag I spatial distributions are reported and also the response of the background gas species O_2 and Ar when being displaced by the Ag plume.

For the O_2 background, the aforementioned division of the plume in the early stages is evidently solely composed of Ag species. The O I excitation is slightly ahead and enclosing the Ag plasma. In the initial stages (0.5 µs-1.2 µs) a propagation of excitations can be seen in the O_2 background, probably a shockwave excitation travelling through the background gas. Above 1.2 µs the O I transforms into a hemispherical shape opposing the Ag species and around ~2.5 µs forces them into such an hemispherical shape.

With the Ar background, the Ag I dynamics show the characteristic arrow-like shape. The Ar I shape is atypical as it is spherical already at the early stages of expansion and located just in front of the Ag I plume. This Ar I emitting sphere remains until ~1 µs when it seems to be penetrated by the energetic Ag plume, forming two complementary shapes as shown in Fig.4.12ab at the 1.4 µs timeframe (the repetition of the boomerang-like shape of Ar I is probably due to a shockwave excitation).

Time resolved spatial distribution of species (wavelength selected, 100ns gating)									
O$_2$ 1x10^{-1}mbar Room temp.	O I 777.54 nm								
	Ag I 827.35 nm								
Ar 1x10^{-1}mbar Room temp.	Ag I 827.35 nm								
	Ar I 811.53 nm								
Time after laser pulse		0.2µs	0.5µs	0.7µs	1µs	1.2µs	1.5µs	2µs	2.5µs
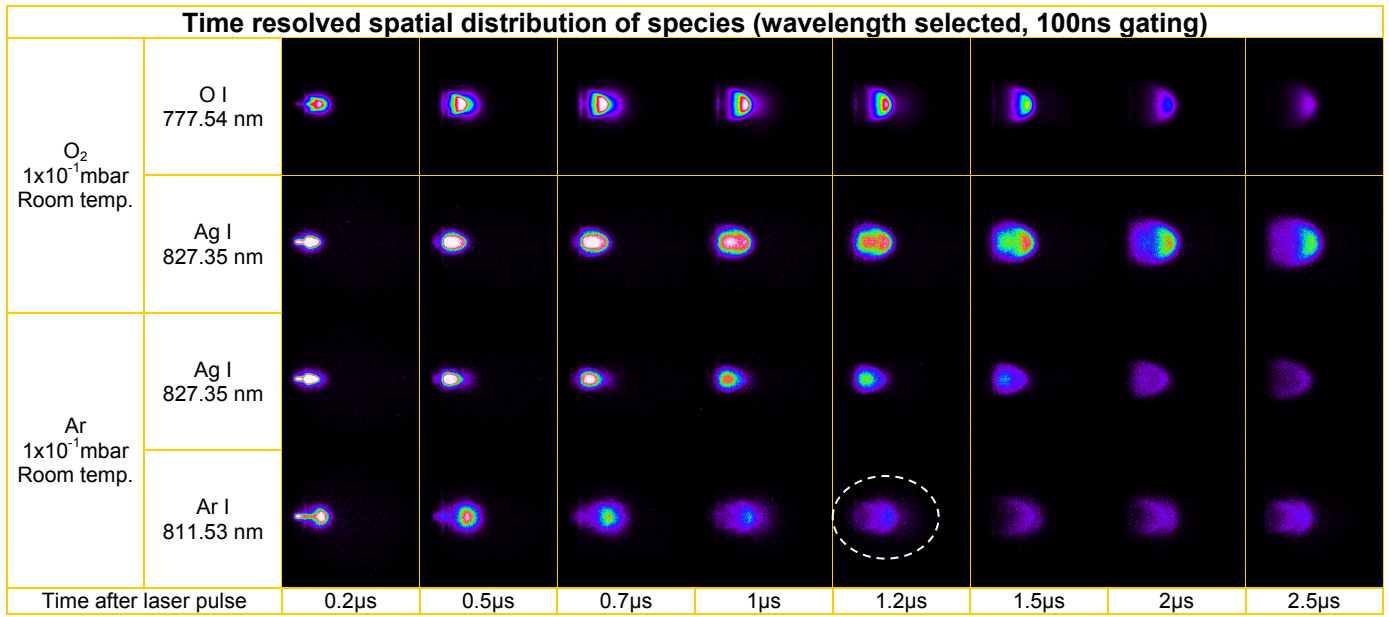
Fig.4.11. Species selected imaging of the early expansion stages for 1x10^{-1} mbar O$_2$ and Ar. All images share the same intensity scales, although the reported intensities are dependent on wavelength choice and filter efficiency, and are not directly comparable. The re-shaping of the Ar I distribution has been highlighted using a dashed curve.
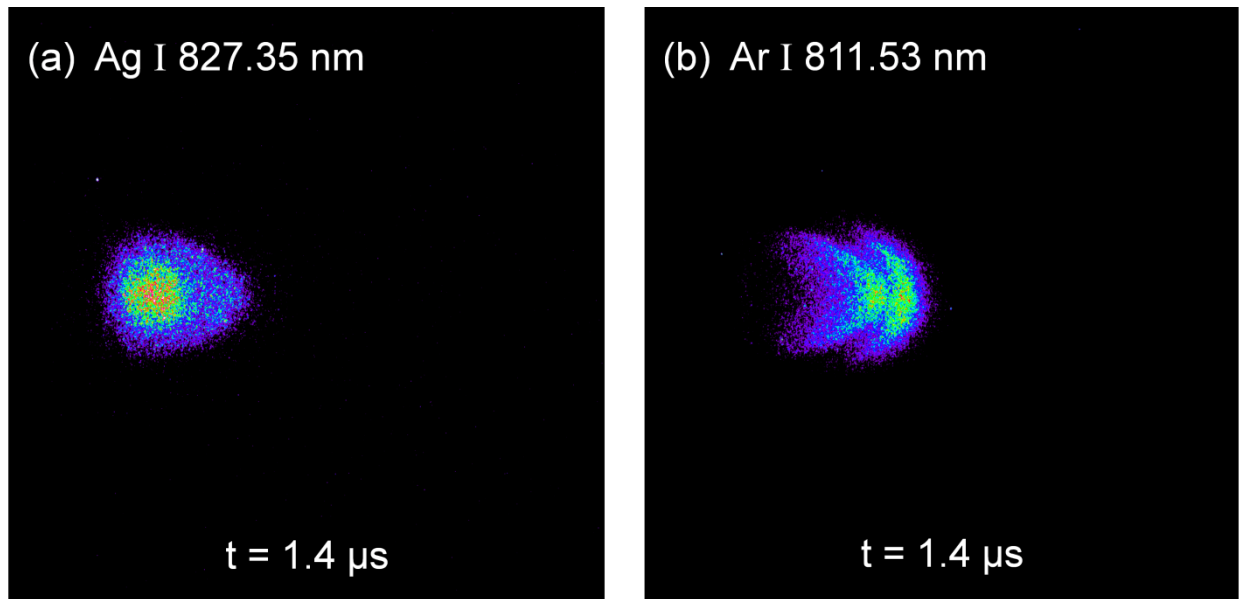
Fig.4.12. Complimentary images of Ag I and Ar I spatial distributions at the same time frame of 1.4µs. 100 accumulations were used to increase image resolution. The gradients are normalized to the maximum counts for each image.

4.1.3   Substrate heating influence on plasma plume expansion

The results shown so far were for room temperature depositions, which is not necessarily the case for most PLD depositions. We now add substrate heating to the experiments while keeping all other parameters as before to understand its influence on the plasma plume expansion dynamics.

Substrate heating is considered to have a strong influence on film growth once the species arrive at the substrate but does not seem to have a direct influence on the plume expansion.

However several studies have analysed the influence of substrate heating on the plasma plume expansion [65, 81, 85] and show that it does have an influence as the heat transfer from the substrate to the background gas creates a density gradient that affects the expansion dynamics of the plasma plume. This is now further investigated both experimentally and numerically.

As expected there is no effect of substrate heating (600°C) on the plume expansion for vacuum (Fig.4.13). In the case of $1x10^{-1}$mbar, both O_2 and Ar background gases exhibit the same effect: higher substrate temperatures bring a much shorter time of arrival to the substrate and reduced emission intensities compared to room temperature experiments. The arrival time for O_2 is now 6 µs vs. 10 µs, while for Ar it is <13 µs vs. 28 µs for the non-heated substrate. The plume front for O_2 at 5 µs shows lower intensities than its lateral sides due to the O_2 density decay in the proximity of the heated substrate. This was not the case at room temperature and highlights the reduction in gas density as the substrate is approached. Furthermore, the light emitting volume above the substrate shows lower intensities when compared to room temperature with maxima of 270'000 counts per pixel without heating vs. 70'000 counts per pixel for 600°.
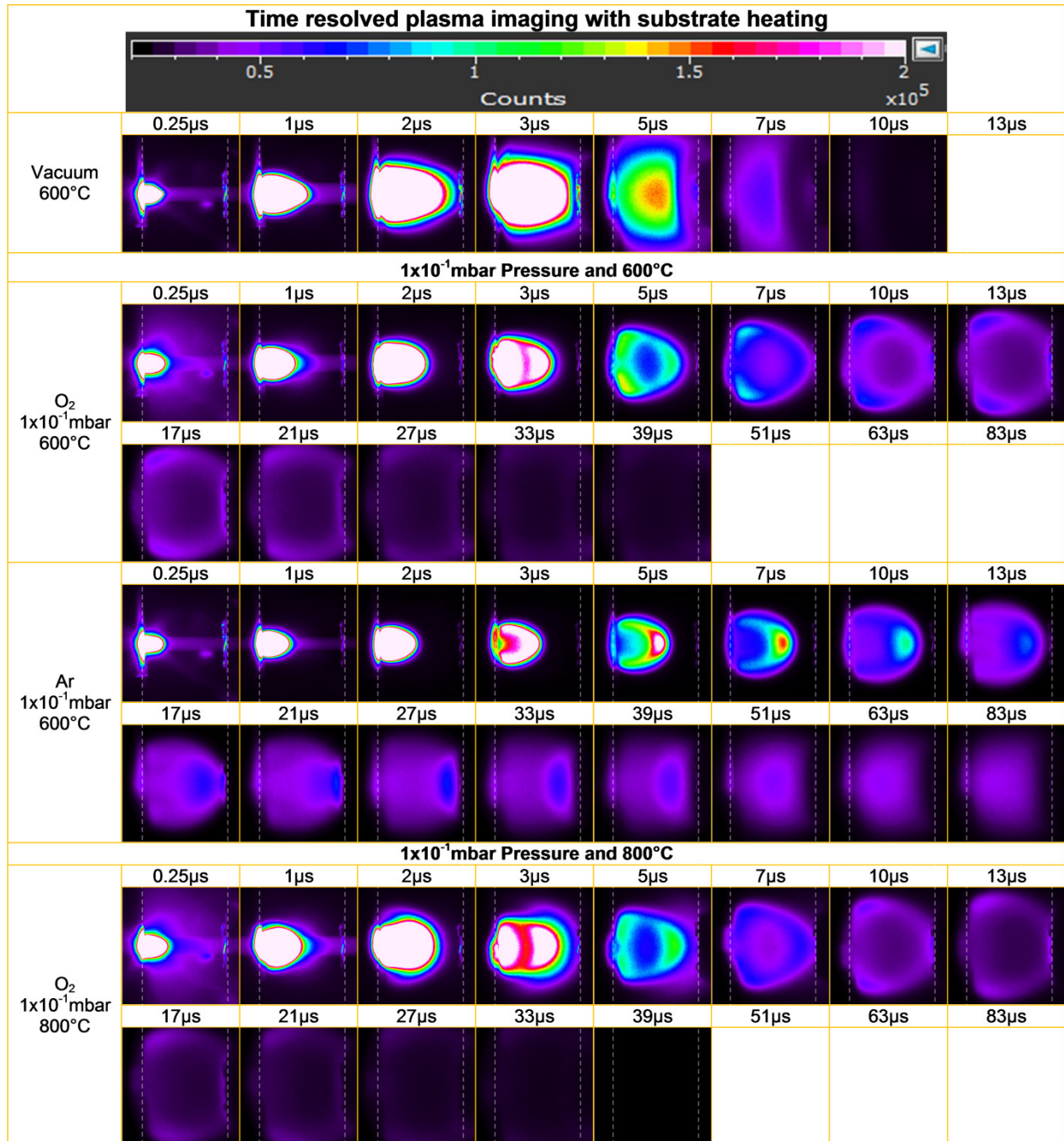
Fig.4.13. Time resolved plasma imaging for vacuum, $1x10^{-2}$mbar and $1x10^{-1}$mbar for O_2 and Ar background gases with substrate heating. The intensity scale is the same as with the RT experiments.

In the case of Ar the emission intensity is much lower above 5 µs than for room temperature experiments once the plume has reached 25 mm and is only 15 mm away from the substrate. This suggests a lower number of collisions and excitations when arriving at the substrate due to the reduced background gas density.

An estimation of this density gradient due to heat transfer is presented in [81, 85] in which a conductive heat transfer, a wall temperature jump and a linear temperature profile are assumed. However this is not a simple task as the gas density/rarefaction and thus the heat transfer regime, as defined by the Knudsen number ($K=\lambda/d$, where λ is the mean free path and d the characteristic length) is not in the conductive regime (Kn>>1), but in the Knudsen regime

(1>*Kn*>0.01). In this regime heat transfer is governed by viscosity as well as by molecular phenomena [86]. Analytical equations are available for the conductive and the free molecular regime (*Kn*>1: heat transfer is governed by molecular flow and hence directly proportional to the gas pressure), but not for the Knudsen regime in which numerical methods are needed. Nonetheless it is possible to delimit the range of densities by resolving for the other two heat transfer regimes for which analytical equations are available.

In the viscous regime (*Kn*>>1) the Fourier equation q_x=-k dT/dx with a temperature jump boundary condition is solved [86] together with the energy balance equation $dq_x/dx = 0$. For this particular case of heat transfer between two parallel planes the boundary conditions to define the constants resulting from the integration are:

$$T - T_0 = \begin{cases} \zeta_T l \frac{dT}{dx} & at\ x = 0 \\ \Delta T - \zeta_T l \frac{dT}{dx} & at\ x = d\,, \end{cases}$$

(4.1)

Obtaining the following temperature distribution:

$$T(x) = T_0 + \Delta T\left[(\tfrac{x}{d} + \tfrac{\zeta_T}{\delta})(1 + \tfrac{2\zeta_T}{\delta})^{-1}\right],\ for\ Kn \ll 1\,,$$

(4.2)

Were d = 40mm, $\delta = \frac{1}{Kn}$ is the gas rarefaction parameter, ζ_T the temperature jump coefficient with a recommended value of $\zeta_T = 1.954$ [86] and l is the Knudsen layer thickness. In the free molecular regime (*Kn*<<1) the linearized Boltzmann equation is solved analytically, see chapter 4.2 in [87], giving the following temperature profile:

$$T = T_0 + \tfrac{1}{2}\Delta T,\ for\ Kn \gg 1\,,$$

(4.3)

This means that the temperature is constant between the walls and equal to the average value. In addition the target temperature due to radiative heat transfer is also taken into account from experimental measurements with ~220°C (210°C at 1x10^{-1}mbar Ar and 235°C in vacuum) and ~290°C (280° at 1x10^{-1}mbar Ar and 300°C in vacuum) for the 600°C and 800°C cases respectively.

The temperature and density profiles (ideal gas law) are shown in Fig.4.14 and Fig.4.15 respectively. The solution of the equations show, that the heat transfer from the walls to the background gas is reduced with increasing vacuum and the discontinuity in temperature between both differing phases is seen (the temperature of the gas is not equal to that of the wall, which is emulated by the "jump" boundary solution). For the given pressures, the assumption of a conductive heat transfer regime is not ideal and gas densities are

underestimated in the proximity of the heater and overestimated in the proximity of the target. This can be clearly seen in Fig.4.15a.
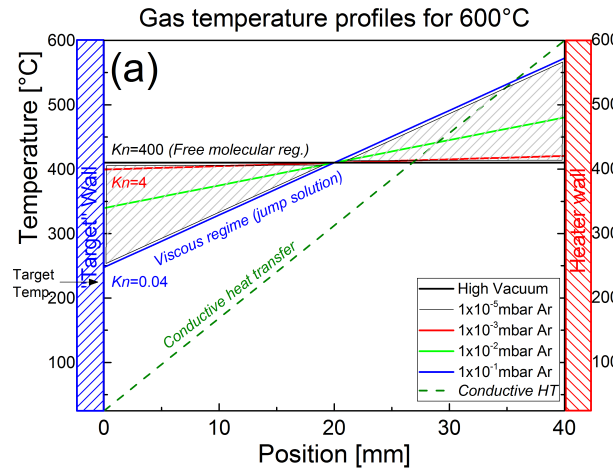
Fig.4.14. Background gas temperature profiles for different pressures according to the heat transfer regime (defined by Knudsen number) for two parallel and infinite plates at different temperatures.

Nonetheless the conclusion is similar, substrate heating has a strong influence on the background gas density which for the case of 600°C can be estimated as an average density of ~45% RT density, while for 800°C it translates into ~37%.
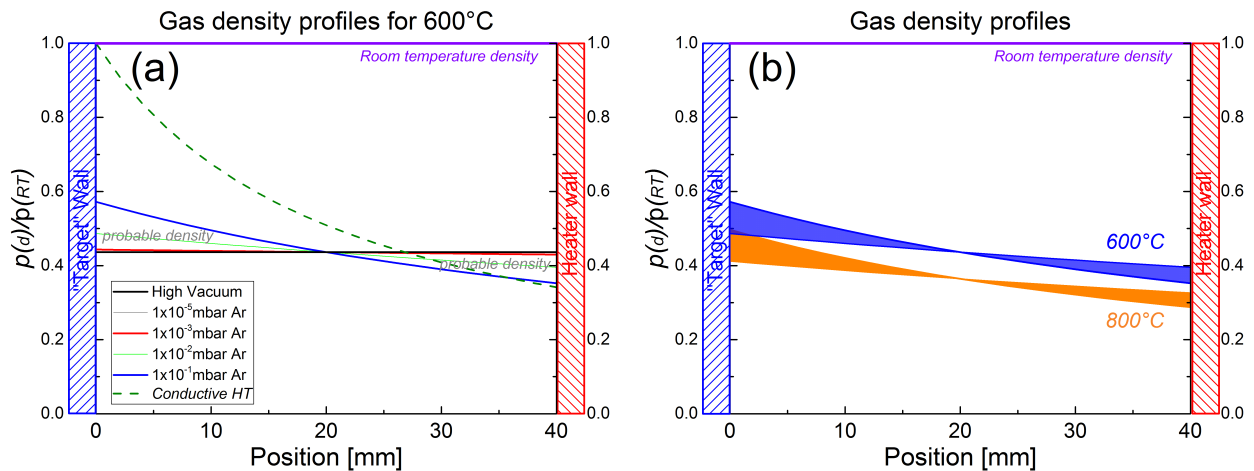
Fig.4.15. Background gas density profiles for different pressures according to the heat transfer regime (defined by Knudsen number) for two parallel and infinite plates at different temperatures (a). Probable gas density profiles referenced to room temperature density for 600°C and 800°C substrate temperature (b). Note: target wall has different temperature according to experimental measurements during heating (~100°C and ~150°C for the 600°C and 800°C cases respectively).

In addition, the rebound effect appears, but with a diminished intensity and at a time frame of 17 µs instead of the 31 µs (RT). Interestingly, in the heated case there is no non-light-emitting volume above the substrate and the rebound can be seen starting from the substrate surface (Fig.4.16). This is a direct consequence of the reduced gas density in the proximity of the substrate holder due to its heating, which causes less gas species to be trapped although the overall chamber pressure remains the same as before. In terms of rebound velocity in Ar,

contrary to the room temperature case, for 600°C there is no increase in velocity. The plasma emitting species arrive at the substrate with a velocity of ~1'400 m/s and rebound with a velocity of ~830 m/s. This is again a consequence of having less species trapped against the substrate holder which creates a lower local pressure in comparison to RT measurements and a lower rebound velocity.
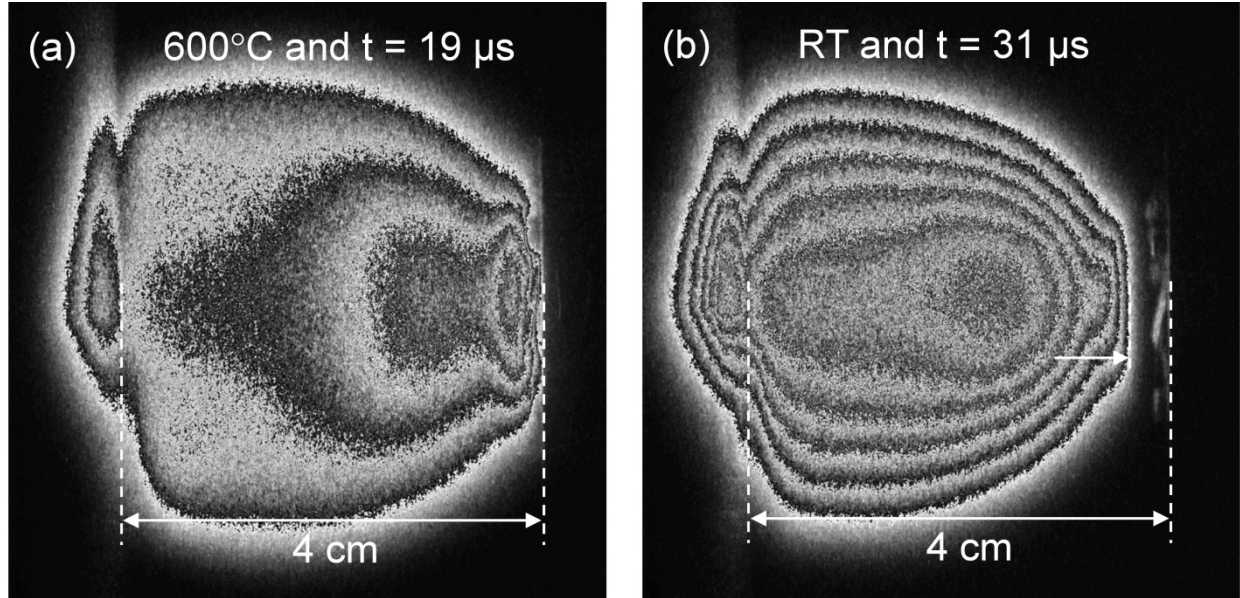
Fig.4.16. Rebound effect in Ar at $1x10^{-1}$mbar for substrate heating at 600° (a) and at room temperature (b). The position of the target and the substrate is highlighted to show the non-emitting volume in the room temperature case (b).

4.1.4   Analysis of position-resolved plasma velocities

The position-resolved velocity charts provide a similar picture with respect to substrate heating and are shown in Fig.4.17. The plasma expansion in vacuum is not influenced by the substrate heating and retains a quasi-constant velocity of ~20'000 m/s. The plasma species at $1x10^{-1}$mbar O_2 (Fig.4.17a) show very similar velocity values for heated and unheated substrate during the initial 25 mm after which 600°C and 800°C temperatures maintain velocities of 4'000-5'500 m/s (with 800°C slightly faster than the 600°C case) while the expansion of the plasma species in the unheated case reduces this velocity considerably in the last 15 mm (down to 1'500 m/s). This is no surprise as the changes in gas density are expected to increase the closer one gets to the heated area (with diminishing density for the heated cases). Additionally the undulation of the velocity values is also present in the heated cases.

With respect to Ar (Fig.4.17 b), the results are similar but with a stronger reduction of velocities. The plasma expansion when heating the substrate to 600°C diverges from the non-heated one already at 20 mm distance and keeps a higher velocity in the last 5 mm (1'400 m/s vs. 280 m/s).
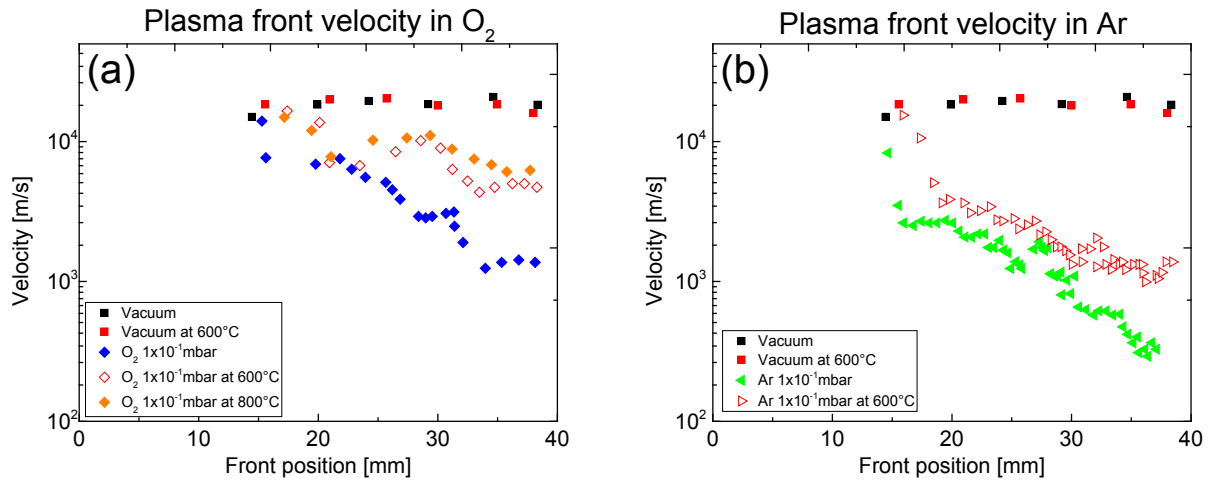
Fig.4.17. Times of arrival to substrate for different background gases, pressures and substrate temperatures. (a) for room temperature and (b) for high temperature measurements.

4.1.5 Times of arrival

Although the velocity charts have been shown previously, it is also relevant to report on the time of arrival at the substrate for the different pressures and heating temperatures. As there is a marked velocity variability throughout the entire expansion (except for vacuum).

The results are reported in Fig.4.18 in which in vacuum the plasma species arrive at the substrate in the shortest time (~1.75 µs). At 1×10^{-2} mbar both O_2 and Ar background gases are able to affect the expansion, with arrival times of 2.75 µs and 3 µs respectively.

At the highest pressure of 1×10^{-1} mbar the arrival times when using O_2 or Ar are considerably different. With the species expanding in O_2 needing ~9.75 µs to reach the substrate (at room temperature) while for those expanding in Ar needing ~28 µs (three times more). Both of which are in strong contrast with the arrival times in vacuum.

The aforementioned timing results are for room temperature experiments. Raising the substrate temperature causes the mentioned reduction in gas density close to the substrate. The expansion in vacuum is not affected, while for the experiments at 1×10^{-1} mbar the reduction in time of arrival is considerable for both O_2 ($t_{RT} = 9.75$ µs, $t_{600°} = 6$ µs and $t_{800°} = 3.25$ µs) and Ar ($t_{RT} = 27$ µs and $t_{600°} = 12.25$ µs). For Ar at 600°C it is ~45% for the time of arrival at RT, while for O_2 it is ~61% and ~33% at 600°C and 800°C, respectively. These experimental values are in agreement with the estimated gas densities due to heating from section 4.1.3: ~45% at 600°C and ~37% at 800°C.
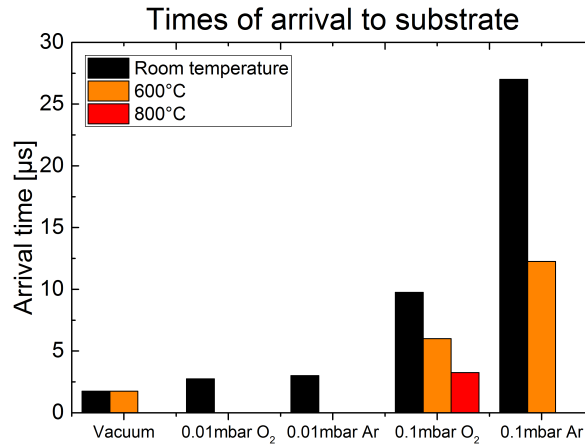
Fig.4.18. Times of arrival to substrate for different background gases, pressures and substrate temperatures. Note: the experiment with 0.1 mbar Ar at 800°C was not done.

4.1.6   Conclusions

Time resolved imaging of the plasma expansion for the different deposition pressures and temperatures provides a detailed insight into the PLD process. In vacuum the expansion is strongly forward peaked and the high arrival velocities of the species to the substrate causes them to rebound. Once the pressure is sufficient there is a transition from a forward peaked to a spherical expansion. However, during the initial stages of the expansion, the plume is not affected by the surrounding background gas. For the same given pressure, Ar shows a higher stopping power than molecular O_2 (related to its higher mass and van der Waals volume).

At the highest tested pressure of 1×10^{-1} mbar, both background gases show that upon arrival of the species to the substrate a transient high pressure is created above the substrate (~5 mm thickness). This seems to be a consequence of the trapping and compression of background gas species between the expanding plume and the substrate holder. In the case of Ar, an unexpected rebound of plasma species is detected rebounding all the way back to the originally ablated target. Surprisingly, the rebound velocity is higher than the arrival velocity, evidencing a spring-like behaviour. This rebound follows a different mechanism than the one observed in vacuum, as it is not caused by a direct reflection from the substrate surface. In the case of O_2 an area of intense emission of light is seen which surpasses the intensities measured at the plasma plume front at 3-5 μs. This emission is mostly generated by Ag I and a metal oxygen species (evidenced for LaO). A slight rebound is also seen for O_2, but it is masked by the higher intensities near the substrate region.

The effect on the plasma dynamics due to substrate heating was also analysed. It shows no influence for vacuum conditions and for higher pressures the results evidence a gradual decay in background gas density the closer one gets to the heated substrate. Expansion velocities are increased and consequently times of arrival are reduced. The O_2 rich layer and the rebound

effect continue to appear, but with reduced intensity. Analytical estimations of the gas densities are developed that would allow adjusting the background gas pressure to achieve similar densities if the substrate temperature is varied (used in 3.2.3 to estimate suitable deposition pressures when heating the substrates up to 780°C).

Based on these results, the following question will be addressed next. Can these findings for Ag be transferred to target materials with a complex composition e.g. $La_{0.4}Ca_{.0.6}MnO_3$? The main focus is on the plasma dynamics (also at a long time scale) and how does the film composition change as a consequence of the changes observed during the plasma expansion.

4.2   Plasma plume dynamics and rebounds of $La_{0.4}Ca_{0.6}MnO_3$

4.2.1   Experimental details and emission spectra

To continue the investigation of Ag, the study focuses now on the thesis material $La_{0.4}Ca_{0.6}MnO_3$. A more complex material that will validate the findings from Ag experiments and at the same time help to understand the compositional and thickness variations of the films produced with it and reported in chapter 3. These plasma imaging experiments are exactly the same as for Ag with the exception of the target material and the absence of substrate heating. An image of this particular experimental setup is shown in Fig.4.19.
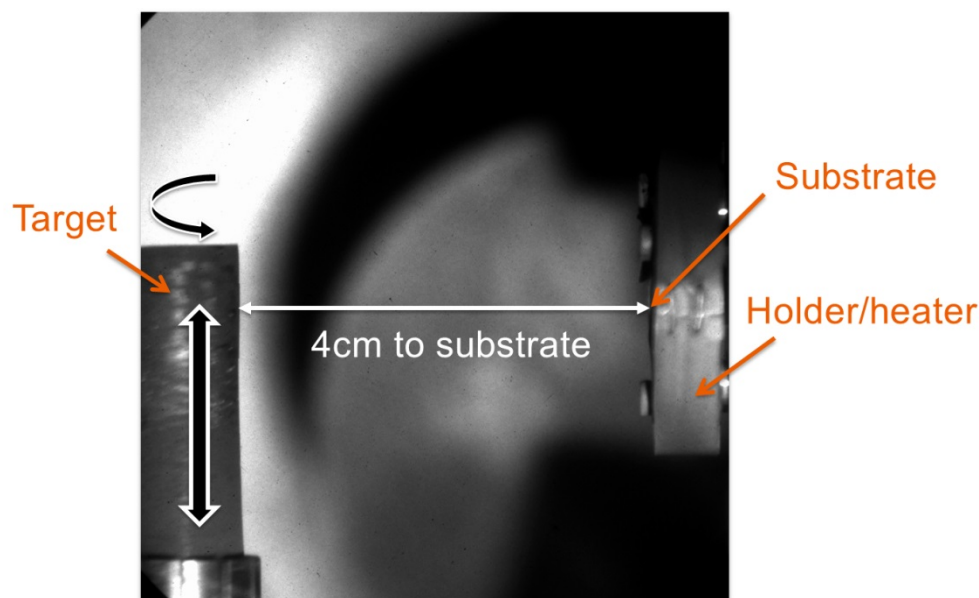
Fig.4.19. Image of the experimental setup with the $La_{0.4}Ca_{0.6}MnO_3$ target on the left and a substrate 4 cm away on the right hand side. The substrate is mounted on an un-heated substrate-holder. The image was captured using the same ICCD at the same position as for the experiments

To record the emission spectrum between 550-830 nm the same monochromator setup as for Ag was used. The result for vacuum conditions (Fig.4.20) shows the high amount of emission lines and the difficulty to select suitable emission lines with respect to the species and line width. Some emission lines were identified using references [77, 78], although the final

selection was based on the recommendations from [78] and are listed in Table 4.2. The applied spectral lines were mostly from neutral (I) rather than single ionized states (II). Fig.4.20b has been included to show that the selected line for LaO I (560.25 nm) and the resolution of the AOTF (here, 1 nm FWHM) are appropriate to avoid the overlap with a Ca I line (558.87 nm). Additionally the selected lines for Mn I (Fig.4.20c), La I (Fig.4.20d), and O I (Fig.4.20e) and the corresponding AOTF resolutions have been included for completeness. The originally selected Ca I line (720.22nm) proved inadequate, as it was not intense enough (short life time) to see details clearly at a later time scale and the results are not reported. For consistency all measurements need to be done in one run to keep the camera alignment for all measurements constant.

The selected wavelength values were then used for the AOTF measurements to allow the time-resolved imaging of the different species.

Specie	State	Emission wavelength [nm]	Intensity
LaO	I	560.25	110
Mn	I	602.18	290
La	I	624.993	720
O	I	777.54	870
O	I	777.41	810
O	I	777.19	750
Ar	I	811.531	35000

Table 4.2: Used emission wavelengths of LaO, Mn, La, O and Ar by either arc, spark or discharge excitation [77, 78]. The common nomenclature for emission spectroscopy is used with I = neutral state, II = single ionised and III = double ionised state. Remark: intensities are rough indicators as different observers use different scales and excitation sources.
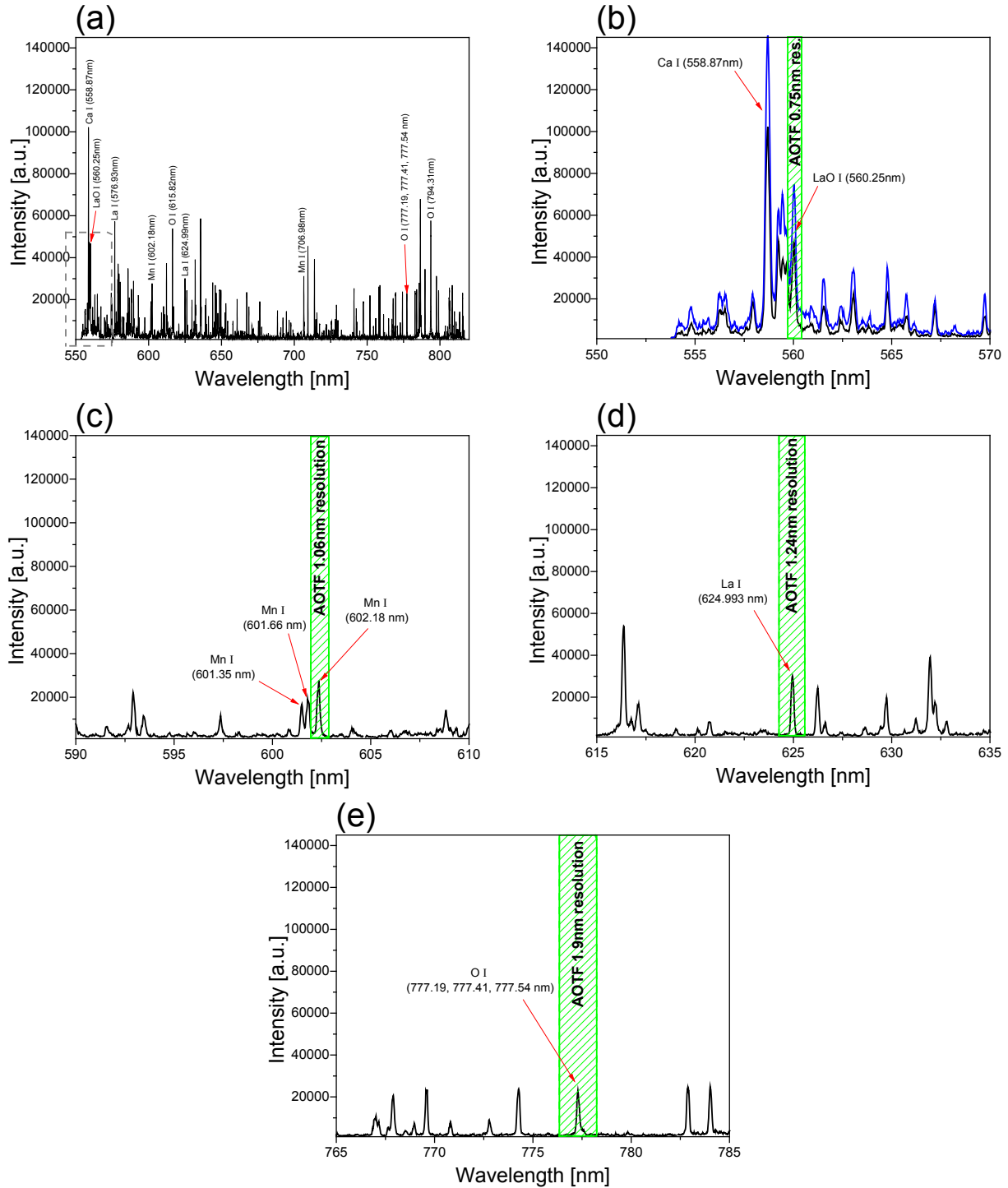
Fig.4.20. Vacuum emission spectra of La$_{0.4}$Ca$_{0.6}$MnO$_3$ with a 200ns delay and 10µs gating from 550-830nm (a), for vacuum and 1x10^{-1}mbar O$_2$ from 550-575 nm (b) and for vacuum from 590-610 nm (c), from 615-635 nm (d) and from 765-785 nm (e). The wavelength resolution of the AOTF for each range is highlighted with a dashed green area. The selected emission wavelengths are highlighted with red arrows. Ar I is not present in the vacuum ablation and was selected directly from the recommendation in [78] for Ar.

4.2.2   Results and discussion

The plume expansions in vacuum, O$_2$ and Ar are shown in Fig.4.22 while the position resolved velocities of the plume front are plotted in Fig.4.23. The velocities were calculated by evaluating

the distances travelled by the plume front along the target normal with respect to time of 3 consecutive frames (100 ns delay between frames in the initial stages <2.5 µs with a 5 ns gating, and 1000 ns delay and a 50 ns gating above). The velocities between the gating change were not calculated nor plotted. The used lens (*f*-number) was the same for all these measurements. Vacuum presents the fastest expansion with the plasma reaching the substrate in less than 1.4 µs corresponding to a velocity of ~30'000 m/s and with an acceleration in its initial stages (marked with a line) until the velocity of the expansion front reaches a maximum (Fig.4.23). This is a known effect for an adiabatic expansion of plasma in vacuum where the initial internal energy gradually becomes kinetic energy of radial motion and reaches a constant maximum velocity [88-90]. After ~2 µs, and consistent with the Ag imaging, the plume front is progressively deformed by what seems to be a rebound of the highly energetic species hitting the substrate-holder (highlighted with a dashed curve and also noticeable in the velocity profile from Fig.4.23). If the substrate holder is removed this curved deformation of the plasma plume does not appear and the plasma expands well beyond the recorded frame (Fig.4.21).
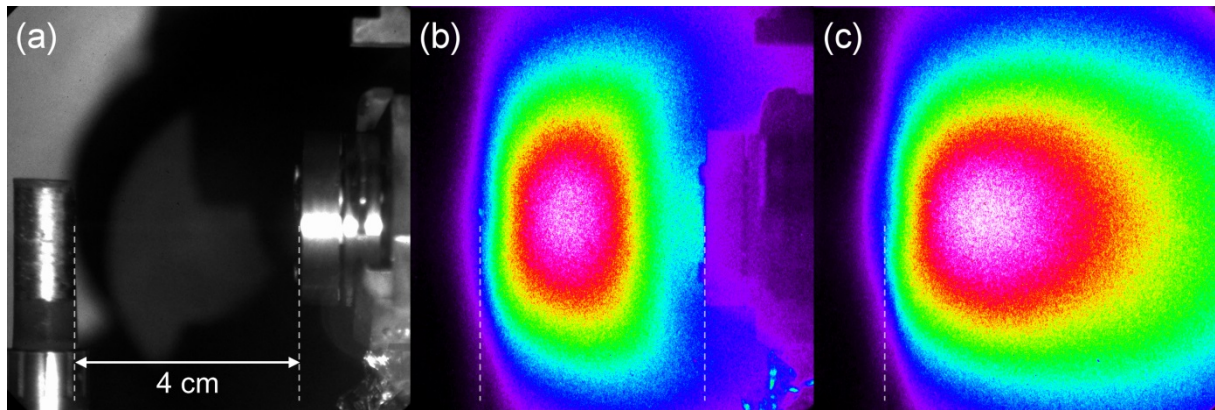
Fig.4.21. Image of the experimental setup (a) with the $La_{0.4}Ca_{0.6}MnO_3$ target on the left and a substrate holder 4 cm away on the right hand side, plasma expansion in vacuum at $t = 5$ µs with the substrate holder present (b) and without (c). Intensity scales are the same for both plasma images.

At $1x10^{-2}$mbar both O_2 and Ar background gases exert a decelerating effect on the plasma expansion and the plume dynamics are clearly different for both gases. As for Ag, the plume expansion in O_2 is more hemispherical with a stronger emission intensity (above 2 µs) and lifetime than in vacuum, while in Ar the plume is narrower and has an arrow-like shape with excitations mostly taking place at the plume front (the plume shape will be explored in detail later in chapter 7). Also the excitation intensity decreases faster than in vacuum, probably due to a quenching process by the annihilation of the excited state species [91]. It is noteworthy that the three decaying emission intensities overlap with each other during the initial 2 µs (Fig.4.24a), after which O_2 shows comparatively higher intensities, although still small when compared to the higher pressures.

A plume splitting is visible at 1 µs and already at this pressure it is noticeable that Ar has a higher stopping power than O_2 (observable at 2 µs and even more at $1x10^{-1}$mbar). In both

cases the rebound of the plasma from the substrate, seen in vacuum, is not visible anymore: the excited species do not reveal any change in direction and continue to arrive at the substrate well beyond 10μs. This is probably due to the kinetic energy reduction of the plasma species from collisions with the background gas.
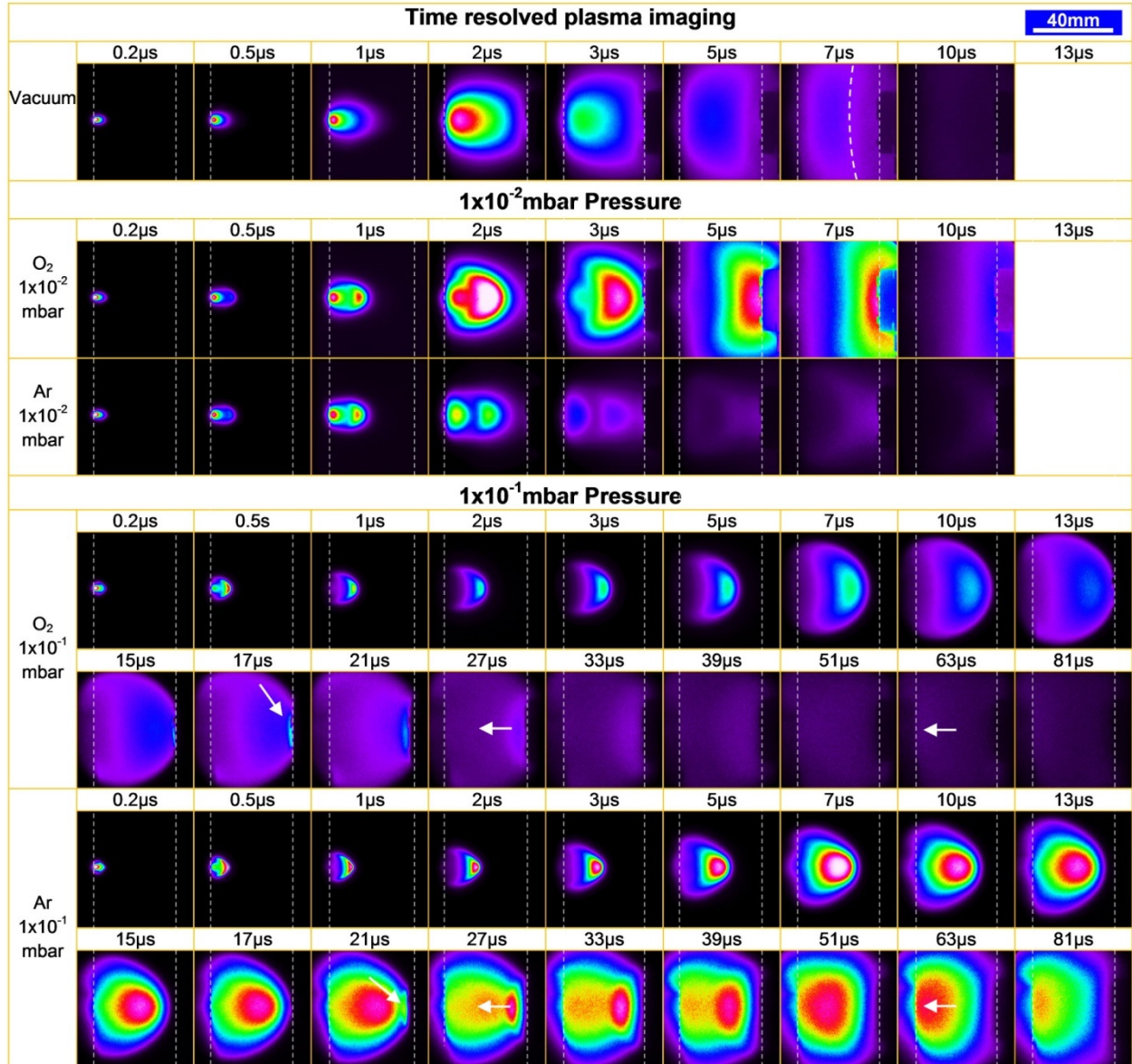
Fig.4.22. ICCD time resolved plasma images without AOTF for an ablation in vacuum, 1×10^{-2}mbar and 1×10^{-1}mbar for O_2 and Ar background gases without substrate heating. The plume expands from the ablated target on the left to the substrate on the right (marked with dashed lines). The rebound in vacuum is highlighted with a dashed curve that follows the border of the compressed plasma. The re-excitation effect in O_2 and the rebound effect in Ar are both highlighted with inclined arrows, while the rebound direction ($t = 27$μs) and the impingement on the ablated target ($t=63$μs) are marked with horizontal arrows. The intensity scales are the same for each independent time frame for vacuum, 1×10^{-2}mbar O_2 and 1×10^{-2}mbar Ar, while 1×10^{-1}mbar O_2 and 1×10^{-1}mbar Ar share a separate time-frame scale (due to their much higher intensities).

At 1×10^{-1}mbar, as for the Ag plasma plume, the expansion dynamics reveals a pronounced change: the plume is completely confined and expands with decreasingly lower velocities

(Fig.4.23) with the times of arrival to the substrate increasing by an order of magnitude (t_{O_2} = 13 µs and t_{Ar} = 17 µs). The emission intensities are higher by an order of magnitude (Fig.4.24) and the plume splitting does not last beyond 0.5µs (when the fast component is also scattered) with strong excitations visible at the plasma front. The latter is in contrast with the Ag case, where excitations were visible throughout the entire plume perimeter including the rear areas (see Fig.4.3 at 7 µs). Nevertheless, the O_2 background expansion does show a clear volume of excited species just above the substrate that lasts for more than 30 µs and in its final stages covers ~2 cm (Fig.4.22, t = 39 µs). While Ar shows a sharper plume front (sharper than the Ag ablation in Ar), expands slower (Fig.4.23) and experiences the same pronounced rebound as Ag once it approaches the substrate (marked with inclined arrows in Fig.4.22, t = 21 µs). The rebound travels all the way back to the ablated target and most likely re-coats it (marked with an arrow at t = 63 µs). It is very likely that the composition of the rebounded plasma will not be the same than the target, as there are different masses and scattering cross sections involved and one can infer that it will modify the target's original composition like other known processes do [2] (i.e.: elemental surface segregation upon cumulative laser irradiation). This potential target contamination is explored in detail in section 4.2.2.2.
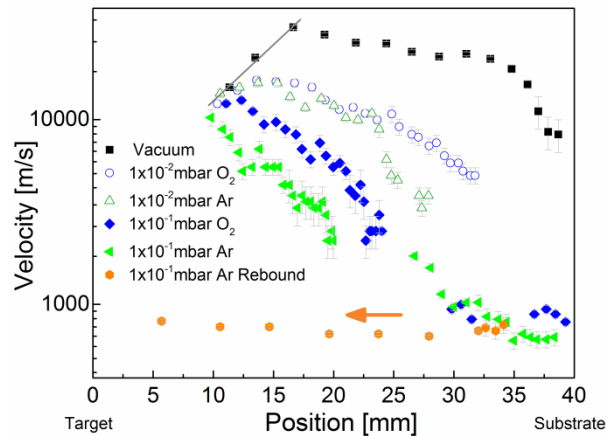
Fig.4.23. Position resolved velocities of the $La_{0.4}Ca_{0.6}MnO_3$ plume front along the target normal for different background gases and pressures. The velocities in the first 10 mm (t<100ns) could not be obtained due to sensor saturation. The time limit of the short-gated measurement (time sequence up to 2.5µs) limited the detected velocities for $1x10^{-2}$mbar O_2 and Ar, and created a position-gap for the higher pressures (the vacuum expansion fitted in the 2.5µs measurement)
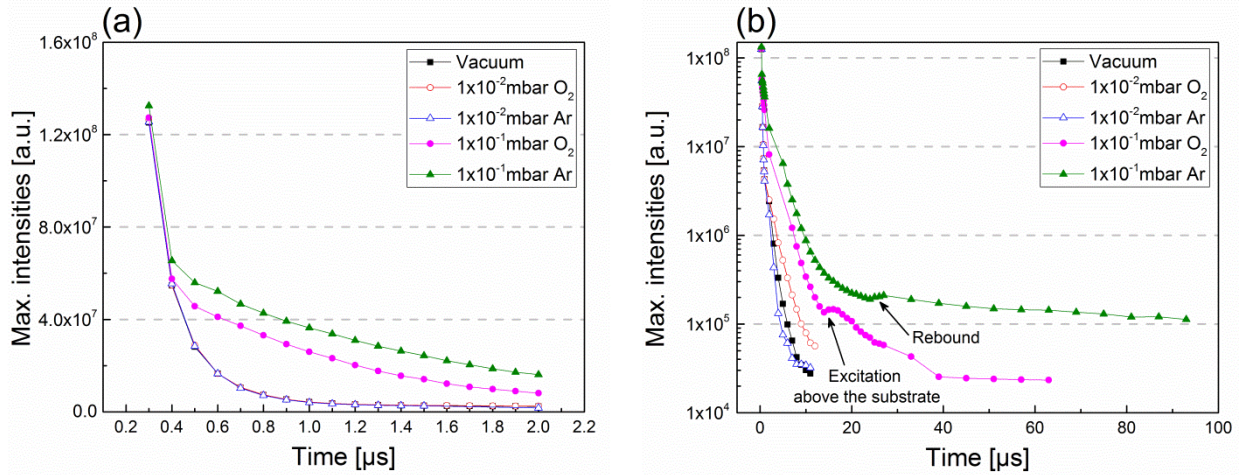
Fig.4.24. Evolution with time of the maximum emission intensities for the five different background gas conditions. Figure (a) focuses on the very high intensities during the initial 2 µs with a linear intensity scale, while (b) covers up to 100 µs and uses a logarithmic scale. The signals were partially saturated for the time-frames below 0.3 µs and were not included. There is an overlapping of the signals for vacuum, 1×10^{-2}mbar O_2 and 1×10^{-2}mbar Ar up to 2 µs.

Concerning emission intensities, both arrival effects are visible in the maximum intensities vs. time chart (Fig.4.24b) and a detailed view of those effects is shown in Fig.4.27. The strong excitation for the deposition in O_2 background takes place just above the substrate/holder and expands with time 1-2 cm away, while in the case of Ar there is no excitation/light emitting volume on top of the substrate holder. Two mm before reaching the substrate, the light emitting plasma plume is stopped and instants later a rebound wave can be seen traveling backwards (Ag showed a 5 mm gap). These rebounds are not caused by the species reflected after hitting the substrate (as in vacuum) but by the compressed gas acting like a spring instead (the same experiment without the substrate holder did not show any of these effects and the plasma expanded beyond 55 mm before the species thermalized Fig.4.26).

For $La_{0.4}Ca_{0.6}MnO_3$, this rebound at RT travels at a constant velocity all the way back to the ablated target and, in contrast to the Ag case, with a similar value as the species arriving at the substrate (720 m/s vs. 650 m/s at arrival, Fig.4.23). This is likely caused by the higher ablation rates (higher number of species) of $La_{0.4}Ca_{0.6}MnO_3$ vs. Ag which for a given compressed background gas energy result in an overall lower rebound velocity. In an O_2 background a rebound is also observed, but the emitted light is much weaker and eclipsed by the mentioned excitation above the substrate (Fig.4.25).
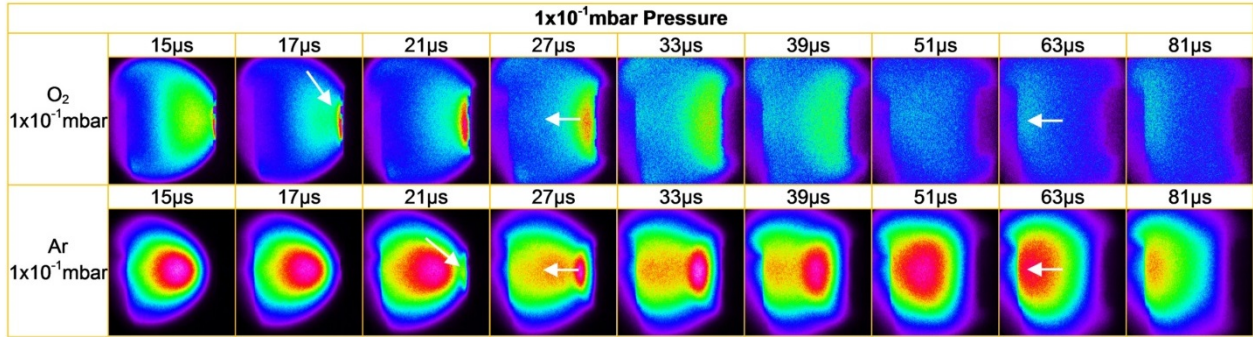
Fig.4.25. ICCD time resolved plasma images of $La_{0.4}Ca_{0.6}MnO_3$ ablation without AOTF at $1x10^{-1}$mbar for O_2 and Ar background gases highlighting the rebound effect. The plume expands from the ablated target on the left to the substrate on the right. The intensity scales are normalized for each single image to maximize contrast. Although weak, the rebound in O_2 background can also be seen.

From the imaging it is evident that the rebound will have important effects on the film thickness and this matches the film thickness results reported in chapter 3 for this pressure (circa 50% loss of deposited material with respect to vacuum). The strong forward oriented thickness profile from vacuum with the peak in the ±40° region disappears and at $1x10^{-1}$mbar Ar a homogenous angular thickness is seen (Fig.4.28). This was originally solely assigned to the higher plasma scattering taking place at these pressures, but is also in agreement with the observed rebound of the plume front which disturbs an angular range of ±25° (given by the substrate holder dimensions and its distance to the target) and might scatter over larger angles in its way back. Thus, a combination of the initially mentioned scattering plus the rebound effect might be a suitable explanation for the disappearance of the forward deposition character and the presence of a homogenous angular thickness as seen in chapter 3.
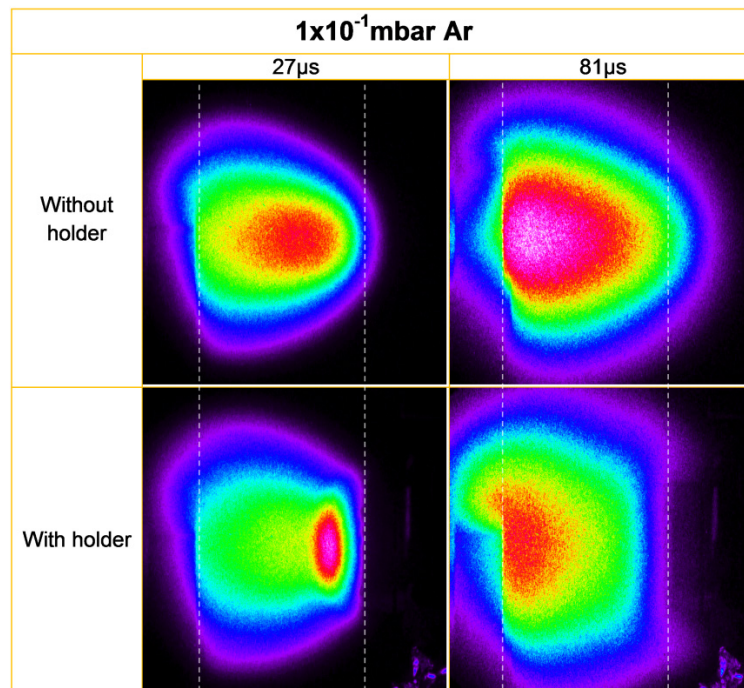
Fig.4.26. ICCD time resolved plasma images without AOTF for an ablation at $1x10^{-1}$mbar Ar without and with substrate holder. The plume expands from the ablated target on the left to the substrate on the right (marked with dashed lines). The intensity scales are the same for each independent time frame.
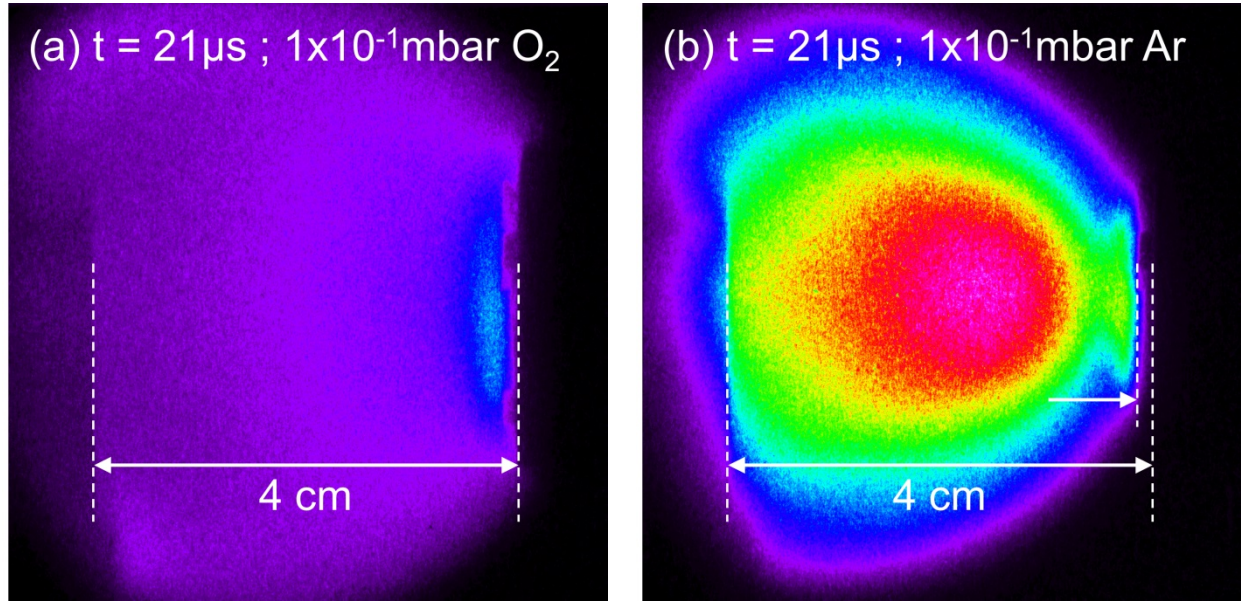
Fig.4.27. Plasma plume arrival behaviour for 1×10^{-1}mbar O_2 (a) Ar (b), both at room temperature and with the same intensity scale. The non-emitting area close to the substrate is highlighted in (b) as well as the positions of target and substrate.
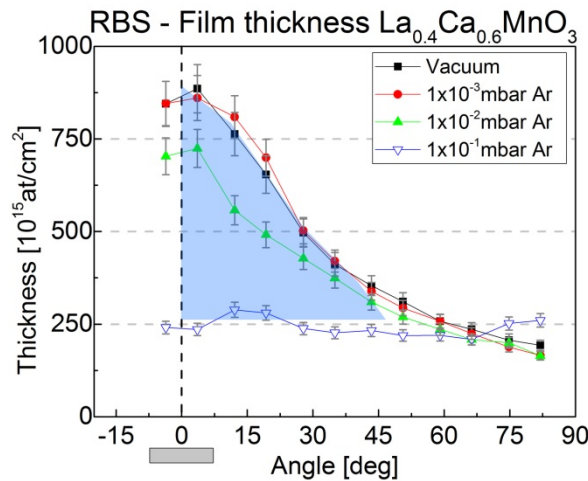
Fig.4.28. Angle resolved film thickness profiles of $La_{0.4}Ca_{0.6}MnO_3$ for four different Ar background gas pressures from [76]. The forward peak thickness disappears at 1×10^{-1}mbar Ar and is highlighted in blue

4.2.2.1 Time-resolved spatial distribution of species

In comparison to the Ag plasma imaging, the use of a multi-element target and selective imaging of the neutral excited species (Fig.4.29) brings a much richer understanding of the plasma expansion dynamics and its compositional deviations. In vacuum the lighter elements present the higher velocities, with O I having the fastest expansion (~30'000 m/s), Mn I the intermediate (~23'000 m/s) and La I (~18'000 m/s) and LaO I the slowest (~17'500 m/s). These velocities were calculated by evaluating the distances travelled by the plume front along the target normal with respect to time of 3 consecutive frames (100 ns delay between frames in the initial stages <2.5 µs) and then calculating the average expansion velocity (only the 100 ns

gated measurements were used). The used lens (f-number) was the same for all these measurements. This also translates into dissimilar arrival times to the substrate according to mass (t_{Oxygen} = 1.2 µs, t_{Mn} = 1.4 µs, t_{La} = 1.6 µs and t_{LaO} = 1.7 µs) and is a direct consequence of kinetic energies and masses, although the calculated kinetic energies do not exactly match: ~71eV for O I , ~151eV for Mn I, ~227eV for La I and ~246eV for LaO I. Nevertheless, the dissimilar arrival times and velocities entail complex interactions of incoming and reflected fluxes of species in addition to the possibility of a preferential bouncing mentioned before.
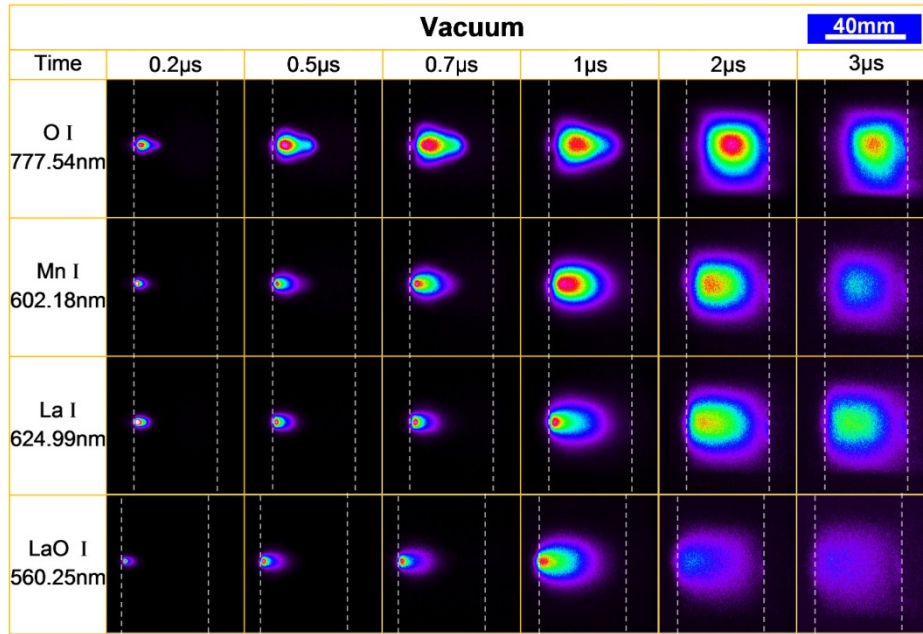
Fig.4.29. Vacuum time-resolved images tracing the spatial distribution of the excited species of O I, Mn I, La I and LaO I. The plume expands from the ablated target on the left to the substrate on the right (marked with dashed lines). The intensity scales have been normalized to the maximum counts for each image (there is a ~20x decrease in intensity from 0.2-3µs). Note: due to the use of a different AOTF for LaO I, the images have a slightly different frame and zoom and the images cannot be directly compared with the other species.

At $1x10^{-2}$mbar the effect is counteracted by the background gas (see Fig.4.30) where the lighter elements and those with higher scattering cross-sections are preferentially scattered by the background gas as compared to heavier species. In both cases, O_2 and Ar, the expansion of Mn I is strongly affected (red arrow in Fig.4.30), now lagging behind La I and LaO I, which are able to penetrate the background gas up to 1µs without major variations with respect to vacuum. The case of O I is harder to assess as in an O_2 background the images are masked by the addition of O_2 gas excitations. An analogous case happens for the Ar background and its Ar I distributions. They are clearly detected and remarkably "arrive" at the substrate in less than 1µs (shockwave excitation). Nevertheless, for the Ar case, the expansion velocity of O I is clearly reduced. The most interesting result, however, is the plume-splitting observed at 2 µs (marked in Fig.4.30 with a dashed ellipse): Mn I species are partially stopped by the background gas while O I and mostly La I are still able to arrive to the substrate (MFP of O at $1x10^{-2}$mbar Ar is 54 mm vs. 21 mm of Mn). This means that films produced with this conditions

will be Mn deficient, which is exactly what was reported in chapter 3. This result is summarized in Fig.4.31, where a deviation of ~13% in Mn/La with respect to target composition was detected at 1×10^{-2} mbar Ar.
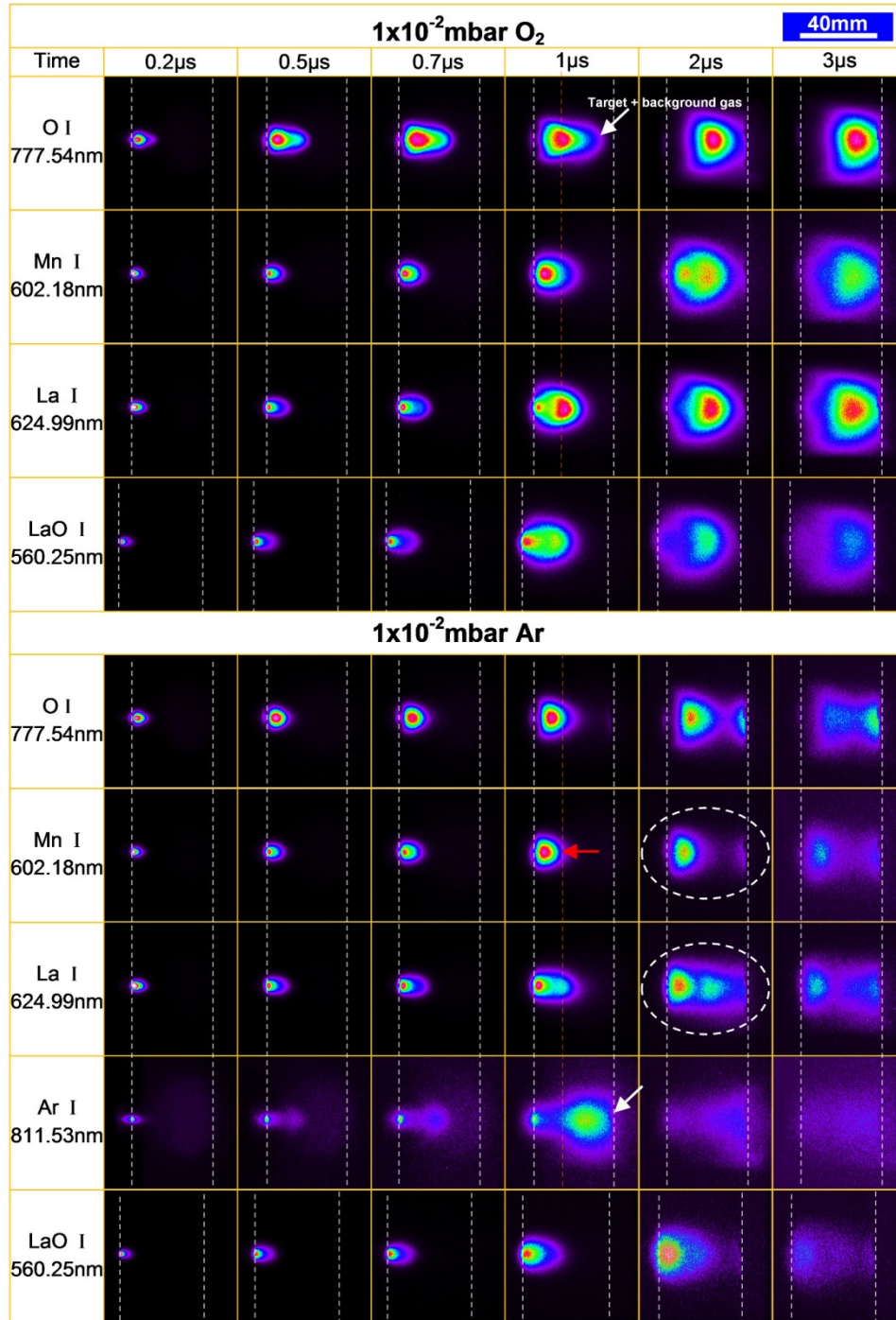
Fig.4.30. Time resolved images tracing the spatial distribution of the excited species of O I, Mn I, La I, LaO I and Ar I. Intensity scale has been normalized to the maximum counts for each image (there is a ~10x decrease in intensity from 0.2-3µs). Note: due to the use of a different AOTF for LaO I, the images have a slightly different frame and zoom and the images cannot be directly compared with the other species.
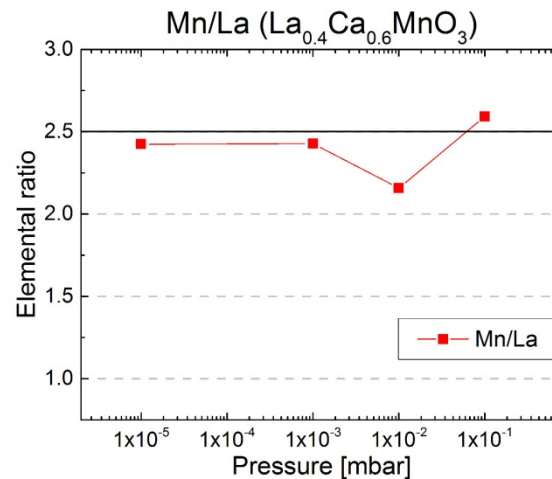
Fig.4.31. Influence of Ar background pressure on the film's Mn/La ratio (from [76]). Composition was obtained by RBS. The horizontal black line represents the target composition (verified by RBS). Note: error bars are smaller than the symbols.

For the highest tested pressure of $1x10^{-1}$mbar and for both gases (Fig.4.32), there are some initial differences in the expansion of the various excited species up to 0.7 µs, with the main one being the larger expansion of O I excitation (mostly in O_2 background). However, the differences quickly disappear and a collective front for all recorded species is seen (vertical line at 2 µs). This translates into a simultaneous and very slow arrival of all species at the substrate (~650 m/s). The LaO I emission is particular in O_2, it shows a larger area of light emission (more chemical reactions) and in Ar a much narrower angular distribution than other species, which is probably related to its different scattering cross section.

Again, the excitation of Ar I from the background gas is detected well in front of the distribution of the other species and which at ~1 µs is disturbed and reshaped by the penetration of the arrow-like expansion of the plume, creating a temporary counterpart (marked with an arrow in Fig.4.32 at 0.7 µs).
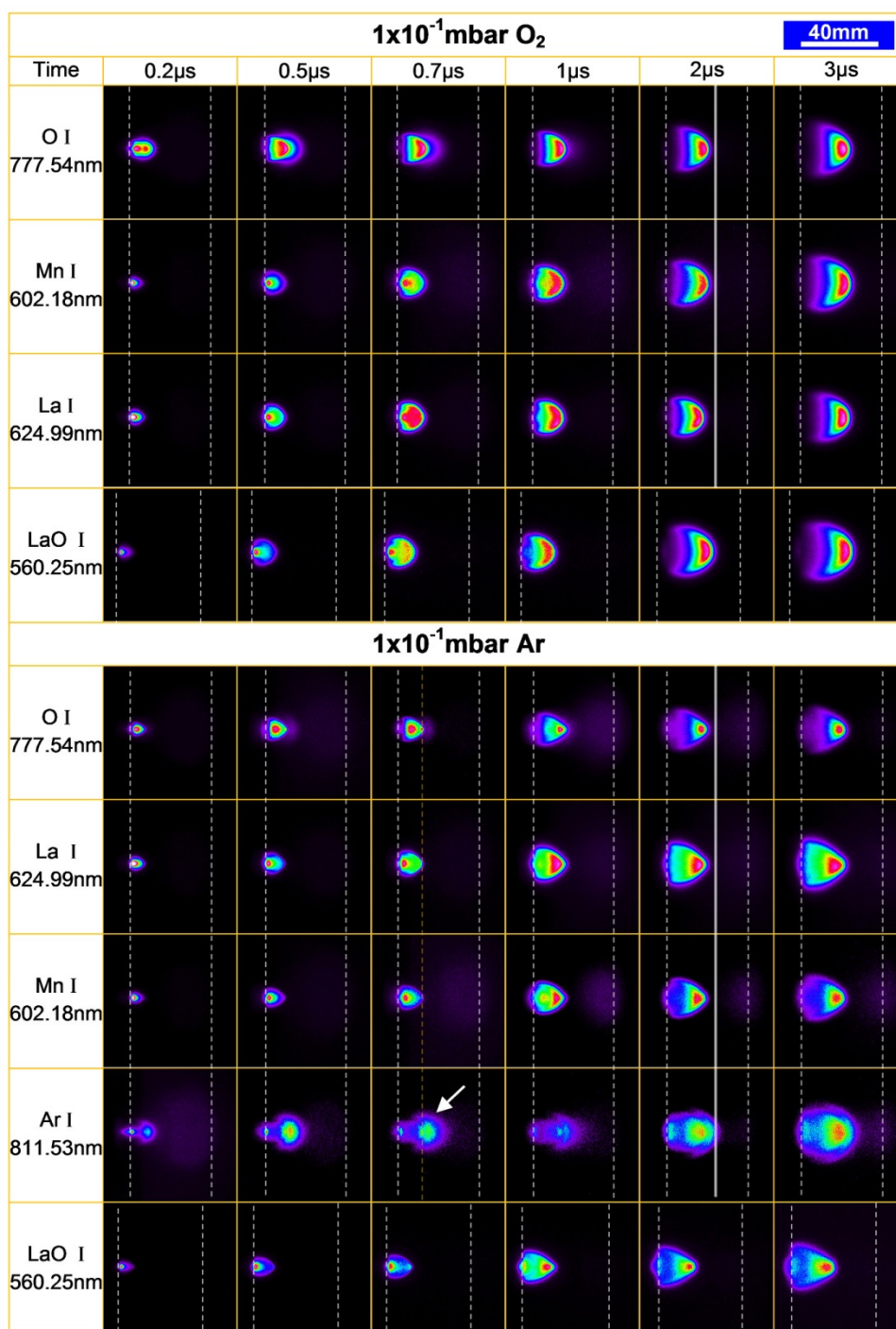
Fig.4.32. Time resolved images tracing the spatial distribution of the excited species of O I, Mn I, La I, LaO I and Ar I. The intensity scale has been normalized to the maximum counts for each image. The excited Ar has been highlighted using an arrow and a dashed line, while the matching fronts of all species (t=2μs) have been marked using a continuous vertical line. Note: due to the use of a different AOTF for LaO I, the images have a slightly different frame and zoom and the images cannot be directly compared with the other species.

Tracing the spatial distributions of the excited neutral species also helps to understand the excitation effect of the plume upon arrival to the substrate, as seen in 1×10^{-1} mbar O_2. The images are shown in Fig.4.33 for different species and indicate that the main source of emission is the excitation and/or formation of LaO I species (which is also the most stable of the different metal oxygen species). They are probably formed once the La penetrates this

temporarily O_2 rich volume. This confirms the assumption of O_2/Ar background gas being trapped between the expanding plasma and the substrate holder. An effect which could be enhanced by carefully engineering an appropriate substrate holder. For example by using an O_2 parabolic "trapper" at 1×10^{-2} mbar O_2 with the substrate located at its vertex. Alternatively an off-axis deposition or the use of a holder with a geometry that reduces the trapping of the background would cancel it. Concerning the rebound effect in Ar, no preferential rebound could be detected in the species resolved images.
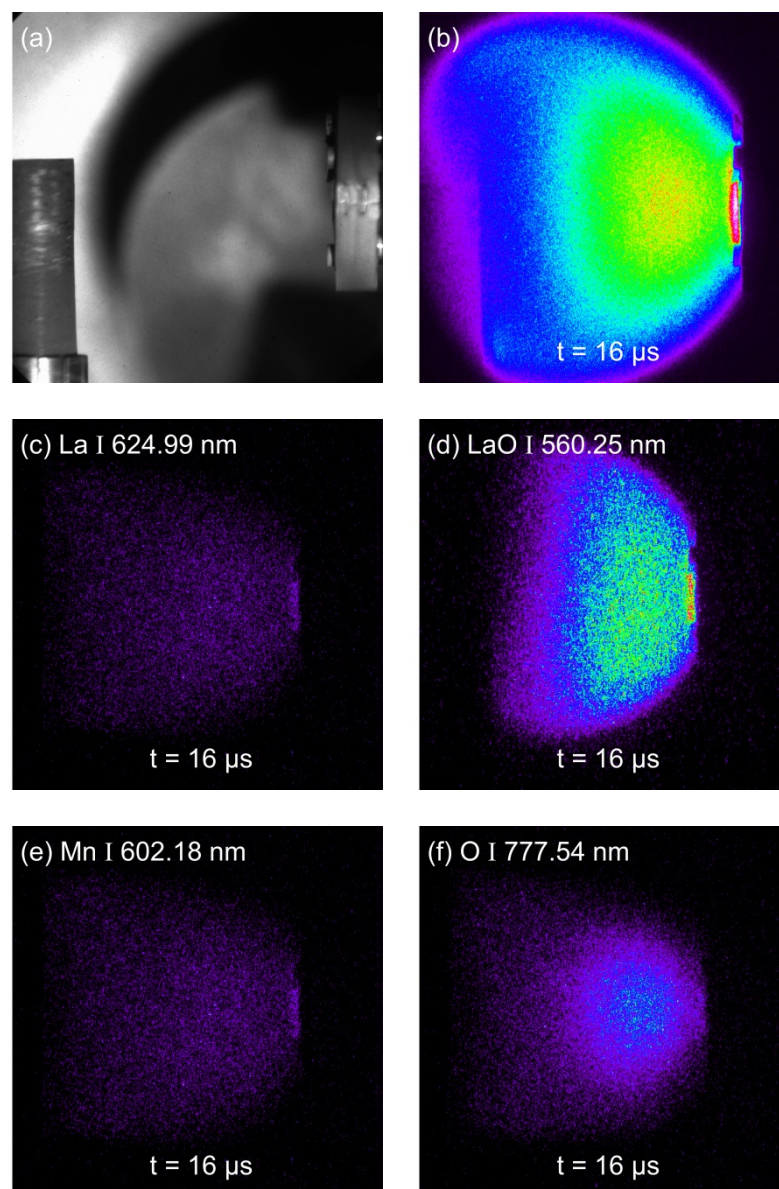
Fig.4.33. ICCD images of $La_{0.4}Ca_{0.6}MnO_3$ at 1×10^{-1} mbar O_2 at t=16µs. (a) Reference image with rod target (left) and substrate holder (right). (b) Image of visible plasma emission (300-1000 nm) showing the high emitting area close to the substrate. Wavelength selected images tracing the spatial distributions of the excited La I (c), LaO I (d), Mn I (e) and O I (f). Intensity scale is the same for all AOTF images, although the transmission efficiency is wavelength dependent and not directly comparable for each image.

4.2.2.2 Thickness and composition of the films deposited from the rebounded material

Two questions arise from the observed rebound effect. First, how much material travels back? Second, what is the composition of the backscattered material going to be? In order to answer those questions a simple experiment was performed. A substrate was positioned at the typical front location (substrate holder) and an additional substrate was 1 mm behind the ablated target, parallel to the substrate holder and perpendicular to the plasma plume expansion axis to capture the rebounded material. The deposition parameters were the same as described in section 4.2.1. The deposition was carried out at 1×10^{-1} mbar Ar and also O_2. Visual inspection of the rebound substrates revealed a film of non-uniform thickness and a clear film discontinuity caused by the shadowing of the target rod in both cases, confirming the significance of the amounts of the rebound material (Fig.4.34). Frontal and rebound films were then measured by RBS and the results are shown in Fig.4.35 and Fig.4.36 for film thickness and film composition respectively.
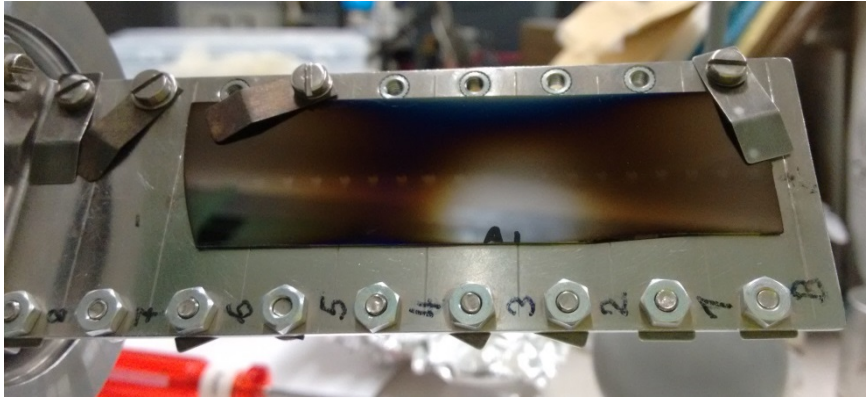
Fig.4.34. Image of the substrate placed behind the $La_{0.4}Ca_{0.6}MnO_3$ target to capture the rebound material. The shadowing from the target itself can be clearly seen. The substrate is placed on the RBS holder after the measurements. The multiple RBS ion beam measurement positions can be seen in the image (rectangular spots).
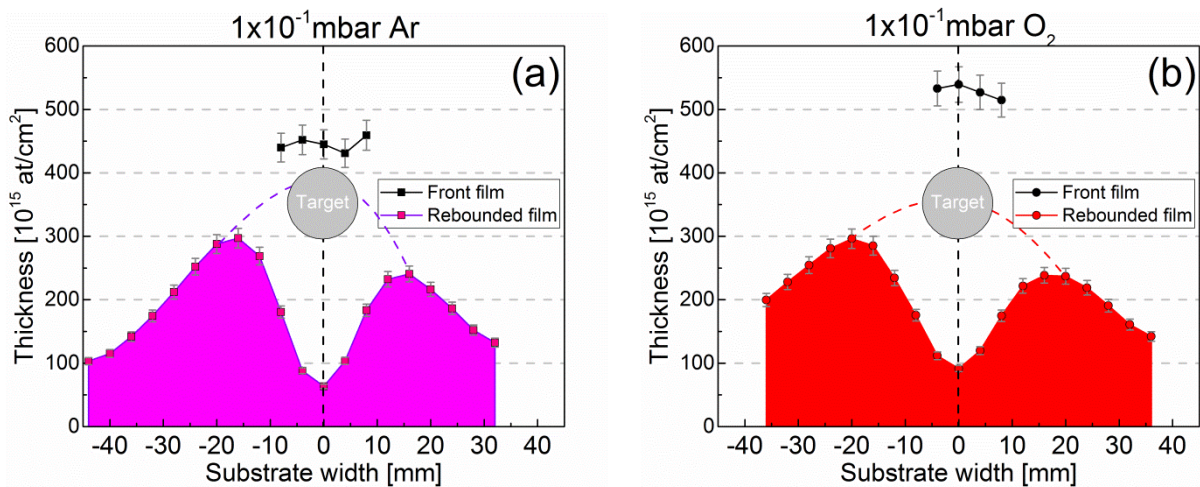
Fig.4.35. Frontal and rebound film thickness profiles for 1×10^{-1} mbar Ar (a) and O_2 (b). The target diameter is shown for reference purposes in grey (shadowing effect) and a visual estimation of the peak thickness is given by the dashed curve.

In terms of thickness, both frontal deposited films show a homogenous thickness while the rebound films show a clear directional deposition with the shadowing of the rod target at the centre position (although a certain film thickness is still detected suggesting that the plume moved around the target). This directionality is in good agreement with the rebound detected in the plasma imaging. The O_2 frontal film is slightly thicker (~20%) than the Ar one, which matches with the lower stopping power of O_2, while the thickness of both rebound films is very similar. In comparison, the proportion of rebound material is lower than the frontal case, but still significant with values of 65% (Ar background) and 53% (O_2 background) of the frontal deposition. In both cases the cosine-like thickness profile of the rebound material is slightly tilted towards the left side, an indication of a very small misalignment between plasma plume axis, frontal area of the substrate holder and rebound substrate (the species travel ~40 mm forward, rebound on the surface of the substrate holder and travel back ~40 mm plus the rod target diameter).
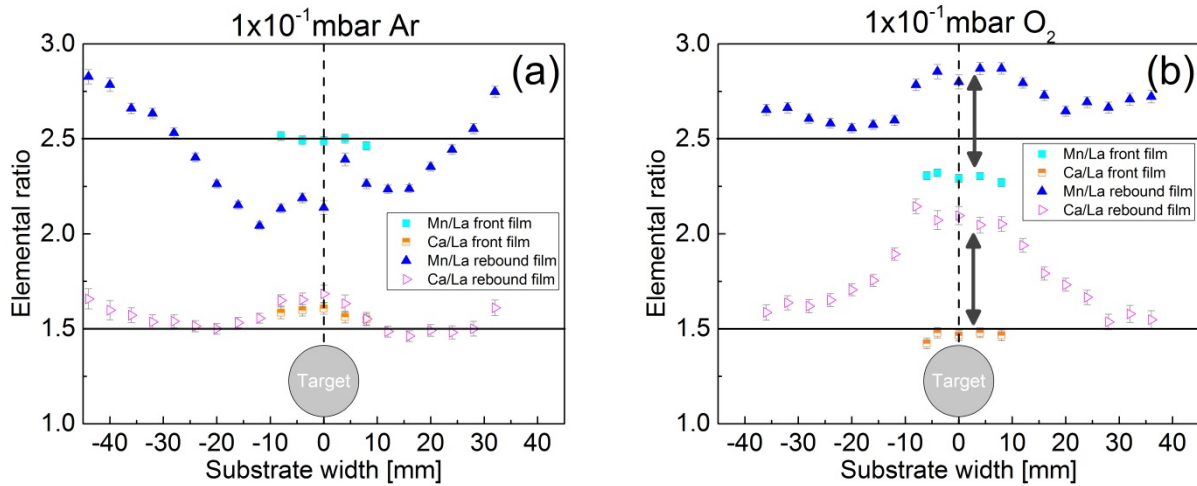
Fig.4.36. Frontal and rebound film cation-ratios profiles for $1x10^{-1}$mbar Ar (a) and O_2 (b). The target diameter is shown for reference purposes in grey (shadowing effect). The black horizontal lines represent the target elemental ratios.

The elemental ratios of the "front films" present little variation along the substrate width and matches the results from chapter 3 for Ar background (enrichment of the light elements Ca and Mn). Alternatively the rebound film composition presents strong variations which reach their maxima at locations close to the "shadowed" area. Once in the "shadowed" area the film composition becomes uniform again. This might evidence that the deposition processes for the frontal film and the "shadowed" area are similar and very different to the directional deposition of the rebound film. Interestingly, in Ar the frontal film and the "shadowed" area of the rebound film tend to similar values, while in O_2 the behaviour is the opposite with diverging ratios (either above or below the target composition, marked with black arrows on Fig.4.36b).

Disregarding the "shadowed" area, in an Ar background (Fig.4.36a) the rebound film is gradually deficient on both light elements in the proximity of the plume axis (or rich in La). A reasonable result, as the centre of the plasma plume has the highest species concentration and

it is expected that the numerous collisions (intra-plume and with the background gas) will preferentially scatter the lighter elements and leave a La rich front plume. Alternatively, in an O_2 background the rebound film becomes La deficient in the proximity of the plume axis (both elemental ratios increase). This deficiency can be explained by looking at the previous step to the rebound, the frontal deposited film. In the particular case of an O_2 background the plasma imaging results (Section 4.2.2.1) evidenced the formation of LaO and preferential deposition of La in such form on the frontal films which then becomes "unavailable" in the rebound wave. The RBS results for the frontal film also show this preferential deposition of La in an O_2 background (both Mn/La and Ca/La ratios decrease). This explains the mentioned diverging behaviour of the composition between the frontal and the shadowed rebound films when depositing in an O_2 background.

Overall the results prove that a significant recoating of the target occurs. A recoating with a composition different than the target and which varies depending on the background gases used. Furthermore, depositing films in O_2 or Ar also affects the film cation content due to the preferential formation of metal oxygen species.

A rough estimation on how the recoating of the target may affect the deposition because of target contamination is presented hereafter. Assuming a rod target with a 12 mm diameter and 20 mm ablation length, the ablation area corresponds to ~754 mm^2. The measured thickness of the rebound material at the peak location is ~100 nm. This has been estimated from the RBS thickness of ~400x10^{15} at/cm^2 and the relationship between at/cm^2 and nm from the profilometer measurements from chapter 3. Due to the rotation of the target, it can be assumed that 50 nm of rebound material will uniformly recoat the ablation area during those 40 min of deposition. Evidently during those 40 min (~7200 pulses) the laser will ablate target material in addition to rebounded material. Assuming a perfect ablation coverage of the whole area (without overlapping nor spacing) it would take ~540 shots to return to the first ablation spot, at which $50 * \frac{540}{7200} = 4nm$ of rebounded material would have been re-deposited. From ablation rates shown later in chapter 7 for 3 J/cm^2 it is estimated that per laser shot an ablation depth of ~21 nm is achieved. This means that ~20% of that ablated material would be rebound material with a different composition to the original one. A significant value when the film physical properties will be strongly dependant on the composition, even more if it is understood that it is not a steady state as the rebounded material will progressively deviate in composition.

4.3   Conclusions

Time, space, and spectral resolved imaging on the laser induced plasma plume of Ag and La$_{0.4}$Ca$_{0.6}$MnO$_3$ target has been performed to understand the arrival of the film's components and the influence of the background gas and pressure. In vacuum, the inverse relationship between the species' mass and expansion velocity cause dissimilar arrival times at the

substrate for the different species. The species arrive with velocities ranging from 18'000 m/s (La I) up to 30'000 m/s (O I) and strong rebound effects were detected which deformed the plasma plume. This could be a source for film composition variations if preferential bouncing would take place.

At $1x10^{-2}$ mbar the higher velocity of the lighter species is reduced by their preferential scattering and a plume splitting can be seen. The heavier La I is still able to reach the substrate, while Mn I is strongly scattered and being stopped by the background gas. The overall arriving species to the substrate are La I enriched. This is in agreement with film compositional analyses by RBS from chapter 3 [76, 92] and confirms the assumption that for certain pressure regimes there is an enrichment of the heavier elements on the film composition as the lighter elements are preferentially scattered.

In contrast, at $1x10^{-1}$ mbar (O_2 and Ar) the background gas confines all species together in a very slow expanding plume (same velocity for all species). It was found that the plume expansion in this relatively high pressure traps a portion of the background gas against the substrate holder, creating a transient high local pressure with remarkable effects once the plume reaches the substrate. For O_2 it creates a "long-lived" volume of excited species (mainly LaO I species) just above the substrate which expands up to 2 cm from the substrate and a slight rebound is seen, while for Ar the rebound wave is clearly seen traveling backwards. In both cases the thickness of the recoated layer on the target is not insignificant, and more importantly, the composition of the recoated layer is very different compared to the initial target composition (background gas dependent). Thus the complete target will be recoated, and depending on the size of the target, rastering pattern and ablation rate, the recoated layer could make up a substantial part of newly ablated material (estimated as ~20%). This itself raises questions of how accurately can a film composition be controlled and how significant is the impact on creating defects in the as-grown film due to the unintentional and non-stoichiometric transfer of species. In addition, the transient high local pressure could be utilized to incorporate more oxygen into a film by careful engineering of an appropriate substrate holder. Also, it was found that the use of O_2 enhances the formation of LaO and the preferential deposition of La in such form in comparison to Ar.

In addition, the influence of substrate heating on the background gas was presented. Experimental position resolved velocities and times-of-arrival evidenced such influence and the effect on gas density was quantified by using analytical equations of heat transfer to a rarefied gas. The obtained density variations matched the reductions in times-of-arrival and enable the PLD user to estimate an equivalent pressure when substrate temperature is varied.

5

The influence of the laser spot geometry

In PLD and laser ablation in general, the use of a rectangular or a beam spot with a non-circular geometry leads to the so called flip-over effect. Here, the longest dimension of the laser spot results in the shortest direction of the plasma plume expansion. It is a purely gas-dynamical effect and has been mainly reported for vacuum depositions of single element targets. It is particularly noticeable when the aspect ratio of the beam spot is large. In this chapter the flip-over effect is investigated in vacuum and at three relevant background-gas pressures using $La_{0.4}Ca_{0.6}MnO_3$ and following two complimentary approaches. Film based methods (RBS) for film thickness and composition and by probe based methods (MS) for angular kinetic energies and chemical reactions. The implications of these experiments are not limited to the flip-over effect solely, but provide guidance to PLD users attempting large area depositions by varying the spot dimensions in combination with laser beam rastering.

5.1   Basics of the flip-over effect

In PLD the choice of the laser spot shape and size is not trivial and has a strong influence on the angular distribution of film thickness and composition [2, 8, 14-20]. It originates from the fact that a bigger laser spot would not have an additive property of angular distributions of smaller spots (Fig.5.1ab), but rather a narrowing of the expansion dynamics (Fig.5.1c).
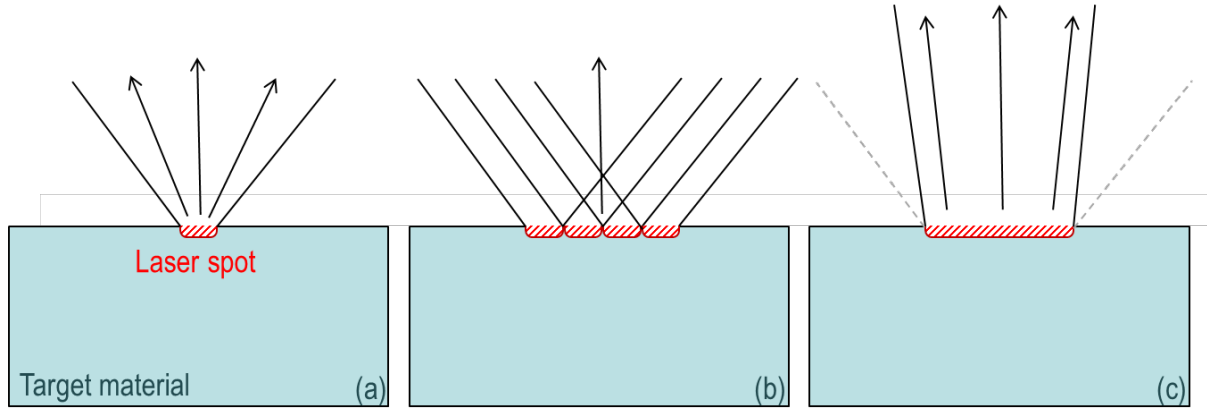
Fig.5.1. Conceptual sketches showing the plume expansion for a small spot (a), the misleading and incorrect expansion for a bigger spot assumed as an addition of smaller ones (b) and the correct and narrower plume expansion for a bigger spot (c).

One of the most fascinating effects of such expansion dynamics is the so-called flip-over effect. It is a specific laser ablation phenomenon, which occurs when using a non-circular laser spot. The longest dimension of the laser spot results in the shortest direction of the deposition pattern and vice versa. For example, for an elliptical laser spot the plasma plume expansion "appears" to be turned by 90° with respect to the laser spot orientation since the plasma plume appears broader in the shorter dimension of the laser spot and shorter in the longer direction. Thus the name, flip-over effect. Nevertheless, it is a purely gas-dynamical phenomenon and the apparent turn is not necessarily restricted to 90° (Fig.5.3) [14]. It originates from the fact that the narrowing of the deposition profile increases with the number of intra-plume collisions, which increase roughly as the ratio of the initial plume dimensions (given by the spot size) to the atoms' Knudsen layer MFP [2].

The flip-over effect has been frequently reported when investigating the angular distribution of species ablated in vacuum. Very often the analysis has been done for elliptical laser spots and by looking at the thickness of the deposited pattern [8, 15, 93, 94]. In other cases, the temporal evolution of the expanding plasma has been studied. An example is shown in reference [16] where a rectangular laser spot of 1mm x 2.4mm and time-resolved imaging was used to probe the plasma plume in 3 dimensions to provide a visualization of the effect. Mostly, the flip-over effect is studied using single element targets whereas the resulting film composition when using multi-element targets is little explored [17]. Additionally, modelling the plasma expansion by

adiabatic expansion or isothermal expansion equations have all shown the prediction of the flip-over effect [8, 14, 15, 18, 19].
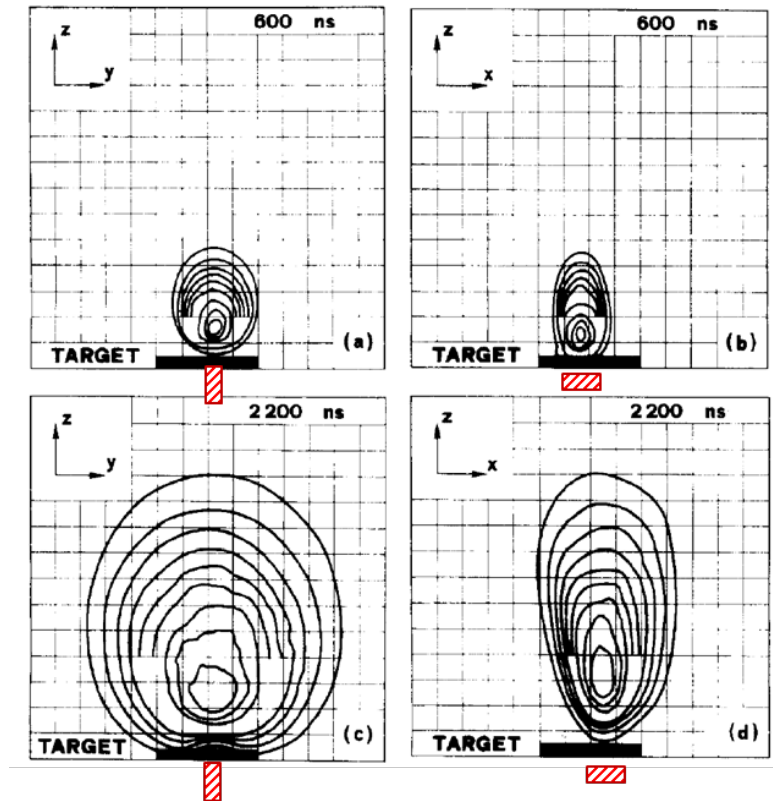
Fig.5.2. Luminescence of plume measured with an intensified CCD camera. The laser spot size has been included for informational purposes and has the following dimensions: 2.4 x 1 mm^2 on the X and Y axes, respectively. Source [16].

Although not strictly related to the plasma expansion analysis, *Kelly and Miotello* [14] explored the deposition of debris around the craters of ablated polyimide targets for different spot shapes in air (Fig.5.3). These patterns show turns of 60°, 45° or even new shapes. Although not explained in their article these results can be understood by referring to the original definition of the flip-over effect: the longest direction of the laser spot results in the shortest direction of deposition. Assuming that everything expands from the centre outwards and drawing on the picture an inscribed circle with the shortest dimension (in blue) and a circumscribed circle with the longest dimension (in red). One can verify that the deposited debris expands more in the shortest dimension and less in the longest. It is even more interesting for Fig.5.3c as the transition from the long dimensions to the shorter happens in a non-linear fashion as one moves along the angle. The shortening of the long dimension is initially very fast, explaining the abrupt deposited pattern recorded. Such clear images for different laser spot shapes provide a better visualization of the flip-over effect than the previously mentioned studies with rectangular or elliptical laser spots, as the complexity of the spot shapes reveals the particularities of the plasma plume expansion results.
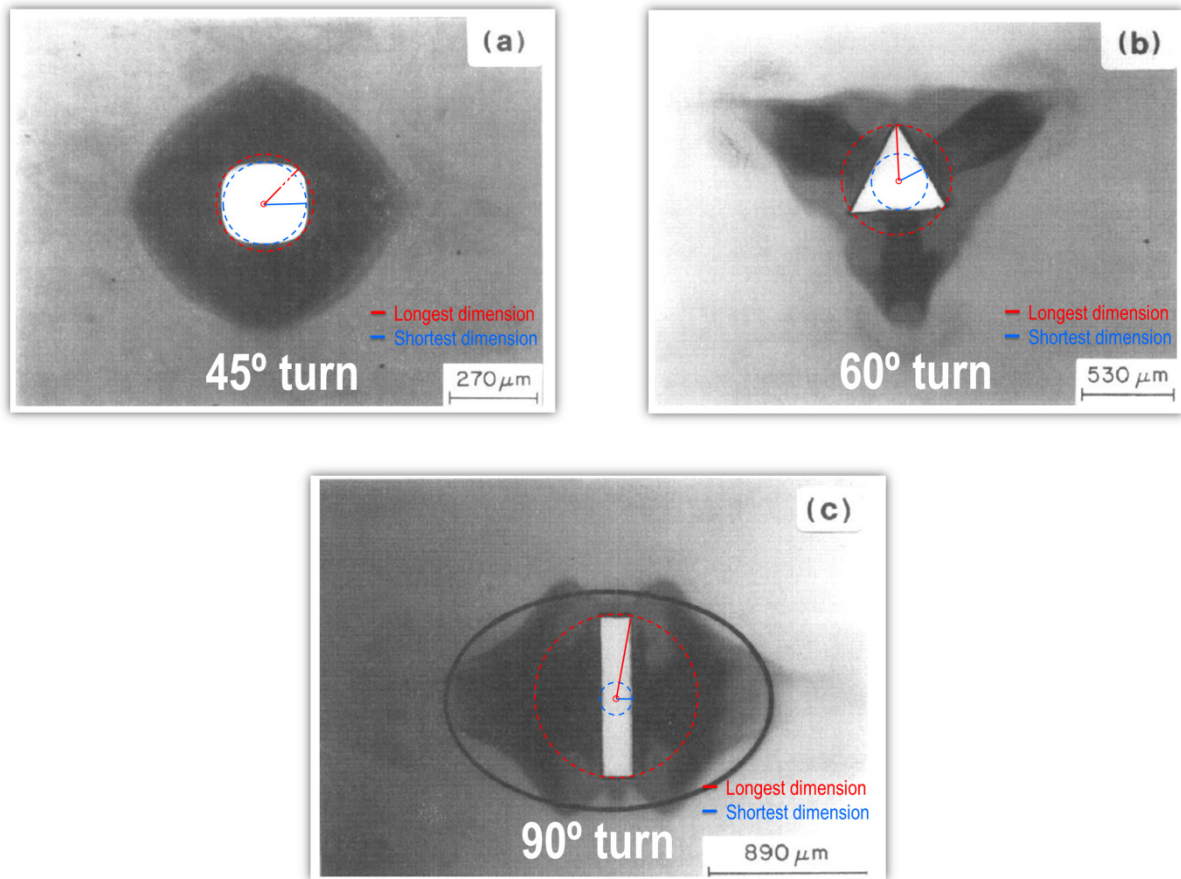
Fig.5.3. Modified images from [14] of deposited material on the surface of a polyimide target exposed to 50 laser pulses in air for different laser spot shapes (308nm, ~20ns, ~0.25J/cm^2). An explanation in red and blue colours has been added to the images to visually explain the debris patterns.

Further complexity can be achieved by careful manufacturing of new laser masks. For instance, using the ETHZ and the PSI logos in different scales as contours for such masks and ablating polyimide substrates. The results for different sizes of the ETHZ logos are shown in Fig.5.4. In them the shorter dimension of the spot geometry results in the longest angular expansion. Furthermore, despite the smaller dimensions of the reduced logo and its lower amount of ablated material, the redeposited debris has a similar reach as the pattern of the bigger logo. It is evident that the flip-over effect is much more than just a simple rotation. Obviously a comparison between the PSI and ETHZ logo is necessary (Fig.5.5) and similar conclusions can be drawn.
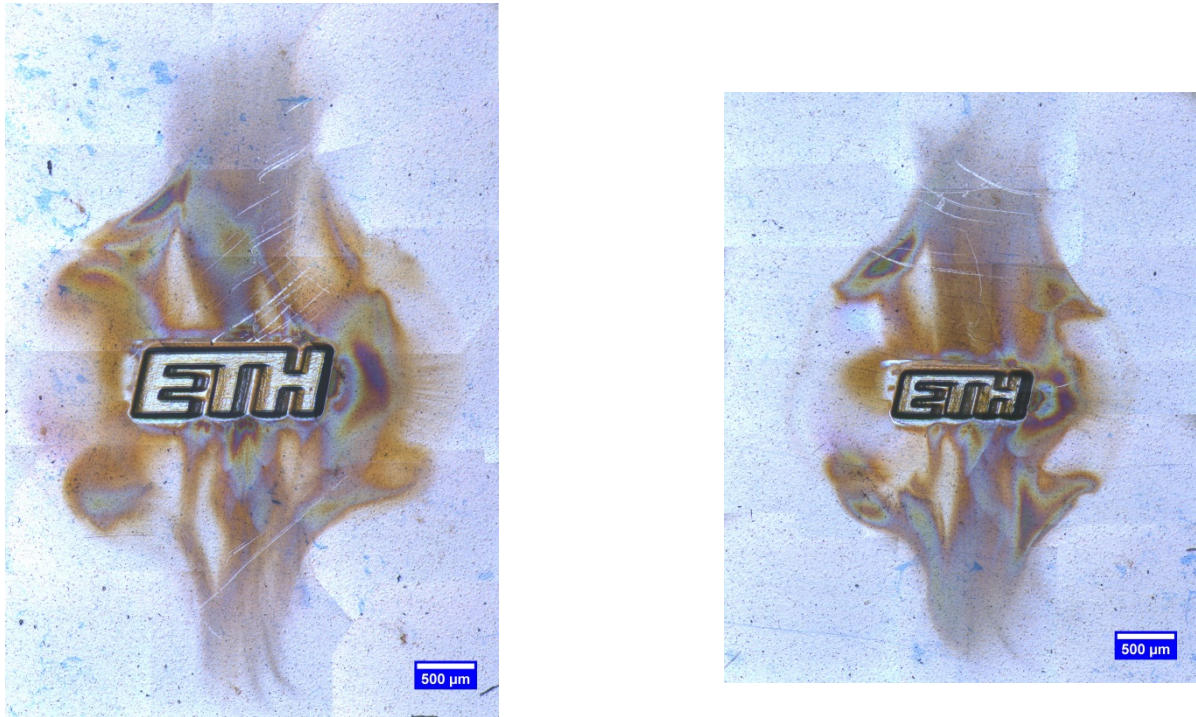
Fig.5.4. Optical images of the ablated polyimide using a 660 x 1700 µm ETH logo (left) and a 375 x 1300 µm logo (right). The different expansion dynamics can be seen in the debris patterns.
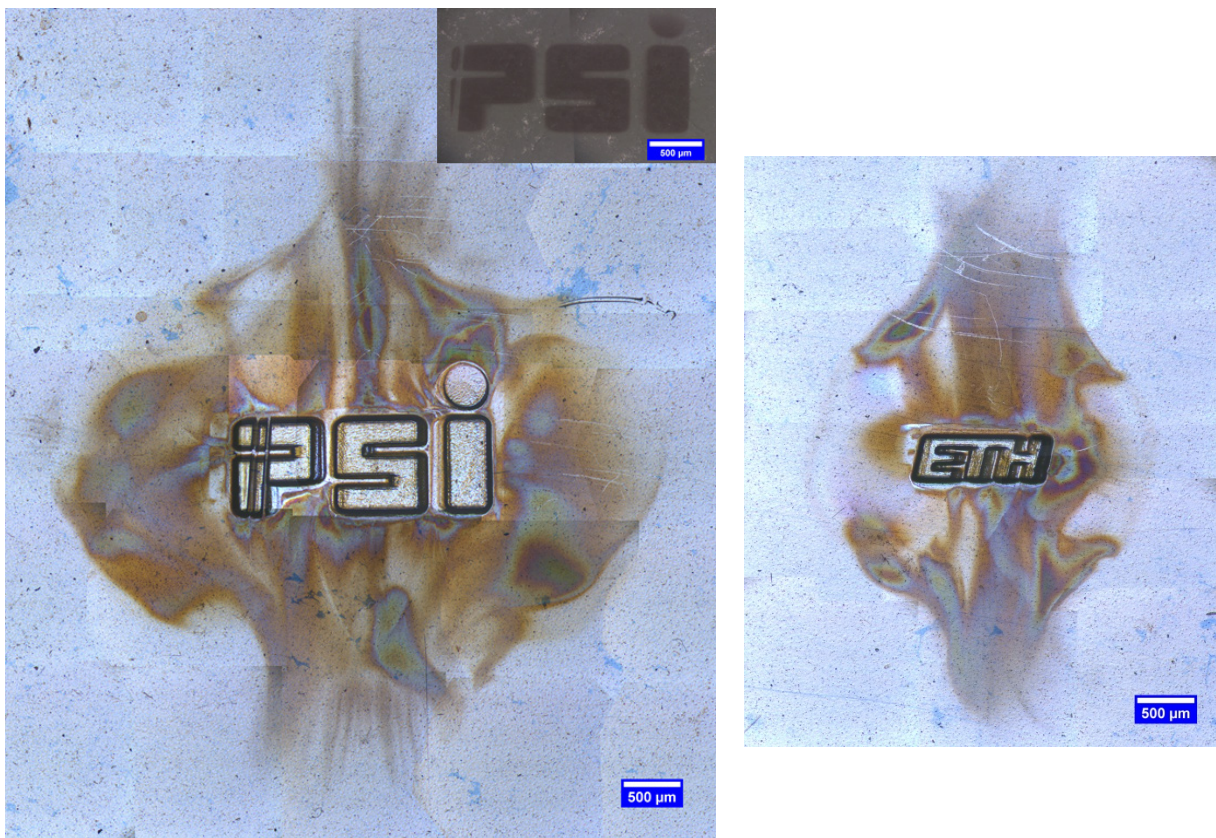
Fig.5.5. Optical images of ablated polyimide using a 840 x 2270µm PSI logo (left) and a 375 x 1300µm ETHZ logo (right). The different expansion dynamics can be seen in the debris patterns.

In summary, despite the interest in the flip-over effect, most studies are limited to vacuum ablation and single elemental targets. The more commonly used depositing pressure range of $1x10^{-2}$-$1x10^{-1}$mbar and ablation from multi-elemental targets are less explored. Nevertheless, in [20] the effect is studied at $5x10^{-2}$mbar Ar and a broadening of the plasma plume with the higher background gas pressure is reported. Unfortunately, the research was limited to one single pressure and the ablation of Ag. Therefore, a detailed understanding of the flip-over effect at higher background gas pressures and using multi-element targets is very relevant for PLD and remains an open question.

5.2   Investigating the flip over effect using film based methods (RBS)

5.2.1   Specific experimental details

To capture the evolution of the flip-over effect with pressure the ablation experiments were performed with very similar parameters as reported in previous chapters. A laser fluence of 2 J/cm^2 and a repetition rate of 3 Hz for 40 min was used. A mask ensured a skewed laser spot of 1 mm x 2.6 mm on the ablated target ideal for the study of the flip-over effect. The films were deposited onto two aluminium foils with 99.999% purity and 20 µm thickness. These Al substrates were placed perpendicular to each other in a vertical and horizontal position on the "semi-sphere" substrate holder as depicted in Fig.5.6.

All the depositions were performed at room temperature and at four different background pressures: vacuum ($1x10^{-6}$mbar), $1x10^{-3}$mbar, $1x10^{-2}$mbar and $1x10^{-1}$mbar with Ar as background gas to reduce possible chemical reactions with the background environment in order to simplify the interpretation of the results. After the deposition, the composition and the thickness of the films for the vertically and horizontally mounted foils were measured using RBS.
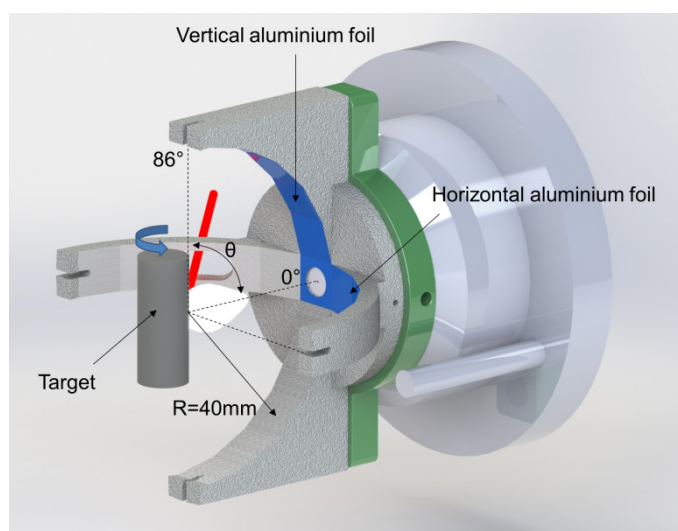
Fig.5.6. 3D render of the "semi-sphere" holder with two aluminium foils mounted on the vertical and horizontal axes. The holder is attached on a structure of the UHV chamber.

5.2.2   Film thickness variation with background gas pressure

The angular RBS thickness profiles are shown in Fig.5.7. Like in previous chapters the centre position of the deposition profile is marked with a vertical dashed line and the typical substrate size of 10 mm x 10 mm is shown by means of a rectangular grey box in the +-10° range. In general, the results show the characteristic strongly forward directed deposition of PLD. In addition, the comparison between the vertical and horizontal thickness profiles evidences the appearance of the flip-over effect: The vertical aluminium foil (broader deposition pattern) matches the shorter laser spot dimension (1 mm), while the horizontal thickness profile matches the longest spot dimension (2.6 mm).

The vacuum results (Fig.5.7a) show a higher rate of deposited material on the axis with the shortest laser spot dimension (vertical axis) than on the longest (horizontal axis) as often reported [8, 15, 17, 20]. In both cases there is still material being deposited at angles as high as 86°. At $1x10^{-3}$mbar (Fig.5.7b) the interaction with the background gas is still very small (MFP ≈ 100mm) and the thickness profiles are very similar to a vacuum ablation. Although the film thickness in vacuum is slightly thinner at 0°± 5°, this cannot be explained by higher kinetic energies in vacuum resulting in sputtering of the growing film by arriving species, but is probably a consequence of a slight misalignment between the plasma plume and the measured locations. The precise alignment of the plasma plume with the holder when ablating a cylindrical target is highly sensitive, apart from visual alignment using the lens stage, more precise approaches would be using the MS and searching for the appearance of the long energetic tails (which if not properly aligned would go unnoticed) or using a long pin tool emerging from the holder, although the latter would involve reopening the chamber for its removal. Differences in the angular thickness profile appear at $1x10^{-2}$mbar (Fig.5.7c) as was clearly visualized in the plasma plume imaging chapter. The calculated MFP is ~10 mm and the amount of interaction of the ablated species with the background gas as they travel towards the aluminium foils is sufficient to reduce the peak thickness from ~1400x10^{15}at/cm^2 for vacuum ablation to ~1200x10^{15}at/cm^2. Nevertheless, the consequences of the flip-over effect are still very noticeable even at this relatively high pressure. At $1x10^{-1}$mbar (Fig.5.7) the flip-over effect disappears and the films on the vertical and horizontal substrates show a similar thickness over the entire angular range. This is no surprise, as it was at this pressure when the rebound effect occurs cancelling the forward directed deposition and transforming it into a diffusion-like process due to the numerous interactions with the background gas [50]. This is certainly different to the ablation results in air of polyimide shown in Fig.5.4 and [14], where the flip-over effect is still present. A plausible explanation is that the effect is captured at ~0.5mm distance from the ablation spot and on the target itself, while in this case the analysis is at a distance of 40 mm from the target. As in chapter 3, at this particular pressure regime, the thickness at high angles for the horizontal foil is significantly higher than at the lower pressure ranges (300x10^{15}at/cm^2 vs. 170x10^{15}at/cm^2) but still slightly lower compared to the vertical direction.

Resembling a homogenous spherical deposition, which is almost independent of the angular location.
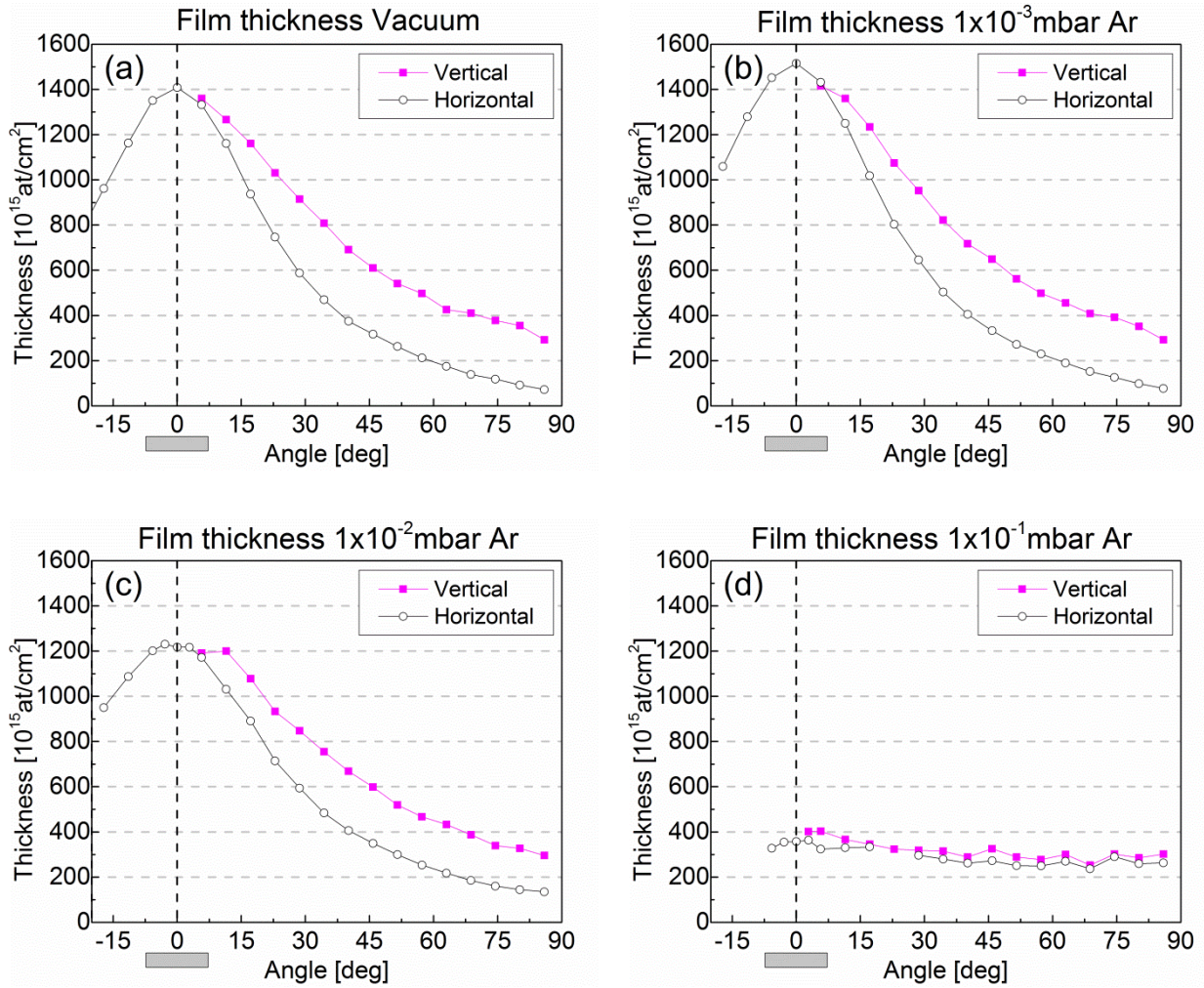
Fig.5.7. Angle-resolved film thicknesses for the vertical and horizontal aluminium substrate foils for four different argon background-gas pressures. The films were deposited using the "semi-sphere" substrate holder, which kept the distance of target to substrate constant at 40mm. The thicknesses were obtained by RBS and are expressed in at/cm^2 to avoid estimating the film density. The grey rectangle at +/-10° represents the typical PLD depositing area.

Concerning the broadening of the deposition profiles for metals with the pressure reported in [20], i.e. for 5x10^{-2}mbar Ar, we cannot draw the same conclusion as stated in [8]. If one plots the data in normalized thickness units for 1x10^{-2}mbar, the same conclusion can be reached (Fig.5.8a). However, the film thickness in absolute units (Fig.5.8.b) provides a better physical understanding and shows that the effect of increased pressure is a reduction of the peaking character in the horizontal direction (highlighted with a green arrow) compared to the vacuum ablation. It also shows that at high angles, the angular distributions are very similar for both pressure ranges.
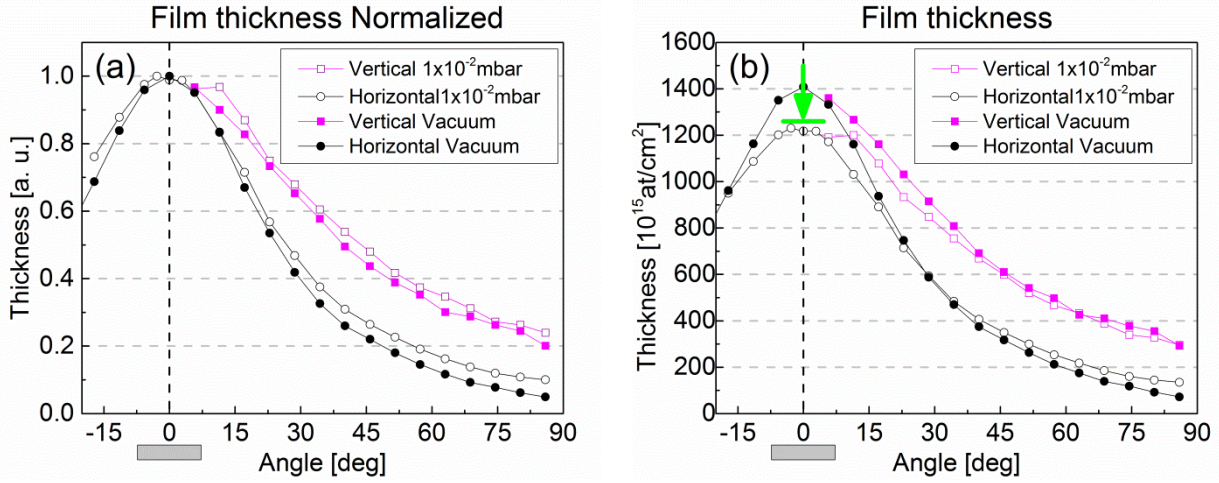
Fig.5.8. Comparison of angle-resolved film thicknesses for vacuum vs. 1x10⁻²mbar Ar deposition conditions. In (a) normalized units and (b) in at/cm² The broadening of deposition profile with increased pressure is only noticeable in (a) due to the normalization. In (b) the main variation is the reduction of the thickness at the central locations (0°).

Overall, the thickness vs. angle results show that the disappearance of the flip-over effect for this particular target material, and selected ablation conditions takes place in the pressure window between 1x10⁻²mbar to 1x10⁻¹mbar as the reported rebound of the plasma against the substrate holder takes away the directional component of the deposition.

5.2.2.1 Analysis of the film thickness angular distribution

It is interesting to compare the thickness profiles for the vacuum ablation with two common analytical expressions: The $cos^n\theta$ formula and the isentropic expansion model from Anisimov et al. [80]. The former is a purely empirical approximation found very often in literature for film thickness *F*(B):

$$F(\theta) = F(0)\,cos^n\theta + B\cos\theta \qquad (5.1)$$

With *F(0)* being the film thickness at 0° angle (peak thickness). The equation represents a strong peak in forward direction superimposed on a $\cos\theta$ background, which in many cases is not included (*B*=0). The value of *n* is typically in the range of 5-30 and often used to compare the peak sharpness of different deposition profiles [2, 70, 95]. However, this expression works best for small angles [96], namely, circa ±40°. For the experimental data (Fig.5.9a) the fitting fails at angles above 60° for the vertical thickness profile. The underlying reason is that this expression predicts the deposition per unit area on a planar surface at a certain distance from the target. Therefore at angles close to 90° the distance from target to substrate tends to infinity and the deposited film thickness $\lim_{\theta\to 90} F(\theta) = 0$. For these particular experiments, the semi-spherical holder captures the polar distribution of species at a fixed distance of 40 mm for all angles with a finite film thickness at angles close to 90°. Alternatively, an expression can be

derived from the Anisimov model that predicts the deposition on a hemispherical surface centred at the ablation spot [97]:

$$F(\theta) = \frac{F(0)(1+tan^2\theta)^{3/2}}{(1+k^2tan^2\theta)^{3/2}} \tag{5.2}$$

in which the fitting parameter *k* (where $k = Z_{inf}/Y_{inf}$ for the angular emission in the y-z plane) is the aspect ratio of the semi-ellipsoidal plasma plume when $t \to \infty$. As with the parameter *n*, a larger *k* corresponds to a more forward peaked expansion. Furthermore, contrary to the previous expression, the film thickness at angles close to 90° does not tend to *zero*, but to $\lim_{\theta \to 90} F(\theta) = F(0)/k^3$. Fitting the Anisimov model to the data for vacuum ablation (Fig.5.9b) shows a very good agreement with the measured data for all angles.
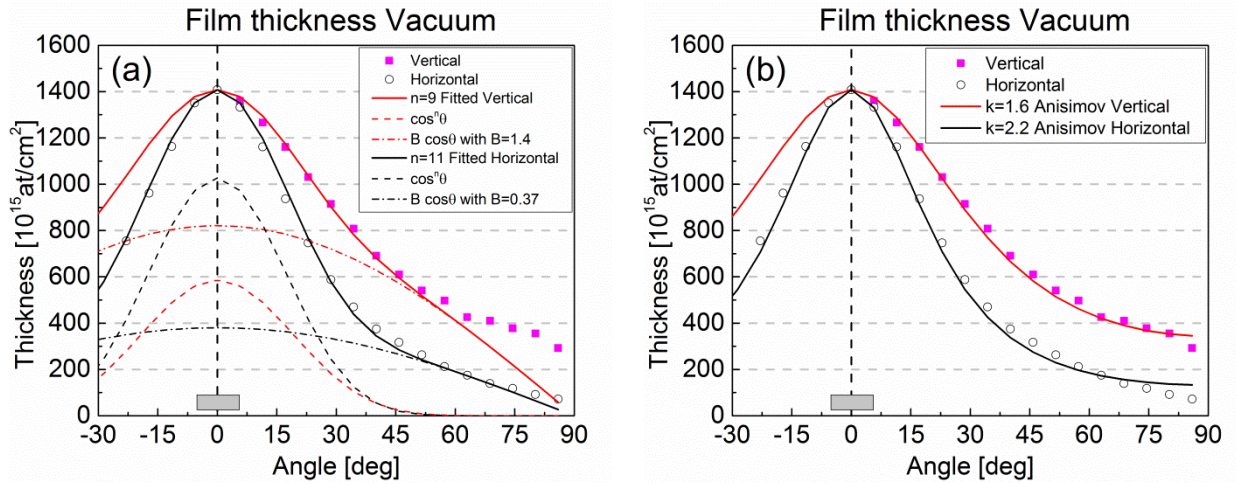
Fig.5.9. Measured (symbols) and fitted (solid lines) angular distributions in vacuum conditions using (a) cos^n Eq. (5.1) and (b) the Anisimov model expression for an hemispherical surface Eq. (5.2).

5.2.2.2 Film composition variation with background gas pressure

Fig.5.10b shows the angular composition profiles (horizontal and vertical) obtained by RBS for vacuum ablation. The results are plotted as the elemental ratios of Mn/La and Ca/La for different angular locations. The horizontal blue and red lines represent the target elemental ratios for Mn/La and Ca/La respectively. Both vertical compositional profiles for Mn/La and Ca/La are very similar to results using a 1 mm x 1.4mm laser spot reported in chapter 3. This is not surprising since the vertical laser spot dimensions are the same (1 mm), as well as the vertical orientation of the aluminium foil. In both experimental sets (vacuum conditions), the Mn/La composition is close to the target composition at small angles and starts to diverge considerably at angles above ~55°. For the horizontal direction (unique to this particular chapter), the Mn/La composition diverges already at ~30° reaching up to 30% deviation. This strong compositional deviation is also noted for Ca/La, which can be as large as 17% from the nominal composition. It is interesting to note that for both vertical and horizontal aluminium foils,

these Mn/La compositional deviations begin once the film thickness is below ~600x10^{15}at/cm^2, corresponding to an angle of ~30° for the horizontal profile and ~55° for the vertical one (marked with dashed blue lines in Fig.5.10a,b).
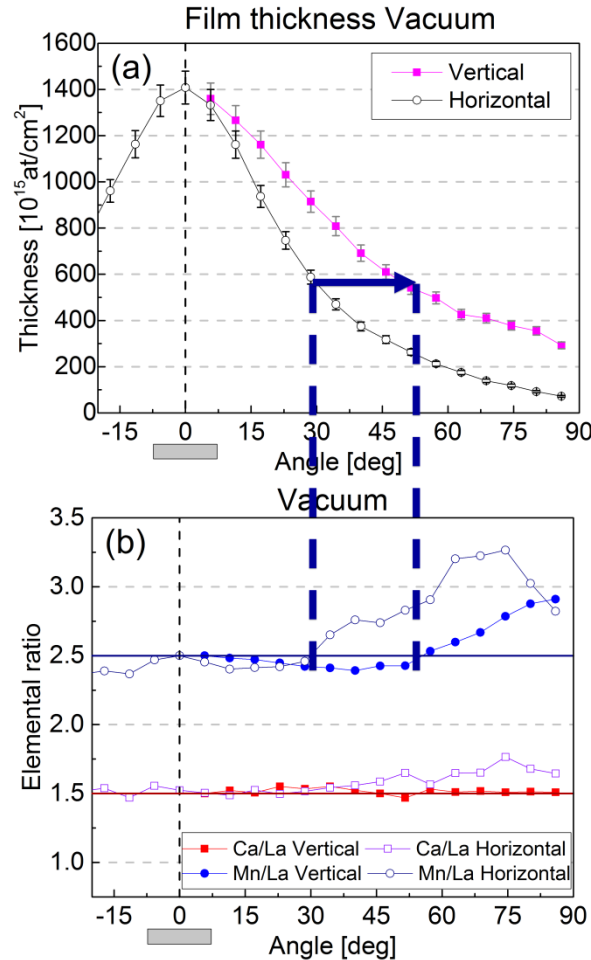
Fig.5.10. Angle-resolved film thickness (a) and composition (b) for the vertical and horizontal aluminium substrate foils for vacuum conditions. The results were obtained by RBS and the horizontal lines in (b) represent the target composition. Note: error bars are smaller than the symbols.

Similar to the fitting of the analytical expressions for film thickness, the high angular range is also an area of interest in terms of composition. The authors of Ref. [2, 6, 55] suggest that the deposition is made up of two components: an ablated component with a similar composition like the target material and an evaporated component with a composition which could differ from the target. The ablated component is strongly forward oriented and presumably rides on top of the evaporated component which covers most of the angular range. This evaporated component might diverge from the target composition due to preferential vaporization in low irradiated areas (e.g. common for any Gaussian energy beam profile, but not in flat top energy profiles as in our case). Following this reasoning, the narrowing of the thickness profile due to the longer dimension of the laser spot could leave a broader angular range to be disturbed by

the composition of the evaporated component and could explain the compositional variations seen at high angles. Furthermore, the frequent use of Eq.(5.1) for fitting, which is the sum of two functions, indirectly suggests a two component mechanism.

However, this is in strong contrast with the better fitting of Anisimov's Eq.(5.2). This expression is derived from a mathematical model purely based on gas dynamic equations. It describes the isentropic expansion of the plasma plume starting from an initial stage as a dense vapour plume, namely, already after the vaporization of all the participating material. There is thus no second evaporated component in the model and although there are reports on preferential vaporization of elements in alloys (i.e.: brass at low ablation fluences [98, 99]) this is so far not experimentally proven for complex oxides (discussed in 3.4 and also not fitting for all species analysed).

Concerning the higher pressure regimes, the composition profile for an ablation at 1×10^{-3}mbar (Fig.5.11b) and vacuum (Fig.5.11a), are similar for both elemental ratios and both directions. It is at 1×10^{-2}mbar (Fig.5.11c), where significant changes are observed. At this pressure collisional interactions with the background gas take place and are the main driver for the compositional changes in comparison to vacuum conditions as was visually seen by plasma imaging (chapter 4) and measured in the films (chapter 3). These interactions with the background gas result in small changes in the thickness profiles, whereas the composition profiles change strongly. There is a general reduction of both lighter elements with respect to La shown by a drop in the composition for Mn/La (A=55 vs. A=139) and Ca/La (A=40 vs. A=139). This is particularly pronounced at the centre of the plasma plume, where the film composition shows the strongest change at this pressure: 2.125 Mn/La (instead of 2.5) and 1.3 for Ca/La (instead of 1.5). This shows a deviation from the target composition of ~15%, very similar to the results reported in chapter 3. This is a relevant aspect, since the range of ±10° is the typical angular range used by standard PLD users. Such loss of the light components at lower pressures compared to heavier elements has also been shown in Monte Carlo simulations of a binary target with m1 :m2 = 1:5 [100] and in experimental reports [50] and it is a well-known issue when performing PLD using multi-elemental materials containing lithium (due to scattering and also sputtering) [23, 32].

Additionally, at the highest deposition pressure of 1×10^{-1}mbar (Fig.5.11d) even the heaviest element La is scattered. At this pressure the kinetic energy of species in the plume is strongly reduced (<20eV) and as the plasma imaging revealed all species are travelling together. A strong rebound takes place causing the thickness profiles to become constant for the entire angular range with the plume species reaching the substrate through diffusion into the background gas [50]. The composition profile for Ca/La hardly varies and is the same like in the target for both the vertical and horizontal substrate orientation. In contrast, the Mn/La ratio is not constant at 2.67 as in [76], but varies in the range of 2.6-3, which is not yet understood.

Fig.5.11. Angle-resolved film thickness (a) and composition (b) for the vertical and horizontal aluminium substrate foils for vacuum conditions. The results were obtained by RBS and the horizontal lines in (b) represent the target composition. Note: error bars are smaller than the symbols.
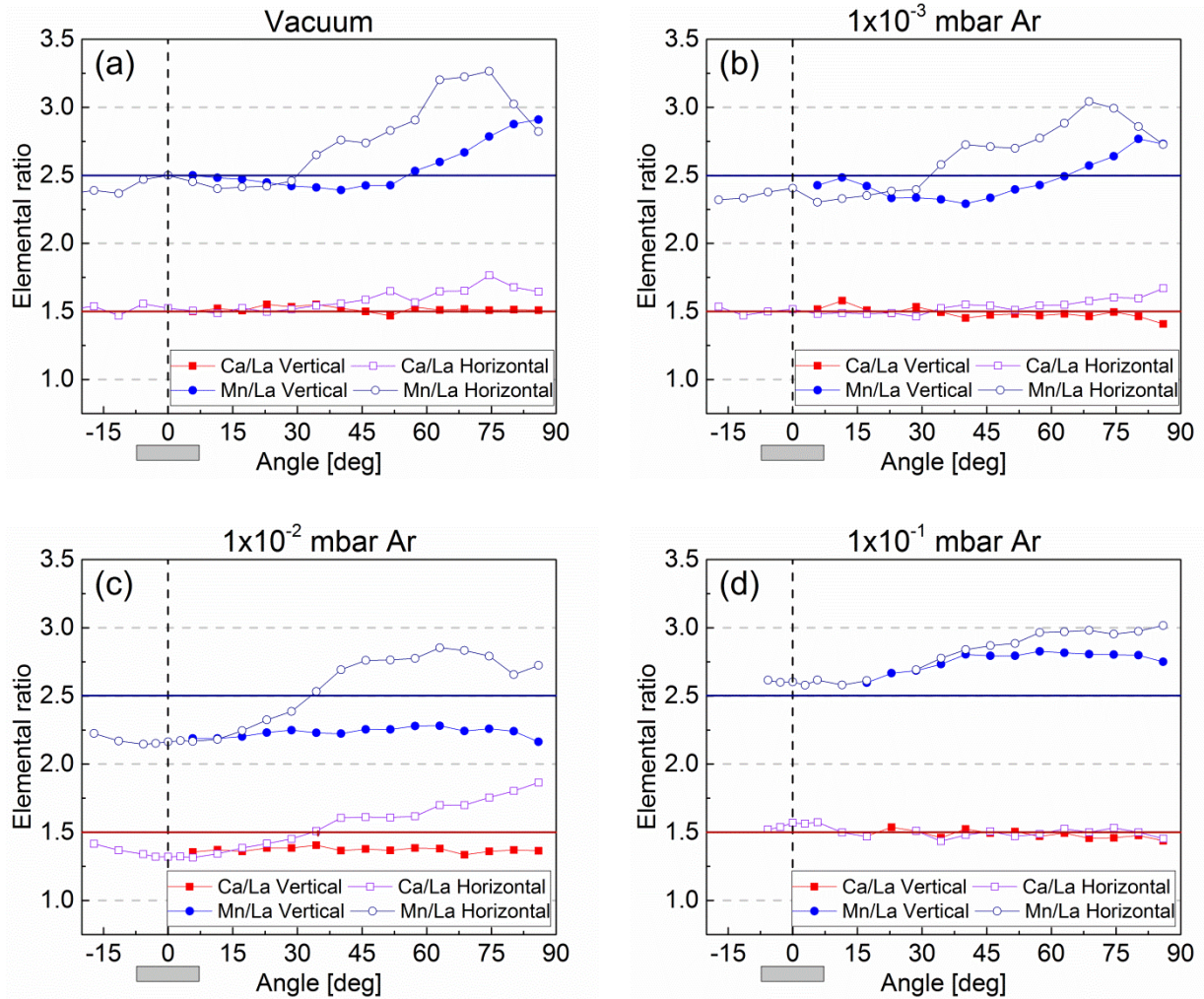
5.3 Investigating the flip over effect using probe based methods (MS)

5.3.1 Specific experimental details

Complimentary to the film based method, plasma plume probing was performed using the Hiden Analytical high-energy quadrupole mass spectrometer (MS) and the target rotation holder described in Chapter 2. The aim was to understand the changes in the angular distribution of species in the plasma plume when the laser spot dimension changes. For this purpose two different spot geometries were used while keeping the fluence constant (2 J/cm^2): 1 x 1 mm and 1.8 x 1.8 mm. Instead of the rod target, a disk target was used to allow suitable angular rotations. The target had an RBS verified composition of La$_{0.33}$Ca$_{0.66}$MnO$_3$. Both measurements were performed in vacuum to avoid any masking of the results by the background gas (i.e.: preferential scattering by the background gas). The MS measurement recorded the following species: La$^+$, Ca$^+$, Mn$^+$, O$^-$, LaO$^+$, CaO$^+$ and MnO$^+$.

5.1.2 Results

As reported in chapter 2, the use of the target rotation holder requires the systematic switching of masks to keep the same spot size for each angular measurement. If the masks would not be changed the spot dimension in the plane of rotation would vary, thus modifying the angular distribution of the probed plasma plume at each particular angle due to the flip-over effect. Thus the flip-over effect itself would disturb a proper measurement. Images of the consequences of not switching the mask between angular rotations of the target can be seen in Fig.5.12. where polyimide was used to trace the debris patterns after ablation. Fig.5.12a shows the intended square laser spot with the flip-over effect producing a 45° turn of the expansion pattern, while Fig.5.12b shows the change in the plume expansion due to the shortening of one of the laser spot dimensions. In summary, changes in masks as a function of the ablation angle are mandatory to be sure the same plume is being probed.
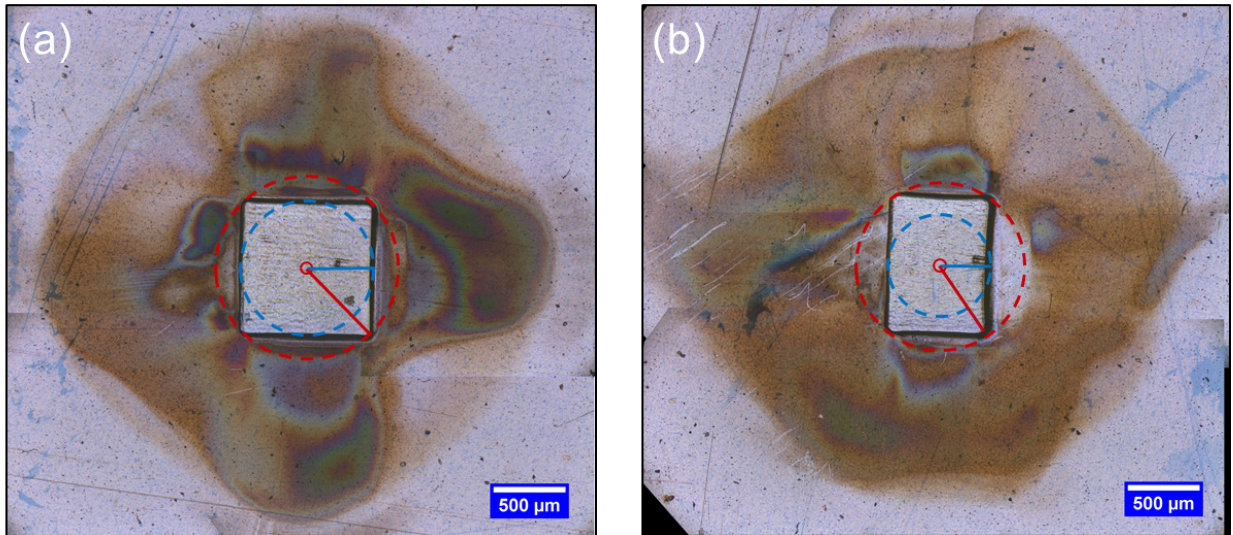
Fig.5.12. Optical images of polyimides ablated with two different laser spot dimensions because of the geometrical changes originating from the angular tilting. The re-condensed debris patterns with a 45° turn evidence the flip-over effect.

The angle resolved MS measurements for the smaller spot are presented first, followed by a comparison against the bigger spot later. The measurements for the 1 x 1 mm spot show the expected highly energetic forward deposition of PLD (Fig.5.13abc). As an example the angular variation of the kinetic energy profile of La$^+$ is shown in Fig.5.13a, with long energy distributions reaching up to ~500eV at 0° angle. These long tails gradually disappear as the probed angle is increased, with 90° showing only La$^+$ species with energies below 50eV, but still a certain amount as was seen in the film thickness measurements. Fig.5.13b shows a comparison between the average kinetic energy of La$^+$ species, calculated by:

$$Avg.\ K. = \frac{\sum_{k=0eV}^{k=1000eV}\left(k*Counts_{at\ k}\right)}{\sum_{k=0eV}^{k=1000eV}(Counts_{at\ k})} \tag{5.3}$$

and the maximum kinetic energy (max. kin. energies of counts detected with more than 5 times the noise levels). There is a strong difference between them throughout the entire angular range highlighting this long distribution profile (i.e.: at 0° the average energy is ~100eV vs. ~500eV for the maximum energy). It also shows that although a great portion of species have energies <100eV a certain number of highly energetic species are present and will most likely damage the film. The bump at 72° is probably caused by the switching of mask at that location as the mask used from 24-66° is always the same and at both extremes the ablation spot is 70 µm wider than the ideal 1x1 mm (more details in Fig.2.9). This is estimated as a ~6.5% decrease in fluence (~1.87J/cm^2 vs. 2 J/cm^2) which is clearly noticed by counts and kinetic energy increases when switching masks at 72°.

Mn$^+$ (Fig.5.13c) shows similar changes like La$^+$ of its kinetic energy profiles with angular location but with two marked differences: the maximum energies detected are lower and the profiles for each angle stop abruptly when reaching the maximum energies (except for 0°) instead of gradually like for La$^+$. It seems that both characteristics are strongly related to the lower mass of Mn vs. La and their intra-plume collisions. This will be explored in more details and for additional target materials in 6.2.1.

Another remarkable finding is the high energy of the species at high angles (>30°). This is not from a thermal evaporation, which should be <1eV, and proves that the composition at large angles is not due to thermal evaporation as has been suggested very often [6, 55, 101] (discussed earlier in 5.2.2.2).
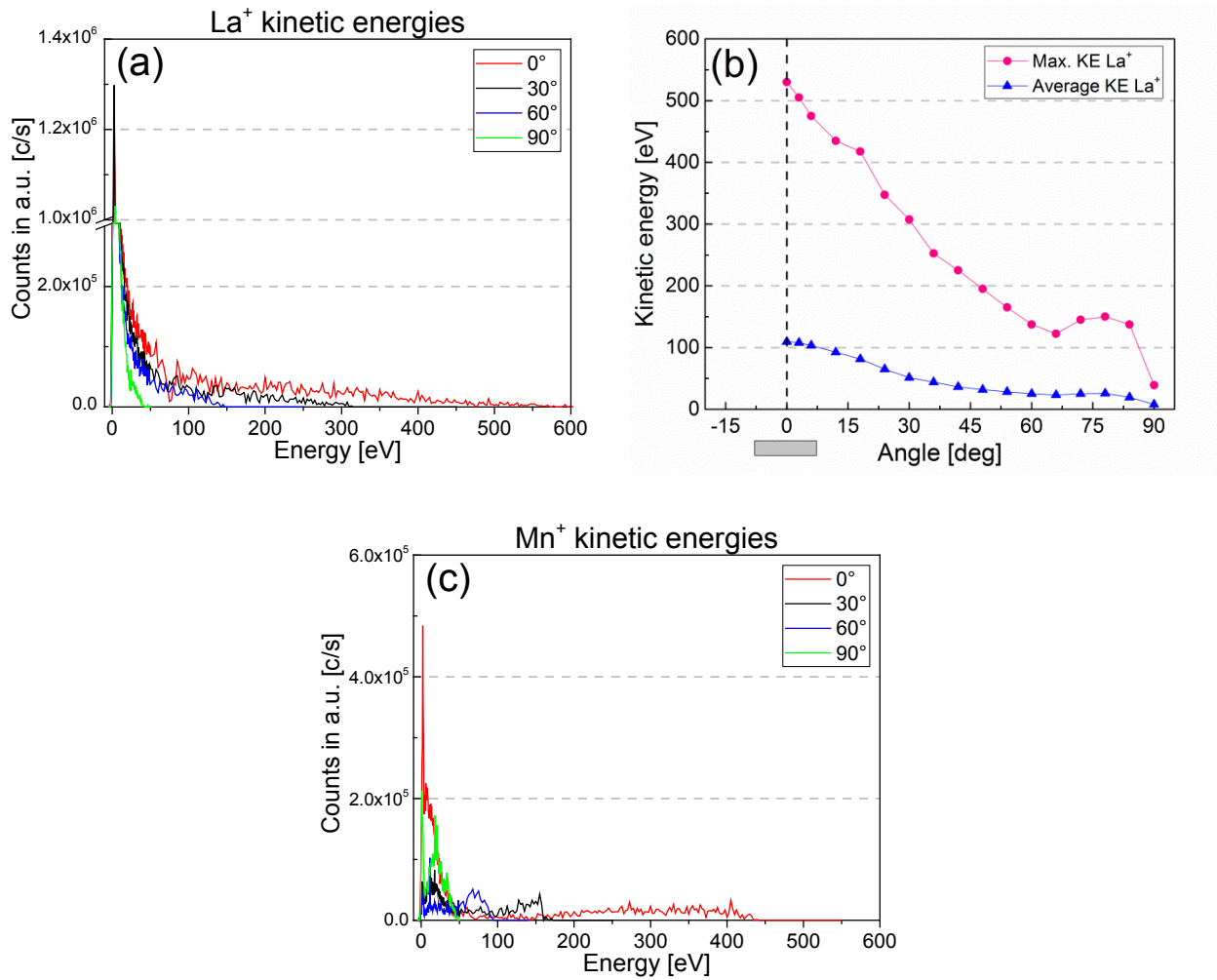
Fig.5.13. Kinetic energy profiles from $La_{0.33}Ca_{0.66}MnO_3$ ablation measured at different angles for La^+(a). Mn^+(c) and comparison of maximum vs. average kinetic energies of La^+ (b) for the different angular locations.

An integration of the total counts from the kinetic energy profiles is presented in Fig.5.14 for the different angular locations and for the two spot sizes. The use of a larger spot size for the same fluence results in the expected higher amount of deposited material, although for an ablation area ~3 times larger the increase in integrated total counts is barely ~20%. The purpose of this investigation is to verify the core cause of the flip-over effect, that more species travelling together results in a more forward oriented profile and vice-versa. Given the dependence between the total amount of species and the spot size, it is necessary to normalize the counts to enable a proper assessment of the changes in the forward character of the deposition.

This is presented in Fig.5.14b and shows the predicted narrowing of the deposition profile when the spot size is increased (more species travelling together) and the increased scattering at high angles when less species are present with a crossing between both profiles at around 35°. This is a confirmation of the flip-over effect.
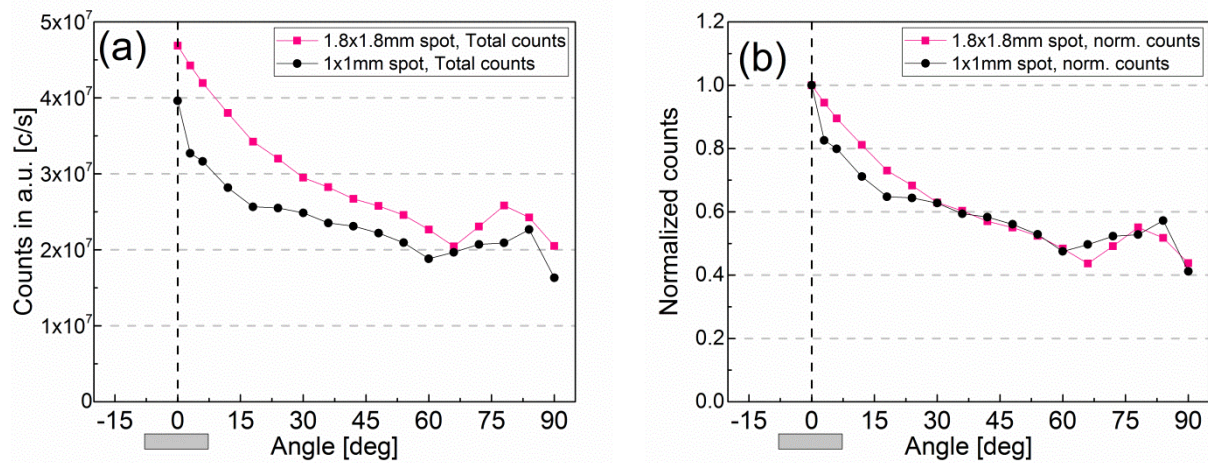
Fig.5.14. Angle resolved total counts from $La_{0.33}Ca_{0.66}MnO_3$ ablation for the two different laser spot sizes (a) and their normalized plots (b).

The same conclusion can be drawn when analysing the influence of the spot size in the angle-resolved maximum kinetic energies for the different species presented in Fig.5.15 (note: no counts were detected for CaO^+ and MnO^+). All cations show a similar profile, with the maximum kinetic energies being the highest for La^+ (~520eV), then Mn^+ (~430eV) and Ca^+ (~310eV). In all cases the use of a larger laser spot yields higher maximum energies at the centre of the plume and lower energies at high angles. The latter is not a direct consequence of the larger spot size, but a result of the increased scattering at high angles of the smaller spot due to the smaller amount of material travelling together. Alternatively, the energy profiles for O^- and LaO^+ are very different to the cation profiles with energies below ~50eV and very flat profiles. This evidences that they are generated following a very different process than the cations, with LaO^+ even rising in energy as the angles increase (from ~20eV to ~30eV).
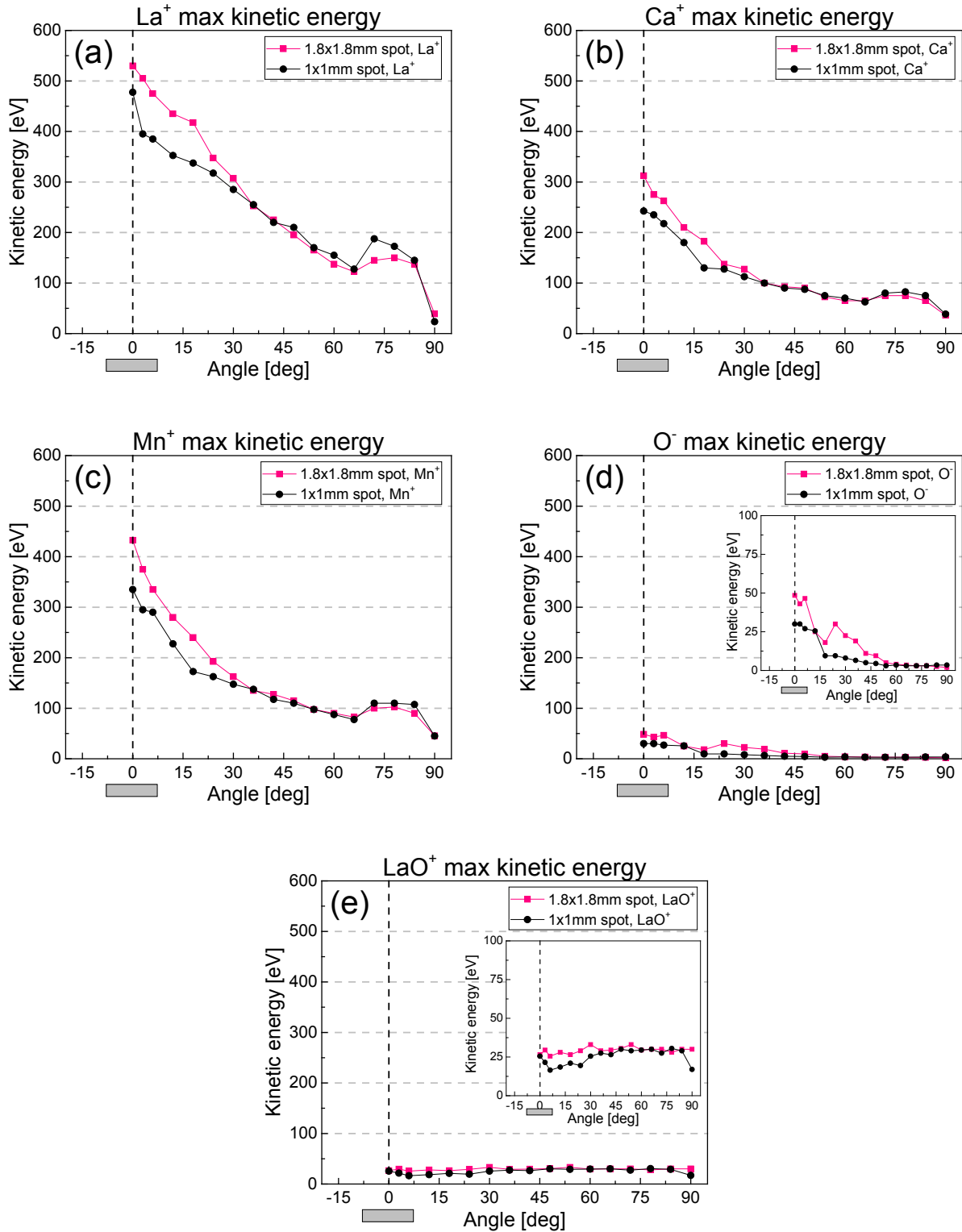
Fig.5.15. Angle-resolved maximum kinetic energies from $La_{0.33}Ca_{0.66}MnO_3$ ablation for the two different laser spot sizes of La^+(a), Ca^+ (b), Mn^+(c), O^-(d) and LaO^+(e).

The profiles of the calculated average kinetic energies shown in Fig.5.16 evidence the long tails of the profiles as there is a 6 fold jump between these and the maximum kinetic energies reported before. The exceptions being O^- and LaO^+ where the maximum and average kinetic energies are similar, evidencing compact profiles with hardly any tail.
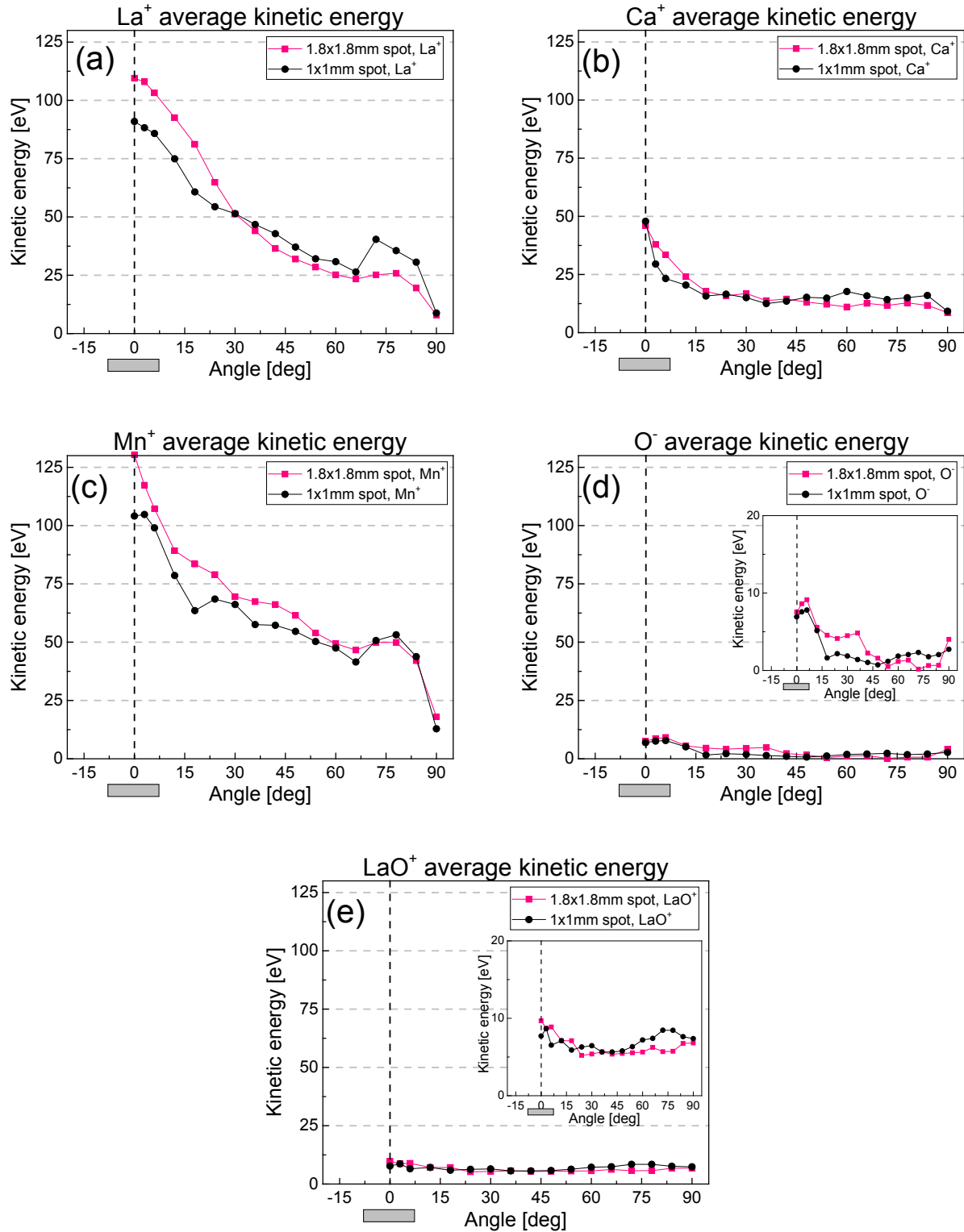
Fig.5.16. Angle-resolved average kinetic energies from La$_{0.33}$Ca$_{0.66}$MnO$_3$ ablation for the two different laser spot sizes of La$^+$(a), Ca$^+$ (b), Mn$^+$(c), O$^-$(d) and LaO$^+$(e).

With the aim of revealing any preferential scattering among the cations, a comparison of energy variations between the big and the smaller spot sizes is shown in Fig.5.17. No consistent preferential scattering could be seen. The strongest energy variations take place at the centre of the plume for the maximum kinetic energies (Fig.5.17a), while for the average kinetic

energies the strongest variations take place at high angles (Fig.5.17b). This is reasonable as it is expected that the increase in counts at high angles is due to scattering, thus with reduced maximum energies. In both cases the transition from energy reduction to energy increase as one moves along the angle is present (the smaller spot yields an increase in scattering towards high angles). The changes at 90° deviate in both occurrences, although 90° is experimentally borderline.
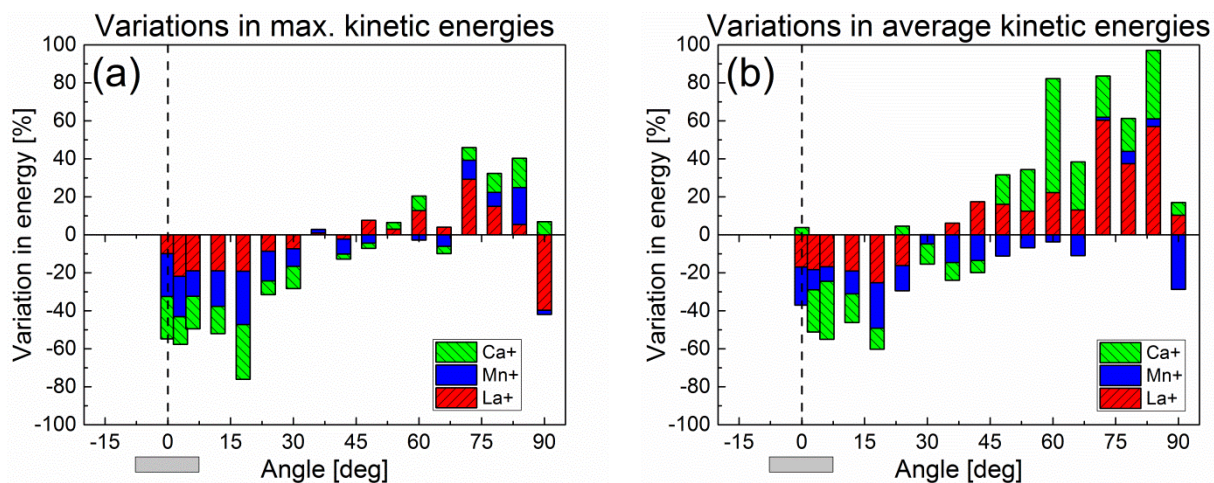
Fig.5.17. Angle-resolved changes in kinetic energies from $La_{0.33}Ca_{0.66}MnO_3$ ablation when using a smaller laser spot for the max. kinetic energies (a) and for the average (b).

5.4   Conclusions

The commonly stated definition of the flip-over effect as a 90° rotation is misleading. There is no physical rotation of the plasma plume as it emerges as a consequence of the plasma expansion dynamics and it can be a 90°, 60°, 45° or any other angle depending on the particular laser spot shape. A more suitable description would be "crowd-effect"[1] as it is a matter of the amount of ejected material travelling together.

Its analysis by MS measurements showed a consistent variation of the angular kinetic energy profiles depending on the laser spot dimensions (both for the maximum and average energies). The smaller the spot size the lower the kinetic energies at the plume centre and the higher at high angles (due to increased scattering). This is due to the reduced amount of species travelling together (crowd-effect), the main cause of the flip-over effect. A preferential scattering of the cations due to the spot change could not be distinguished. Independent of its naming, the flip-over effect will probably remain as a mere curiosity for the standard PLD user who commonly works in the +-10° range. However, what will not be a curiosity are the consistent strong compositional variations caused by the background-gas pressure in the films deposited close to the centre of the plasma plume. Additionally, the use of a larger laser spot opens another door to compositional control by placing substrates at angles between 30-85°. In our particular case, this has taken the already noticeable deviation of 15% at the centre of the plasma plume to 30% at angles of 60-80°.

Alternatively, the reported angular results in terms of both thickness and composition will certainly be relevant for PLD users attempting large area depositions by varying the spot dimensions in combination with laser beam rastering and the use of synchronized masks, as the larger substrate will otherwise "catch" the phase at high angles.

In addition, it was proven that the belief that the angular distribution in PLD consists of an stoichiometric component riding on a broader evaporative component is not true. This has been shown for $La_{0.4}Ca_{0.6}MnO_3$ and will be shown for $CaTiO_3$ in chapter 5, evidencing that the findings can be extended to additional PLD materials (the original belief was built solely from the ablation of $YBa_2Cu_3O_7$ [55]).

---

[1] S. Orlando 2015, pers. comm., 13 May

6 The effect of background pressure and angular location assessed by mass spectrometry

The investigations of the PLD process reported in the previous chapters started by focusing on the produced films. It continued with plasma plume imaging which allowed visualizing and understanding further the dynamics of the different emitting species before arriving at the substrate. In this chapter the investigation continues by focusing again on the plasma plume and using angle-resolved mass spectrometry measurements to gain an insight into the angular resolved plasma chemistry. It continues the work from *Jikun Chen* for $La_{0.6}Sr_{0.4}MnO_3$ [102] where the plasma plume properties were investigated at the plume central axis finding that positive metal oxygen species were the main product from the reactions with O_2 and that the oxidization probability was largely influenced by the stability of the metal oxygen ions as compared to the background gas molecule. In addition, it was found that the main oxygen contributor to the film is the background gas (except in vacuum) by using targets with ^{18}O isotope as a tracer. The aim now is to verify those results for this thesis' model system $La_{0.4}Ca_{0.6}MnO_3$, expand them to the entire plume angular range and gain an insight into the chemical reactions of the different species between themselves and the background gas before arrival at the substrate. Evidently with a focus on correlating the findings to the previous RBS and species resolved plasma imaging results.

6.1   Mass spectrometry of $La_{0.33}Ca_{0.66}MnO_3$

6.1.1   Verification of angular ionic counts as a film thickness indicator

Inherently mass spectrometry is an ion measuring instrument as it selects species based on their masses and charges (positive or negative). Neutrals can be measured, too, but they need to be subsequently ionised prior detection. Here, species dependant ionization probabilities and the varying kinetic energies increase the uncertainty of their quantitative measurement. Therefore only ionic species (positive and negative) have been investigated using mass spectrometry (MS).

The question that naturally arises when conducting angular MS ion measurements is: Are ionic species a good indicator for thickness? With this purpose a first verification of angular ionic counts was performed for three pressure regimes: Vacuum, $1x10^{-2}$mbar and $1x10^{-1}$mbar O_2. The laser fluence used was 2 J/cm^2 with a spot size of 1 x 1 mm and a target to MS distance of 40 mm.

Similar to the MS measurements in chapter 5, the total counts of selected ions for the ablated $La_{0.4}Ca_{0.6}MnO_3$ (i.e.: La^+, Ca^+, Mn^+, O^-, LaO^+, CaO^+ and MnO^+) were obtained for all energies and plotted angle-resolved for the different pressures. The results are shown in Fig.6.1a together with the film thickness results from RBS in Ar (Fig.6.1b). It is noteworthy that the irregularity in counts between 66-72° for vacuum probably originates from a discontinuity in fluence (~6.5%) caused by the mask switch between 66-72° where the profile is already rather flat. This was discussed in chapter 5 and will also be visible in the kinetic energy profiles.

Both, MS and RBS angular dependencies show a strong forward direction for vacuum and $1x10^{-2}$mbar, whereas at $1x10^{-1}$mbar the angular distribution is flat. In vacuum, the thickness is 4 and 3.7 times larger compared to $1x10^{-1}$mbar for MS and RBS, respectively. There is a good qualitative agreement between both types of measurements, plasma ions and film atoms. There are, however, also some quantitative differences. At angles above 60° all film thicknesses are similar, which is not the case for the MS measurements where only vacuum and $1x10^{-2}$mbar partially match. However, the most striking result is the higher counts at $1x10^{-2}$mbar O_2 compared to vacuum.
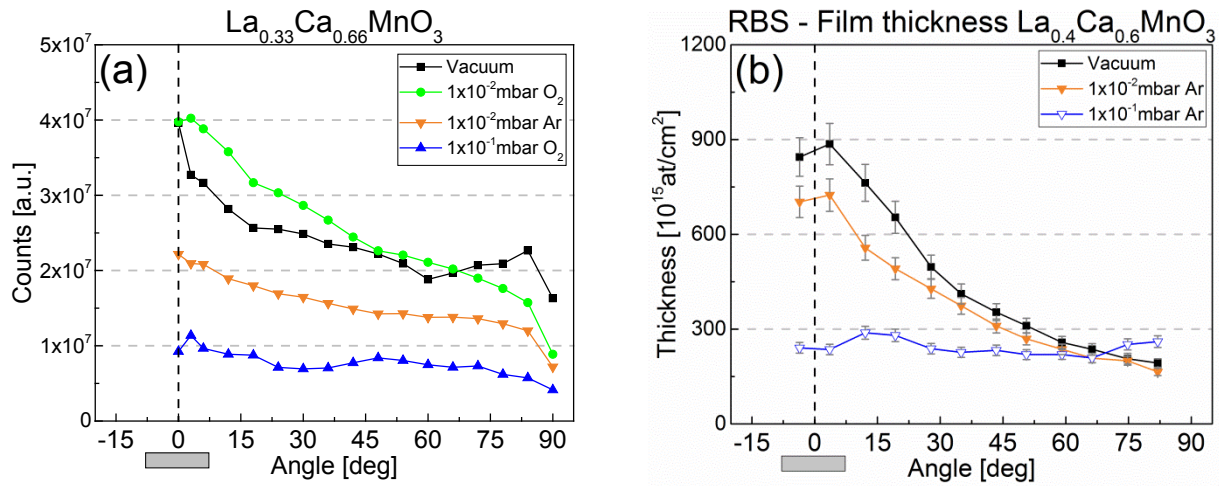
Fig.6.1. Angle-resolved ionic MS counts (a) and RBS film measurements (b) for different pressures. MS measurements counted the following species: La^+. Ca^+, Mn^+, O^-, LaO^+, Cao^+ and MnO^+.

This can be explained as follows, MS measurements were setup to count the following species: La^+, Ca^+, Mn^+, O^-, LaO^+, CaO^+ and MnO^+. The total counts plotted in Fig.6.1a are the total sum of all these species. If the results are plotted in terms of total cations (for clarity, cations refer solely to atomic cations while molecular cations are here defined as metal oxygen species) and total counts like in Fig.6.2 the source of such "count" increase at $1x10^{-2}$mbar O_2 has a clear cause: the additionally created metal oxygen species and O^-. This is precisely the objective of probing the plasma plume by MS, to understand the plasma chemical reactions prior to arrival at the substrate which in this case would have been invisible to a film based analysis.

In vacuum (Fig.6.2a) and $1x10^{-1}$mbar O_2 (Fig.6.2c) most counts come predominantly from the cations (small differences between cation and total counts). It is at $1x10^{-2}$mbar O_2 were the greatest increase is detected, with almost twice as many metal oxygen species and O^- (main contributor) than cations. If the plume is probed at the same pressure but with Ar as background gas (Fig.6.2d), the cations counts are still the same but metal oxygen species and mostly O^- are barely noticed. In this case vacuum has then higher total counts than $1x10^{-2}$mbar.

It is important to remark that Ar^+ and Ca^+ are likely to overlap in the MS signals causing an overestimation of the Ca^+ counts. Additional experiments were performed using $EuAlO_3$ as target in an Ar background and it was found that there is indeed Ar^+: at $1x10^{-2}$mbar it is close to 10% of other element signals, however, at $1x10^{-2}$mbar it is insignificant.
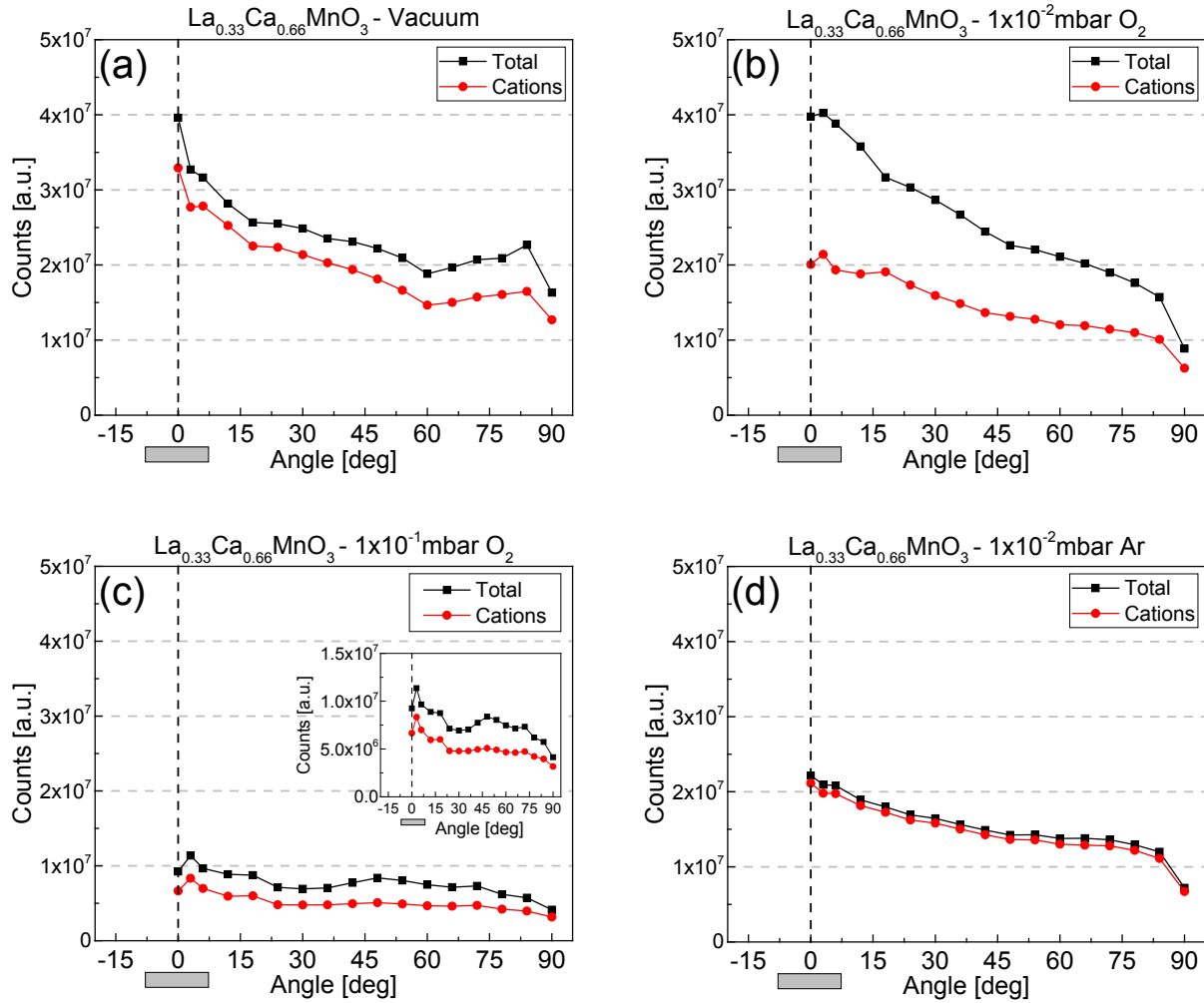
Fig.6.2. Angle-resolved ionic counts of all cations and also total counts for vacuum (a), 1×10^{-2}mbar O$_2$ (b), 1×10^{-1}mbar O$_2$ (c), and 1×10^{-2}mbar Ar (d).

6.1.2   Overview on potential plasma chemistry

Before going into detail with the different plume species and potential chemical reactions, an overview of the plasma chemistry possibilities is provided. It is divided in three areas. First, the potential plasma plume species (ions, neutrals an electrons) and possible states are described. Second, a list of potential states for the molecular O$_2$ background are also reported, as its interaction with the plume species will not be necessarily limited to the O$_2$ neutral state. Third a potential reaction set between plasma plume species and background gas states is shown.

Concerning the plume, it might contain the different target elemental species in a large variety of states. Some examples of which are shown in table 6.1. It is expected that apart from neutrals, a significant portion of the species will be ions (i.e.: ionized fractions of 0.2-0.5 have been reported for similar fluences with ns pulses but for metals [66]) and mainly in a positive state due to the electrons escaping after laser irradiation [59, 103]. In addition, some species will be in excited state, for instance the excited neutrals from the plasma plume imaging in chapter 4. Others might be generated from intra-plume reactions and/or collisions. Furthermore

the different species present in the plume will have wide-ranging and high kinetic energies, velocities, space distributions, and densities, already evidencing the complexity of this particular plasma chemistry.

Potential plume species	Detection technique (potential)
e^-	(Langmuir probe)
M	(MS neutrals)
M*	Plasma imaging
M^+	MS
$(M^+)^*$	(Plasma imaging)
MO	(MS neutrals)
MO*	Plasma imaging
MO^+	MS
$(MO^+)^*$	Plasma imaging
MO^-	(MS)
O	(MS neutrals)
O*	Plasma imaging
O^-	MS
O^+	(MS)

Table 6.1. Potential plume species, detected species and method of identification, and preferred method of detection in brackets for those not measured. Note: *M* stands for metallic species and * for excited state.

Alternatively the O_2 background will not be limited to molecular oxygen as during the plume expansion various fluxes of species will expand at different time frames (i.e.: electrons) or different sub-products from previous chemical reactions might take part in further reactions. A possible O_2 background reaction set is provided in table 6.2 (from [104, 105]). It is worth mentioning that those reported reactions have been elaborated in the context of standard gas-phase reactions unlike the fast expanding and dense PLD plasma which is more complex.

Potential oxygen background reactions			Threshold [eV]	
$O_2 + e^- + (O_2)$	$\rightarrow$	$O_2^- + (O_2)$	0.051 (three body attachment)	(1a)
$O_2 + e^-$	$\rightarrow$	$O(^3P) + O^-$	4.2 (dissociative attachment)	
$O_2 + e^-$	$\rightarrow$	$O(^3P) + O(^3P) + e^-$	5.58	
$O_2 + e^-$	$\rightarrow$	$O(^1D) + O(^3P) + e^-$	8.4	
$O_2 + e^-$	$\rightarrow$	$O_2^+ + e^- + e^-$	12.1	
$O(^3P) + e^-$	$\rightarrow$	$O^+ + e^- + e^-$		
$O(^3P) + e^-$	$\rightarrow$	$O(^1D) + e^-$		
$O(^1D) + O_2$	$\rightarrow$	$O(^3P) + O_2$		
$O(^1D) + O(^3P)$	$\rightarrow$	$O(^3P) + O(^3P)$		
$O(^1D) + e^-$	$\rightarrow$	$O^+ + e^- + e^-$		
$O + e^-$	$\rightarrow$	O^-		(1b)
$O^- + e^-$	$\rightarrow$	$O(^3P) + e^- + e^-$		
$O^- + O_2^+$	$\rightarrow$	$O(^3P) + O_2$		
$O^- + O^+$	$\rightarrow$	$O(^3P) + O(^3P)$		

Table 6.2. Potential reactions for background oxygen with some threshold energy values.

Interestingly, the ablation of $La_{0.4}Ca_{0.6}MnO_3$ in this same chamber has shown electron energies ~0.7-1.1 eV [106] (Langmuir probe measurements) which fulfil the reported energy needs for electron attachment to molecular oxygen of reaction 1a (sub eV [107]) or to atomic oxygen (1b) but not those for O_2 dissociative attachment ~4.2 eV [105].

At this point a range of possible chemical reactions between the plume species and background species can be drafted (table 6.3). Evidently given the broad range of possibilities as well as the complexity of the plume dynamics the objective of listing the complete set of reaction paths is not possible within the framework of this thesis. The reported list is therefore focused on the most well studied reactions to show the breadth of what might be happening. A few selected examples which have been well studied in the literature will be discussed in more detail.

Potential reactions with the background gas			
$M^+ + O_2$	$\rightarrow$	$MO^+ + O$	(2a)
$M^+ + O_2$	$\rightarrow$	MO_2^+	(2b)
$MO^+ + O_2$	$\rightarrow$	$MO_2^+ + O$	(2c)
$M^+ + O$	$\rightarrow$	MO^+	(2d)
$M + O$	$\rightarrow$	MO	(2e)
$M^+ + O^-$	$\rightarrow$	MO	(2f)
$(M^+)^* + O_2$	$\rightarrow$	$MO^+ + O$	(2g)

Table 6.3. Potential reactions of plume species with the O_2 background gas.

O-atom transfer reaction 2a is a usual reaction channel observed for transition metals and is strongly dependant on the O-atom affinity [104], with $La^+ = 8.93$ eV $>$ $Ti^+ = 6.88$eV $>$ Ca+ $= 3.57$ eV $>$ $Mn^+ = 2.95$ eV [108, 109]. Interestingly no reaction products were observed for Mn^+ in any case [104]. Reaction path 2b, with the exclusive addition of O_2, was observed for many transition metals but not for the ones related to this thesis: La^+, Ti^+ nor Mn^+ (Ca^+ was not included in that particular study). 2c is an additional O-atom abstraction, but is only observed with ions such as Nb^+, Ta^+, Mo^+ and W^+ (for the experimental conditions used in [104]).

In particular no secondary reactions are observed for LaO^+. Neither LaO_2^+ nor LaO_3^+ were detected as secondary products [110]. Given these boundary conditions and the already stated complexity of the process, it was decided to focus the research mostly on the MO^+ species as it seems the most likely pathway. However, it is understood that there are many other possibilities.

6.1.3 Analysis of plasma species

The results for the different pressures of the measured anions and cations are shown in Fig.6.3 while metal oxygen species are shown in Fig.6.5. Already in vacuum (Fig.6.3a) the La^+ counts are considerably higher than Ca^+ and Mn^+, even though the content of La^+ in the target is the lowest (this was also detected in the MS measurements using the larger laser spot). This seems either a complementary imbalance in neutrals state which goes unnoticed as these were not measured or, most likely, the result of the elemental ionization energies. The different ionization energies are shown in table 6.4 in increasing order, where La has the lowest ionization energy (5.5769 eV) and Mn the highest (7.4340 eV). This could explain why although Mn is the element with the highest proportion (with the exception of O) La shows the highest ionic counts. In addition the high mass resolution of the MS measurements (~0.2 amu but up to 0.01 amu if selected) would not count the isotopes outside the selected mass for each element. This would not affect La and Mn measurements but slightly affect Ca (96.941% abundance of A = 39.96 amu [77]) and mainly Ti (73.72% abundance of A = 47.95 amu [77]) which will be reported later for $CaTiO_3$. A list of isotopes of the relevant elements, their abundances, and the selected mass for the MS (in bold) is shown in table 6.5 for reference. In any case this should be kept in mind when analysing the results keeping the focus on the qualitative changes.

In vacuum there are counts of O^- which must originate from the target and, in contrast to the other cations, are mostly detected at the centre of the plume (0-40°). When the pressure is raised to $1x10^{-2}$mbar O_2 three important changes are detected (Fig.6.3b). First there is a strong increase in O^- counts throughout the entire angular range with the central region of the plume showing the highest increase. The integrated area is 8.5 times the vacuum case (originating from the background gas). Second there is a strong drop in La^+ counts to numbers similar to Mn^+ which could evidence a transformation of La^+ to a metal oxygen species which will be explored later. Third, in contrast to La^+, Mn^+ and Ca^+ barely change.

Element	Ionization energy [eV]
La	5.5769
Ca	6.1132
Ti	6.8281
Mn	7.4340
O	13.6181

Table 6.4. Ionization energies in increasing order for La, Ca, Ti, Mn, and O from [77].

Element	Isotope	Mass [amu]	Abundance [%]
O	^{16}O	**15.99491461957**	**99.757**
O	^{17}O	16.9991317565	0.038
O	^{18}O	17.9991596129	0.205
Ca	^{40}Ca	**39.962590863**	**96.941**
Ca	^{42}Ca	41.95861783	0.647
Ca	^{43}Ca	42.95876644	0.135
Ca	^{44}Ca	43.9554816	2.086
Ca	^{45}Ca	44.9561864	
Ca	^{46}Ca	45.9536890	0.004
Ca	^{47}Ca	46.9545424	
Ca	^{48}Ca	47.95252277	0.187
Ti	^{46}Ti	45.9526277	8.25
Ti	^{47}Ti	46.9517588	7.44
Ti	^{48}Ti	**47.9479420**	**73.72**
Ti	^{49}Ti	48.9478657	5.41
Ti	^{50}Ti	49.9447869	5.18
Mn	^{54}Mn	53.9403576	
Mn	^{55}Mn	**54.9380439**	**100**
La	^{138}La	137.907115	0.090
La	^{139}La	**138.9063563**	**99.910**

Table 6.5. List of isotopes and their abundances for O, Ca, Ti, Mn, and La from [77]. The isotopes with the highest abundances are highlighted in bold and were used in MS measurements.

Concerning oxygen, It is known that the film oxygen content partly originates from the target itself, the background gas or even the substrate [102]. With the latter being the smaller source for this material and the background gas the major contributor at pressures ≥1×10^{-2}mbar O_2. It is estimated that ~50-100% originated from the background gas with the largest values taking place at the highest pressures (i.e.: 2×10^{-1}mbar O_2). A value which would match the proportions detected when measuring O^-.

The 1×10^{-1}mbar Ar results are remarkably different to O_2 (see Fig.6.3d). There is very little O^- as expected due to the use of Ar (three times less O^- than in vacuum), but La^+ also decreases

to similar levels as for 1×10^{-2}mbar O_2. Finally at 1×10^{-1} mbar O_2, Ca^+ and Mn^+ decrease slightly, but in contrast La^+ is not detected at all (additional measurements at 1×10^{-1}mbar showed that this is not the case in Ar).
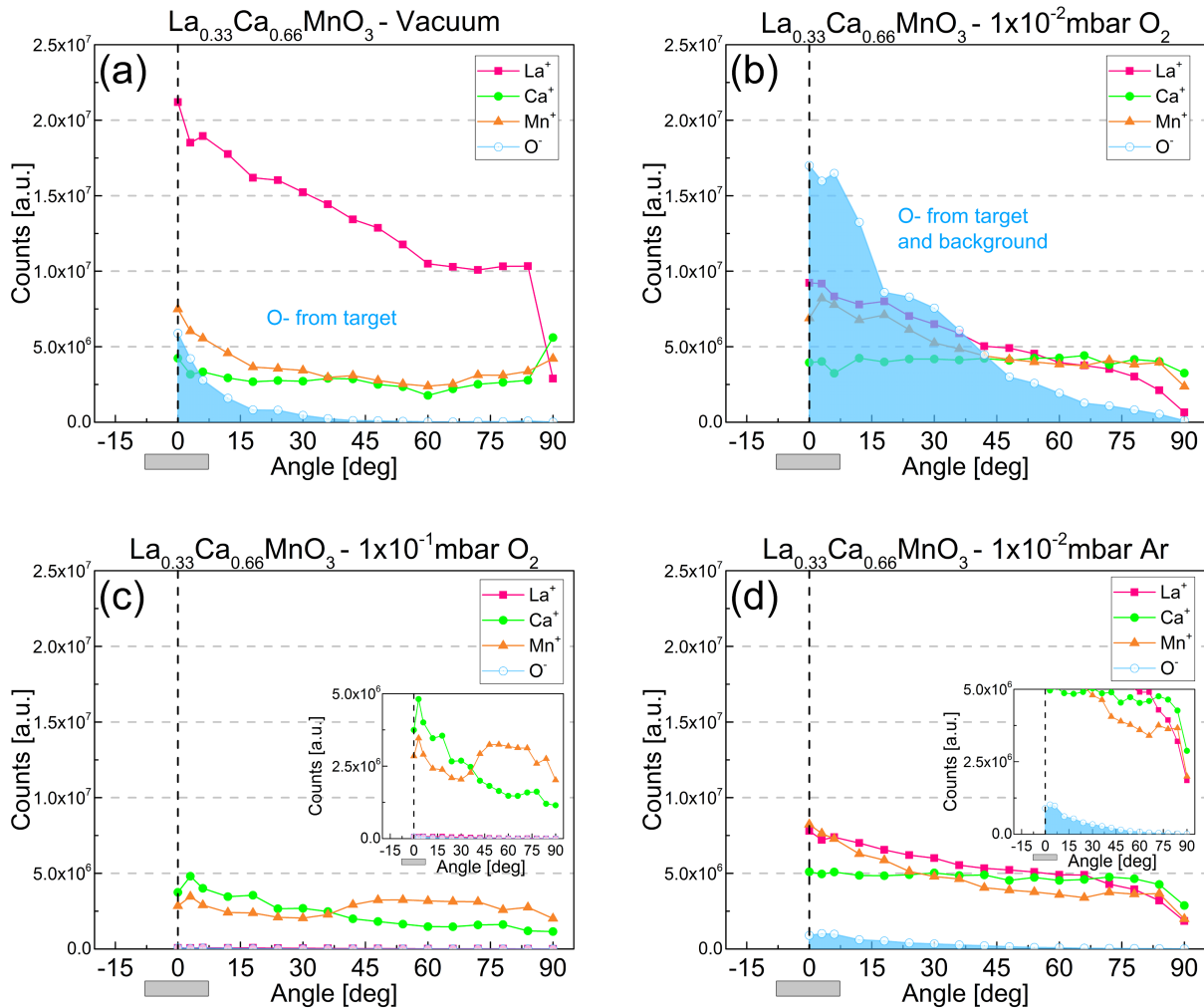
Fig.6.3. Angle-resolved detected counts of La^+, Ca^+, Mn^+, and O^- for vacuum (a), 1×10^{-2}mbar O_2 (b), 1×10^{-1}mbar O_2 (c), and 1×10^{-2}mbar Ar (d).

At this point it is already clear that there are dissimilar behaviours between cations when a background gas is added (mainly La^+ vs. Ca^+ and Mn^+). Not only mass wise, but also chemically as is evidenced when using an O_2 background gas. This is in good agreement with Chen *et al.* [67] where it was found that with increasing O_2 pressure species with a large dissociation energy (>O_2 dissociation energy i.e. 5.15 eV) are preferentially formed and that at such pressures the background oxygen is the main contributor to the film oxygen composition. Fig.6.4 has been added to visualize the dependency between dissociation energies and detected metal oxygen species (with Ti and La highlighted with vertical arrows).
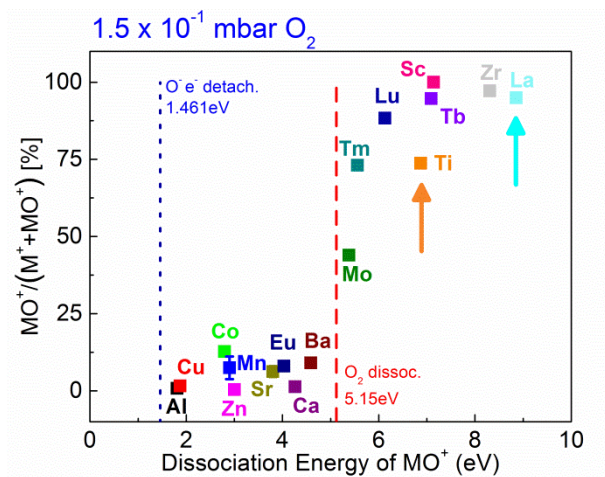
Fig.6.4. From [1] showing the ratio of MO$^+$/(M$^+$ + MO$^+$) vs. dissociation energy of MO$^+$ species as determined at 1.5x 10^{-1}mbar O$_2$ The MO$^+$/(M$^+$ +MO$^+$) value for a metallic element is the mean value obtained from different oxide targets with the corresponding standard derivation. The dashed red line represents the dissociation energy of (O$_2$) = 5.15 eV [111] while the dashed blue line the O$^-$ electron detachment energy of 1.461 eV [112].

A closer look at the metal oxygen species is provided in Fig.6.5 where vacuum (Fig.6.5a) shows a noticeable amount of LaO$^+$ which increases with angular location. There are no CaO$^+$ nor MnO$^+$ species detected and this is the case for all pressure regimes.
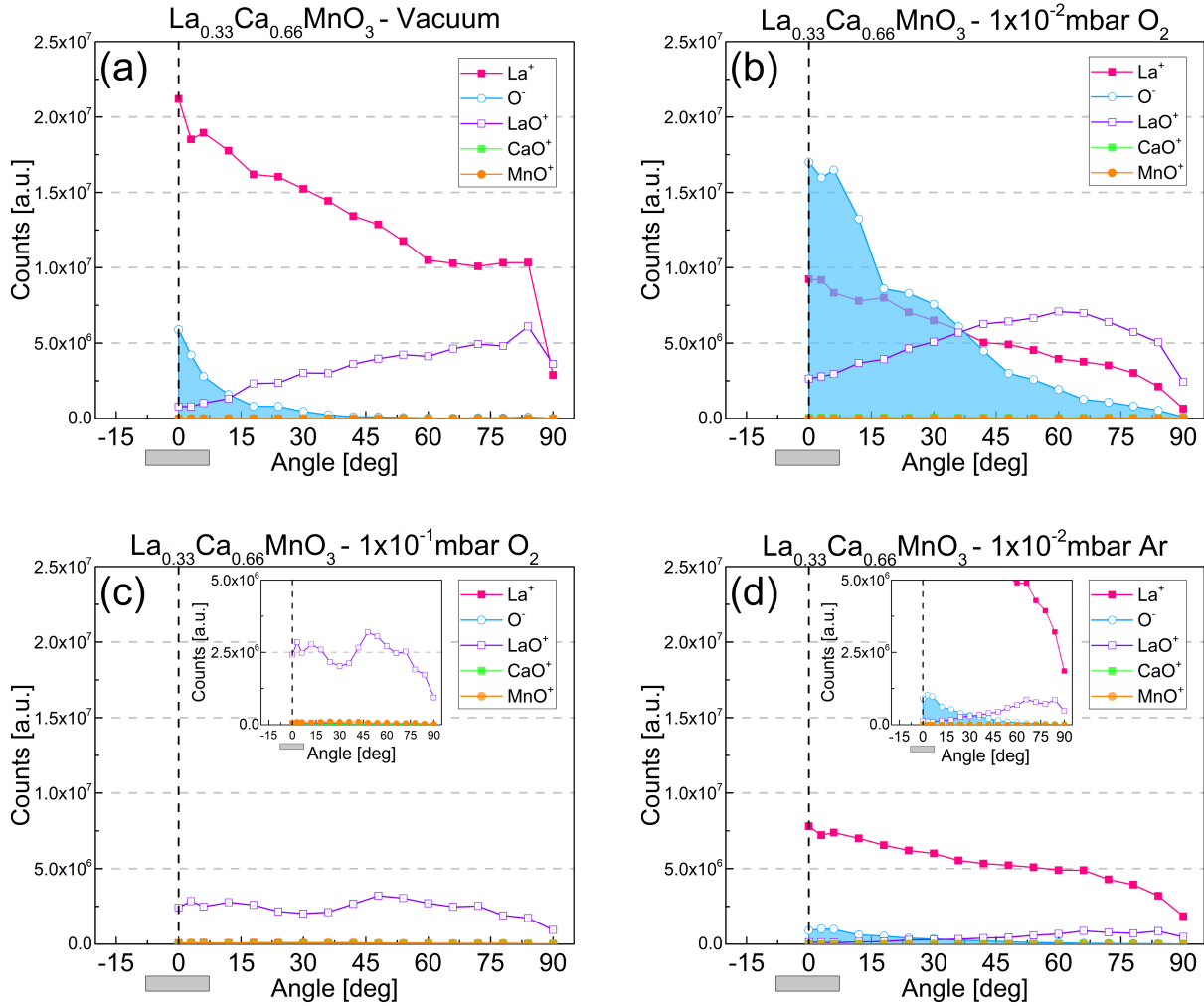
Fig.6.5. Angle-resolved detected counts of La$^+$, O$^-$, LaO$^+$, CaO$^+$, and MnO$^+$ for vacuum (a), 1x10^{-2}mbar O$_2$ (b), 1x10^{-1}mbar O$_2$ (c), and 1x10^{-2}mbar Ar (d).

At 1x10^{-2}mbar O$_2$ (Fig.6.5b) the aforementioned increase in O$^-$ and LaO$^+$ and decrease in La$^+$ is detected. The most relevant result is, however, that there is an increase in LaO$^+$ (50% more than in vacuum) probably formed through one of the reactions paths described in table 6.3 between La and O species (table 6.2). This could explain a reduction in La$^+$ (~3% of the total counts in vacuum), but not the strong reduction detected (60%). In contrast at 1x10^{-2}mbar Ar (Fig.6.5d), although there is a decrease in La$^+$ to similar values as in O$_2$, there are hardly any traces of LaO$^+$ species. A reaction like 2f could be taking place creating neutral LaO, although given the low counts of O$^-$ in this Ar background it is more likely to be a conversion of La$^+$ to neutral La. In any case this represents a reduction of LaO$^+$ species compared to vacuum and suggests that an Ar environment strongly diminishes the amounts of metal oxygen species due to the lack of an oxidizing reagent from the background.

At 1x10^{-1}mbar O$_2$ (Fig.6.5c) although it seems that there is a reduction of LaO$^+$ species compared to the other pressures, that is not exactly the case. If its percentage with respect to

the film's thickness is taken into account there is a clear increase in LaO^+ contribution to "the film" (Fig.6.6) with an increase of close to 30% vs. the original ~8% (mostly at 0-30°).

This increase in LaO^+ formation at this pressure was seen by selective plasma plume imaging (chapter 4) where the compression of the background gas by the expanding plume would cause an O_2 rich volume just above the substrate holder which would enhance the formation of LaO (and also a subsequent rebound of the plume). For the MS case the rebound is also present and could explain the measured relative increase in LaO^+. The MS orifice cap has a flat face with similar diameter as the substrate holder used in the plasma imaging experiments. Nonetheless it is important to mention that during the angular probing this flat face is always kept normal to the angle being probed and the rebound was also detected when probing at high angles (not reported in this work but experimentally verified). This means that the physical geometry of the MS is modifying the probed plasma at each measured angle for pressures above 1×10^{-1}mbar.
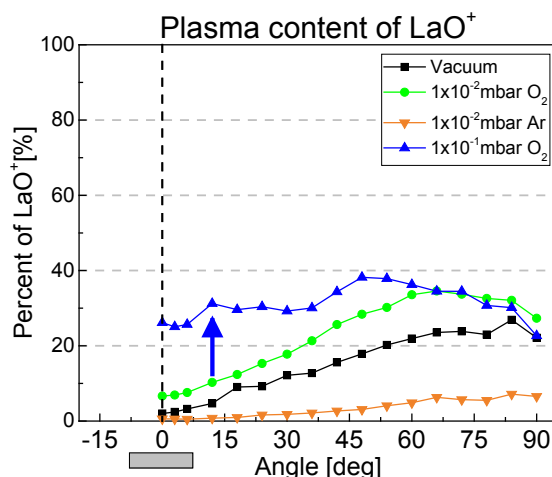
Fig.6.6. Angle-resolved LaO^+ percentage with respect to total counts for vacuum, 1×10^{-2}mbar O_2. 1×10^{-1}mbar O_2 and 1×10^{-2}mbar Ar.

6.1.4 Angle resolved kinetic energies of ionic species

Apart from ion counts the MS measurements also provide the kinetic energy profiles for the different measured species. For simplicity and following the same procedure as in chapter 5 the kinetic energies are reported as average and maximum kinetic energies.

The average kinetic energies of the different species are shown in Fig.6.7 (except for CaO^+ and MnO^+ due to the limited number of counts). The kinetic energy profiles are strongly forward oriented for all cations and pressures except for 1×10^{-1}mbar O_2. In vacuum (Fig.6.6a) Mn^+ shows the highest average energies at the centre of the plume (~100eV), followed closely by La^+ (~90eV), and with Ca^+ at much lower values (<50eV). While O^- and LaO^+ show much lower energies (>10eV) and no preferred directionality, evidencing a different arrival mechanism. Raising the pressure causes Ca^+ and Mn^+ to experience a reduction in average kinetic

energies: ~19% for Ca$^+$ and ~18% for Mn$^+$ in O$_2$ and ~30% and ~20% in Ar respectively (calculated by averaging the changes in the 0-30° region). While surprisingly the average kinetic energy increases for La$^+$ in O$_2$ background (~35%) or remains unchanged in Ar (~2%). This general reduction of the kinetic energies of light species (Ca$^+$ and Mn$^+$) while the heavier La$^+$ is not affected matches very well with the RBS measurements and the plasma imaging measurements reported in the previous chapters. At such pressure the MFP is shorter than the target to MS orifice distance (~20 mm vs. 40 mm) and a small number of interactions are expected which would affect the lighter species stronger than the heavier La$^+$ (i.e.: Mn$^+$ and Ca$^+$). However, this increase in average velocity of La$^+$ is remarkable. It is noteworthy that these are the reported average velocities, not the maximum velocities.
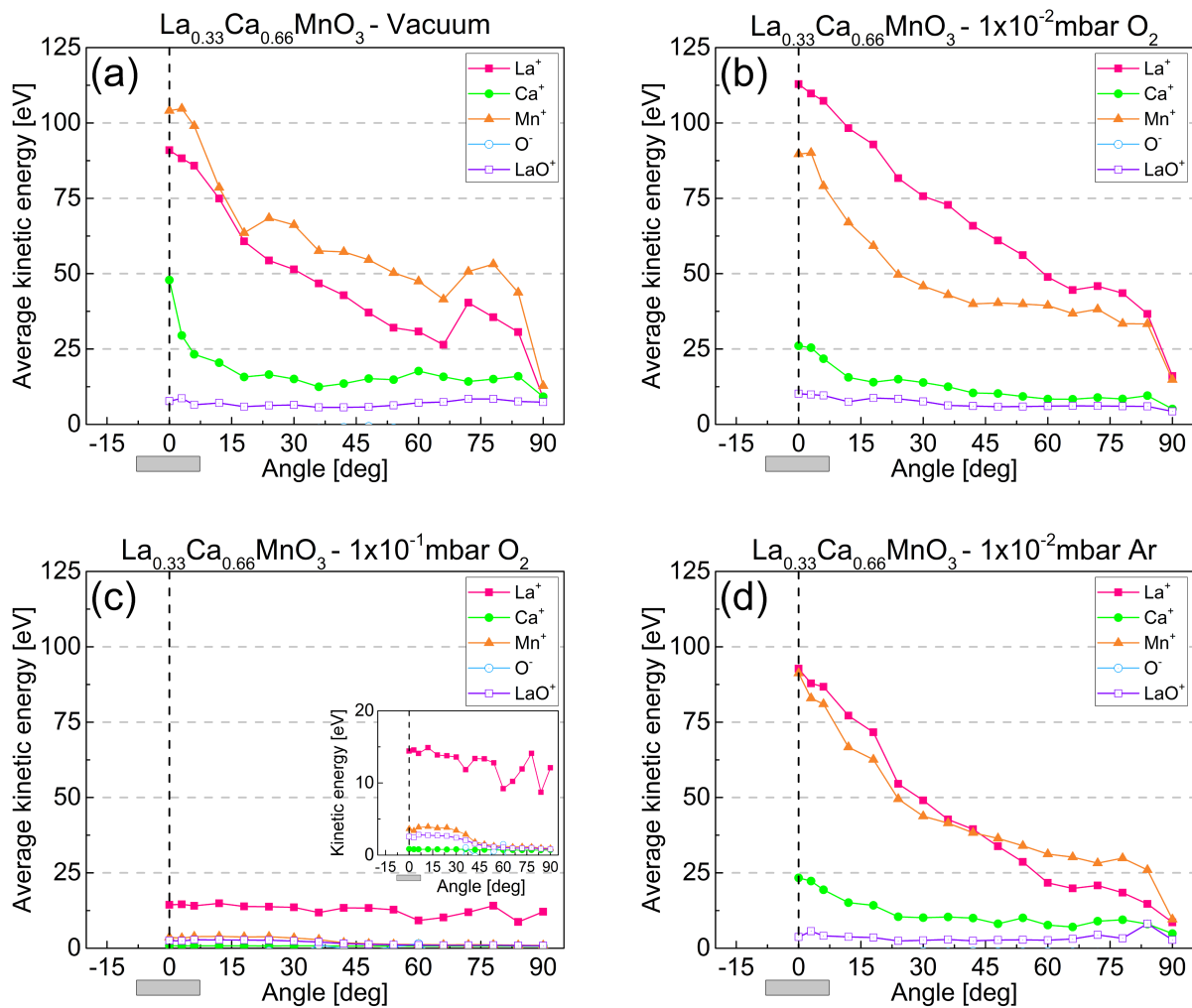
Fig.6.7. Angle-resolved average kinetic energies of the different ionic species for vacuum (a), 1x10^{-2}mbar O$_2$ (b), 1x10^{-1}mbar O$_2$ (c), and 1x10^{-2}mbar Ar (d).

In contrast at 1x10^{-1}mbar O$_2$ (Fig.6.7c), the kinetic energies vary very little with angular location and La$^+$ presents higher kinetic energies (although the counts are very low due to the decrease in thickness). Both results are expected as at this pressure the plume is confined with all species traveling together and expands spherically in all directions (chapter 4). This would

translate into low kinetic energies with small angular variations in which the species with the highest mass would show the highest kinetic energies (La+). Although the kinetic energy of La$^+$ is 3.8 times higher than Mn$^+$ (mass ratio of 2.5) and 19 times higher than Ca$^+$ (mass ratio of 3.5).

Concerning the maximum detected energies, the results are shown in Fig.6.8 for the different species independently and their evolution with pressure. Similarly to the average kinetic energies the angular profiles show the characteristic forward direction for the cations. However, the values are 5 times higher than the average values, evidencing energy profiles with very long ranges (especially for La$^+$ Fig.6.8a and Fig.6.9a). For the particular case of La$^+$, the maximum kinetic energy at the centre of the plume is close to 500 eV, higher than the 350 eV from Mn$^+$ (Fig.6.8c) and the 250eV for Ca$^+$ (Fig.6.8b). This clear increase in kinetic energy with mass was also reported in the plasma imaging chapter where the selective imaging showed that in vacuum the neutral species presented the following kinetic energies: ~227eV for La I, ~151eV for Mn I, ~71eV for O I. Both the MS kinetic energies of Mn$^+$ and La$^+$ are close to 2.25 times the estimated energies from the recorded velocities of the excited neutrals (plasma imaging). It was expected that the velocity of the ions would be higher than those of the neutrals [41, 83] as was also seen for Ag and Ag$^+$ (Fig.4.8). Although plasma imaging will still carry its intrinsic limitation: only the excited species are seen.

There is a similar pattern between mass and kinetic energies detected with both measuring approaches (selective plasma imaging and MS), the underlying reason of this behaviour will be discussed later in the chapter.
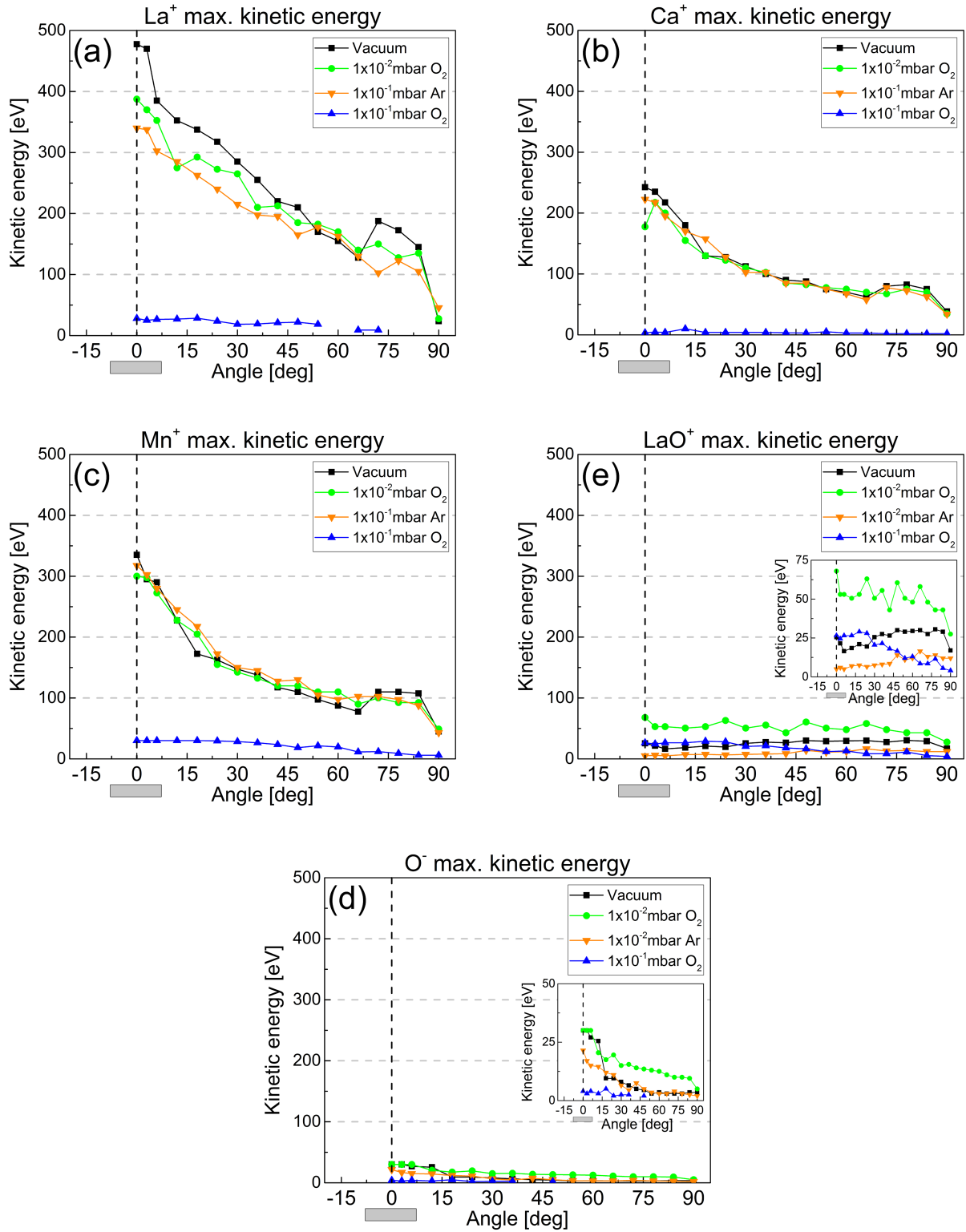
Fig.6.8. Angle-resolved maximum kinetic energies for the two different laser spot sizes of La$^+$(a), Ca$^+$ (b), Mn$^+$(c), O$^-$ (d) and LaO$^+$(e).

In terms of the evolution of the energies with pressure, La$^+$ shows the strongest change in maximum kinetic energies from vacuum to 1x10^{-2}mbar. In particular in Ar background where other cations barely suffer any changes with pressure. A very surprising outcome since at 1x10^{-2}mbar O$_2$ the average kinetic energy of La$^+$ has increased. It is relevant to point out that

this decrease occurs particularly at the centre of the plasma plume (<30°). In contrast Mn^+ and Ca^+ showed a reduction in average kinetic energy at such pressures, but do not have a reduction in maximum energies. This could be interpreted by the plasma plume imaging results as it was shown that ions and neutrals share similar expansion dynamics (Fig.4.8). More specifically by the imaged plume splitting of the lighter elements. A separation of the plasma plume where some species arrive collision-less or with very little collisions at the MS (fast component) while others undergo scattering with the background gas (slow component). Species-selective imaging showed that despite La I species having the highest energies, it expands the slowest (after LaO) travelling at ~18'000 m/s behind Mn I (~23'000 m/s) and O I (~30'000 m/s). The plume splitting of the lighter species happens ahead of the La expansion and might cause the La species to collide with the slow components of the plume splitted species. In such a case the La^+ species with the highest energies would be the ones to break through the slow-moving components, reducing their energies slightly and clearing the expansion path for the slower La species. To verify this, the kinetic energy profiles of the cations for the different pressures at the centre of the plume are shown in Fig.6.9. Both Ca^+ (Fig.6.9b) and Mn^+ (Fig.6.9c) maintain some of the counts at the maximum energies (Ca^+ ~250 eV and Mn^+ ~350eV), the counts in the intermediate energy region increase (50-150 eV for Ca^+ and 75-200 eV for Mn^+) and an increase at very low energies is seen (<10 eV), while La^+ (Fig.6.9a), which shows very large ranges, experiences a general disappearance of the counts with high energies and a reduction of low energy ions (probably recombining with oxygen). These would match well with the recorded plume splitting and the interaction of fluxes. Interestingly both Ca^+ and Mn^+ have marked stops in counts at high energies (~250 and ~350 eV respectively), while La^+ shows a gradual decrease.

At the highest pressure of 1×10^{-1} mbar (Fig.6.8) all the maximum kinetic energies are drastically reduced to values very similar to the average energies. The kinetic energy profiles do not present long ranges anymore and are compacted into a slow expanding plume where all species travel together as was seen in the time resolved plasma plume images.

It is noteworthy that the particular stop of counts at high energies also takes place for the different pressures (previously mentioned for Fig.5.13). The lower mass elements present abrupt stops (Mn^+ and Ca^+) while the higher mass element La^+ presents gradual decays. This seems to be related to the intra-plume collisions and elemental masses and is discussed in more detail in (6.2.1).
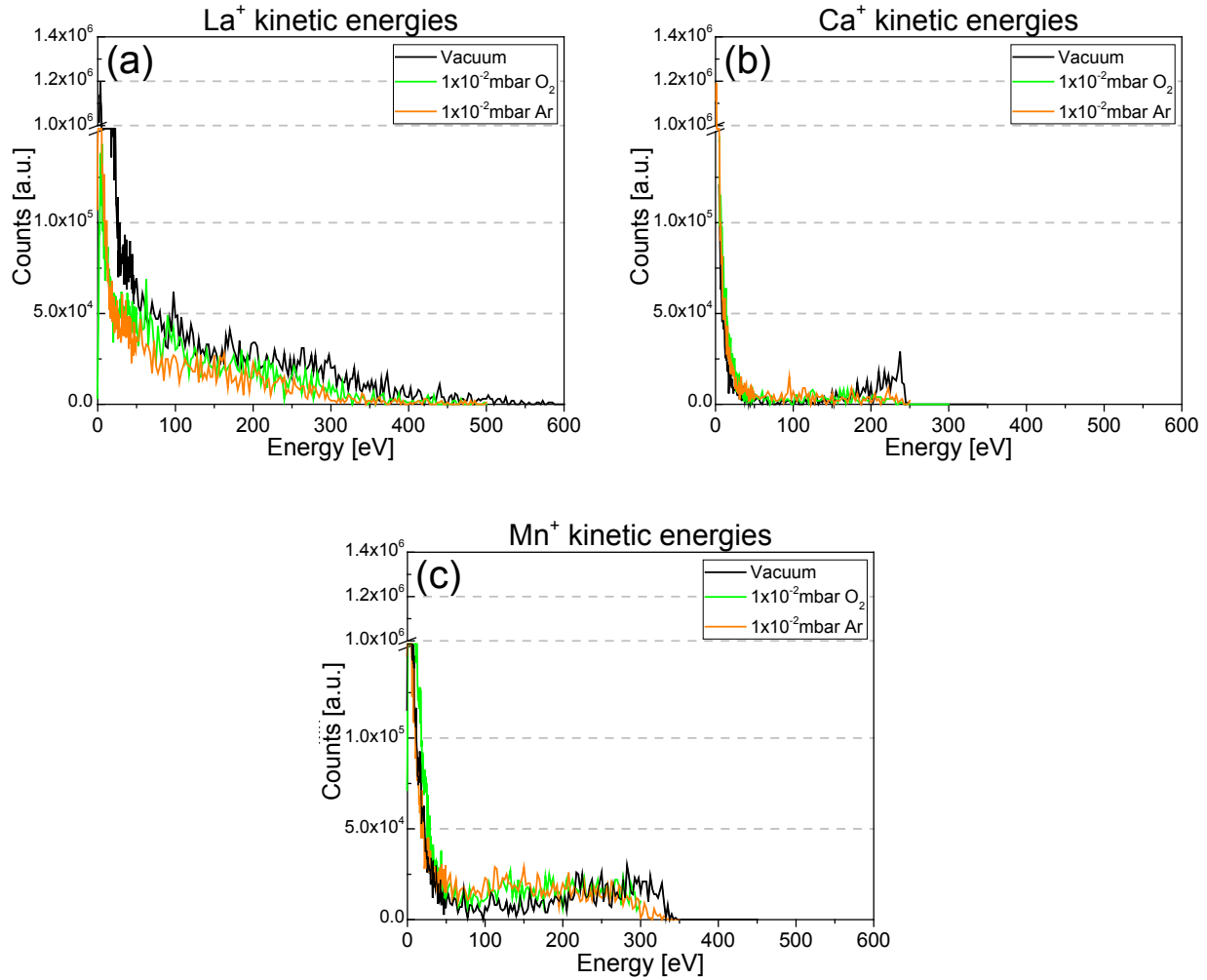
Fig.6.9. Kinetic energy profiles for different pressures of La^+ (a), Ca^+ (b) and Mn^+ (c).

6.1.5 Conclusions for $La_{0.33}Ca_{0.66}MnO_3$

In summary, angle resolved MS measurements are a complimentary tool to species selective plasma imaging for plasma analysis and allow a better understanding of the chemical reactions taking place. Results from imaging were corroborated by MS. While the main finding was that an O_2 background is an important source of oxygen for the metal oxygen species and probably for the film and that LaO^+ is preferentially formed or more stable compared to CaO^+ and MnO^+, which is in agreement with the findings from Chen *et al.* [67].

The next natural step is to validate the presented findings for an additional perovskite material and to verify if these results are extendable to additional PLD materials. With this aim the following sections of the chapter focus on $CaTiO_3$. A material already used in chapter 3 in which the masses of the participating elements are very similar ($A_{Ca} = 40$ and $A_{Ti} = 47.9$) but the dissociations energies are not ($CaO^+ = 4.768$ eV and $TiO^+ = 6.768$ eV [111]).

6.2   Mass spectrometry of CaTiO$_3$

The same angular experiments were carried out for CaTiO$_3$ with the same fluence (2 J/cm^2), spot geometry (1 x 1 mm), and target to MS distance (40 mm). The integrated counts of the measured species plotted in Fig.6.10 show similar trends as observed for La$_{0.33}$Ca$_{0.66}$MnO$_3$: A forward oriented deposition at all pressures except 1x10^{-1}mbar O$_2$. The latter is not as constant as for La$_{0.33}$Ca$_{0.66}$MnO$_3$ and shows still a slight forward character in agreement with the RBS film thickness measurements (see Fig.6.10c). As for La$_{0.33}$Ca$_{0.66}$MnO$_3$, 1x10^{-2}mbar O$_2$ shows higher ion counts than in vacuum which is contrary to the film thickness measurements (RBS) and was explained before for La$_{0.33}$Ca$_{0.66}$MnO$_3$ by the increase in metal oxygen species and mostly O$^-$ counts at such background pressure. Although this is not the case for CaTiO$_3$ as will be seen in the following paragraph. Interestingly, all four different pressures have matching total counts at high angles (>60°) which is in good agreement with the film thickness measurements (Fig.6.10c) which was not the case for La$_{0.33}$Ca$_{0.66}$MnO$_3$ but the reason is not yet clear. These are different elements with different ionization energies and the formation of neutrals also needs to be considered to clearly asses it.
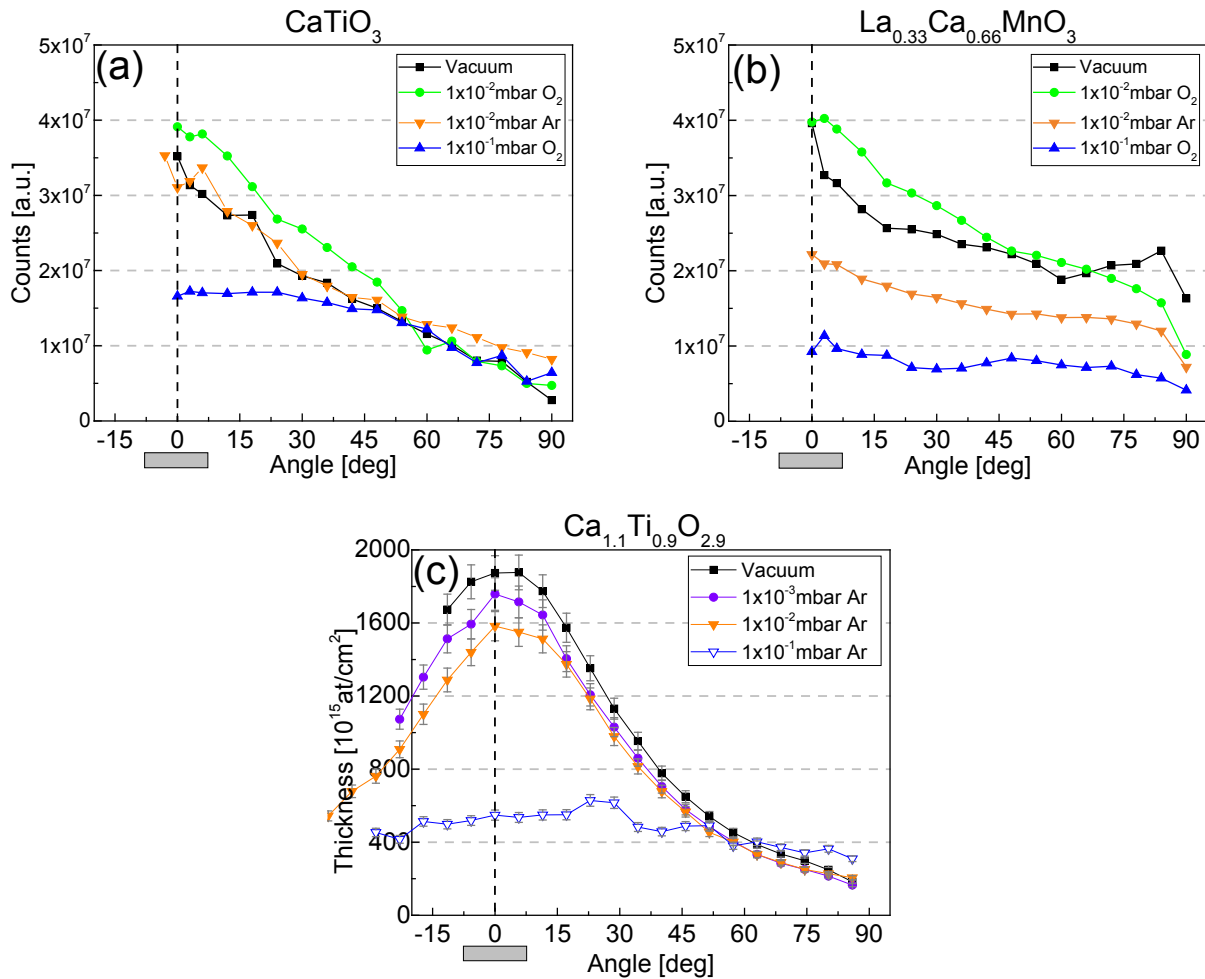
Fig.6.10. Angle-resolved ionic MS counts for CaTiO$_3$ (a), La$_{0.33}$Ca$_{0.66}$MnO$_3$ (b) and RBS film measurements of CaTiO$_3$ (c) for different pressures. MS measurements counted the following species: La$^+$, Ca$^+$, Mn$^+$, Ti$^+$, O$^-$, LaO$^+$, CaO$^+$, MnO$^+$ and TiO$^+$.

A comparison between the total counts and cation counts is presented in Fig.6.11 to evaluate the rate of metal oxygen species and O^- (similar to $La_{0.33}Ca_{0.66}MnO_3$). The results show that at 1×10^{-2}mbar O_2 the increase in counts compared to vacuum does not originate from metal oxygen species or O^- as their contribution to the total signal is very low. Thus the increase in counts originates from the predominant cations and more specifically due to the increase in detected Ca^+ counts (Fig.6.17ab). This behaviour is rather surprising as the counts of Ti^+ do not change while for $La_{0.33}Ca_{0.66}MnO_3$, La^+ experiences a strong drop in counts. A possible reason could be that the reduction in kinetic energies at such pressure diminishes the rebound in vacuum as the species impinge with lower velocities on the holder (noticed by plasma imaging) or that complimentary changes take place in the non-measured neutrals, but the explanation for the drop in La^+ would still remain unclear.
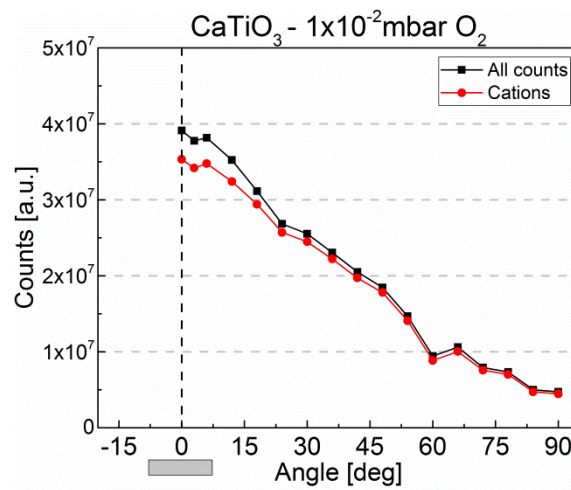
Fig.6.11. Angle-resolved ionic counts of all cations and also total counts for 1 $\times 10^{-2}$mbar O_2

6.2.1   Angle resolved kinetic energies of ionic species

The kinetic energy profiles are very similar in shape and values for both cations in vacuum. Ca^+ reaches a maximum energy of ~145eV and Ti^+ ~165eV (see Fig.6.12). In both cases there is a marked stop in maximum energies (similar to Ca^+ and Mn^+ in $La_{0.33}Ca_{0.66}MnO_3$ Fig.6.9). It is interesting that for Ca^+ in $CaTiO_3$ a lower maximum energy is attained than for $La_{0.33}Ca_{0.66}MnO_3$ where it was ~250eV for the same experimental conditions. A possible explanation could be different laser absorption properties of the material, which will be explored in more detail in the following pages.

At 1×10^{-2}mbar there is no major change in both Ca^+ and Ti^+ profiles compared to vacuum with the exception of an increased peak at very low energies. However, with increasing pressure their behaviours differ. Although both are compacted to the slow expanding plume with all species combined (low energies <10eV), the Ca^+ counts are kept and increase to higher counts while Ti^+ is considerably reduced. This is already an indication of a different behaviour of Ti

when interacting with the background gas as will be seen in the metal oxygen species section (6.2.4).
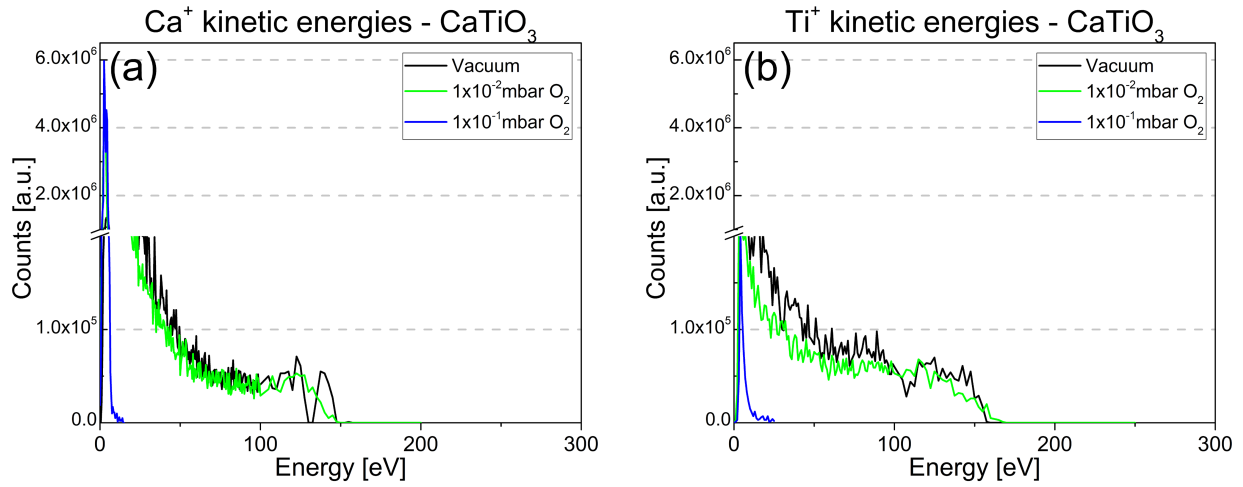
Fig.6.12. Kinetic energy profiles for different pressures of Ca$^+$ (a) and Ti$^+$ (b).

The average kinetic energies of the different species (Fig.6.13a) show the overall higher kinetic energy for Ti$^+$ with its highest values at ~48 eV at the centre of the plasma plume. Ca$^+$ also shows its highest energies at the centre with values of ~28 eV. In contrast O$^-$ is only detected at such an angular range of high kinetic energies but with values of ~6 eV. With increasing pressure (Fig.6.13b), the values for Ti$^+$ change very little at the centre of the plume but are reduced at high angles (from 25 eV to 15-20 eV). Differently, Ca$^+$ evidences more the interactions with the O$_2$ background reducing its average kinetic energies at the centre and also lateral sides of the plume reaching values below 10 eV. This matches the same results for La$_{0.33}$Ca$_{0.66}$MnO$_3$, where the lightest element Ca$^+$ is consistently the most affected cation with the O$_2$ background gas. The MFP (from table 3.1) at 1x10^{-2}mbar Ar for Ca is ~15 mm (atomic radius of 180 pm) and for Ti ~21 mm (atomic radius of 140 pm). The collision probability for Ca$^+$ is therefore higher than for Ti$^+$.
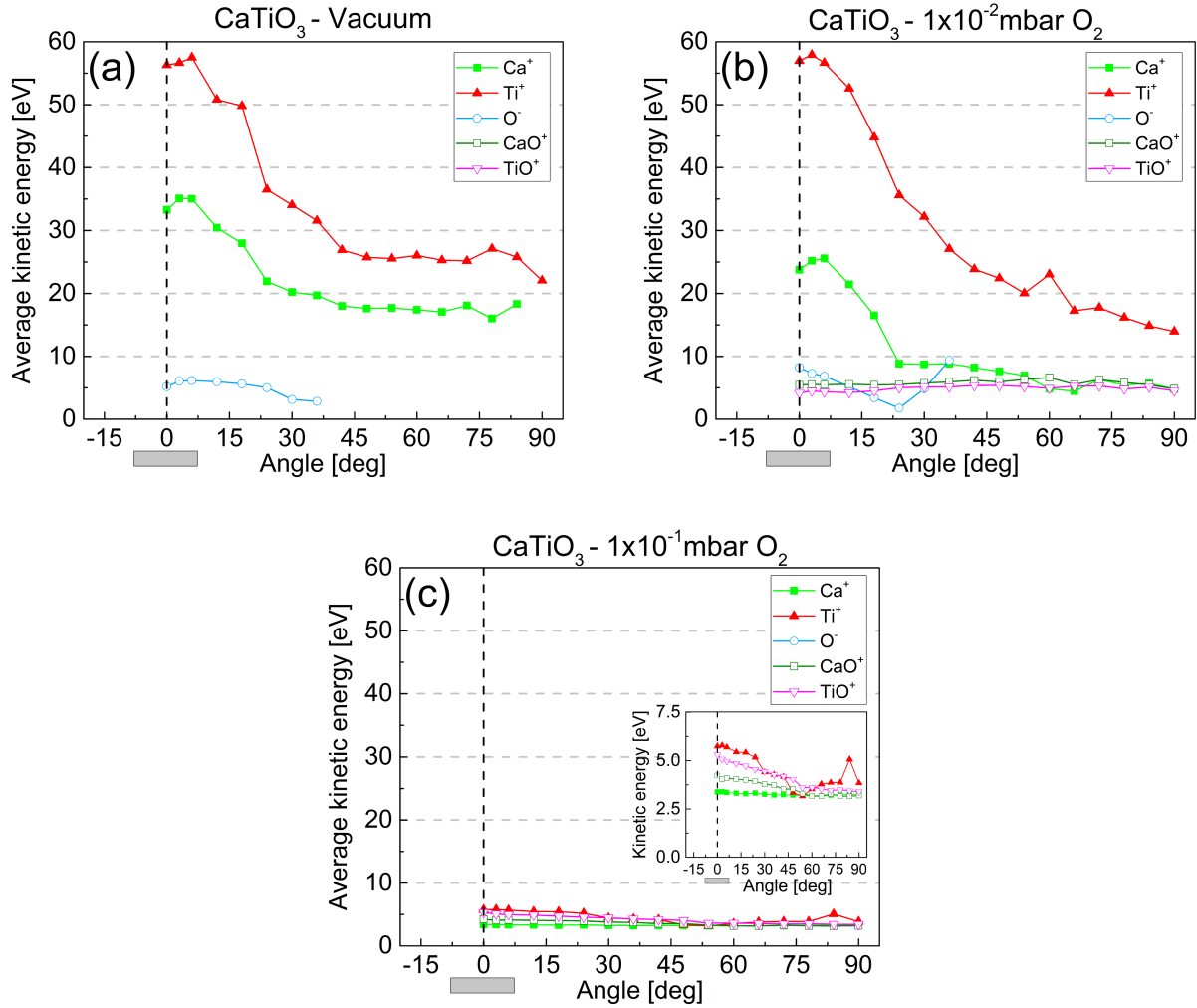
Fig.6.13. Average kinetic energy profiles of Ca^+, Ti^+, O^-, CaO^+, and TiO^+ for vacuum (a), $1x10^{-2}$mbar O_2 (b), and $1x10^{-1}$mbar O_2 (c).

Finally, at $1x10^{-1}$mbar O_2 (Fig.6.13c), all species travel together, the average kinetic energies are very low, constant throughout the angular range and the heavier cations show slightly higher energies. This is likely the consequence of having a higher mass while travelling at the same velocity.

The comparison of the maximum kinetic energies of the different ionic species brings back the topic that higher mass elements show higher maximum energies. This has been consistently found by plasma imaging (neutrals), MS of $La_{0.33}Ca_{0.66}MnO_3$, and $CaTiO_3$. It has also been reported by other sources using Langmuir probe measurements for different materials, laser wavelengths and fluences [66, 113].To follow this relationship, additional target materials with high elemental mass ratios were ablated in vacuum with two different fluences (2 J/cm^2 and 3 J/cm^2) and the plasma plumes were measured by MS. In total 5 target materials were tested: $EuAlO_3$, $YBa_2Cu_3O_7$, $La_{0.4}Ca_{0.6}Mn_{0.9}Ru_{0.1}O_3$, $CaTiO_3$, and $La_{0.4}Ca_{0.6}MnO_3$ ($La_{0.4}Ca_{0.6}MnO_3$ was repeated using a rod target to keep the same setup like for the other materials and brought similar kinetic energies as before for 2 J/cm^2). The increase in fluence brought similar increases

of ~30% in both the maximum and the average kinetic energies (for each element of the different materials). The results are shown in Fig.6.14 for the maximum kinetic energies detected of the different ions and target materials vs. atomic mass, with Fig.6.14a being for a fluence of 2 J/cm^2 and Fig.6.14b for 3 J/cm^2.
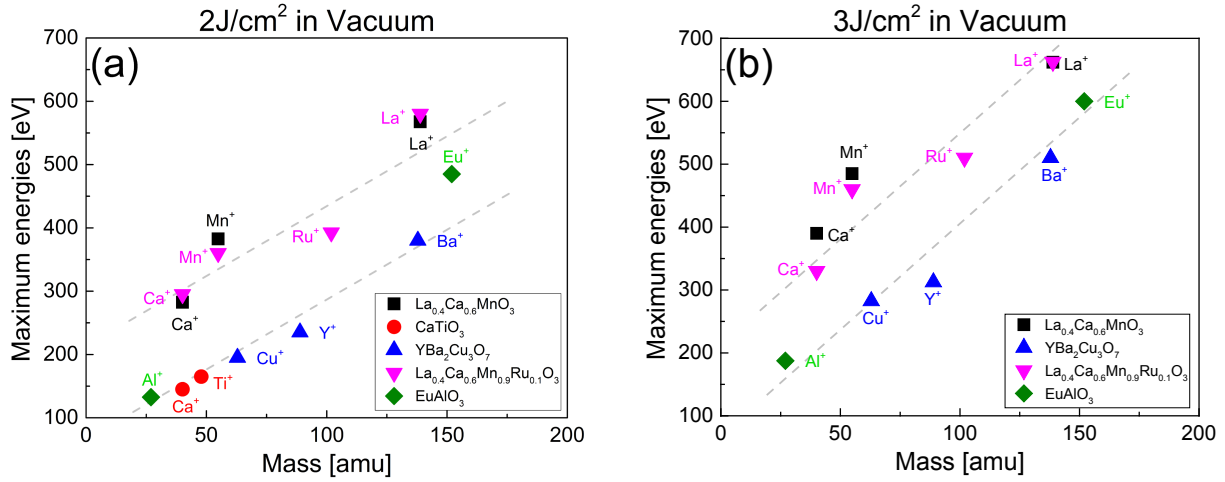
Fig.6.14. Maximum kinetic energies detected in vacuum for the different ions and target materials vs. atomic mass. Note: CaTiO$_3$ has not been measured at 3 J/cm^2. The dashed lines are a guide to the eye.

Both fluences suggest a direct relationship between atomic mass and maximum kinetic energies (no similar relationship was found for the average kinetic energies). A relationship that is kept for the different ablated targets but which shifts vertically depending on the ablated material (even when comparing the same elements such as Ca$^+$), this is very likely due to the different energy absorption per volume (dissimilar laser absorption properties). The same amount of energy might be coupled to a lower number of atoms resulting in higher kinetic energies. To resolve this the ablation rates of the different tested materials for a fluence of 3 J/cm^2 were measured (by weighing the targets before and after ~10'000 pulses) and are shown in table 6.6 in increasing order.

Material	Ablation rate at 3 J/cm^2 [ng/pulse]
La$_{0.4}$Ca$_{0.6}$Mn$_{0.9}$Ru$_{0.1}$O$_3$	170
La$_{0.4}$Ca$_{0.6}$MnO$_3$	178
EuAlO$_3$	211
CaTiO$_3$	222
YBa$_2$Cu$_3$O$_7$	400

Table 6.6. Ablation rates in ng/pulse for different materials using a fluence of 3 J/cm^2 and measured by weighing the target before and after ~10'000 pulses.

The ablation rates and the vertical shifting of the relationship between atomic mass and maximum kinetic energies are in good agreement. La$_{0.4}$Ca$_{0.6}$Mn$_{0.9}$Ru$_{0.1}$O$_3$ and La$_{0.4}$Ca$_{0.6}$MnO$_3$ have the lowest ablation rates, thus the smallest volume of material to absorb the same amount

of energy, yielding much higher kinetic energies. $EuAlO_3$, $CaTiO_3$ and $YBa_2Cu_3O_7$ have increasing ablation rates matching the vertical lowering of the maximum kinetic energies relationship, with $YBa_2Cu_3O_7$ presenting the highest ablation rate with 400 ng/pulse. In the particular case of $La_{0.4}Ca_{0.6}Mn_{0.9}Ru_{0.1}O_3$, the small addition of Ru to $La_{0.4}Ca_{0.6}MnO_3$ does not change the absorption properties strongly and shows very similar ablation rates like $La_{0.4}Ca_{0.6}MnO_3$ while adding Ru^+ to the comparison.

Furthermore the increase in fluence (Fig.6.14b) brings a similar vertical shift in maximum ionic energies (~90 eV), as seen for the different targets, while keeping a comparable slope. In both fluence cases the relationship between mass and maximum kinetic energies is ~1:3 with the intersection of the energy axis varying between 50-250 eV (increasing with fluence as seen in chapter 5). The underlying reason for such kinetic energy relationship with mass is explained in the following paragraphs. They are the result of discussions with N.M. Bulgakova and A.V. Bulgakov who gave strong input and provided the suggested model[2].

With ns laser ablation, a long-living double layer is formed due to laser light absorption by the generated plasma plume, leading to an acceleration of plume electrons and even formation of two-temperature electron distributions with high-energy tails [114]. Assuming a "quasi-uniform" double layer with a long life time at the plume front (in comparison with the ns pulse), it is expected that ions of different masses should have a similar kinetic energy. However, this double layer is not uniform in space and evolves with time.
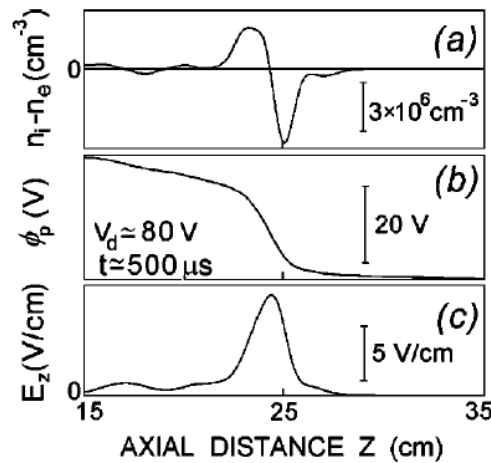
Fig.6.15. Typical scheme of double layer in the front of expanding plasma. (a) Electrons tend to go ahead of the expanding plasma plume due to higher velocity; this creates a double layer of charged particles, negatively and positively charged slabs. (b) Due to the double layer, electric potential is dropping from the quasi-neutral plasma core to the very front of the expanding plume. (c) The resulting electric field has a peak-shaped distribution with a near-zero level in the quasi-neutral plume core, the maximum in the region of highest gradient of the electric potential, and dropping to zero in the front of the cloud of escaped electrons. From [114], adapted from [115]

Assuming a dynamic double layer as presented in Fig.6.15, the following mechanism for ion acceleration could explain the observed tendency of higher energy for the heavier ions (Fig.6.16). The double layer develops from the very beginning of the laser plume expansion

---

[2] N.M. Bulgakova and A.V. Bulgakov 2016, pers. comm., Sep.

due to high-velocity electrons which are escaping from the plume in its front [116]. Being in the same region of the double layer, lighter ions obtain higher velocity, compared to heavier ones, according to Newton's law $m\frac{d\vec{v}}{dt} = e\vec{E}$. With time, the accelerated light ions leave behind the heavier ions (seen in the plasma imaging chapter) and move to the plume front where the electric field is smaller (Fig. 3b). Thus, the heavier ions stay longer in the region of the ambipolar field with the higher intensity and are subject to a longer and, hence, stronger acceleration.

○ electrons; ● light ions; ● heavy ions
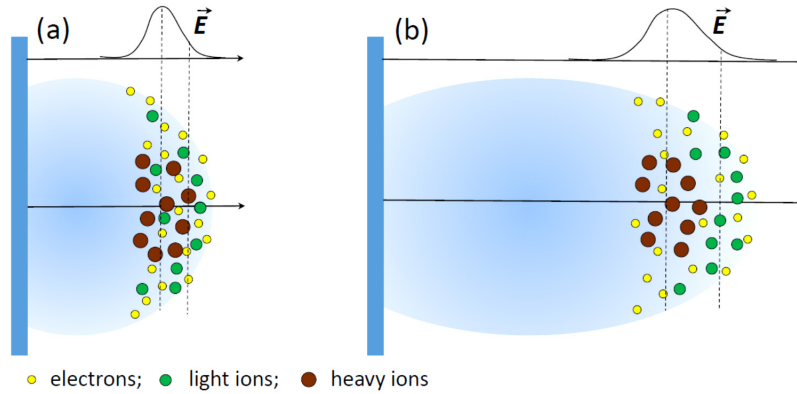
Fig.6.16. Schematics of double layer evolution and ion acceleration in a pulsed laser plume demonstrating the mechanism responsible for higher energy of heavier ions. The enrichment of the axis with heavier ions/neutrals as a result of off-axis scattering of lighter ions (in accordance with [116]) was also observed by MS but was slightly masked by the different ionization energies.

In addition, the sudden or gradual stop of counts at high energies depending of the element with the highest mass in the plume is detected consistently for all target materials (not shown here). In all cases the element with the highest mass (i.e.: La^+, Eu^+ and Ba^+) is mainly the only one to present gradual decays vs. the abrupt stops for the lower mass elements. The relevant exception is $CaTiO_3$ (shown in Fig.6.12) where the stop is abrupt in both cases, this is reasonable as both elements have similar masses. In general it seems very likely that this is a consequence of the intra-plume collisions and the different masses which cause the lighter elements to loose energy vs. the heavier ones during the initial stages of the plume expansion.

6.2.2 Analysis of plasma cations and anions

As with $La_{0.33}Ca_{0.66}MnO_3$ vacuum ablation shows a small amount of O^- close to the centre of the plume (<30°). This oxygen originates from the target and is ~40% less than the amount detected with the ablation of $La_{0.33}Ca_{0.66}MnO_3$. One cation is preferentially detected (Ca^+) and this seems related to its lower ionization energy shown in table 6.4 (Ca = 6.1132 eV vs. Ti = 6.8281 eV). At $1x10^{-2}$mbar O_2, the number of Ca^+ species show a marked increase at all angles, while Ti^+ experiences a slight drop in counts. In addition the O^- signal increases very little in the narrow angular range, which is in contrast to the $La_{0.33}Ca_{0.66}MnO_3$ measurements. The addition of background O^- is minimal compared to the 8.5 times increase from the previous

$La_{0.33}Ca_{0.66}MnO_3$. At $1x10^{-1}$mbar O_2, the same results as for $La_{0.33}Ca_{0.66}MnO_3$ appear again: O^- and Ti^+ cannot be detected any more (the cation with the highest dissociation energy for its metal oxygen species). It is very likely that TiO^+ should be the preferentially detected metal oxygen species in such a plasma plume. Additionally, the number of Ca^+ is reduced in the forward direction but essentially unchanged at high angles. A potential reason is a preferential scattering of the forward directed Ca^+ species which are redistributed towards larger angles. At the same time Ca^+ at higher angles are also scattered and drop out of the angular line of MS measurements, but their loss is compensated by these species scattered from the plume centre.
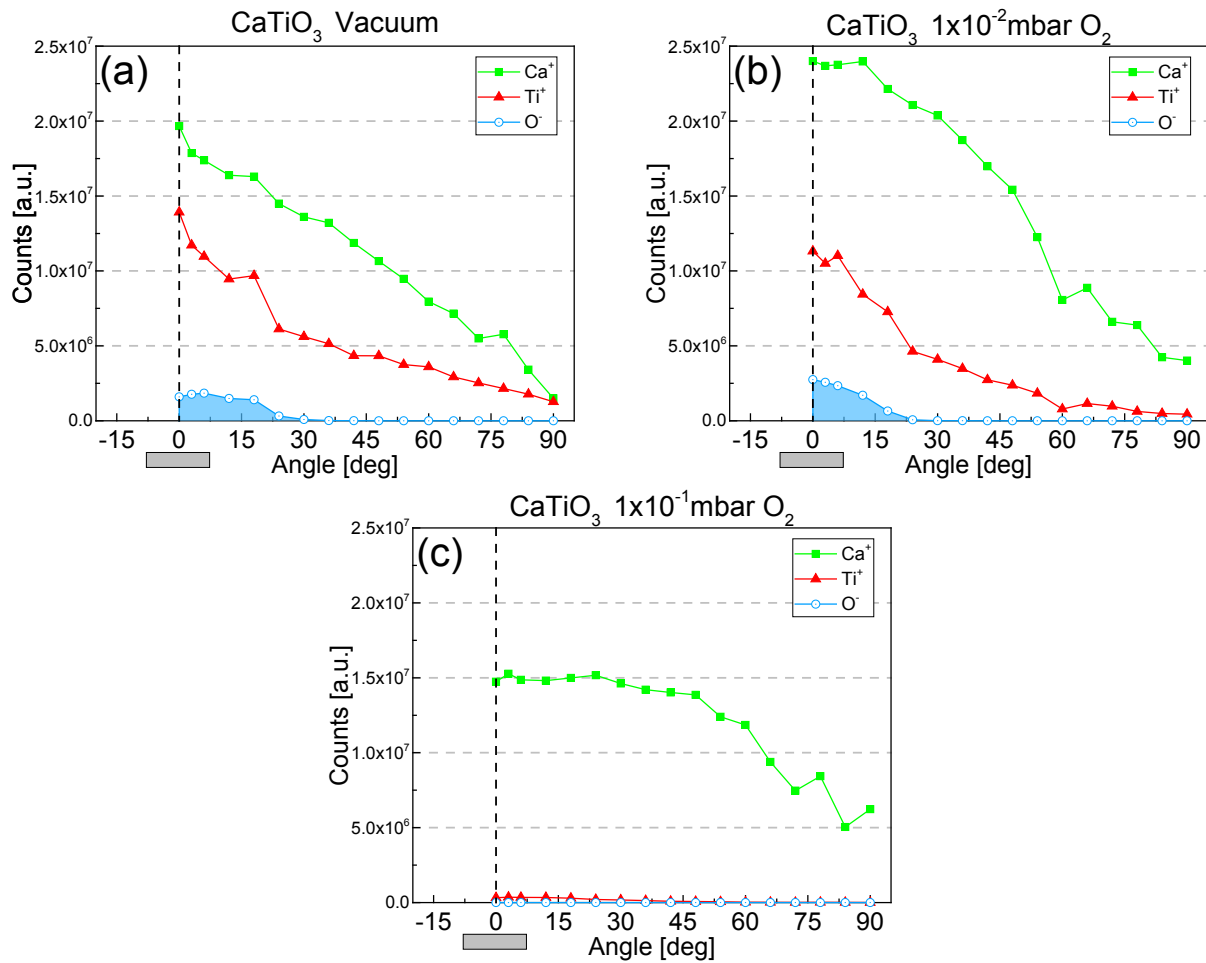
Fig.6.17. Angle-resolved detected counts of Ca^+, Ti^+, and O^- for vacuum (a), $1x10^{-2}$mbar O_2 (b), and $1x10^{-1}$mbar O_2 (c).

6.2.3 Clarifying the rate of generation of O^- from the background gas

From the $La_{0.33}Ca_{0.66}MnO_3$ MS measurements, it was noticeable that the O^- angular profiles and intensities at $1x10^{-2}$mbar O_2 were matching the areas of maximum plume energies and material (the centre of the plume). With most of the film oxygen coming from the background gas it is likely that these O^- counts originate from the dissociation of the background molecular O_2. This could follow similar reactions like those described in table 6.2, yielding O-atoms in different states, which may be directly O^- or follow reactions to form it by electron attachment. However,

all the listed reactions are based on electron impact and from Langmuir probe measurements it is known that the detected electron energies are too low (<<4.2 eV for electron dissociative attachment). It seems reasonable that the O_2 dissociation might be caused by collision induced dissociation by the plasma species.

Simulations of O on O_2 and O_2 on O_2 collisions show maximum collisional dissociation cross sections appearing in the 30-40eV range [117] and minimum values in the ~20 eV range. The detected kinetic energy profiles of the different plume species are indeed sufficient to surpass the literature reported values.

In the case of $La_{0.33}Ca_{0.66}MnO_3$ the average kinetic energies were much larger and the detected O^- was noticeable, while for $CaTiO_3$ the energies were low and the O^- counts too. If the average kinetic energy profiles for vacuum are plotted together with the O^- counts (angle resolved, see Fig.6.18a), the relationship between plasma energies and O^- generation becomes clear. Lower kinetic energies results in a lower O^- detection. The centre of the plume, which has the highest kinetic energies, is also the location with the highest O^- counts (maximum values are not used as the long tails translate into very small amounts of species at such energies). There appears to be a minimum kinetic energy (~35eV) for O^- detection after which there seems to be a linear relationship between kinetic energy and O^- detection. Interestingly it is a similar value to the electron energy that shows the maximum cross section for O_2 dissociation, ~33.5 eV [118]. If the energy scale is shifted to similar energy values (Fig.6.18b) there is a good match between kinetic energy profiles and O^- detection. Alternatively at 1×10^{-1}mbar the energy of all species is very low (<10eV) and hardly any O^- is detected.
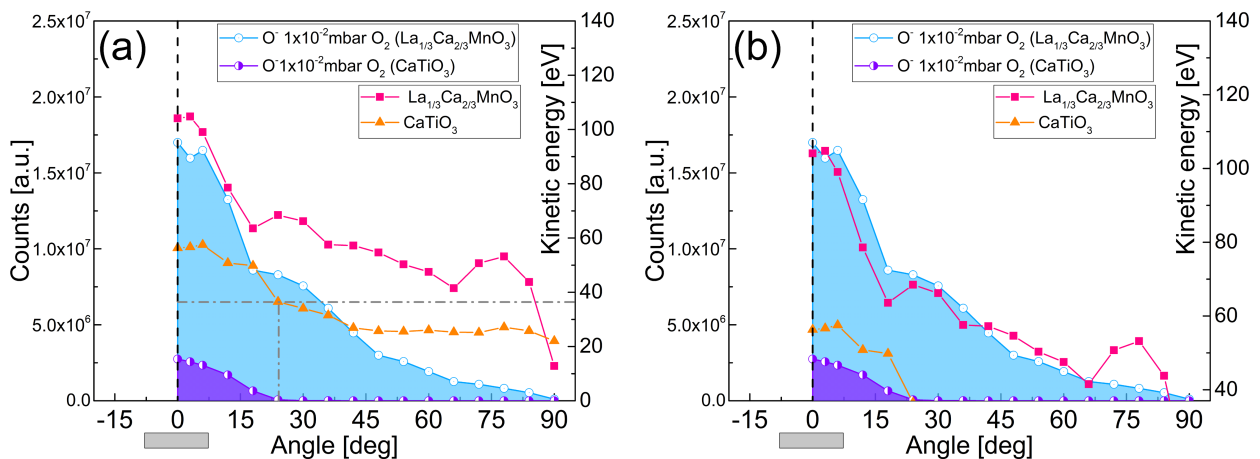
Fig.6.18. Angle resolved counts of O^- from $La_{0.33}Ca_{0.66}MnO_3$ and $CaTiO_3$ and average kinetic energies in vacuum (a). While (b) is the same data with the kinetic energy scale starting at 37eV.

6.2.4   The metal oxygen species

With the cations and O^- variations analysed, the metal oxygen species complete the picture with measurements shown in Fig.6.19.

In vacuum (Fig.6.19a) no metal oxygen species are detected for $CaTiO_3$. This is in contrast to $La_{0.33}Ca_{0.66}MnO_3$ were a considerable amount of LaO^+ is detected and which increases at

higher angles. At $1x10^{-2}$mbar CaO^+ and TiO^+ appear in similar amounts but very low. Finally at $1x10^{-1}$mbar O_2, there is more TiO^+ than CaO^+ present and mostly at the centre of the plasma plume. This is the same angular region where O^- was detected at lower pressures which might be an indication of the presence of single O atoms following the O_2 molecule dissociation process described in table 6.2 (but by ion impact). This preferential detection of TiO^+ is in good agreement with the correlation between dissociation energies and counts of metal oxygen species (Fig.6.9), as TiO^+ has a dissociation energy larger than O_2 (6.9 > 5.15 eV) and CaO^+ is smaller (4.07eV). Any collision between CaO^+ and the O_2 background gas will preferentially dissociate CaO^+, while for TiO^+, O_2 would be the dissociated molecule. Nevertheless, the neutral species should be explored to have a better understanding.

Furthermore, it has been reported that more MO^+ species in the plasma seem to result in higher oxygen content of films [67]. Thus, to incorporate a high amount of background O_2 into a film it is likely that two conditions should be met. First, the plasma species should have sufficient kinetic energy to dissociate O_2 into single O atoms by collisions. Second, a suitable metal oxygen species should be present with a higher dissociation energy than the O_2 molecule to enable incorporation.
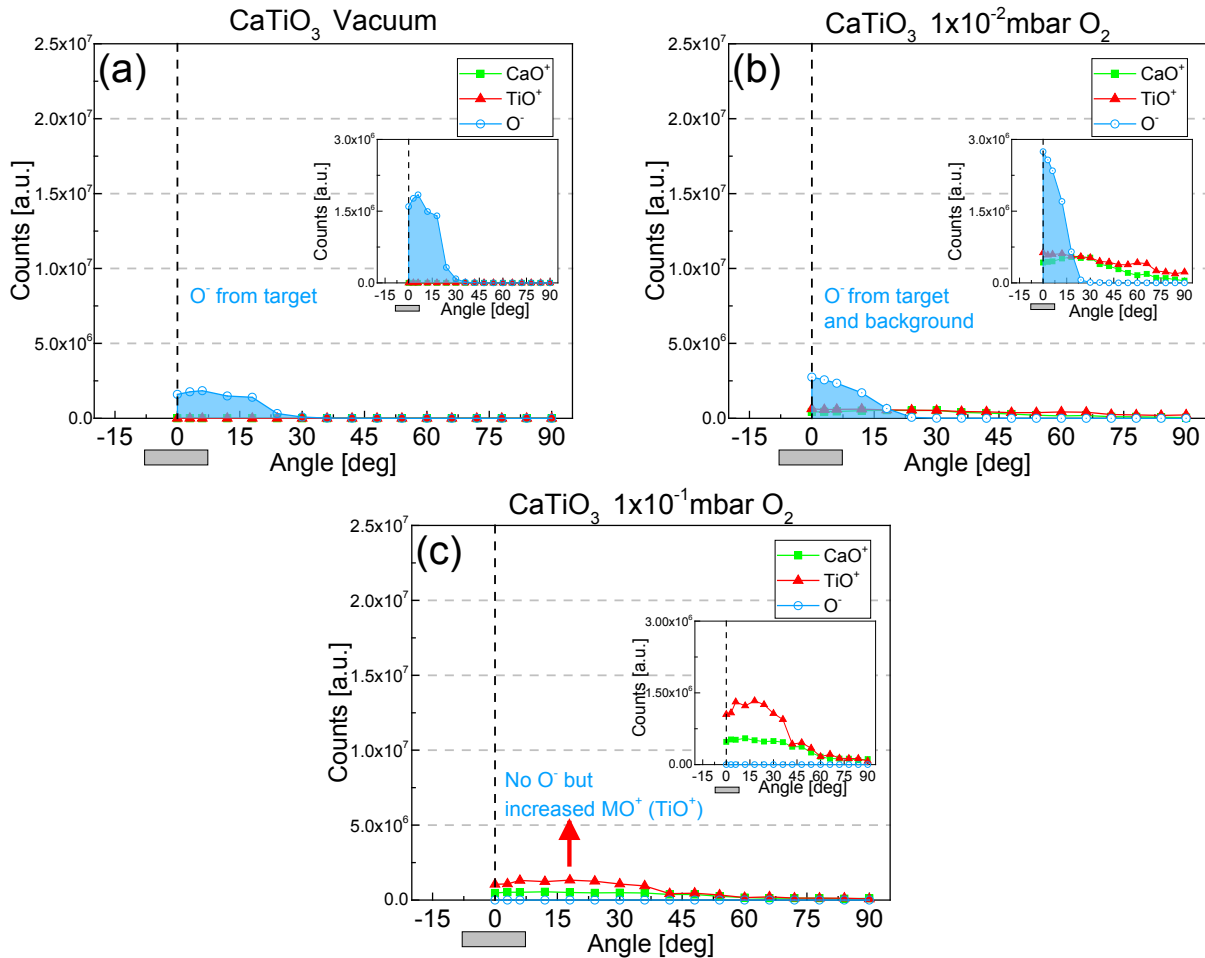
Fig.6.19. Angle resolved counts of CaO^+, TiO^+ and O^- for vacuum (a), $1x10^{-2}$mbar O_2 (b), and $1x10^{-1}$mbar O_2 (c). The increase in TiO^+ at $1x10^{-1}$mbar O_2 has been highlighted in (c) using a red arrow.

6.3   Conclusions

The results from the angular plasma probing using MS are overall consistent with data from other methods and promising for further investigations. Despite particular uncertainties concerning preferential ionization or the missing neutral's evolution for different species, the revealed trends are consistent and match many findings from previous chapters therefore validating this approach. Furthermore it ratifies the findings from Chen *et al.*[102] concerning a preferential formation of metal oxygen species with high dissociation energies. This has been verified angle-resolved for two different perovskite materials with very different mass ratios. At the same time the efficiency for dissociation of the O_2 background gas has been linked to the kinetic energy of the species.

The kinetic energies are strongly dependant on the mass of the participating elements, with higher masses yielding higher kinetic energies. This could be explained by the formation of a double layer in the plasma plume due to the interaction of the ns laser pulse with the plume. This electric field would accelerate the ions and in particular, due to their mass, the heavier ions would remain longer in the ambipolar filed resulting in longer and, therefore, stronger accelerations. In addition, the detected maximum kinetic energies are also different for different target materials (laser absorption dependence) and they increase with fluence.

7

The influence of laser fluence and background gas on the plasma plume expansion

To provide a wider understanding of the particular characteristics of pulsed laser deposition of $La_{0.4}Ca_{0.6}MnO_3$ a study on the influence of laser fluence is presented hereafter. It starts by analysing the specific ablation rates on the target, continues by measuring the deposition rates using a QCM (quartz crystal microbalance) located at the typical substrate location and completes the overview by using plasma imaging to visualize the material distribution in the plume. In all cases the fluence is varied within the typical PLD values for this material (~1-4 J/cm^2) and in the plasma imaging section the pressure is also varied evidencing the strong relationship between laser fluence and background gas pressure.

7.1   The effect of laser fluence

7.1.1   Ablation rates

The ablation rates for $La_{0.4}Ca_{0.6}MnO_3$ were measured by weighing the target before and after ablation at ambient pressure with ~10'000 pulses or more (rep. rate of 10 Hz) using a scale with a resolution of 0.1 mg. This method was preferred in comparison to crater depth measurements (after continuous ablation on the same spot) to avoid the uncertainty of dissimilar ablation rates during the initial pulses on a polished surface (changes in laser absorption by radiation induced defects, i.e.: incubation at very low fluences) and also the changes in removal rate as the crater depth increased (i.e.: due to re-condensation on the crater walls, changes in surface normal, escape of ablated material...). Additionally no estimation of material density is needed nor simplification of the crater's real volume. The entire ablation surface of the target already had a steady state of physical and chemical modifications due to repeated ablations to ensure similar conditions as when depositing by PLD for long durations (>30min).

The measurements were performed at ambient pressure for practical reasons (>20 ablation rate experiments for several target materials that would each require opening, closing of the chamber and attaining vacuum). The atmospheric pressure could influence the transport of ablated materials, cause re-condensed debris on the target surface and the confinement of the vapour plume will increase the attenuation of the incident laser light resulting in lower ablation rates [10]. The first two effects are reported to have little influence on ablation rates [119], however the latter, as the ns pulses interact strongly with the plume due to their duration, might have an important influence due to plasma shielding. A more detailed discussion would also require covering the plasma target interactions. One control experiment in vacuum was performed with a fluence of 3 J/cm^2, showing an ablation rate of ~256 ng/pulse vs. 180 ng/pulse for the ambient pressure experiments. This evidences an underestimation of the mass loss of ~30% at ambient pressure compared to vacuum which could originate from re-condensed debris and/or plasma shielding. It is expected that this difference will be smaller for lower fluences, as less material will be ablated and prone to plasma shielding, and larger for higher fluences. Nevertheless this ambient pressure measurement approach was chosen for practical reasons with the knowledge to take on a systematic error.

The material removal rates per pulse are shown in Fig.7.1 for the different fluences. The upper values in fluence were limited to 4.8 J/cm^2 due to laser power limitations and the lower range due to weighing scale resolution. The limited number of low fluence measurements do not allow a proper visualization of this area were small changes in fluence are expected to bring strong changes in ablation rate. A linear regime is visible (~1-3 J/cm^2) and the expected logarithmic behaviour in ablation rate seems to start at ~4 J/cm^2. The results show the expected increase

in removal rates with increasing fluence which is in agreement with the exponential decay of intensity with depth given by the Beer Lambert law:

$$I(z) = I_0 \, e^{-\alpha_{eff} z} \tag{7.1}$$

Where I_0 is the initial intensity at the surface after considering reflection losses and α_{eff} the material's effective absorption coefficient as the material's initial α may change during incubation (if the target get e.g. black), an aspect which will not be analysed as the measuring procedure will give the average of the changed material which is what finally matters for this deposition process. Overall, a higher initial intensity translates into a higher penetration depth for reaching a certain intensity level and thus higher ablation rates.
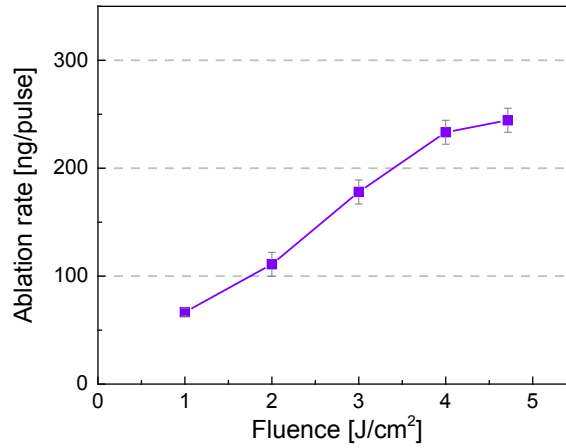
Fig.7.1. Ablation rates in ng/pulse for $La_{0.4}Ca_{0.6}MnO_3$ at different laser fluences for a spot of 1 x 1.4 mm

7.1.2 Estimation of deposition efficiency

With the ablation rates it is now possible to do a rough estimation of deposition efficiency using the film thicknesses reported in chapter 3 (~110 nm thickness for the substrates at the centre of the plume using a fluence of 2 J/cm^2, a spot of 1.4 mm^2, 3 Hz and a duration of 40min).

Assuming a density of ~6.03 g/cm^3 for $La_{0.4}Ca_{0.6}MnO_3$ [120], taking the ablation rate of ~110 ng/pulse (for a fluence of 2 J/cm^2) and a laser spot of 1.4 mm^2 it is possible to estimate an ablation depth of ~14 nm/pulse on the target (~21 nm/pulse for 3 J/cm^2). With respect to the film of 10x10 mm the deposition rate on that surface is 0.014 nm/pulse for the 7'200 pulses. A comparison in terms of ablated vs. deposited mass on such substrate (10x10 mm with a thickness of 110 nm) would render an ablation of ~110 ng/pulse for a deposition of ~9.2 ng/pulse. This is a deposition efficiency of ~8.4% for the vacuum conditions which was the case that produced the thickest films. For the 1x10^{-1}mbar Ar, which produced films with a thickness of ~55 nm, it would be reduced to ~4.2% (4.6 ng/pulse). In general it seems a remarkably low and unwished deposition efficiency (similar values have been reported in our

group by T. Dumont for $LiMn_2O_4$ [121]), but it is precisely these very low deposition rates "per pulse" what brings ultimately the great film growth properties PLD can offer.

7.1.3   Quartz crystal microbalance

Using the QCM described in chapter 2 it is possible to get a better understanding of the effect of fluence on the deposition rates and how the different pressures might affect them (Ar and O_2). The QCM is positioned at the typical substrate location of 40 mm with respect to the target and its surface is normal to the plume expansion axis. For each measurement point ~1000 pulses were performed allowing a good linear fit to obtain the slope of the frequency change vs. pulse. The deposited mass per pulse is then calculated following Sauerbrey's equation (Eq. 2.1) taking into account that the 14 mm diameter of the quartz crystal is partially covered by its housing allowing only a diameter of 8.17 mm to be coated. The results for the different fluences and pressures are presented in Fig.7.2a. They show the expected increase in deposition rates once the ablation threshold of ~0.25 J/cm^2 is surpassed. The deposition rates seem to increase linearly with pressure with the exception being at the very low fluences (<0.5 J/cm^2). The values for the different pressures match the film thickness findings from chapter 3 (RBS) with vacuum presenting the highest deposition rates followed by $1x10^{-2}$mbar and then $1x10^{-1}$mbar. The O_2 background gas shows a lower stopping power than Ar due its lower mass and Van der Waals volume (see discussion in 4.1.2).

A comparison between the deposited ablation rates measured by QCM and the target ablation rates is presented in Fig.7.2b. They show again the considerable difference between ablated and deposited mass (close to two orders of magnitude). Interestingly, the trends with increasing fluence are similar when plotted on a logarithmic scale.
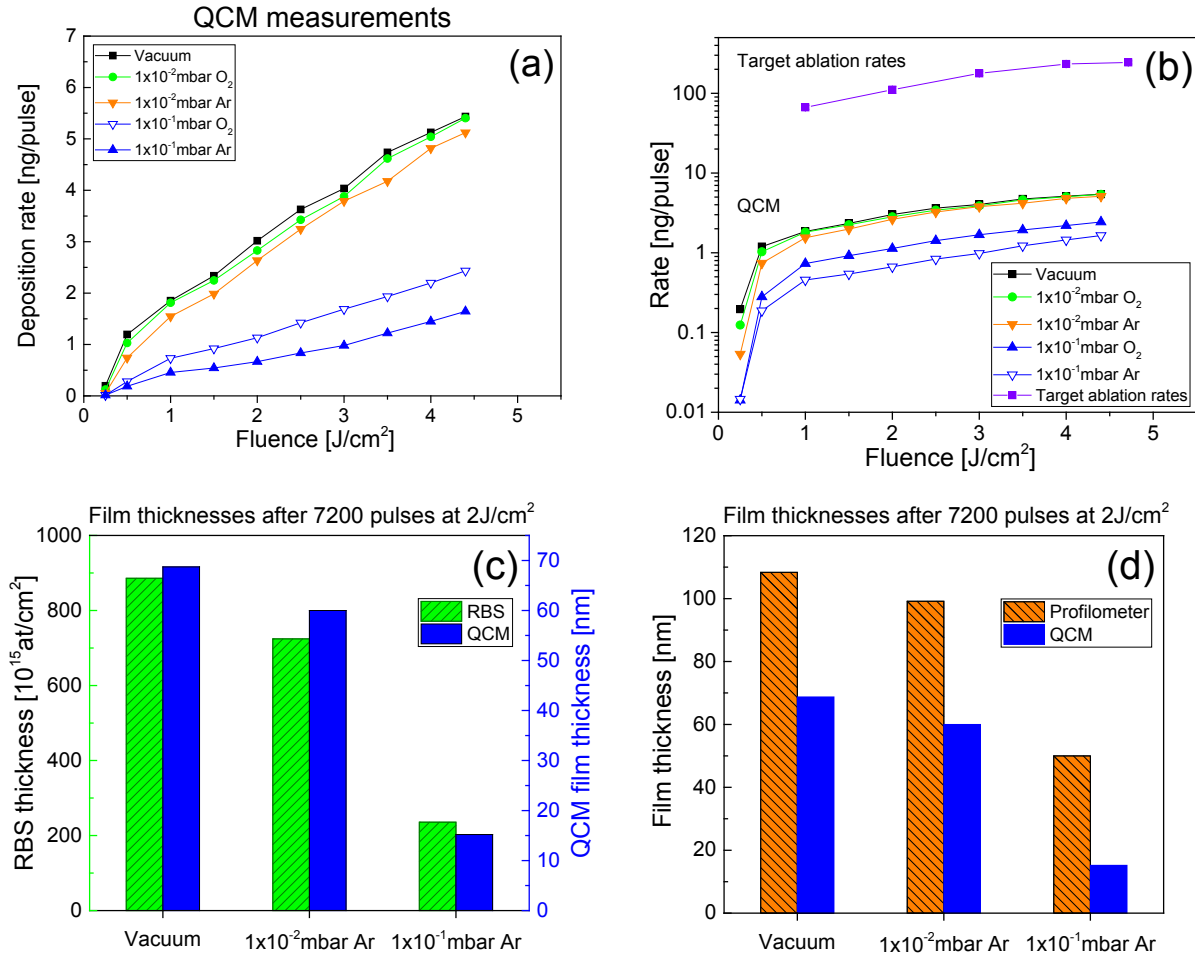
Fig.7.2. QCM deposition rates for different laser fluences (a), a comparison between the QCM deposition rates and the target ablation rates per pulse (b), between the film thicknesses for the different pressures after 7200 pulses with a fluence of 2 J/cm^2 from RBS and QCM measurements (c), and between the QCM and profilometer measurements (d).

From the estimated deposition rates per pulse it is possible to perform an additional comparison between RBS and QCM measurements of the deposited film thicknesses after 7200 pulses and 2 J/cm^2. This is shown in Fig.7.2c for vacuum, 1x10^{-2}mbar Ar, and 1x10^{-1}mbar Ar. The RBS results are from the measurements presented in chapter 3. Despite the difference in measurements units, they both show a corresponding decrease in thickness with increasing pressure. Furthermore, the same comparison with the profilometer film thickness values from chapter 3 (in nm) also shows a similar trend but it seems that ~40 nm are consistently missing for all pressures. This is likely to be a systematic instrumental error.

In addition, the deposition rate values obtained by the QCM measurements allow a rough estimate of the number of pulses required for the growth of one unit cell. For example, in vacuum an ablation at 2 J/cm^2 results in a film deposition rate of ~0.01 nm/pulse. The growth of one unit cell (~7.6 Å [68]) requires therefore ~76 pulses, a number which is very similar to literature values obtained by in-situ RHEED measurements (reflection high-energy electron diffraction) for the same fluence and material (~60 pulses/unit cell) [122].

In general, the sensitivity of the QCM per pulse is remarkable apart from the simplicity with which measurements at different pressures can be performed making it an ideal tool for studying film deposition rates.

7.1.4 Mass spectrometry

In comparison to QCM measurements, the MS probes a very small portion of the plasma plume through a 30 µm orifice. However, it provides a valuable complimentary analysis with information concerning the different ionic species and their kinetic energies. Besides, due to the fast execution of each measurement, a higher number of experiments could be performed which allowed a larger number of fluence measurements.

The integrated counts for the different ionic species measured in vacuum are shown in Fig.7.3ab. They show an ablation threshold of ~0.25 J/cm^2, followed by a noticeable increase with fluence to reach a steady state number of ions at around ~1.5J/cm^2. Dissimilar ablation takes place close to the ablation threshold (i.e.: for LaO$^+$), this is a regime where preferential ablation may take place (for multi-element materials) and which is strongly recommended to avoid in PLD if one aims to achieve reproducible results [6]. As seen in previous chapters, there seems to be no quantitative correlation between the ionic counts of La$^+$, Ca$^+$, and Mn$^+$ and the target composition due to the preferential ionization of elements. Mn$^+$ and Ca$^+$ reach saturation above a certain fluence (~2 J/cm^2) while counts of La$^+$ and O$^-$ continue to increase with fluence. This would not translate in La enrichment in the film with increasing fluence but rather a lack of information concerning neutral count evolution with fluence. The increase in ions with fluence is reasonable as the stronger pulse interaction with the plasma plume would generate a larger percentage of ions and a preferential ionization of the one with the lowest ionization energy i.e. La. No MnO$^+$ nor CaO$^+$ were detected.
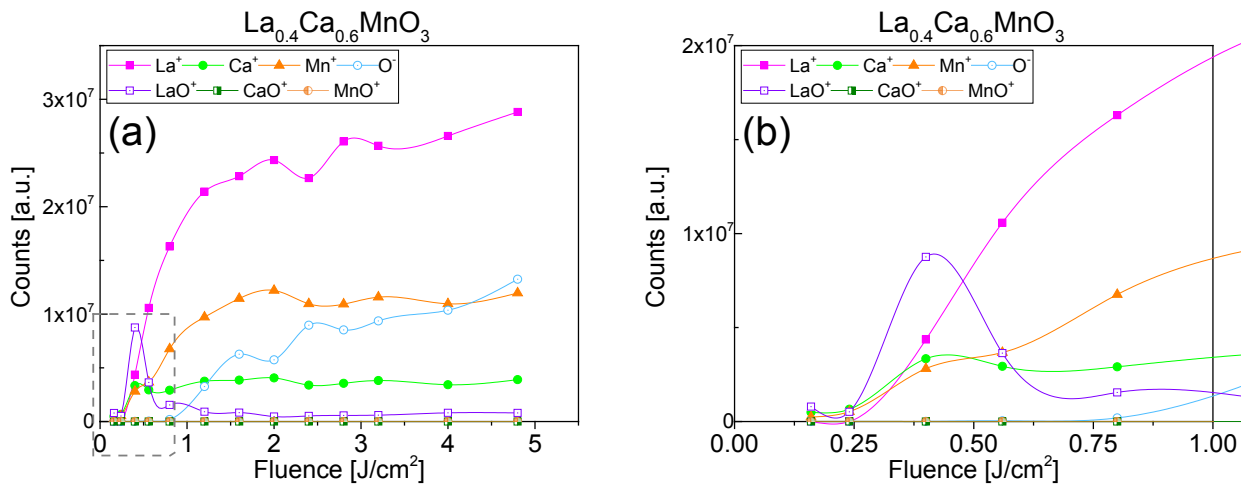
Fig.7.3. MS ionic counts in vacuum of La$^+$, Ca$^+$, Mn$^+$, O$^-$, LaO$^+$, CaO$^+$ and MnO$^+$ for different laser fluences (a) and zoomed view in the 0-1 J/cm^2 region (b). The solid lines serve as visual guidance.

A comparison between MS total ionic counts and ablation rates is shown in Fig.7.4. The match is not particularly good, with underestimations or overestimations in most fluence ranges, probably either because of the lack of information about the neutrals (MS) or the plasma plume shielding from the ablation at ambient pressure or a combination of both. In any case this was expected given the fundamental differences between both approaches, although the general tendency of increase in counts or ablation rates with increased fluence is still seen.
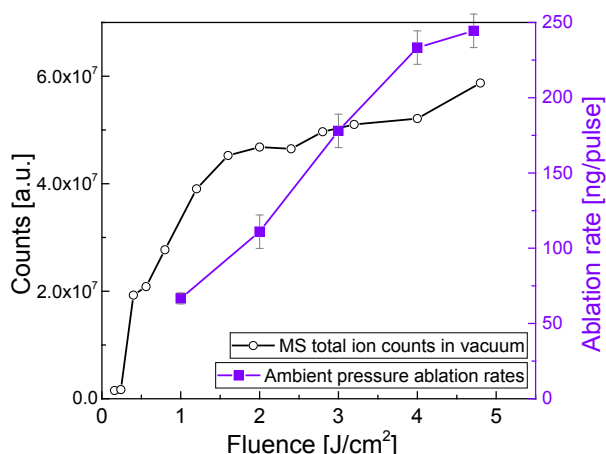
Fig.7.4. Comparison of MS total ionic counts in vacuum vs. ablation rates measured by weight losses at ambient pressure.

Apart from the total counts, the kinetic energy profiles for some of the measured species are shown in Fig.7.5a for La$^+$ and in Fig.7.5b for Mn$^+$. There is a noticeable increase in maximum ionic energies with increased fluence for both species. For instance from 1.6 J/cm^2 to 4.8 J/cm^2 the long distribution is stretched up to nearly twice the kinetic energy values. In the case of La$^+$ it even surpasses the equipment measuring limit of 1'000 eV. It is clear that those users with a MS limited to just 100 eV would miss a great portion of the plume species, even for fluences as low as 0.4 J/cm^2.

In addition, the heavier La$^+$ shows gradual decays in counts at high energies compared to Mn$^+$. In the latter the stops in counts at the higher detected energies are more abrupt with decreasing fluences. Mn$^+$ at 4.8 J/cm^2 is the only one to present a gradual decay in counts at high energies like La$^+$ (for all fluences). As discussed in 6.2.1, this behaviour seems related to the intra-plume collisions and the preferential scattering/energy losses of the elements with the lower masses. When fluence is decreased the kinetic energies are reduced and consequently the scattering probability/cross sections increase.
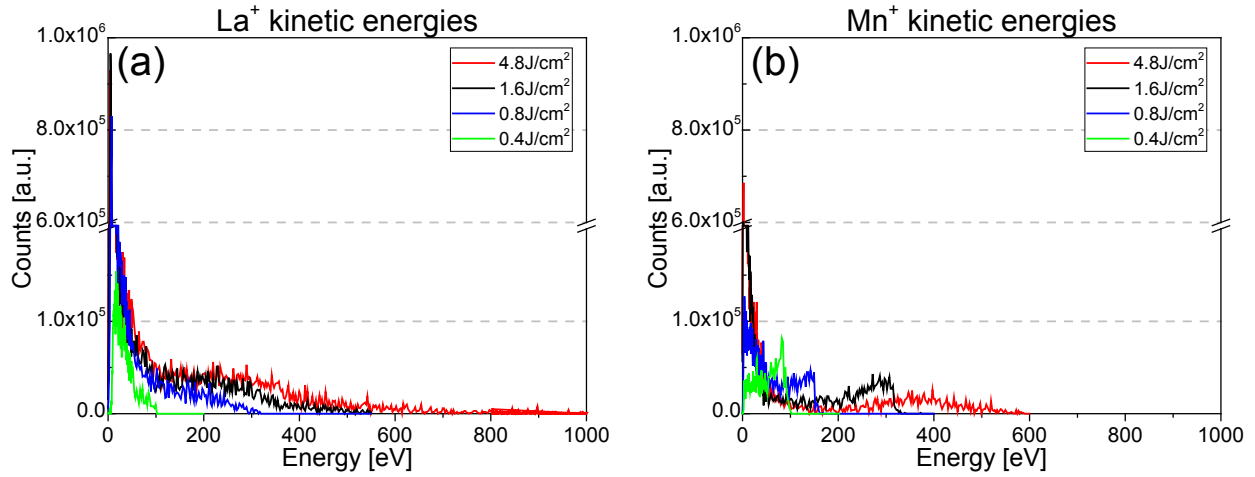
Fig.7.5. Kinetic energy profiles in vacuum for different fluences of La$^+$ (a) and Mn$^+$(b).

A comparison between the different cations' kinetic energies is presented in Fig.7.6a for the average and in Fig.7.6b for the maximum kinetic energies. All cations show a large difference between average and maximum kinetic energies (close to 4-7 times) evidencing long range profiles. The increase in fluence results in a steeper increase in maximum kinetic energies in comparison to average values, although in both cases there is a consistent increase. Again the relationship between the atomic masses of the different cations and the maximum kinetic energies is visible with La$^+$ showing the highest energies and Ca$^+$ the smallest. The presence of these highly energetic La$^+$ ions could be very damaging for a deposited film (i.e.: sputtering creating defects etc.) and the use of a background gas is often applied to reduce the kinetic energies.
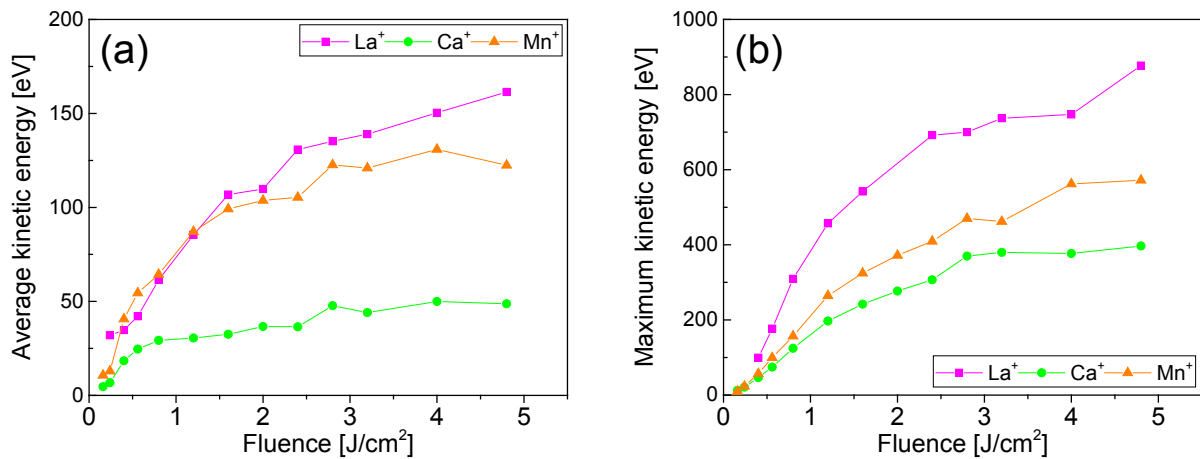
Fig.7.6. Kinetic energies of the cations: average values (a) and maxima (b). The solid lines are a guide to the eye. Note: the energy scales are different to improve their visualization.

7.1.5 Plasma plume imaging

The influence of laser fluence on the plasma expansion dynamics is now assessed by time resolved imaging. Initially for vacuum and then for 1x10^{-2}mbar Ar and O$_2$ which were the

pressures which showed the strongest compositional changes in the deposited films due to the plume splitting and preferential scattering of the lighter elements (as seen in chapter 4).

The emission intensities were significantly different, not only depending on the different time frames or background pressures but also with increasing laser fluences. A comparison between the time resolved maximum emission intensities for the different pressures and gases is presented in Fig.7.7 for the ablation at 4 J/cm^2. The intensities have been corrected according to the gating used (using overlapping time frames).

The three cases presented show a similar emission intensity decaying process which can be divided into three distinct stages. First, during the initial ~1 µs there is a large amount of excited species formed by the laser ablation process which decay strongly. There is no significant difference between the various backgrounds in this initial stage. Second, between 1-2 µs, there are two competing processes, the initial emission decay vs. the re-excitation of species due to some collisions (intra-plume and/or with the background gas). The differences between the background gases and vacuum becomes visible, with 1×10^{-2}mbar O_2 already maintaining higher emission intensities followed by vacuum and 1×10^{-2}mbar Ar the lowest (probably due to a quenching process by the annihilation of the excited state species [91]). Finally, the third stage at ~2 µs and above, shows a slow and long decay of emission intensities in which the emission from the re-excited species is losing against the lifetime decays. 1×10^{-2}mbar O_2, as was presented in chapter 4, sustains the emissions intensities for longer periods of time (chemical reactions of the plume with the background gas) and the stronger decay does not appear until ~4 µs but is still higher than vacuum and Ar. Vacuum shows an interesting irregularity at ~3 µs (highlighted with a dashed circle). This can be explained by the rebound of the plume against the substrate holder recorded for the vacuum cases which temporarily causes a collision of incoming and reflected fluxes. As a consequence the emission intensities are enhanced for a short period of time compensating the intensity decay after which the intensity levels are similar as for Ar (were no rebound takes place).
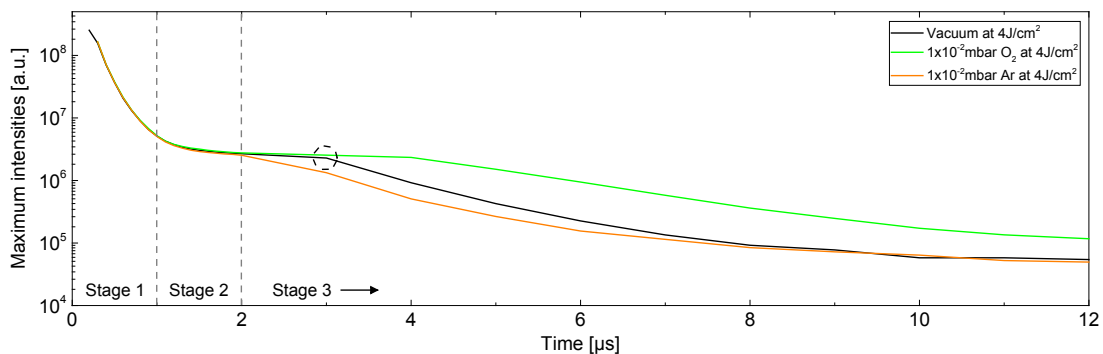
Fig.7.7. Time resolved maximum emission intensities for the 4J/cm^2 ablation in vacuum, 1×10^{-2}mbar O_2 and 1×10^{-2}mbar Ar. Note: the intensities were corrected according to the used gating (shared time frames)

Keeping in mind the differences in emission intensities between the various pressures, the influence in plasma plume dynamics of the laser fluence is assessed in the following pages. The results are shown in Fig.7.8 for vacuum, Fig.7.9 for $1x10^{-2}$mbar Ar, and Fig.7.10 for $1x10^{-2}$mbar O_2. The three of them have independent intensity scales and should not be directly compared (refer to Fig.7.7 for this). Moreover, each time frame has an independent intensity scale due to the strong changes in emission during the plume expansion (a time resolved intensity profile has been added for reference below the images). It is each time frame which keeps the same intensity scale for the different fluences tested. In this way an understanding of the influence of fluence on emission intensities and dynamics can be reached.

As seen in chapter 4, vacuum (Fig.7.8) has the fastest expansion, is strongly forward directed and the rebound can be seen (marked with a dashed curve for the highest fluence). At the lowest fluence of 0.5 J/cm^2 no rebound is visible. Below that level, at 0.25 J/cm^2 hardly any light emission could be recorded and the images had to be rescaled to allow some visualization although not presented here (MS measurements also showed a very low number of counts).

The increase in fluence yields higher emission intensities with 4 J/cm^2 showing the highest intensities beyond the initial expansion (>1μs). The most noticeable aspect, however, is the increase in expansion velocity with fluence which can be noticed by tracing the plume front location for each time frame. This has been highlighted for the 1 μs case using a dashed line in Fig.7.8. From the MS measurements reported earlier in the chapter it is known that apart from having higher ablation rates with increasing fluence, higher fluences also yield higher expanding velocities (kinetic energies).

With the addition of a background gas the dynamics become more complex and appealing. At $1x10^{-2}$mbar Ar (Fig.7.9) the increase in fluence results in increasing emission intensities and expansion velocities (same as in vacuum). However it is the plume splitting what reveals the strongest influence of the laser fluence. Chapter 4 reported on such effect for a fluence of 3 J/cm^2 and at $1x10^{-2}$mbar Ar. If the fluence is reduced the fast component of the plume arrives later to the substrate, decreases in intensity and less emitting species arrive to the substrate. This is clearly visible in the 3 μs time frame in Fig.7.9. For fluences below 1.5 J/cm^2 there is no longer a clear plume splitting observed but a single slow expanding plume front. Alternatively if a fluence of 4 J/cm^2 is used the opposite is observed, with the highest plume splitting intensities and shortest arrival times recorded (highlighted with a dashed ellipse at 3 μs).

With $1x10^{-2}$mbar O_2 (Fig.7.10) a similar pattern like in Ar can be seen with the particularity that the fast component of the plume splitting presents much higher intensities than the slow component ($t = 3$ μs). This is likely caused by emission from products of the chemical reactions of the plume front with the background gas. Additionally, the plume emission shape appears more spherical in comparison with Ar where most of the emission occurred at a narrow angle in

the plume front due to collisional interactions with the background gas (where the highly energetic species are).

In summary, for certain pressures it is possible to navigate from a slow expanding regime contained by the background gas to a plume splitting or perhaps a vacuum like regime (free expansion, not shown) by varying the laser fluence. These measurements show, that it is a competition between the density of background gas and plasma plume species which determine the plume expansion properties (fluence dependence). If their energy is too low they will be confined, if it is very high they will expand like in a lower pressure regime. The compositional deviations reported in chapter 3 (RBS measured films) for a pressure regime of 1×10^{-2}mbar Ar and a fluence of 2 J/cm^2 would occur at lower pressures if a lower fluence was used and vice versa.
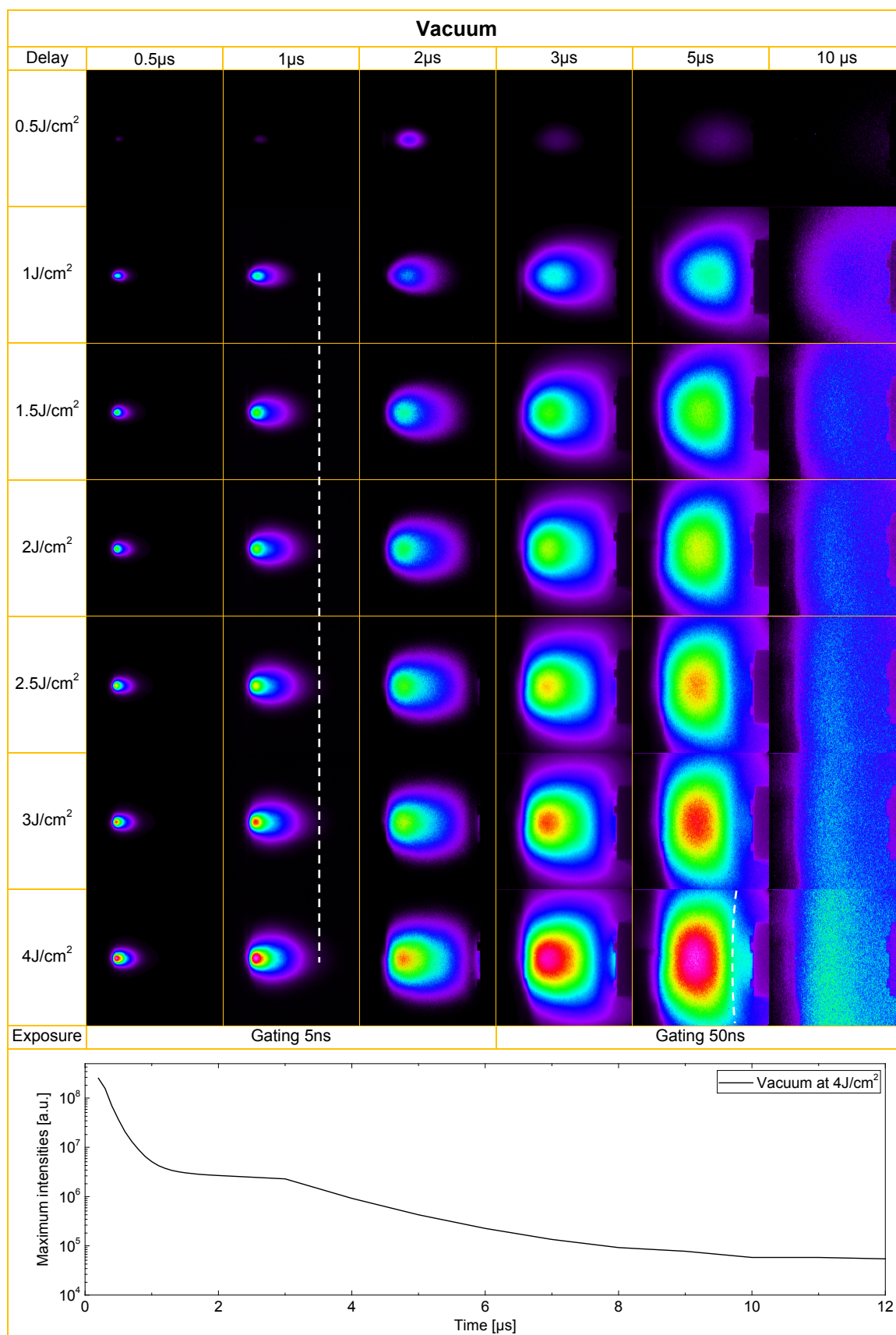
Fig.7.8. ICCD time resolved plasma imaging for vacuum without substrate heating for different fluences. Images of visible light (200 nm-1000 nm) with no filter applied. The plume expands from the ablated target on the left to the substrate on the right. All images for each time frame share the same intensity scale. A chart of the evolution of the time resolved maximum emission intensities for the 4J/cm² ablation is presented to evidence the strong decay in light emission. Two different gatings were used to adequately capture the plasma expansion dynamics (5 ns and 50 ns).
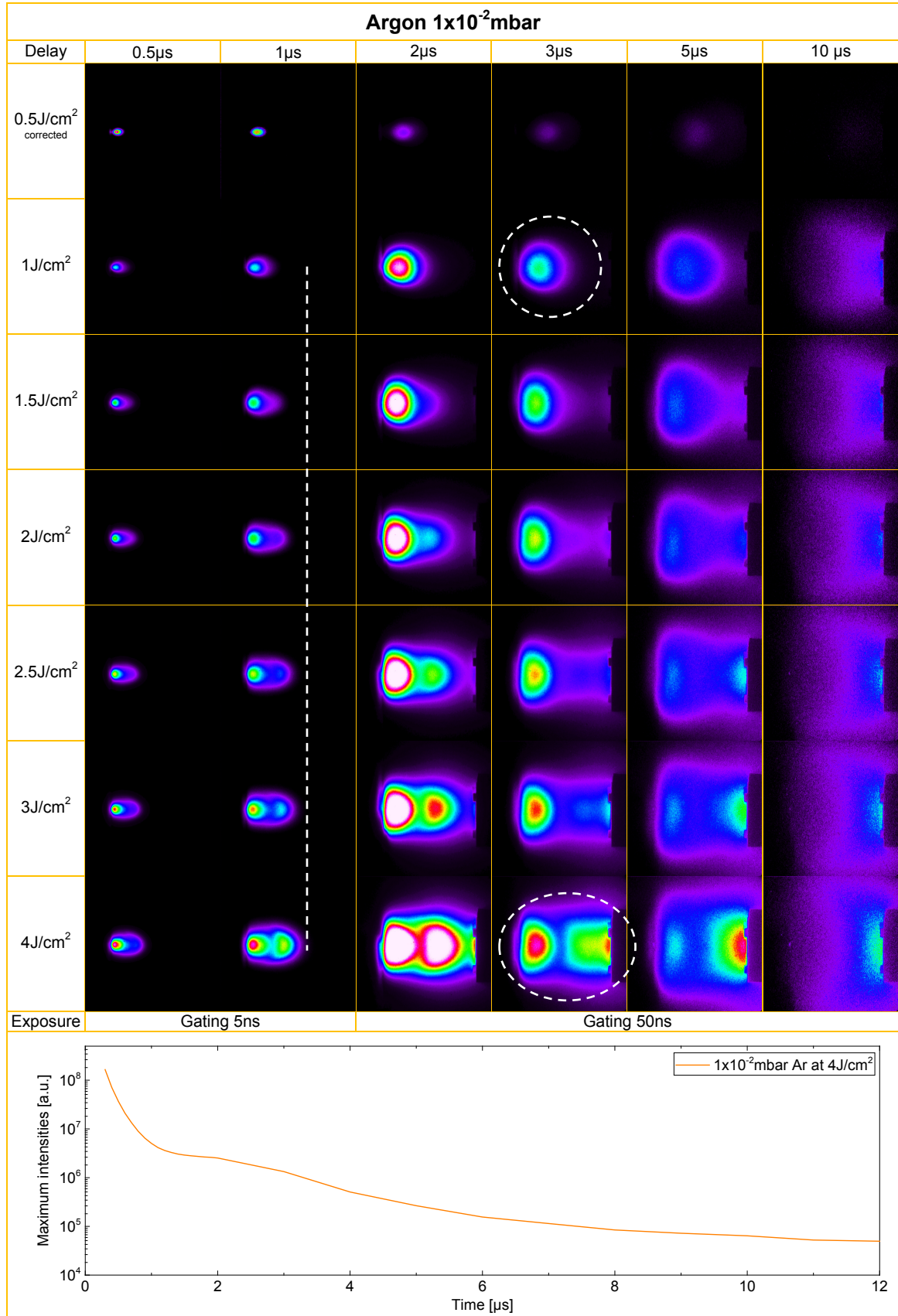
Fig.7.9. ICCD time resolved plasma imaging for 1x10⁻²mbar Ar without substrate heating for different fluences. Images of visible light (200 nm-1000 nm) with no filter applied. The plume expands from the ablated target on the left to the substrate on the right. All images for each time frame share the same intensity scale. A chart of the evolution of the time resolved maximum emission intensities for the 4J/cm² ablation is presented to evidence the strong decay in light emission. Two different gatings were used to adequately capture the plasma expansion dynamics (5 ns and 50 ns).
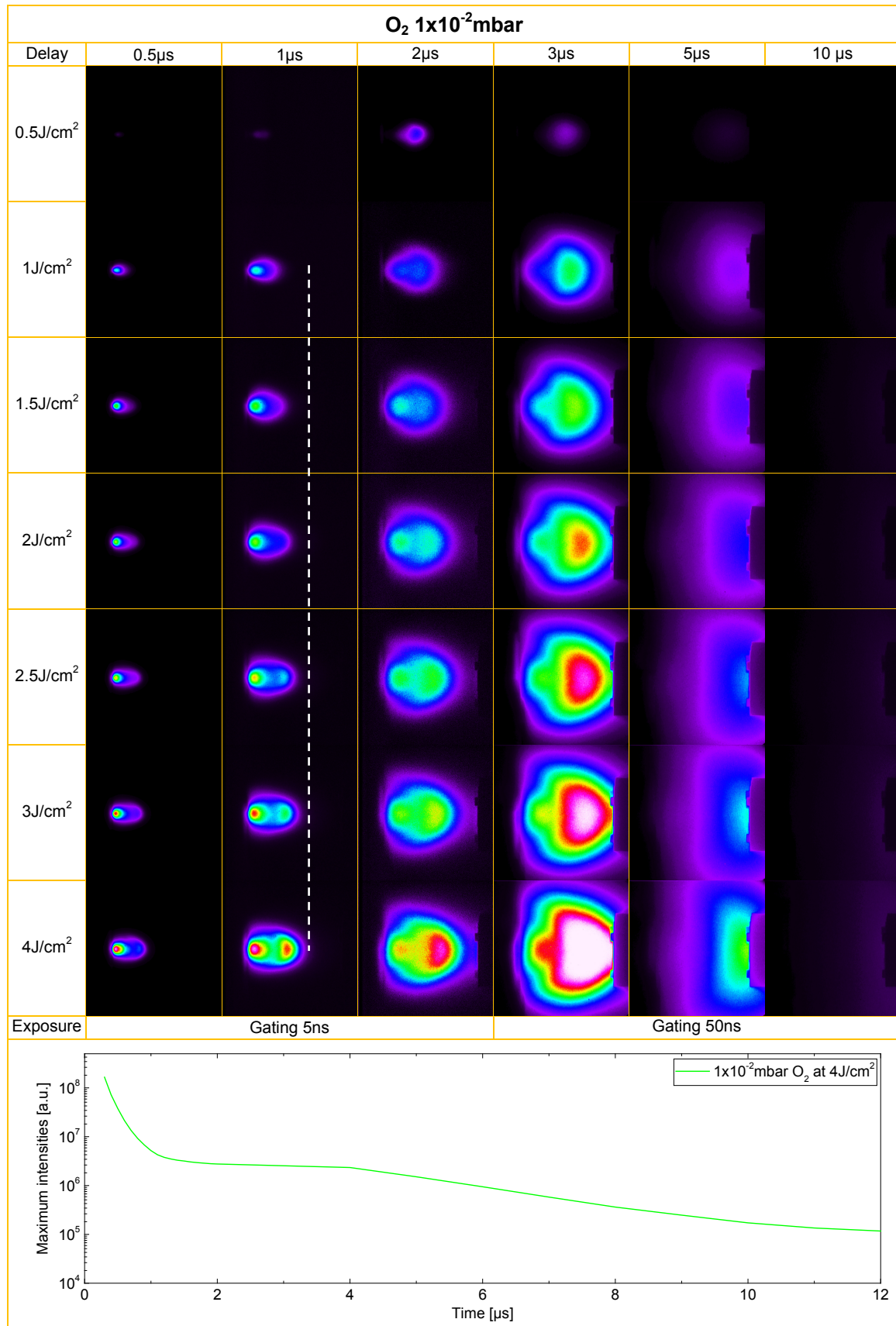
Fig.7.10. ICCD time resolved plasma imaging for 1×10^{-2} mbar O_2 without substrate heating for different fluences. Images of visible light (200 nm-1000 nm) with no filter applied. The plume expands from the ablated target on the left to the substrate on the right. All images for each time frame share the same intensity scale. A chart of the evolution of the time resolved maximum emission intensities for the $4J/cm^2$ ablation is presented to evidence the strong decay in light emission. Two different gatings were used to adequately capture the plasma expansion dynamics (5 ns and 50 ns).

7.2   The effect of high background pressures on the plasma plume shape

From the previous imaging results it seems that a ns glimpse at the plasma plume shape should be sufficient to identify the regime in which the deposition is taking place. From the vacuum regime with a strong forward deposition that slightly rebounds upon arrival at the substrate, to the diffusion-like regime with a very slow expansion velocity with intense rebounds passing through the transition regime with its characteristic plume splitting. However the pressures explored so far have been just three: vacuum, $1x10^{-2}$mbar, and $1x10^{-1}$mbar. The following pages explore these regimes with additional pressures and verify if there is indeed a fundamental difference in plasma plume shape when using Ar or O_2 as background gases (arrow like form for Ar vs. spherical for O_2). A fluence of 3 J/cm^2 was used for all the following measurements.

The results are shown in Fig.7.11 for Ar and Fig.7.13 for O_2. In both cases the pressures are explored starting from $1x10^{-3}$mbar followed by subsequent and approximately doubling of the pressures up to $5x10^{-1}$mbar. The intensity scales are all different for each single image to maximize contrast due to the very strong emission intensity variations with pressure. For reference, a chart of the time evolution of the maximum emission intensities for some of the different pressures is shown below the images.

The results for the expansion of $La_{0.4}Ca_{0.6}MnO_3$ in Ar show clearly the boundary pressures at which the expansion regime changes. Vacuum ($1x10^{-5}$mbar) and $1x10^{-3}$mbar show very similar profiles and the latter has not been included due to space limitations. It is at ~$2.5x10^{-3}$mbar were the transition from the vacuum expansion to the transition regime begins. The plume expansion shows shorter travelled distances for the same time frame evidencing that the background gas pressure is sufficient to start affecting the plume. The split emission at >3µs is caused by the collision at the substrate and is not considered plume splitting. It is at $7.5x10^{-3}$mbar when the plume splitting can be noticed (<1µs). As the pressure is raised the plume splitting becomes clearer and happens earlier in time (at $1x10^{-2}$mbar it is visible at ~0.7µs although not shown in the figure). No rebound of material is detected in the transition regime. The shift to the diffusion like regime begins at $2.5x10^{-2}$mbar with the initial plume splitting visible below 0.5 µs but quickly stopped by the background gas forming a slow expanding plume with all species traveling together (inferred from the selective imaging results from chapter 4). Interestingly the rebound of the plasma plume upon arrival at the substrate does not take place until a pressure of $7.5x10^{-2}$mbar is reached (highlighted with an arrow) and gets delayed in time with higher pressures due to the slower expanding velocities. Once in the diffusion regime there is a clear reduction of the expansion velocities with pressure (highlighted with a dashed line at 1µs)

$1x10^{-1}$mbar Ar shapes the plume to an arrow like profile up to ~2µs, with higher pressures enhancing that effect beyond that time frame. At $3x10^{-1}$mbar and above the arrow like shape is

progressively transformed into an "octopus" like shape. The relatively high background pressure confines most species in a very slow expanding plume, but it seems that the highly energetic species located at its centre are able to perforate it evolving with time into a "snow-plough" like expansion. An expansion that also rebounds once it arrives at the substrate but this takes place at an even later time frame (~33μs for $3x10^{-1}$mbar Ar and ~45μs for $5x10^{-1}$mbar Ar). Some of the increases in emission intensities due to these rebound effects are visible in the maximum intensity profiles vs. time added as reference in the bottom part of Fig.7.11. The chart also evidences the almost two orders of magnitude increase in intensities for the highest pressure regimes.

In the case of an O_2 background (Fig.7.13) the plasma plume expansion dynamics are very similar to Ar but with some particularities. The shift from the vacuum like to the transition regime is very clear and also takes place at $2.5x10^{-3}$mbar where the initial interactions with the background gas excite the plume front apart from lowering its expansion velocity. The plume splitting can be seen at $5x10^{-3}$mbar O_2 (t = ~3μs), a lower pressure compared to Ar, most likely because of the higher emission of O_2 vs. Ar at these pressures (Fig.7.7) which makes it easier to observe. This means that probably at $5x10^{-3}$mbar Ar the plume splitting (that will deviate the film composition) is also taking place but is not observable using plasma imaging. As pressure is raised the plume splitting happens earlier in time. This has been highlighted in Fig.7.13 using a dashed arrow from 3 μs at $5x10^{-3}$mbar to 0.5 μs at $1x10^{-2}$mbar. The evolution to the diffusion like regime also takes place at ~$2.5x10^{-2}$mbar with all species confined by the background gas at around ~1 μs. The emission above the substrate upon arrival is clearly visible at 10 μs at $7.5x10^{-2}$mbar O_2. Coincidentally a similar arrival time was shown for Ar but at the lower pressure of $5x10^{-2}$mbar Ar (higher stopping power). The plasma plume shape in the diffusion like regime is very similar to the Ar case in comparison with the transition regime where the fast component of the split plume showed much higher and distributed excitations compared to Ar.

At $1x10^{-1}$mbar O_2 the arrow like form of the plume is not visible but it appears at the following higher pressure of $3x10^{-1}$mbar. In addition the "snow-plough" like expansion does not appear until $5x10^{-1}$mbar. Thus the plume shape seems strongly dependent on the stopping power of the background gas (kinetics and pressure) with O_2 requiring higher pressure than Ar to achieve similar plume dynamics. Although in the transition regime O_2 evidences a more intense and wider spherical front of the split plume. This is reasonable since the level of confinement of the plume at this pressure is low allowing a wider spatial distribution of scattered species some of which react with the O_2 background gas. For Ar the emission comes mostly from energetic collisional interactions, where scattered species are not contributing to the emission intensity (no chemical reactions possible to form excited state species, i.e.: La*+O → LaO*).

Concerning the excitation effect above the substrate for O_2, like the rebound in Ar, it is also delayed in time with increasing pressures (highlighted with an arrow at 10 μs at $7.5x10^{-2}$mbar in

Fig.7.13) and is clearly visible as irregularities in the max. intensities vs. time chart in Fig.7.13. The rebound of material back to the ablated target in O_2 is also visible.

	0.5µs	1µs	3µs	5µs	10 µs	20 µs	45µs	
Argon								
Vacuum								**Vacuum like regime**
2.5x10⁻³ mbar Ar								
5x10⁻³ mbar Ar								
7.5x10⁻³ mbar Ar								**Plume splitting begins**
1x10⁻² mbar Ar								**Transition regime**
2.5x10⁻² mbar Ar								**Diffusion like regime**
5x10⁻² mbar Ar								
7.5x10⁻² mbar Ar								
1x10⁻¹ mbar Ar								
3x10⁻¹ mbar Ar								
5x10⁻¹ mbar Ar								
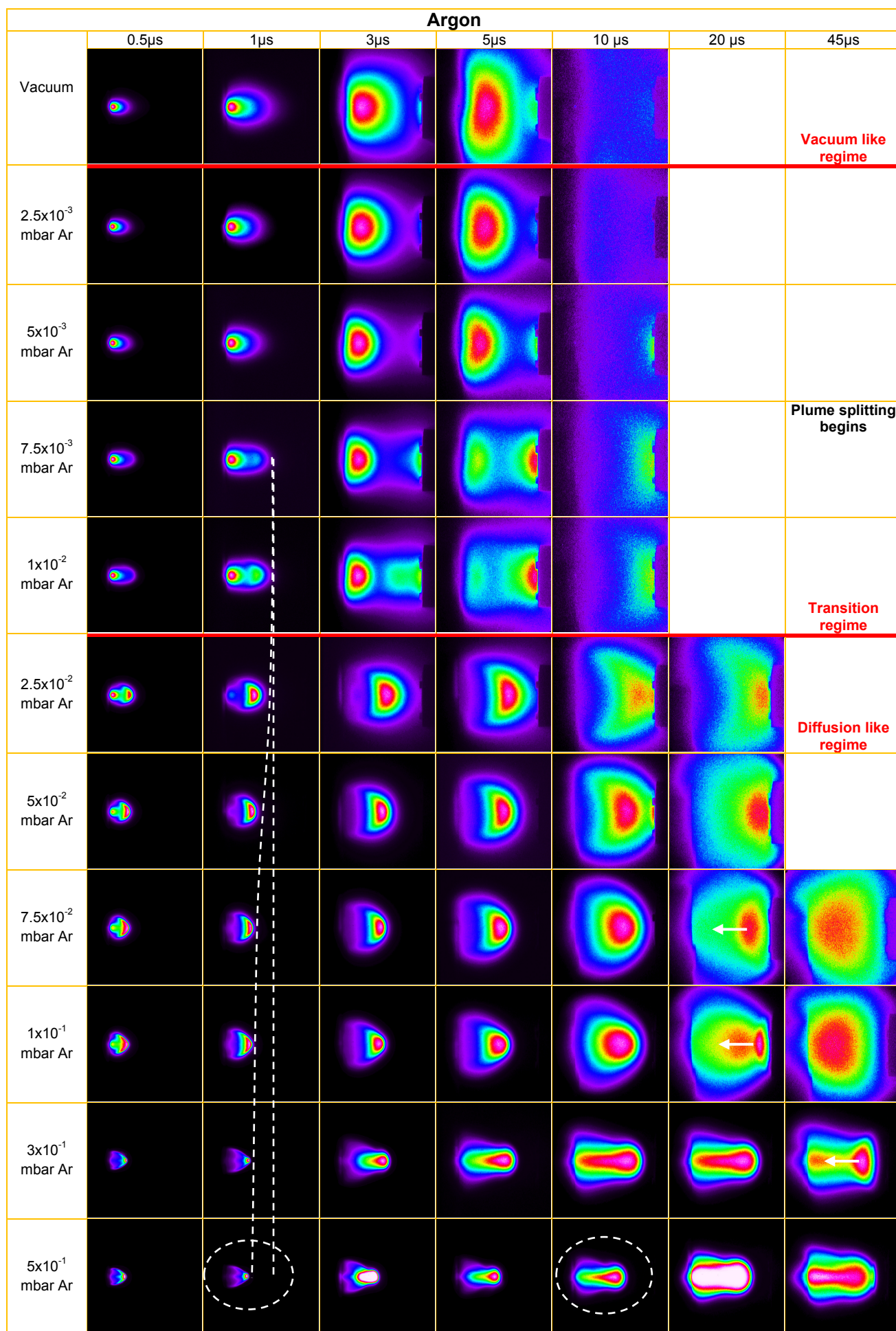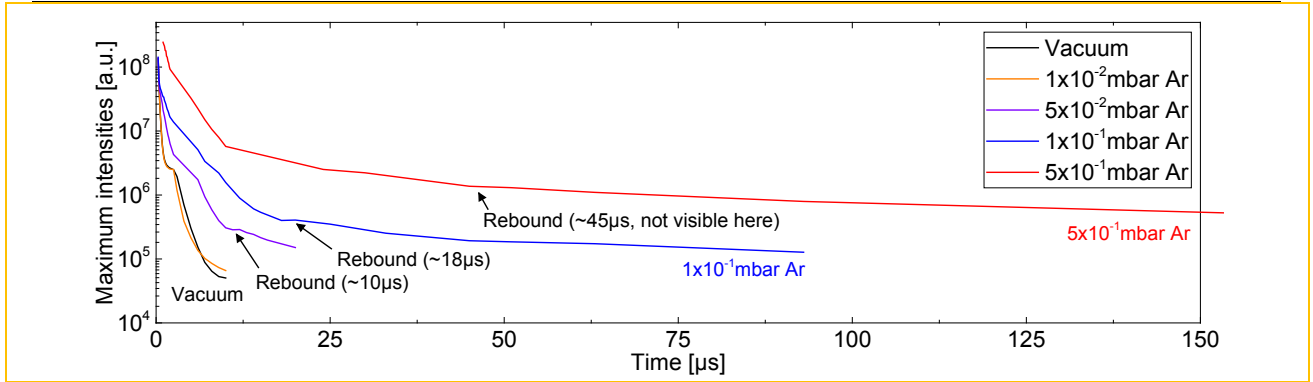
Fig.7.11. ICCD time resolved plasma imaging for different Ar pressures without substrate heating. Images of visible light (200 nm-1000 nm) with no filter applied. The plume expands from the ablated target on the left to the substrate on the right. Due to the strong intensity variations with pressure each single image has an individual intensity scale applied to maximize contrast. A chart of the evolution of the time resolved maximum emission intensities for several pressures is presented as reference to the strong an varied decays in emission intensities.

	0.5µs	1µs	3µs	5µs	10 µs	20 µs	**33µs**
Vacuum							**Vacuum like regime**
2.5×10^{-3} mbar O_2							
5×10^{-3} mbar O_2							**Plume splitting begins**
7.5×10^{-3} mbar O_2							
1×10^{-2} mbar O_2							**Transition regime**
2.5×10^{-2} mbar O_2							**Diffusion like regime**
5×10^{-2} mbar O_2							
7.5×10^{-2} mbar O_2							
1×10^{-1} mbar O_2							
3×10^{-1} mbar O_2							
5×10^{-1} mbar O_2							

Fig.7.13. ICCD time resolved plasma imaging for different O_2 pressures without substrate heating. Images of visible light (200 nm-1000 nm) with no filter applied. The plume expands from the ablated target on the left to the substrate on the right. Due to the strong intensity variations with pressure each single image has an individual intensity scale applied to maximize contrast. A chart of the evolution of the time resolved maximum emission intensities at various pressures is presented as reference to the strong and varied decays in emission intensities.

7.3   Conclusions

This chapter covered the influence of laser fluence and pressure in the ablation of $La_{0.4}Ca_{0.6}MnO_3$ and its plume dynamics. It has shown that the fluence has a strong effect not only on the ablation rates but also on the kinetic energies of the ablated species (average and maximum). A noticeable portion of the species had values considerably above 100 eV and the use of a MS limited to 100 eV would hinder most investigations of the plasma plume. Furthermore with kinetic energies already above 50 eV the sputtering yield increase considerably [36] and these highly energetic species are a likely source of defects to the deposited film unless a background gas is used to reduce their velocities. A background gas with a pressure suitable for the used fluence, as fluence shifts the plume expansion dynamics from one regime to another at a similar pressure.

In addition, detailed plasma plume imaging for many pressures has shown at which pressures the change from one pressure regime to another takes place (for a fluence of 3 J/cm^2, with the substrate and at RT). Mainly, that the shaping of the plasma plume is strongly related to the stopping power (scattering cross section and mass) and pressure of the background gas, with O_2 requiring slightly higher pressures than Ar to achieve similar effects.

8 Conclusions and outlook

Clearly, the complexity of PLD is nothing but fascinating. How a seemingly simple process of pulsed laser absorption, material ablation, and subsequent deposition of a film on a substrate can bring such complexity is remarkable. One can understand the struggle and frustration of many PLD users as what at first seems an insignificant change in the deposition parameters (i.e.: a pressure change, a slight misalignment of the plume with respect to the substrate or a change in substrate temperature which would influence the local gas density) can have dramatic consequences for the film growth and subsequent physical properties of a grown film.

At this point the question if a congruent transfer in PLD is possible has been explored in detail. Congruent transfer is indeed possible, but a thorough understanding of the process and the influence of its parameters is needed. The presented work has analysed the effects of the main process and deposition parameters in terms of film thickness and composition with the intention of providing guidance to the PLD users.

One of the main drivers to achieve a congruent transfer are the mass ratios of multi-elemental targets. For this reason five different multi-element oxides materials have been investigated (including the thesis central material $La_{0.4}Ca_{0.6}MnO_3$) to show the challenges and solutions to achieve a congruent transfer. Compositional deviations with respect to target composition are common with reported deviations of up to ~70% at certain pressures. The understanding of such deviations has also been reported and classified in the initially mentioned three sources of compositional changes: target, plume and substrate effects.

Target ablation effects

With respect to target effects, laser fluence and its interrelationship with the background gas through kinetic energy was shown. At a fixed pressure, higher fluences yield higher kinetic energies and ablation rates. This is equivalent to shift the plume expansion regimes to higher pressures since more plume species interact. Alternatively, the use of very low fluences can cause havoc in the congruent transfer goal as MS measurements have shown very strong changes in proportions of detected ionic species compared to higher fluences.

The influence of laser spot geometry was also assessed. The flip-over effect results in strong changes not only in thickness but also in film composition and does not disappear until high pressure regimes are used, where all species are confined together ($1x10^{-1}$ mbar and above when having the substrate at 40 mm).

Plume effects

The plasma plume has been identified as the main location where compositional changes take place. The relationship between background gas and elemental mass ratios is the major source for compositional changes. This has been verified for 5 different target materials and a relationship between mass ratios and compositional deviations was found. A possible explanation is that at precise pressure windows preferential scattering of the lighter elements takes place and an enrichment of the heavier elements in the films occurs. This was verified by film composition methods (RBS), plasma imaging as well as MS, providing a consistent picture of this effect in terms of neutral (excited species) and ions. Furthermore with increasing target to substrate distance the deviations increase until the heavier elements are also scattered either by the distance travelled or by the use of a higher background pressure. When depositing multi-element materials with high mass-ratios the selection of the background gas pressure is critical.

A selection which is not absolute as it was shown that fluence and substrate heating can shift the expansion regime to different pressure values. Both will require higher pressures to achieve similar results, with the latter causing a density gradient in the background gas. Analytical estimations of the gas densities were shown that would allow adjusting the background gas pressure to achieve similar densities if the substrate temperature is varied. In both mentioned cases careful plasma imaging can quickly identify the regime by looking at the plume shape which was also shown to be greatly affected by pressure and stopping power of the background gas (scattering cross section and mass).

Additionally, MS measurements of the plume confirmed the preferential formation of metal oxygen species with high dissociation energies. Moreover, the efficiency on the dissociation of O_2 has been linked to the kinetic energy of the species, which was found to be strongly dependant on the mass of the participating elements with higher masses yielding higher kinetic energies (double layer effect combined with longer acceleration times).

Furthermore the selected pressure might reduce or cancel the strong forward character of PLD and yield a loss in material deposition efficiency of ~70%. Although at first it seemed that complete scattering was its cause, surprisingly it was found that at such pressure regimes, where all species expand together, the substrate and substrate holder play a major role.

Substrate effects

Apart from the substrate angular location which strongly affects film thickness and composition, the substrate and its holder have a strong and unexpected interaction with the plasma plume. It was found that at high pressure regimes ($>5\times10^{-2}$mbar) a transient high local pressure is generated above the substrate surface due to the trapping of the background gas (it is estimated to increase the local pressure by a factor of 10), which in the case of Ar generates a rebound of the plume that recoats the ablated target and in the case of O_2 creates in addition strong excitations above the substrate assigned to metal oxygen species (mainly LaO^+ for $La_{0.4}Ca_{0.6}MnO_3$). The recoating of the target was found to have a very different composition with respect to the original composition (background gas dependent) and to be significant with a thickness similar to the deposited film and constituting ~20% of the ablated material per pulse. Furthermore, the composition of this rebounded material will progressively deviate with time from the original target composition (no steady state). This itself raises questions of how accurately can a film composition be controlled and how significant is the impact on creating defects in the as-grown film due to the unintentional and non-stoichiometric transfer of species.

A slight rebound was also detected in vacuum but in this case caused by the subsequent rebound upon impingement on the holder of the highly energetic species which were also found to have dissimilar arrival times for the different species.

In summary, the reported results show the dependency of target elemental mass ratios, background pressure, laser fluence, angular location, and laser spot geometry as these were the parameters explored in these experiments. It is therefore strongly recommended to measure the composition of the deposited films to avoid reaching erroneous conclusions when measuring their functional performances.

Outlook

There are evidently remaining open questions which would be worth exploring. They have been briefly listed below for clarity:

1. Design and testing of a substrate holder that takes advantage of the excitation effect above the substrate utilized to incorporate more oxygen into a film (i.e.: parabolic). Species resolved plasma imaging through a carefully designed viewing window would allow assessing its effectiveness. A considerable challenge would be how to heat the substrate and avoid non-uniform heating when using this particular holder.

2. Species selected plasma plume imaging in an N_2O environment using the imaging parameters described in the thesis (image accumulations are fundamental to increase image contrast at longer time frames).

3. Angle-resolved MS measurements with additional species such as neutrals to get a clearer picture of the plasma plume chemistry.

4. Repetition of the 5 target materials experiments at additional pressures to identify if and how the slope of mass vs. compositional deviations changes with pressure.

5. Species resolved imaging to identify the chemistry aspect more clearly, also angle resolved.

6. Study of the influence of the laser wavelength on the plasma plume dynamics by imaging and angle resolved MS.

7. Investigation on how important the re-excitation effect above the substrate is for film composition. Using a selection of metals that will not show this effect and comparing the film composition in terms of metal and oxygen content.

8. Further studies on the influence of angular positions of heated substrates on film composition and properties.

9. Tracing the origin of O^- using a target with $^{18}O_2$ isotope.

Bibliography

[1] D. Dijkkamp, T. Venkatesan, X. Wu, S. Shaheen, N. Jisrawi, Y. Min-Lee, W. McLean, M. Croft, Preparation of Y-Ba-Cu oxide superconductor thin films using pulsed laser evaporation from high Tc bulk material, Applied Physics Letters, 51 (1987) 619-621.

[2] D.B. Chrisey, G.K. Hubler, Pulsed laser deposition of thin films, Wiley, New York, 1994.

[3] T. Venkatesan, Pulsed laser deposition—invention or discovery?, Journal of Physics D: Applied Physics, 47 (2014) 034001.

[4] A.J. Millis, Lattice effects in magnetoresistive manganese perovskites, Nature, 392 (1998) 147-150.

[5] H.M. Christen, G. Eres, Recent advances in pulsed-laser deposition of complex oxides, Journal of Physics: Condensed Matter, 20 (2008) 264005.

[6] J. Schou, Physical aspects of the pulsed laser deposition technique: The stoichiometric transfer of material from target to film, Applied Surface Science, 255 (2009) 5191-5198.

[7] R. Eason, Pulsed laser deposition of thin films: applications-led growth of functional materials, John Wiley & Sons, 2007.

[8] T. Donnelly, J.G. Lunney, S. Amoruso, R. Bruzzese, X. Wang, X. Ni, Angular distributions of plume components in ultrafast laser ablation of metal targets, Applied Physics A: Materials Science and Processing, 100 (2010) 569-574.

[9] R.E. Russo, X. Mao, H. Liu, J. Gonzalez, S.S. Mao, Laser ablation in analytical chemistry—a review, Talanta, 57 (2002) 425-451.

[10] D.W. Bäuerle, Laser processing and chemistry, Springer Science & Business Media, 2013.

[11] C. Liu, X. Mao, S. Mao, X. Zeng, R. Greif, R. Russo, Nanosecond and femtosecond laser ablation of brass: particulate and ICPMS measurements, Analytical Chemistry, 76 (2004) 379-383.

[12] W. Kautek, B. Roas, L. Schultz, Formation of Y-Ba-Cu-oxide thin films by pulsed laser deposition: A comparative study in the UV, visible and IR range, Thin Solid Films, 191 (1990) 317-334.

[13] H. Liu, X. Mao, J. Yoo, R. Russo, Early phase laser induced plasma diagnostics and mass removal during single-pulse laser ablation of silicon, Spectrochimica Acta Part B: Atomic Spectroscopy, 54 (1999) 1607-1624.

[14] R. Kelly, A. Miotello, Laser-pulse sputtering of atoms and molecules Part II. Recondensation effects, Nuclear Instruments and Methods in Physics Research Section B: Beam Interactions with Materials and Atoms, 91 (1994) 682-691.

[15] R.K. Singh, J. Narayan, Pulsed-laser evaporation technique for deposition of thin films: Physics and theoretical model, Physical Review B, 41 (1990) 8843-8859.

[16] A. Mele, A. Giardini Guidoni, R. Kelly, A. Miotello, S. Orlando, R. Teghil, Spatial distribution of laser-ablated material by probing a plasma plume in three dimensions, Applied Surface Science, 96–98 (1996) 102-111.

[17] M. Tyunina, S. Leppävuori, Effects of laser fluence, size, and shape of the laser focal spot in pulsed laser deposition using a multielemental target, Journal of Applied Physics, 87 (2000) 8132-8142.

[18] A. Miotello, R. Kelly, B. Braren, C.E. Otis, Novel geometrical effects observed in debris when polymers are laser sputtered, Applied Physics Letters, 61 (1992) 2784-2786.

[19] J. Schou, B. Toftmann, S. Amoruso, Dynamics of a laser-produced silver plume in an oxygen background gas, in, 2004, pp. 110-120.

[20] N. Pryds, J. Schou, S. Linderoth, The spatial thickness distribution of metal films produced by large area pulsed laser deposition, Applied Surface Science, 253 (2007) 8231-8234.

[21] M.M. Urtasun, Perovskite Thin Films Deposited by Pulsed Reactive Crossed Beam Laser Ablation as Model Systems for Electrochemical Applications, 2005.

[22] S. Gurlui, M. Agop, P. Nica, M. Ziskind, C. Focsa, Experimental and theoretical investigations of a laser-produced aluminum plasma, Physical Review E, 78 (2008) 026405.

[23] S. Canulescu, E.L. Papadopoulou, D. Anglos, T. Lippert, C.W. Schneider, A. Wokaun, Mechanisms of the laser plume expansion during the ablation of $LiMn_2O_4$, Journal of Applied Physics, 105 (2009) 063107.

[24] A. Sambri, C. Aruta, E. Di Gennaro, X. Wang, U.S. di Uccio, F.M. Granozio, S. Amoruso, Effects of oxygen background pressure on the stoichiometry of a $LaGaO_3$ laser ablation plume investigated by time and spectrally resolved two-dimensional imaging, Journal of Applied Physics, 119 (2016) 125301.

[25] D.M. Packwood, S. Shiraki, T. Hitosugi, Effects of Atomic Collisions on the Stoichiometry of Thin Films Prepared by Pulsed Laser Deposition, Physical Review Letters, 111 (2013) 036101.

[26] S.S. Harilal, Influence of spot size on propagation dynamics of laser-produced tin plasma, Journal of Applied Physics, 102 (2007) 123306.

[27] I. Marozau, A. Shkabko, G. Dinescu, M. Döbeli, T. Lippert, D. Logvinovich, M. Mallepell, C. Schneider, A. Weidenkaff, A. Wokaun, Pulsed laser deposition and characterization of nitrogen-substituted $SrTiO_3$ thin films, Applied Surface Science, 255 (2009) 5252-5255.

[28] J. Budai, S. Tóth, Z. Tóth, M. Koós, Diamond-like carbon films prepared by reactive pulsed laser deposition in hydrogen and methane ambient, Applied Surface Science, 253 (2007) 8220-8225.

[29] L. You, N.T. Chua, K. Yao, L. Chen, J. Wang, Influence of oxygen pressure on the ferroelectric properties of epitaxial $BiFeO_3$ thin films by pulsed laser deposition, Physical Review B, 80 (2009) 024105.

[30] J.S. Horwitz, K.S. Grabowski, D.B. Chrisey, R.E. Leuchtner, Insitu deposition of epitaxial $PbZr_xTi_{(1-x)}O_3$ thin films by pulsed laser deposition, Applied Physics Letters, 59 (1991) 1565-1567.

[31] T. Ohnishi, B.T. Hang, X. Xu, M. Osada, K. Takada, Quality control of epitaxial $LiCoO_2$ thin films grown by pulsed laser deposition, Journal of Materials Research, 25 (2010) 1886-1889.

[32] T. Dumont, T. Lippert, M. Döbeli, H. Grimmer, J. Ufheil, P. Novák, A. Würsig, U. Vogt, A. Wokaun, Influence of experimental parameter on the Li-content of $LiMn_2O_4$

electrodes produced by pulsed laser deposition, Applied Surface Science, 252 (2006) 4902-4906.

[33] D. O'Mahony, J. Lunney, T. Dumont, S. Canulescu, T. Lippert, A. Wokaun, Laser-produced plasma ion characteristics in laser ablation of lithium manganate, Applied Surface Science, 254 (2007) 811-815.

[34] J. Gonzalo, J. Siegel, A. Perea, D. Puerto, V. Resta, M. Galvan-Sosa, C.N. Afonso, Imaging self-sputtering and backscattering from the substrate during pulsed laser deposition of gold, Physical Review B, 76 (2007) 035435.

[35] K. Kondoh, M. Suwa, K. Morita, Energy dependence of particle reflection coefficient of ions from solid surfaces in the low energy region below 200 eV, Nuclear Instruments and Methods in Physics Research Section B: Beam Interactions with Materials and Atoms, 78 (1993) 68-71.

[36] H. Andersen, H. Bay, Sputtering yield measurements, in: R. Behrisch (Ed.) Sputtering by Particle Bombardment I, Springer Berlin Heidelberg, 1981, pp. 145-218.

[37] R. Behrisch, W. Eckstein, Sputtering by particle bombardment: experiments and computer calculations from threshold to MeV energies, Springer Science & Business Media, 2007.

[38] M. Mandeljc, M. Kosec, S. Gabuda, S. Kozlova, S. Erenburg, N. Bausk, XANES spectroscopy study of Pb (Ti, Zr) O_3 ferroelectric thin films, Integrated Ferroelectrics, 67 (2004) 191-199.

[39] M. Mandeljc, B. Malič, M. Kosec, G. Dražič, Crystallization of zirconium-rich PLZT thin films below 500 C, Integrated Ferroelectrics, 46 (2002) 329-338.

[40] D.B. Geohegan, A.A. Puretzky, Species-resolved imaging and gated photon counting spectroscopy of laser ablation plume dynamics during KrF and ArF laser PLD of amorphous diamond films, MRS Online Proceedings Library Archive, 397 (1995).

[41] A. Voevodin, J. Jones, J. Zabinski, Characterization of ZrO_2/Y_2O_3 laser ablation plasma in vacuum, oxygen, and argon environments, Journal of Applied Physics, 88 (2000) 1088-1096.

[42] K. Shimamoto, M. Döbeli, T. Lippert, C.W. Schneider, Cation ratio and ferroelectric properties of TbMnO3 epitaxial films grown by pulsed laser deposition, Journal of Applied Physics, 119 (2016) 184102.

[43] G. Sauerbrey, Verwendung von Schwingquarzen zur Wägung dünner Schichten und zur Mikrowägung, Zeitschrift für physik, 155 (1959) 206-222.

[44] A. Srivastava, P. Sakthivel, Quartz-crystal microbalance study for characterizing atomic oxygen in plasma ash tools, Journal of Vacuum Science & Technology A, 19 (2001) 97-100.

[45] M. Bator, Investigation of the magnetic and magnetoelectric properties of orthorhombic $REMnO_3$ thin films, in, Diss. Eidgenössische Technische Hochschule ETH Zürich, Nr. 20987, 2013, 2013.

[46] M. Nastasi, J.W. Mayer, Y. Wang, Ion beam analysis: fundamentals and applications, CRC Press, 2014.

[47] W.-K. Chu, J.W. Mayer, M.-A. Nicolet, Backscattering spectroscopy, in, Academic Press, New York, 1978.

[48] Y. Wang, M. Nastasi, Y. Wang, M. Nastasi, Handbook of Modern Ion Beam Analysis, Materials Research Society, Pittsburgh, PA, (2010).

[49] C. Jeynes, N.P. Barradas, E. Szilágyi, Accurate Determination of Quantity of Material in Thin Films by Rutherford Backscattering Spectrometry, Analytical Chemistry, 84 (2012) 6061-6069.

[50] S. Wicklein, A. Sambri, S. Amoruso, X. Wang, R. Bruzzese, A. Koehl, R. Dittmann, Pulsed laser ablation of complex oxides: The role of congruent ablation and preferential scattering for the film stoichiometry, Applied Physics Letters, 101 (2012) 131601.

[51] C.-R. Cho, A. Grishin, Background oxygen effects on pulsed laser deposited $Na_{0.5}K_{0.5}NbO_3$ films: From superparaelectric state to ferroelectricity, Journal of Applied Physics, 87 (2000) 4439-4448.

[52] C. Kottler, M. Döbeli, F. Glaus, M. Suter, A spectrometer for low energy heavy ion ERDA, Nuclear Instruments and Methods in Physics Research Section B: Beam Interactions with Materials and Atoms, 248 (2006) 155-162.

[53] M. Simon, M. Döbeli, A. Müller, H.-A. Synal, In-air STIM with a capillary microprobe, Nuclear Instruments and Methods in Physics Research Section B: Beam Interactions with Materials and Atoms, 273 (2012) 237-240.

[54] S. Heiroth, Pulsed laser deposition of functional electroceramic thin films for micro solid oxide fuel cell applications in, 2010.

[55] T. Venkatesan, X.D. Wu, A. Inam, J.B. Wachtman, Observation of two distinct components during pulsed laser deposition of high T_c superconducting films, Applied Physics Letters, 52 (1988) 1193-1195.

[56] T.C. Droubay, L. Qiao, T.C. Kaspar, M.H. Engelhard, V. Shutthanandan, S.A. Chambers, Nonstoichiometric material transfer in the pulsed laser deposition of $LaAlO_3$, Applied Physics Letters, 97 (2010).

[57] R.E. Muenchausen, K.M. Hubbard, S. Foltyn, R.C. Estler, N.S. Nogar, C. Jenkins, Effects of beam parameters on excimer laser deposition of $YBa_2Cu_3O_{7-\delta}$, Applied Physics Letters, 56 (1990) 578-580.

[58] R. Pérez Casero, F. Kerhervé, J.P. Enard, J. Perrière, P. Regnier, Study of laser ablation of BiSrCaCuO, Applied Surface Science, 54 (1992) 147-153.

[59] J. Schou, Laser beam-solid interactions: fundamental aspects, Elsevier, 2006.

[60] N. Izyumskaya, Y. Alivov, H. Morkoç, Oxides, Oxides, and More Oxides: High-κ Oxides, Ferroelectrics, Ferromagnetics, and Multiferroics, Critical Reviews in Solid State and Materials Sciences, 34 (2009) 89-179.

[61] R. Hott, R. Kleiner, T. Wolf, G. Zwicknagl, Superconducting Materials — A Topical Overview, in: A. Narlikar (Ed.) Frontiers in Superconducting Materials, Springer Berlin Heidelberg, 2005, pp. 1-69.

[62] J.M.D. Coey, M. Coey, S. Viret, M. von, Mixed-valence manganites, Advances in Physics, 58 (2009) 571-697.

[63] D. Ali, M.Z. Butt, M. Khaleeq-ur-Rahman, Ablation yield and angular distribution of ablated particles from laser-irradiated metals: The most fundamental determining factor, Applied Surface Science, 257 (2011) 2854-2860.

[64] H. Dang, Q. Qin, Angular distribution of laser-ablated species from a $Pr_{0.67}Sr_{0.33}MnO_3$ target, Physical Review B, 60 (1999) 11187-11192.

[65] S. Amoruso, C. Aruta, R. Bruzzese, X. Wang, U. Scotti di Uccio, Substrate heating influence on the deposition rate of oxides during pulsed laser deposition in ambient gas, Applied Physics Letters, 98 (2011) 101501.

[66] B. Thestrup, B. Toftmann, J. Schou, B. Doggett, J.G. Lunney, Ion dynamics in laser ablation plumes from selected metals at 355 nm, Applied Surface Science, 197–198 (2002) 175-180.

[67] J. Chen, M. Döbeli, D. Stender, K. Conder, A. Wokaun, C.W. Schneider, T. Lippert, Plasma interactions determine the composition in pulsed laser deposited thin films, Applied Physics Letters, 105 (2014) 114104.

[68] S. Faaland, K. Knudsen, M.-A. Einarsrud, L. Rørmark, R. Høier, T. Grande, Structure, stoichiometry, and phase purity of calcium substituted lanthanum manganite powders, Journal of Solid State Chemistry, 140 (1998) 320-330.

[69] M. Khaleeq-ur-Rahman, D. Ali, M.Z. Butt, Angular distribution of ions produced by laser ablation of magnesium with special reference to sublimation energy, Vacuum, 85 (2010) 170-175.

[70] I. Konomi, T. Motohiro, T. Asaoka, Angular distribution of atoms ejected by laser ablation of different metals, Journal of Applied Physics, 106 (2009).

[71] 8 - Thermochemical data, in: W.F.G.C. Totemeier (Ed.) Smithells Metals Reference Book (Eighth Edition), Butterworth-Heinemann, Oxford, 2004, pp. 1-58.

[72] J.W. Arblaster, Chapter 258 - Selected Values of the Thermodynamic Properties of Scandium, Yttrium, and the Lanthanide Elements, in: G.B. Jean-Claude, K.P. Vitalij (Eds.) Handbook on the Physics and Chemistry of Rare Earths, Elsevier, 2013, pp. 321-565.

[73] J.J. Dubowski, S. Tanev, Photon-based Nanoscience and Nanobiotechnology, Springer Science & Business Media, 2007.

[74] J. Schou, B. Toftmann, S. Amoruso, Dynamics of a laser-produced silver plume in an oxygen background gas, in: High-Power Laser Ablation V, 2004, pp. 110-120.

[75] S. Amoruso, B. Toftmann, J. Schou, Thermalization of a UV laser ablation plume in a background gas: From a directed to a diffusionlike flow, Physical Review E, 69 (2004) 056403.

[76] A. Ojeda-G-P, C.W. Schneider, M. Döbeli, T. Lippert, A. Wokaun, Angular distribution of species in pulsed laser deposition of $La_xCa_{1-x}MnO_3$, Applied Surface Science, 336 (2015) 150-156.

[77] W.M. Haynes, CRC handbook of chemistry and physics, CRC press, 2014.

[78] F. Phelps III, MIT wavelength tables. Volume 2. Wavelengths by element, 1982.

[79] S.S. Batsanov, Van der Waals Radii of Elements, Inorganic Materials, 37 871-885.

[80] S.I. Anisimov, B.S. Luk'yanchuk, A. Luches, An analytical model for three-dimensional laser plume expansion into vacuum in hydrodynamic regime, Applied Surface Science, 96–98 (1996) 24-32.

[81] A. Sambri, S. Amoruso, X. Wang, F.M. Granozio, R. Bruzzese, Plume propagation dynamics of complex oxides in oxygen, Journal of Applied Physics, 104 (2008) 053304.

[82] D. Marla, U.V. Bhandarkar, S.S. Joshi, Critical assessment of the issues in the modeling of ablation and plasma expansion processes in the pulsed laser deposition of metals, Journal of Applied Physics, 109 (2011) 021101.

[83] D.B. Geohegan, D.N. Mashburn, Characterization of ground-state neutral and ion transport during laser ablation of Y1Ba2Cu3O7−x using transient optical absorption spectroscopy, Applied Physics Letters, 55 (1989) 2345-2347.

[84] S. Heiroth, J. Koch, T. Lippert, A. Wokaun, D. Günther, F. Garrelie, M. Guillermin, Laser ablation characteristics of yttria-doped zirconia in the nanosecond and femtosecond regimes, Journal of Applied Physics, 107 (2010) 014908.

[85] S. Amoruso, R. Bruzzese, Substrate heating influence on plume propagation during pulsed laser deposition of complex oxides, Applied Physics Letters, 91 (2007) 151501-151501.

[86] K. Jousten, Handbook of vacuum technology, John Wiley & Sons, 2008.

[87] M. Kogan, Rarefied Gas Dynamics, Plenum Press, New York, 2 (1969) l.

[88] P. Mora, Plasma Expansion into a Vacuum, Physical Review Letters, 90 (2003) 185002.

[89] J.E. Crow, P.L. Auer, J.E. Allen, The expansion of a plasma into a vacuum, Journal of Plasma Physics, 14 (1975) 65-76.

[90] Y.B. Zeldovich, Y.P. Raizer, Physics of shock waves and high-temperature hydrodynamic phenomena, in, DTIC Document, 1965.

[91] Y.M. Ibrahim, E.H. Alsharaeh, M.S. El-Shall, Evidence for Penning Ionization in the Generation of Electronically Excited States of Transition Metal Cations by Laser Vaporization, The Journal of Physical Chemistry B, 108 (2004) 3959-3962.

[92] A. Ojeda-G-P, C.W. Schneider, M. Döbeli, T. Lippert, A. Wokaun, The flip-over effect in pulsed laser deposition: Is it relevant at high background gas pressures?, Applied Surface Science, 357, Part B (2015) 2055-2062.

[93] B. Toftmann, J. Schou, J. Lunney, Dynamics of the plume produced by nanosecond ultraviolet laser ablation of metals, Physical Review B, 67 (2003) 104101.

[94] I. Gornushkin, S. Shabanov, N. Omenetto, J. Winefordner, Nonisothermal asymmetric expansion of laser induced plasmas into vacuum, Journal of applied physics, 100 (2006) 073304.

[95] E. Buttini, A. Thum-Jäger, K. Rohr, The mass dependence of the jet formation in laser-produced particle beams, Journal of Physics D: Applied Physics, 31 (1998) 2165.

[96] J. Schou, Chapter 2 - Laser Beam-Solid Interactions: Fundamental Aspects, in: Y. Pauleau (Ed.) Materials Surface Processing by Directed Energy Techniques, Elsevier, Oxford, 2006, pp. 35-66.

[97] T.N. Hansen, J. Schou, J.G. Lunney, Langmuir probe study of plasma expansion in pulsed laser ablation, Appl Phys A, 69 (1999) S601-S604.

[98] O.V. Borisov, X.L. Mao, A. Fernandez, M. Caetano, R.E. Russo, Inductively coupled plasma mass spectrometric study of non-linear calibration behavior during laser ablation of binary Cu–Zn Alloys, Spectrochimica Acta Part B: Atomic Spectroscopy, 54 (1999) 1351-1365.

[99] X.L. Mao, A.C. Ciocan, R.E. Russo, Preferential Vaporization during Laser Ablation Inductively Coupled Plasma Atomic Emission Spectroscopy, Appl. Spectrosc., 52 (1998) 913-918.

[100] T.E. Itina, W. Marine, M. Autric, Monte Carlo simulation of pulsed laser ablation from two-component target into diluted ambient gas, Journal of Applied Physics, 82 (1997) 3536-3542.

[101] H. Dang, Z. Han, Q. Qin, Angle- and time-resolved mass spectrometric study on pulsed laser ablation of an La-Ca-Mn-O target, Science in China Series A: Mathematics, 41 (1998) 1309-1314.

[102] J. Chen, Analysis of Laser-Induced Plasmas Utilizing $^{18}O_2$ as Oxygen Tracer, in, Diss., Eidgenössische Technische Hochschule ETH Zürich, Nr. 22019, 2014.

[103] C. Phipps, Laser ablation and its applications, Springer, 2007.

[104] G.K. Koyanagi, D. Caraiman, V. Blagojevic, D.K. Bohme, Gas-phase reactions of transition-metal ions with molecular oxygen: room-temperature kinetics and periodicities in reactivity, The Journal of Physical Chemistry A, 106 (2002) 4581-4590.

[105] I. Stefanovic, N.K. Bibinov, A.A. Deryugin, I.P. Vinogradov, A.P. Napartovich, K. Wiesemann, Kinetics of ozone and nitric oxides in dielectric barrier discharges in O_2/NO_x and N_2/O_2 /NO_x mixtures, Plasma Sources Science and Technology, 10 (2001) 406.

[106] J. Chen, J.G. Lunney, T. Lippert, A. Ojeda-GP, D. Stender, C.W. Schneider, A. Wokaun, Langmuir probe measurements and mass spectrometry of plasma plumes generated by laser ablation of $La_{0.4}Ca_{0.6}MnO_3$, Journal of Applied Physics, 116 (2014) 073303.

[107] L. Chanin, A. Phelps, M. Biondi, Measurements of the attachment of low-energy electrons to oxygen molecules, Physical Review, 128 (1962) 219.

[108] D. Schröder, H. Schwarz, S. Shaik, Characterization, orbital description, and reactivity patterns of transition-metal oxo species in the gas phase, in: Metal-Oxo and Metal-Peroxo Species in Catalytic Oxidations, Springer, 2000, pp. 91-123.

[109] E.R. Fisher, J.L. Elkind, D.E. Clemmer, R. Georgiadis, S.K. Loh, N. Aristov, L.S. Sunderlin, P.B. Armentrout, Reactions of fourth-period metal ions (Ca^+-Zn^+) with O_2: Metal-oxide ion bond energies, The Journal of Chemical Physics, 93 (1990) 2676-2691.

[110] G.K. Koyanagi, D.K. Bohme, Oxidation reactions of lanthanide cations with N_2O and O_2: Periodicities in reactivity, The Journal of Physical Chemistry A, 105 (2001) 8964-8968.

[111] M.H. Stans, Bond dissociation energies in simple molecules, NIST Spec. Publ, 1 (1970).

[112] W. Chaibi, J.R. Peláez, C. Blondel, C. Drag, C. Delsart, Effect of a magnetic field in photodetachment microscopy, The European Physical Journal D, 58 (2010) 29-37.

[113] L. Torrisi, L. Andò, G. Ciavola, S. Gammino, A. Barnà, Angular distribution of ejected atoms from Nd:YAG laser irradiating metals, Review of Scientific Instruments, 72 (2001) 68-72.

[114] N.M. Bulgakova, A.V. Bulgakov, O.F. Bobrenok, Double layer effects in laser-ablation plasma plumes, Physical Review E, 62 (2000) 5624.

[115] G. Hairapetian, R. Stenzel, Particle dynamics and current-free double layers in an expanding, collisionless, two-electron-population plasma, Physics of Fluids B: Plasma Physics (1989-1993), 3 (1991) 899-914.

[116] A. Morozov, A. Evtushenko, A. Bulgakov, Gas-dynamic acceleration of laser-ablation plumes: Hyperthermal particle energies under thermal vaporization, Applied Physics Letters, 106 (2015) 054107.

[117] R. Johnson, M. Liu, C. Tully, Collisional dissociation cross sections for $O+O_2$, CO and N_2, O_2+O_2, $N+N_2$, and N_2+N_2, Planetary and Space Science, 50 (2002) 123-128.

[118] P. Cosby, Electron-impact dissociation of oxygen, The Journal of chemical physics, 98 (1993) 9560-9569.

[119] A. Wynne, B. Stuart, Rate dependence of short-pulse laser ablation of metals in air and vacuum, Appl Phys A, 76 (2003) 373-378.

[120] J. Turcaud, K. Morrison, A. Berenov, N.M. Alford, K. Sandeman, L. Cohen, Microstructural control and tuning of thermal conductivity in $La_{0.67}Ca_{0.33}MnO_{3\pm\delta}$, Scripta Materialia, 68 (2013) 510-513.

[121] T.P. Dumont, Laser interaction with materials: From transparent materials to thin films, in, Diss., Naturwissenschaften, Eidgenössische Technische Hochschule ETH Zürich, Nr. 16620, 2006, 2006.

[122] V.K. Malik, I. Marozau, S. Das, B. Doggett, D.K. Satapathy, M. Uribe-Laverde, N. Biskup, M. Varela, C. Schneider, C. Marcelot, Pulsed laser deposition growth of heteroepitaxial $YBa_2Cu_3O_7/La_{0.67}Ca_{0.33}MnO_3$ superlattices on $NdGaO_3$ and $Sr_{0.7}La_{0.3}Al_{0.65}Ta_{0.35}O_3$ substrates, Physical Review B, 85 (2012) 054514.

Curriculum vitae

Name	Alejandro Ojeda González-Posada

Date of birth	24th August 1981

Place of birth	Las Palmas de Gran Canaria, Spain

Nationality	Spanish

Education

2013-2016	Doctoral thesis *"Physical processes in pulsed laser deposition"*, Swiss Federal Institute of Technology Zürich (ETHZ) and Paul Scherrer Institut (PSI, Energy and Environment Research Department, Materials Group), Switzerland
	Supervisors: Prof. Dr. A. Wokaun and Prof. Dr. T. Lippert
2007-2008	MSc in racing engine design with the thesis: "*Investigation of oil leakage in a camshaft phasing system by computer simulations and experiments*", Oxford Brookes University, United Kingdom
2005-2006	Eng. thesis: "*Simulation of variable valve timing and lift on a natural gas turbo engine"*, Politecnico di Torino (Erasmus programme) and Universidad de Las Palmas de Gran Canaria, Italy and Spain
1999-2005	Ingeniero superior industrial (especialidad mecánica), Universidad de Las Palmas de Gran Canaria, Spain
1995-1999	Jesuits school of Las Palmas de Gran Canaria, Spain

Professional experience

2014-today	Co-founder and Managing director at UrbanAlps AG, Switzerland
2009-2013	Project leader in R&D projects for future technologies, ALSTOM Power, Switzerland
2007-2007	Drivetrain test engineer, NISSAN Technical Centre Europe, Barcelona, Spain

Publications

Reviewed papers

A. Ojeda-G-P, C.W. Schneider, M. Döbeli, T. Lippert, A. Wokaun, *The importance of pressure and mass ratios when depositing multi-element oxide thin films by pulsed laser deposition*, *Applied Surface Science* 389 (2016): 126-134.

A. Ojeda-G-P, C.W. Schneider, M. Döbeli, T. Lippert, A. Wokaun, *Angular distribution of species in pulsed laser deposition of $La_xCa_{1-x}MnO_3$*, Applied Surface Science, 336 (2015) 150-156.

A. Ojeda-G-P, C.W. Schneider, M. Döbeli, T. Lippert, A. Wokaun, *The flip-over effect in pulsed laser deposition: Is it relevant at high background gas pressures?,* Applied Surface Science, 357, Part B (2015) 2055-2062.

A. Ojeda-G-P, C.W. Schneider, T. Lippert, A. Wokaun, *Pressure and temperature dependence of the laser-induced plasma plume dynamics*, Journal of Applied Physics, 120, 225301 (2016)

J. Chen, J.G. Lunney, T. Lippert, A. Ojeda-G-P, D. Stender, C.W. Schneider, A. Wokaun, *Langmuir probe measurements and mass spectrometry of plasma plumes generated by laser ablation of $La_{0.4}Ca_{0.6}MnO_3$*, Journal of Applied Physics, 116 (2014) 073303.

Oral presentations

A. Ojeda-G-P, C.W. Schneider, M. Döbeli, T. Lippert, A. Wokaun, *Plasma plume dynamics and rebounds in pulsed laser deposition: influence of background gas choice, pressure and substrate heating,* E-MRS Spring Meeting, 2-6th May 2016, Lille, France.
Graduate student award.

A. Ojeda-G-P, C.W. Schneider, M. Döbeli, T. Lippert, A. Wokaun, *The flip-over-effect in pulsed laser deposition: Is it relevant at high background gas pressures?* E-MRS Spring Meeting, 11-15th May 2015, Lille, France.

A. Ojeda-G-P, C.W. Schneider, M. Döbeli, T. Lippert, A. Wokaun, *Angular distribution of species in pulsed laser deposition of $La_xCa_{1-x}MnO_3$,* E-MRS Spring Meeting, 26-30th May 2014, Lille, France.
Awarded best student talk.

Poster presentations

A. Ojeda-G-P, C.W. Schneider, M. Döbeli, T. Lippert, A. Wokaun *, Angle resolved mass spectrometry in pulsed laser deposition – an insight into plasma chemistry,* E-MRS Spring Meeting, 2-6th May 2016, Lille, France.

A. Ojeda-G-P, C.W. Schneider, M. Döbeli, T. Lippert, A. Wokaun *, Finding paths for composition control of thin films using Pulsed Laser Deposition (PLD),* CCMX Advanced Course, 3-7th November 2014, Zürich, Switzerland.